

Development of Fast Timing Array at VECC and its Application in Nuclear Structure Study around $Z = 50$ and $N = 82$ Shell Closure

By

Shaikh Safikul Alam

PHYS04201404007

Variable Energy Cyclotron Centre, Kolkata

*A thesis submitted to the
Board of Studies in Physical Sciences*

In partial fulfillment of requirements

for the Degree of

DOCTOR OF PHILOSOPHY

of

HOMI BHABHA NATIONAL INSTITUTE

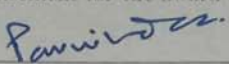


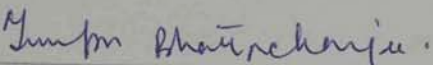
December, 2020

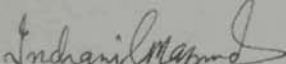
Homi Bhabha National Institute

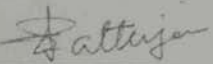
Recommendations of the Viva Voce Committee

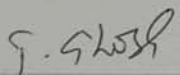
As members of the Viva Voce Committee, we certify that we have read the dissertation prepared by Shaikh Safikul Alam entitled "Development of Fast Timing Array at VECC and its Application in Nuclear Structure Study around $Z = 50$ and $N = 82$ Shell Closure" and recommend that it may be accepted as fulfilling the thesis requirement for the award of Degree of Doctor of Philosophy.

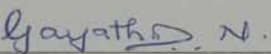

Chairman - Dr. Parnika Das Date: 18/6/2021.


Guide Convener - Dr. Tumpa Bhattacharjee Date: 18/06/2021


Examiner - Prof. Indranil Majumdar Date: 18/06/2021

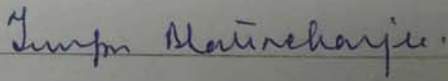

Member 1 - Prof. Sukalyan Chattopadhyay (Saha Inst. of Nucl. Phys.) Date: 18/06/2021


Member 2 - Dr. Tilak Kumar Ghosh Date: 18/06/2021


Member 3 - Dr. (Mrs.) Gayathri N. Banerjee Date: 18/6/2021

Final approval and acceptance of this thesis is contingent upon the candidate's submission of the final copies of the thesis to HBNI.

I/We hereby certify that I/We have read this thesis prepared under my direction and recommend that it may be accepted as fulfilling the thesis requirement.

Date: 18/06/2021 Guide: 
Place: VECC, Kolkata. Dr. Tumpa Bhattacharjee

¹This page is to be included only for final submission after successful completion of viva voce.

STATEMENT BY AUTHOR

This dissertation has been submitted in partial fulfillment of requirements for an advanced degree at Homi Bhabha National Institute (HBNI) and is deposited in the Library to be made available to borrowers under rules of the HBNI.

Brief quotations from this dissertation are allowable without special permission, provided that accurate acknowledgement of source is made. Requests for permission for extended quotation from or reproduction of this manuscript in whole or in part may be granted by the Competent Authority of HBNI when in his or her judgment the proposed use of the material is in the interests of scholarship. In all other instances, however, permission must be obtained from the author.

Shaikh Sajikul Alam
18/06/2021

(Shaikh Sajikul Alam)

DECLARATION

I, hereby declare that the investigation presented in the thesis has been carried out by me. The work is original and has not been submitted earlier as a whole or in part for a degree / diploma at this or any other Institution / University.

Shaikh Safikul Alam
18/06/2021

(Shaikh Safikul Alam)

List of Publications arising from the thesis

(A) Published in Peer Reviewed Journal

1. “*Measurement of Electric Quadupole moment in neutron rich $^{131,132}I$ ”
S.S. Alam, D. Banerjee, T. Bhattacharjee, P. Blaha, D. Kumar, A. Saha, M. Saha Sarkar, S. Sarkar, and S.K. Das.
European Physical Journal A 56 (2020) 269.*
2. “*Lifetimes and transition probabilities for the low-lying states in ^{131}I and ^{132}Xe .”
S.S. Alam, T. Bhattacharjee, D. Banerjee, A. Saha, M. Saha Sarkar, and S. Sarkar
Phys. Rev. C 99 (2019) 014306.*
3. “*VECC Array for Nuclear fast Timing and Angular CorRElation Studies (VENTURE)*”
S.S. Alam, T. Bhattacharjee, D. Banerjee, A. Saha, Deepak Pandit, D. Mondal, S. Mukhopadhyay, P. Bhaskar, S.K. Das, S.R. Banerjee.
Nuclear Inst. and Methods in Physics Research A 874 (2017) 103.

(C) In Symposia

1. “*Measurement of Electric Quadupole moment in neutron rich $^{131,132}I$ by Perturbed $\gamma - \gamma$ Angular Correlation Spectroscopy and Theoretical Calculations*”
S.S. Alam, D. Banerjee, T. Bhattacharjee, P. Blaha, M. Saha Sarkar, S. Sarkar, and S.K. Das
Proceedings of the **Inter. Conf. on Hyperfine Interac. and their Appl., HYPERFINE2019.**
2. “*Measurement of Quadupole moments in neutron rich Iodine nuclei*”
S.S. Alam, T. Bhattacharjee, D. Banerjee, A. Saha, M. Saha Sarkar, S. Sarkar, S.K. Das
Proceedings of the **Frontiers in Gamma ray Spectroscopy, FIG2018.**
3. “*Lifetime measurement in neutron rich nuclei around ^{132}Sn* ”
S.S. Alam, D. Banerjee, A. Saha, T. Bhattacharjee
Proceedings of the **DAE Symp. Nucl. Phys. 62 (2017) 212 .**

4. “*Measurement of Quadrupole Moment by Perturbed $\gamma-\gamma$ Angular Correlation in n-rich Iodine nuclei*”
D. Banerjee, S.K Das, **S. Alam**, T. Bhattacharjee, A. Saha
Proceedings of the **DAE-BRNS Nuclear and Radiochemistry Symposium 13 (2017)** .
5. “*Study of Nuclear Structure in odd-odd $^{122,124}I$* ”
S.S. Alam, A. Saha, T. Bhattacharjee, D. Banerjee, Md. A. Asgar, R. Banik, S. Bhattacharyya,
Soumik Bhattacharya, A. Dhal, D. Mondal, G. Mukherjee, S. Mukhopadhyay, S. Pal, D. Pandit, T.
Roy, and S.R. Banerjee.
Proceedings of the **DAE Symp. Nucl. Phys. 61 (2016) 316** .
6. “*Decay spectroscopy of fission fragments around ^{132}Sn* ”
S.S. Alam, D. Banerjee, A. Saha, T. Bhattacharjee, S.K. Das.
Proceedings of the **DAE Symp. Nucl. Phys. 61 (2016) 318** .
7. “*CeBr₃ detector array for measurement of lifetime and transition moment at VECC, Kolkata*”
S.S. Alam, T. Bhattacharjee, D. Banerjee, S. Mukhopadhyay, D. Mondal, A. Saha, D. Pandit, S.
Pal, P. Bhaskar, S.K. Das, S.R. Banerjee
Proceedings of the **DAE Symp. Nucl. Phys. 61 (2016) 320** .
8. “*Fast Timing measurement in neutron rich $^{131,132}I$* ”
S.S. Alam, T. Bhattacharjee, D. Banerjee, A. Saha, P. Das, S.K. Das.
Proceedings of the **DAE Symp. Nucl. Phys. 60 (2015) 270** .

(D) Other Publications (in Peer Reviewed Journals: not related to Thesis)

1. “*Decay spectroscopy of $^{117,118}Sn$* ”
Sangeeta Das, Anik Adhikari, **S.S. Alam**, Sathi Sharma, Suman Aich, Arkabrata Gupta, Y. Sapkota,
Ananya Das, A. Saha, S.K. Dey, Dibyadyuti Pramanik, Abhijit Bisoi, Indrani Ray, T. Bhattacharjee,
C.C. Dey, S. Sarkar, M. saha Sarkar
Nuclear Physics A 1006 (2021) 122079.
2. “*Single crystal HPGe (80%) versus BGO shielded CLOVER detector for high precision decay rate measurements : a comparative study*”

S. Pathak, P. Das, A. K. Sikdar, J. Nandi, S. Bhattacharyya, T. Bhattacharjee, Soumik Bhattacharya, **S.S. Alam**, A. Ray

Journal of Radioanalytical and Nuclear Chemistry 323 (2020) 1353.

3. *“Study of radioactivity built-up and decay with singles time-stamped data”*

S. Das, A. De, B. Dey, S. Sharma, A. Adhikari, **S.S. Alam**, A. Gupta, Y. Sapkota, A. Das, A. Saha, D. Pramanik, T. Bhattacharjee, A. Bisoi, S. Sarkar and M. Saha Sarkar

JINST 14 (2019) T09006.

4. *“Yrast and non-yrast spectroscopy of ^{199}Tl using α -induced reactions”*

Soumik Bhattacharya, S. Bhattacharyya, R. Banik, S. Das Gupta, G. Mukherjee, A. Dhal, **S.S. Alam**, Md. A. Asgar, T. Roy, A. Saha, S. Nandi, T. Bhattacharjee, A. Choudhury, Debasish Mondal, S. Mukhopadhyay, P. Mukhopadhyay, S. Pal, Deepak Pandit, I. Shaik, and S.R. Banerjee.

Phys. Rev. C 98 (2018) 044311.

5. *“Spectroscopy of low lying states in ^{150}Sm ”*

A. Saha, T. Bhattacharjee, **S.S. Alam**, D. Banerjee, M. Saha Sarkar, S. Sarkar, J.B. Gupta, P. Das, Soumik Bhattacharya, Deepak Pandit, R. Guin, S.K. Das, S.R. Banerjee.

Nuclear Physics A 976 (2018) 1.

(E) In Symposia (not related to Thesis)

1. *“Near-yrast exotic structure in ^{199}Hg ”*

Soumik Bhattacharya, S. Bhattacharyya, S. Das Gupta, R. Banik, G. Mukherjee, A. Dhal, S. Nandi, Md. A. Asgar, T. Roy, R. Raut, S.S. Ghugre, S.K. Das, S. Chatterjee, S. Samanta, Shabir Dar, A. Goswami, Sajad Ali, S. Mukhopadhyay, Debasish Mondal, **S.S. Alam**, T. Bhattacharjee, A. Saha, Deepak Pandit, Surajit Pal, S.R. Banerjee, S. Rajbanshi.

Proceedings of the **DAE Symp. Nucl. Phys. 64 (2019) 276.** .

2. *“ $\gamma - \gamma$ fast timing measurements in neutron rich Xenon nuclei”*

S.S. Alam, Devesh Kumar, Shefali Basak, D. Banerjee, S.K. Das, M. Saha Sarkar and T. Bhattacharjee.

Proceedings of the **DAE Symp. Nucl. Phys. 64 (2019) 278.** .

3. *“Lifetime measurements in neutron rich ^{129}Sn and $^{130,132}\text{Te}$ ”*
 Devesh Kumar, T. Bhattacharjee, L. Gerhard, L. Knafla, A. Esmaylzadeh, F. Dunkel, K. Schonaker, J.-M. Régis, **S.S. Alam**, S. Basak, D. Banerjee, Y.H. Kim, U. Koster, M. Saha Sarkar.
 Proceedings of the **DAE Symp. Nucl. Phys. 64 (2019) 280** .
4. *“Lifetime measurement in $N = 88$ Sm using VENTURE array”*
 Shefali Basak, **S.S. Alam**, D. Kumar, A. Saha, D. Banerjee, T. Bhattacharjee.
 Proceedings of the **DAE Symp. Nucl. Phys. 64 (2019) 282** .
5. *“Precise measurement of decay half lives of n-rich iodine isotopes after radiochemical separation”*
 D. Banerjee, D. Kumar, T. Bhattacharjee, S. Basak, **S.S. Alam**.
 Proceedings of the **DAE Symp. Nucl. Phys. 64 (2019) 286** .
6. *“Lifetime measurement of $3/2_1^+$ state of ^{117}Sn ”*
 Sangeeta Das, Suman Aich, A. Adhikari, **S.S. Alam**, Sathi Sharma, B. Dey, Arkabrata Gupta, Y. Sapkota, A. Das, A. Saha, S.K. Dey, Dibyadyut Pramanik, D. Banerjee, T. Bhattacharjee, C.C. Dey, Abhijit Bisoi, S. Sarkar, M. Saha Sarkar
 Proceedings of the **DAE Symp. Nucl. Phys. 63 (2018) 270** .
7. *“Spectroscopy of long lived fission fragments in $A \sim 100-140$ region”*
 Wasim Raja Sk, D. Banerjee, **S.S. Alam**, T. Bhattacharjee, R. Acharya, P.K. Pujari
 Proceedings of the **DAE Symp. Nucl. Phys. 63 (2018) 290** .
8. *“Lifetime measurement of low lying states of ^{27}Si ”*
 Sathi Sharma, Sangeeta Das, Arkajyoti De, Rashika Gupta, A. Gupta, A. Adhikari, A. Das, Y. Sapkota, A. Saha, **S.S. Alam**, S. Bhattacharya, R. Banik, S. Nandi, S. Das, S. Samanta, S. Chatterjee, S. Bhattacharyya, B. Dey, D. Pramanik, A. Bisoi, T. Bhattacharjee, M. Nandy, S. Sarkar, M. Saha Sarkar
 Proceedings of the **DAE Symp. Nucl. Phys. 63 (2018) 320** .
9. *“Spectroscopy of $^{160,161}\text{Ho}$ ”*
 A. Adhikari, D. Pramanik, S. Das, Arkabrata Gupta, Y. Sapkota, Ananya Das, S. Sharma, A. De, A. Saha, **S.S. Alam**, S. Das, S. Samanta, S. Chatterjee, S. Bhattacharya, R. Banik, S. Nandi, R. Raut,

- S.S. Ghugre, S. Bhattacharyya, G. Mukherjee, T. Bhattacharjee, A. Bisoi, M. Saha Sarkar, S. Sarkar
 Proceedings of the **DAE Symp. Nucl. Phys. 63 (2018) 332** .
10. *“Life-time Measurement of levels in $^{160-162}\text{Dy}$ nuclei”*
 A. Adhikari, S. Das, **S.S. Alam**, D. Pramanik, S. Sharma, Y. Sapkota, Arkabrata Gupta, Ananya
 Das, A. Saha, D. Banerjee, T. Bhattacharjee, A. Bisoi, M. Saha Sarkar, S. Sarkar
 Proceedings of the **DAE Symp. Nucl. Phys. 63 (2018) 338** .
11. *“Singles time stamped data in In-beam spectroscopy”*
 Sangeeta Das, Arkajyoti De, B. Dey, Sathi Sharma, A. Adhikari, **S.S. Alam**, Arkabrata Gupta, Y.
 Sapkota, A. Das, A. Saha, Dibyadyuti Pramanik, D. Banerjee, T. Bhattacharjee, Abhijit Bisoi, S.
 Sarkar, M. Saha Sarkar
 Proceedings of the **DAE Symp. Nucl. Phys. 63 (2018) 1144** .
12. *“VECC-INGA: An exploration of nuclear structure with light ions”*
 Soumik Bhattacharya, R. Banik, S. Nandi, Sajad Ali, S. Chatterjee, S. Das, S. Samanta, K. Basu,
 A. Choudhury, A. Adhikari, **S.S. Alam**, Shabir Dar, B. Das, Sangeeta Das, A. Dhal, A. Mondal,
 K. Mondal, P Mukhopadhyay, H. Pai, P. Ray, A. Saha, I. Shaik, C. Bhattacharya, G. Mukherjee, R.
 Raut, S.S. Ghugre, A. Goswami, S. Bhattacharyya
 Proceedings of the **DAE Symp. Nucl. Phys. 63 (2018) 1156** .
13. *“Study of nuclear structure in ^{125}I ”*
S.S. Alam, D. Banerjee, T. Bhattacharjee, A. Saha, S.W. Raja, S. Das, A. Adhikari, A. De, A.
 Gupta, A. Das, Y. Sapkota, S. Sharma, S. Dey Chaudhuri, D. Pramanik, A. Bisoi, M. Saha Sarkar,
 S. Sarkar
 Proceedings of the **DAE Symp. Nucl. Phys. 63 (2018) 356** .
14. *“Pulse processing electronics for $\gamma - \gamma$ fast timing array at VECC”*
S.S. Alam, D. Kumar, D. Banerjee, S. Dey Chaudhuri, T. Bhattacharjee
 Proceedings of the **DAE Symp. Nucl. Phys. 63 (2018) 1212** .
15. *“Determination of Fission Product Yield for Lifetime and Quadrupole Moment Measurement”*
 D. Banerjee, **S.S. Alam**, Sk Wasim Raja, A. Saha, T. Bhattacharjee
 Proceedings of the **DAE Symp. Nucl. Phys. 62 (2017) 424** .

16. *“High spin structure and neutron alignment in ^{197}Tl ”*
 S. Nandi, G. Mukherjee, H. Pai, T. Roy, Md.A. Asgar, A. Dhal, R. Banik, S. Bhattacharya, A. Saha, **S.S. Alam**, S. Bhattacharyya, C. Bhattacharya, P. Roy, T.K. Ghosh, S. Kundu, K. Banerjee, T.K. Rana, R. Pandey, S. Manna, A. Sen, S. Pal, S. Mukhopadhyay, D. Pandit, D. Mondal, T. Bhattacharjee, A. Dey, J.K. Meena, A.K. Saha, J.k. Sahoo, R. Mandal Saha, A. Choudhury, S.R. Banerjee
 Proceedings of the **DAE Symp. Nucl. Phys. 62 (2017) 80** .

17. *“Isomers in $^{117,118}\text{Sn}$ and role of neutron $1h_{11/2}$ orbit”*
 Sangeeta Das, Sathi Sharma, **S.S. Alam**, Arkabrata Gupta, Anik Adhikari, Ananya Das, A. Saha, S.K. Dey, Dibyadyuti Pramanik, Abhijit Bisoi, T. Bhattacharjee, C.C. Dey, S. Sarkar, M. Saha Sarkar
 Proceedings of the **DAE Symp. Nucl. Phys. 62 (2017) 84** .

18. *“Deformed structure based on $\nu i_{13/2}$ orbital in ^{199}Hg ”*
 Soumik Bhattacharya, S. Bhattacharyya, R. Banik, S. Das Gupta, **S.S. Alam**, A. Dhal, Md. A. Asgar, T. Roy, A. Saha, T. Bhattacharjee, S. Mukhopadhyay, D. Pandit, D. Mondal, S. Pal, S.R. Banerjee
 Proceedings of the **DAE Symp. Nucl. Phys. 62 (2017) 118** .

19. *“Decay spectroscopy of ^{118m}Sb ”*
 Sathi Sharma, Sangeeta Das, **S.S. Alam**, Arkabrata Gupta, Anik Adhikari, Ananya Das, A. Saha, Dibyadyuti Pramanik, Abhijit Bisoi, Indrani Ray, T. Bhattacharjee, S. Sarkar, M. Saha Sarkar
 Proceedings of the **DAE Symp. Nucl. Phys. 62 (2017) 204** .

20. *“Angular Correlation and lifetime measurement in ^{150}Pm ”*
 A. Saha, **S.S. Alam**, D. Banerjee, T. Bhattacharjee, S.R. Banerjee
 Proceedings of the **DAE Symp. Nucl. Phys. 61 (2016) 300** .

21. *“VECC array for Nuclear Spectroscopy (VENUS)”*
 Soumik Bhattacharya, R. Banik, **S.S. Alam**, A. Saha, Md. A. Asgar, T. Roy, A. Chowdhury, I. Sheikh, P. Mukhopadhyay, A. Dhal, T. Bhattacharjee, S. Bhattacharyya, G. Mukherjee, S. Mukhopadhyay, D. Mondal, D. Pandit, S. Pal, S.R. Banerjee
 Proceedings of the **DAE Symp. Nucl. Phys. 61 (2016) 98** .

22. “Oblate band structure based on $\pi h_{9/2}$ orbital in ^{199}Tl ”
 Soumik Bhattacharya, S. Bhattacharyya, R. Banik, G. Mukherjee, S. Das Gupta, **S.S. Alam**, A. Dhal, Md. A. Asgar, T. Roy, A. Saha, T. Bhattacharjee, S. Mukhopadhyay, D. Pandit, D. Mondal, S. Pal, S.R. Banerjee
 Proceedings of the **DAE Symp. Nucl. Phys. 61 (2016) 188** .
23. “Half-life and β -feeding measurements of ^{207}Po by γ -spectroscopy method”
 A. Dhal, R. Ghosh, A.G. Nair, G. Mukherjee, Md. A. Asgar, T. Roy, T.K. Rana, T.K. Ghosh, K. Banerjee, S. Kundu, R. Pandey, Pratap Roy, S. Manna, A. Sen, A. Dey, J.K. Meena, J.K. Sahoo, A.K. Saha, R. Banik, Soumik Bhattacharya, A. Saha, **S.S. Alam**, D. Mondal, D. Pandit, S. Mukhopadhyay, S. Pal, T. Bhattacharjee, S. Bhattacharyya, C. Bhattacharya, S.R. Banerjee
 Proceedings of the **DAE Symp. Nucl. Phys. 61 (2016) 266** .
24. “Study of multi-quasiparticle band structures in ^{197}Tl using α -beam”
 G. Mukherjee, S. Nandi, H. Pai, T. Roy, Md. A. Asgar, A. Dhal, R. Banik, Soumik Bhattacharya, A. Saha, **S.S. Alam**, S. Bhattacharyya, C. Bhattacharya, Pratap Roy, T.K. Ghosh, S. Kundu, K. Banerjee, T.K. Rana, R. Pandey, S. Manna, A. Sen, S Pal, S Mukhopadhyay, D. Pandit, D. Mondal, T. Bhattacharjee, A. Dey, J.K. Meena, A.K. Saha, J.K. Sahoo, R. Mondal Saha, A. Choudhury, S.R. Banerjee
 Proceedings of the **DAE Symp. Nucl. Phys. 61 (2016) 270** .
25. “Angular Correlation measurement around $Z=64$ ”
 N. Sensharma, **S.S. Alam**, D. Banerjee, T. Bhattacharjee, A. Saha, S.K. Das
 Proceedings of the **DAE Symp. Nucl. Phys. 60 (2015) 272** .
26. “Search for isomeric state in odd-odd ^{150}Pm ”
 A. Saha, D. Banerjee, T. Bhattacharjee, Deepak Pandit, **S.S. Alam**, P. Das, Soumik Bhattacharya, A. Choudhury, S. Bhattacharyya, A. Mukherjee, R. Guin, S.K. Das, S.R. Banerjee
 Proceedings of the **DAE Symp. Nucl. Phys. 60 (2015) 98** .

Shaikh Safikul Alam
 18/06/2021
 (Shaikh Safikul Alam)

*Dedicated to my late mother Selina Sekh,
who taught me the true meaning of
life and love*

ACKNOWLEDGEMENTS

First and foremost, my sincerest appreciation and gratitude must go to my Ph.D advisor Dr. Tumpa Bhattacharjee for her endless support, motivation, guidance and constant encouragement at every stage of my research work. Whatever I have acquired knowledge during my entire Ph.D work about skillful experimental techniques, specially, the hands-on experience of electronic setup, how to arrange and perform an experiment, how to tackle the critical problems not only during experiment but also in real life, I have learnt from her. It was a great privilege and honor to work and study under your guidance, Ma'am.

I am extremely thankful to my collaborator Dr. Debasish Banerjee for providing us the full access of the RCD lab (VECC). Without his helps and guidance it would have never been possible to complete most of the experimental work carried out in the present thesis. Special thanks to my other collaborators specially, Prof. M. Saha Sarkar (SINP), Prof. Sukhendusekhar Saha (IEST) and Prof. S.K. Das (Ex-Head, ACS, RCD-BARC, VECC) for their helpful guidance in various issues throughout the work. I am extremely thankful to the Cyclotron operators, VECC for providing good quality beams and to the staff of MEG, VECC for different necessary designs and fabrications. I am also thankful to BRNS fellowship for the financial support (Sanction No. 2013/38/02-BRNS/1927 for PRF, BRNS, dated 16 October 2013).

I would like to thank Director (VECC), Dr. Jan-e-Alam (Head, Physics Group, VECC), Dr. S. R. Banerjee (Ex-Head, Phys. Group, VECC), Dr. Chandana Bhattacharjee (Head, Exp. Nucl. Phys. Division, VECC), Dr. Parnika Das (Dean Academic, HBNI, VECC) and Dr. Tilak Ghosh (Dean Students, HBNI, VECC) for their valuable inputs, motivations and supports.

My special thanks also must go to my lab mates- Arunabha da, Devesh and Shefali with whom I have spent the best times at VECC. I also would like to thank all my friends for their lovely and joyful company in this journey.

Finally, my deepest gratitude to my parents for their care, love and priceless support in all the field of my life. I would like to thank to my elder brother and sisters; brothers-in-law and sister-in-law; uncle and aunt; and all my relatives for their unconditional support and encouragement all the time. Special thanks to Nilofar for her constant motivation and mental support to complete this journey. Last, but not least, my heartiest love for Sohail, Ivi, Tan, Ayat, Aqsa, Rahil, Arosh and Abrar for bringing priceless joyful moment in my life.

Shaikh Safikul Alam
18/06/2021

Shaikh Safikul Alam

Contents

Synopsis	v
List of Figures	xxii
List of Tables	xxiv
1 Introduction	1
1.1 Preface	1
1.2 Outline	3
2 Nuclear structure and models	5
2.0.1 Introduction	5
2.0.2 Microscopic approach: Independent particle model or Shell model	6
2.0.3 Spin-orbit coupling: Spherical single particle shell model	8
2.0.4 Deformed nuclear shapes: Nilsson model	10
3 Gamma-ray spectroscopy	19
3.1 Introduction	19
3.1.1 Electromagnetic transition probabilities	20
3.1.2 Internal conversion	24
3.1.3 Nuclear level lifetime	25
3.1.4 Mixing ratio	26
3.1.5 $\gamma - \gamma$ angular correlation	26
3.2 Detection of γ -rays: Interaction with matter	27
3.2.1 Photoelectric absorption	27
3.2.2 Compton scattering	28

3.2.3	Pair production	29
3.3	Important observables used in γ -ray spectroscopy	31
3.3.1	Detector response	31
3.3.2	Energy resolution of a detector	32
3.3.3	Gamma detection efficiency	33
3.3.4	Time resolution of a detector	34
3.4	γ -ray fast timing spectroscopy: Detectors and their uses	35
3.4.1	Semiconductor detector	36
3.4.2	Scintillator detector	38
3.5	Development and use of fast timing array: Literature survey	44
3.5.1	Detectors and PMTs used in the present thesis	45
3.5.2	Testing and development in present thesis work	49
4	Development of <u>VECC</u> Array for <u>Nuclear fast Timing and Angular CorRElation</u>	
	Studies (VENTURE): $\gamma - \gamma$ fast timing measurement	51
4.1	Importance of lifetime measurement in nuclear structure study	51
4.2	Techniques for nuclear lifetime measurement	52
4.2.1	Doppler shift method	53
4.2.2	Electronic method	57
4.2.3	The $\gamma - \gamma$ fast-timing technique	57
4.2.4	MSCD technique	63
4.2.5	GCD technique	68
4.3	Experimental setup for characterization of CeBr ₃ detectors, Development of VENTURE array, MSCD and GCD measurements	70
4.4	Characterization of CeBr ₃ detectors	73
4.4.1	Energy response, resolution and linearity	73
4.4.2	Absolute efficiency	76
4.4.3	Time resolution	76
4.5	Applications of MSCD technique with 2 detectors	78
4.6	Applications of GCD technique with VENTURE array	81

5	VENTURE array for $\gamma - \gamma$ angular correlation measurement	85
5.1	Introduction:	85
5.1.1	$\gamma - \gamma$ directional unperturbed angular correlation:	86
5.1.2	$\gamma - \gamma$ directional perturbed angular correlation:	91
5.2	TDPAC method: Measurement technique of Electric Quadrupole Moment (EQM)	94
5.3	Development of an angular correlation setup	98
5.4	$\gamma - \gamma$ angular correlation measurement in ^{132}I	101
6	Production of neutron-rich nuclei	103
6.0.1	Nuclear fission	105
6.0.2	Experimental procedure: Present work	107
7	Lifetimes and transition probabilities for the low lying states in ^{131}I and ^{132}Xe	113
7.1	Introduction	113
7.2	Experimental details	114
7.3	Results	115
7.4	Shell model calculation	119
7.5	Discussion	123
7.5.1	^{131}I	124
7.5.2	^{132}Xe	129
8	Measurement of EQM in neutron-rich $^{131,132}\text{I}$	131
8.1	Introduction	131
8.2	Methods and materials	132
8.2.1	Production of $^{131,132}\text{I}$ and sample preparation	133
8.2.2	Experimental details	133
8.3	Experimental results	134
8.3.1	Determination of EFG	135
8.3.2	Determination of EQM using TDPAC method	136
8.4	Discussion	141
8.4.1	Evolution of collectivity	141
8.4.2	Shell model calculation	143

9	Testing of VENTURE for in-beam measurement: Lifetime measurement in ^{124}I	145
9.1	Introduction	145
9.2	Experimental details	146
9.3	Generation of PRD curve	148
9.4	Analysis and results	148
9.5	Discussion	152
10	Summary and outlook	155
10.1	Summary	155
10.2	Future outlook	157
	Bibliography	159

List of Figures

1	Setup of VENTURE array in different configuration.	viii
2	The B(E2) values for the decays of ^{131}I and ^{132}Xe levels in comparison to that in neighboring nuclei. The filled circles (red) represents the B(E2) values calculated from the level lifetimes taken from NNDC database [NNDC].	xi
3	Illustration of the manufactured angular correlation setup.	xii
4	Experimental quadrupole moments (magnitude) for the (a) $7/2_1^+$ and (b) $5/2_1^+$ levels of odd-A I are shown as function of neutron number. The adopted values of quadrupole moments have been taken from Ref. [STO16], the maximum and minimum values, known for a particular isotope, have been taken from the IAEA compilation [IAEA]. The value at $N = 78$ for the $5/2_1^+$ level of ^{131}I is measured in the present work and is shown. Linear extrapolations up to $N = 82$ are shown for $7/2^+$ level (black dotted line) and $5/2^+$ level (red dashed and blue solid lines) with different data sets.	xiii
2.1	The evolution of shell structure with the addition of ℓ^2 and spin-orbit term to the simple harmonic oscillator potential. The figure has been taken from Ref. [SAH18a]. Blue lines represent the intruder orbital.	10
2.2	An illustration of various nuclear shapes in $(\beta - \gamma)$ plane using Lunds conventions [AND76].	12
2.3	The Nilsson diagram for Z or $N = 50 - 82$ shell is shown. The diagram has been taken from Ref. [NIL55].	14
2.4	Asymptotic quantum numbers of axially deformed nucleus are shown.	15
3.1	An illustration of photoelectric effect.	28
3.2	An illustration of Compton scattering process.	29
3.3	An illustration of pair production process.	30

3.4	Representation of relative probability (absorption cross-section) of the three types of interactions in Ge ($Z = 32$) and Si ($Z = 14$) as a function of the γ -ray energy has been shown. Image taken from Experiments in Nuclear Science published by EG & G Ortec.	30
3.5	A typical energy spectrum due to Compton and photopeak effect of a gamma detector: (A) shows an ideal γ -ray spectrum and (B) shows a real γ -ray spectrum.	31
3.6	A schematic geometry of the crystals of a clover detector. The crystals are arranged like a four leaf clover.	38
3.7	An illustration of the energy level of an organic scintillator molecule. 'S' denotes the singlet state and 'T' denotes the triplet state.	40
3.8	An illustration of energy band structure along with activator sites of an inorganic scintillation crystal.	41
3.9	A schematic design of a scintillator detector with a PM tube.	42
3.10	An illustration of a schematic design of biasing supply in a PMT (a): refers to the positive polarity biasing supply at the anode and the photocathode is grounded while, (b): refers to the negative polarity biasing supply at the photocathode which must be isolated from ground and the anode is kept at ground potential. Both diagrams are taken from [KNO10] where the other specifications of resistances and capacitors used in the diagram have been given. Only, in case of positive polarity, an extra coupling capacitor C_c must be connected with the anode output to block the anode high voltage but transmit only the signal pulse to the associated electronic circuit at ground potential.	43
3.11	A schematic sketch of the band structure of a LaBr_3 crystal doped with Ce^{3+} ions.	46
3.12	The figure shows the background spectrum of a $1'' \phi \times 1''$ thick $\text{LaBr}_3(5\% \text{Ce})$ crystal coupled with an 8-stage Hamamatsu R2083 PMT. The emission energy peaks of intrinsic activity are clearly visible [CHA20].	47
3.13	A schematic design of a Hamamatsu R9779 PMT and its biasing system [HAM09].	49
4.1	A schematic design of the RDM method.	54
4.2	A schematic design of the DSAM method.	55
4.3	Illustration of a time spectrum due to convolution of a prompt time peak (PRF) with the exponential decay slope.	58
4.4	An illustration of prompt and delayed time distributions for a fast-timing setup.	60

4.5	A simple design of two detector assembly to illustrate delayed and anti-delayed time distribution with prompt response function.	61
4.6	The delayed and anti-delayed time distribution with respective prompt response function. The difference between both the prompt response function gives the PRD whereas, difference between time distribution of delayed and anti-delayed is a measure of PRD with two times of level mean lifetime.	62
4.7	Two prompt timing branches corresponding to detection procedures of feeding and decaying γ -rays by start and stop detector of an ideal setup and also the delayed timing branches having lifetime τ have been shown by the solid curve and dashed curve, respectively. The figure is taken from Ref. [REG10] and is modified slightly.	64
4.8	The linearly combined centroid difference ΔC curve (dashed line) related to lifetime τ is shifted by $+2\tau$ from the PRD curve [REG10].	65
4.9	The VENTURE array of eight CeBr ₃ detectors coupled to the VENUS array of six clover HPGe detectors is shown.	71
4.10	The timing electronics setup used for the signal processing with the VENTURE array.	71
4.11	Stand alone setup of VENTURE array with six CeBr ₃ detectors which are arranged on angular correlation table (discussed in Section 5.3 of Chapter 5).	72
4.12	The energy spectra obtained with CeBr ₃ detector and Clover HPGe detector using a ¹⁵² Eu source.	73
4.13	The experimental and simulated γ spectra for the CeBr ₃ detector using ⁶⁰ Co source.	74
4.14	Few representative energy response curves at different bias voltages.	75
4.15	(a) Variation of FWHM obtained at 622 keV is shown with the applied bias voltages. (b) Variation of FWHM with γ energy at a fixed bias voltage.	75
4.16	The measured efficiency of the CeBr ₃ detector at 16 cm is compared with GEANT3 simulation and add-back efficiency of a Clover HPGe detector.	76
4.17	The time resolution is shown as a function of CF delay.	77
4.18	The time resolution is shown as a function of bias voltage of the PMT.	78
4.19	The TAC spectra obtained with two CeBr ₃ detectors while using the ⁶⁰ Co and ¹⁰⁶ Ru source. The obtained FWHM values are indicated in the corresponding plot.	78

4.20	The energy spectra obtained by gating on different reference energies, viz., (a) 344 keV, (b) 444 keV, (c) 244 keV and (d) 1408 keV transitions, by using the ^{152}Eu source. (e) The energy spectrum obtained with ^{106}Ru source is shown.	79
4.21	Few delayed and anti-delayed time spectra obtained with the two CeBr_3 detector setup using cascades of ^{152}Gd (a,b), ^{152}Sm (c) and ^{106}Pd (d) are shown. The delayed time distributions are shown with blue (dotted) and the anti-delayed with red (solid) line. (For interpretation of the references to colour in this figure legend, the reader is referred to the web version of this article.)	79
4.22	(a) The PRD curve obtained with two CeBr_3 detectors. The solid line shows the fit to these data points by using the function described in Eq. (4.22). (b) The fit residuum is shown for the data points with respect to a 3σ deviation for the PRD curve.	80
4.23	The time difference spectra obtained with different combinations of CeBr_3 detectors of the VENTURE array.	81
4.24	The total spectrum (a) obtained from ^{133}Ba source along with the 302 keV gate (b), 276 keV gate (c) and total spectrum from ^{106}Ru source (d) have been shown.	81
4.25	The delayed and anti-delayed time spectra obtained with the cascades of ^{152}Eu , ^{106}Ru and ^{133}Ba sources using VENTURE array. The delayed time distributions are shown with blue (dotted) and the anti-delayed with red (solid) line.	82
4.26	(a) The ungated energy spectrum. (b) The 244 keV gated spectrum using neighbouring detectors showing ‘ghost peaks’ (c) The 244 keV gated spectrum using non-neighbouring detectors which show clean peaks.	83
4.27	(a) The \overline{PRD} curve obtained with the VENTURE array is shown. The solid line shows the fit to these data points by using the function described in Eq. (4.22). (b) The fit residuum is shown for the data points with respect to a 3σ deviation for the PRD curve.	84
5.1	A schematic diagram of a three level cascade emitting two successive γ -rays along with sublevel splitting and transition between them is shown.	87
5.2	A schematic diagram of arrangement of two detectors for measuring angular correlation has been shown.	88
5.3	A schematic diagram of (a) a pure γ - γ transition and (b) a mixed γ - γ transition.	90

5.4	The figure shows an illustration of the precession of nuclear angular momentum I around the symmetry axis of an EFG [STE55].	94
5.5	Splitting of a $I = 5/2$ state due to interaction of static EFG: (a) when $EFG = 0$; (b) when $EFG \neq 0$ but $\eta = 0$; (c) when EFG and η both are $\neq 0$ [ADL78]. The shift in the levels due to η are not to scale.	95
5.6	Illustration and brief descriptions of the manufactured angular correlation setup.	98
5.7	The simplified decay scheme of ^{60}Ni , as populated from the decay of ^{60}Co source.	99
5.8	The figure shows the distribution of normalized angular correlation $\mathcal{W}(\theta)$ as a function of θ for 1173-1332 keV cascade of ^{60}Ni and the obtained experimental angular correlation coefficient, A_2 and A_4 , from the fitting parameters.	100
5.9	The simplified decay scheme of ^{132}I , as populated from the decay of ^{132}Te source.	100
5.10	The figure shows the distribution of normalized angular correlation $\mathcal{W}(\theta)$ as a function of θ for 228-50 keV cascade of ^{132}I and the obtained experimental angular correlation coefficient, A_2 and A_4 , from the fitting parameters, after incorporating the geometrical correction factor.	101
6.1	The figure shows the chart of nuclides within the border line of proton and neutron drip lines along with $N = Z$ line. The stable nuclei are shown in black squares whereas, the nuclei, already studied or observed, are shown in different grades of color depending on the different decay modes. The white area shows the unknown nuclei which remain mostly on the neutron-rich side. The horizontal and vertical lines represent the number of magic nucleons. The figure taken from [KHAL04] has been modified slightly.	104
6.2	Experimentally observed α -induced fission cross-section of different thorium and uranium isotopes as a function of beam energy.	106
6.3	Mass distribution of fission fragments from thermal neutron induced fission [KRA87].	107
6.4	The experimental setup of electrodeposition technique used, in the present thesis work, for preparation of targets is shown. The figure has been taken from Ref. [SAH18a].	108
6.5	An illustration of Stacked foil arrangement.	109
6.6	The snapshot of the flange and the preparation of stacked foil on it.	109
6.7	The illustration of the fission reaction on ^{nat}U target with α -beam.	110
6.8	The procedure of radiochemical separation technique for separation of tellurium isotopes from fission products is shown.	111

- 7.1 The total projections (without any background subtraction) obtained from the CeBr₃ (blue dash-dotted line) and Clover detectors (red solid line) are shown from CeBr₃-CeBr₃ and CeBr₃-Clover coincidences, respectively. The γ -rays from different isotopes are identified and marked with different colours of text for I(blue), Xe(black) and Cd (red) (contamination). 114
- 7.2 The CeBr₃ energy gated projections of CeBr₃ (blue dash-dotted lines) and Clover (red solid lines) detectors are shown with gate on (a) feeder (630 keV) and (b) decay (668 keV) γ -rays of 630-668 keV cascade of ¹³²Xe. The photopeaks observed in (a) and (b) are marked with \star and $\#$, respectively, in case they arise from known γ - γ coincidences or from the coincidence with the Compton background under the gating transition. The background analysis for this cascade are shown in panels (c) and (d) where ΔC_{BG} values are shown with respect to PRD = 0 at E_{ref} . The PRD curve is also shown with black dashed line by making PRD = 0 at E_{ref} . The red dash-dotted line is drawn to guide the eye for ΔC or PRD = 0. 116
- 7.3 The CeBr₃ energy gated projections of CeBr₃ (blue dash-dotted lines) and Clover (red solid lines) detectors are shown with gate on (a) feeder (1126 keV) and (b) decay (774 keV) γ -rays of 1126-774 keV cascade of ¹³¹I. The background analysis for this cascade are shown in panels (c) and (d) where ΔC_{BG} values are shown with respect to PRD = 0 at E_{ref} . The PRD curve is also shown with black dashed line by making PRD = 0 at E_{ref} . The red dash-dotted line is drawn to guide the eye for ΔC or PRD = 0. 117
- 7.4 The delayed and anti-delayed TAC spectra for few cascades of ¹³²Xe (a - d) and ¹³¹I (e - h) nuclei, used for the lifetime measurement with GCD method. The delayed and anti-delayed time distributions are shown with red (solid) and blue (dotted) lines, respectively. 118
- 7.5 The time distribution obtained for the 102-241 keV cascade with an appropriate background subtraction is shown. 120
- 7.6 The B(E2) values for the decay of 774 keV, 11/2⁺ level in ¹³¹I in comparison to that in neighboring nuclei is shown. The filled circles (red) represent the values calculated from the level lifetimes taken from NNDC database [NNDC] and the open circle (blue) is for ¹³¹I and is measured in the present work. The branching and mixing ratios are taken from NNDC database. 126
- 7.7 The systematics of E1 decays from the 11/2⁻ levels in the iodine nuclei around ¹³²Sn. . . . 126

7.8	The systematics of E1 decays from the $13/2^-$ and $15/2^-$ levels in the I and Sb nuclei around ^{132}Sn	127
7.9	The B(E2) values for the decays of ^{132}Xe levels in comparison to that in neighboring nuclei. The filled circles represent the values calculated from the level lifetimes taken from NNDC database [NNDC]. The open circles are for ^{132}Xe and are measured in the present work. The branching and mixing ratios are taken from NNDC database.	130
8.1	XRD analysis performed after reduction of telluric acid to Te metal followed by annealing. The peaks are marked with the (h, k, l) values corresponding to the crystalline trigonal phase of Te metal with space-group $P3_121$	134
8.2	The simplified decay scheme for ^{132}I , as populated from the decay of ^{132g}Te . The γ -rays of interest in the measurement of EQM are shown in red. The two other γ -rays are shown in blue. The conversion coefficients have been used while showing the intensities of the γ lines (proportional to the width of the transitions) and the converted intensity is indicated with the white portion in the width of the transition. The data has been taken from ENSDF [KHA05].	135
8.3	The simplified decay scheme for ^{131}I , as populated from the decay of ^{131m}Te and relevant in the present measurement. The γ -rays of interest in the measurement of EQM are shown in red. The γ -rays with energy below 600 keV are shown in blue and the higher energy γ -rays are shown in black. The conversion coefficients have been used while showing the intensities of the γ lines (proportional to the width of the transitions) and the converted intensity, if any, is indicated with the white portion in the width of the transition. The data has been taken from ENSDF [KHA06]. The J^π of the levels are adopted from Ref. [ALA19]. The levels marked with * have uncertain J^π which are not shown.	135
8.4	The representative total projection obtained with the BGO suppressed Clover HPGe and the $\text{LaBr}_3(\text{Ce})$ detectors are plotted. The comparison clearly identified the photopeaks required for the subsequent TDPAC analysis and other γ peaks that are generated from the decay of radiochemically separated tellurium activity.	137

- 8.5 The representative gated projections are shown for (a) 50 keV and (b) 150 keV, obtained from the data taken with Clover HPGe and the LaBr₃(Ce) detectors, respectively, corresponding to the 228-50 keV and 452-150 keV cascades of ¹³²I and ¹³¹I, respectively. These projections were used for the generation of coincidence time spectra with $\gamma - \gamma$ energy ('START-STOP') gating in two LaBr₃(Ce) detectors. The close lying contamination peaks from the daughter products, that might arise from the coincidence with underlying Compton background, are also marked. 137
- 8.6 The representative background subtracted time projections are shown for (a) 228-50 keV and (b) 452-150 keV, respectively, obtained from the data taken with the TDPAC setup. The time values in the x-axis is the time difference measured with the TAC module having a total range of 500 ns. The feeding transitions were selected from the 'START' detector and the decaying transition from the 'STOP' detectors of the setup. 138
- 8.7 TDPAC spectra (left) and their Fourier transforms (right) for the 50 keV, 3_1^+ level of ¹³²I and 150 keV, $5/2_1^+$ level of ¹³¹I, respectively. The blue circles correspond to the experimental data and the red solid lines represent the fitting. 140
- 8.8 Experimental quadrupole moments (magnitude) for the (a) $7/2_1^+$ and (b) $5/2_1^+$ levels of odd-A I are shown as a function of neutron number. The adopted values of quadrupole moments have been taken from Ref. [STO16], the maximum and minimum values, known for a particular isotope, have been taken from the IAEA compilation [IAEA]. Errors have been considered but not visible in some cases as the corresponding error bars are smaller than the size of the symbol used. The value at $N = 78$ for the $5/2_1^+$ level of ¹³¹I is measured in the present work and is shown. Linear extrapolations up to $N = 82$ are shown for $7/2^+$ level (black dotted line) and $5/2^+$ level (red dashed and blue solid lines) with different data sets. See text for details. 142
- 8.9 Deformation (magnitude), as deduced from the experimental quadrupole moments, are plotted with neutron numbers. The experimental quadrupole moments for the $5/2_1^+$ levels of odd-A iodine (I), Cesium (Cs), Lanthanum (La) and Praseodymium (Pr) nuclei have been taken from Ref. [STO16], except that of ¹³¹I that is measured in the present work. Errors have been considered but not visible in some cases as the corresponding error bars are smaller than the size of the symbol used. The error is not shown in case of La as it is very high (100%). 143

9.1	Production cross-section of the residues produced in the fusion reaction $^{123}\text{Sb}(\alpha, xn)$ using PACE IV calculation.	147
9.2	In-beam setup of VENTURE array of six CeBr_3 detectors coupled to VENUS array of six Clover detectors is shown.	147
9.3	The PRD curve (a) obtained with the VENTURE array of in-beam setup and the fit residuum (b) along with 3σ have been shown.	149
9.4	The level scheme of ^{124}I taken from Ref. [MOO11] has been shown.	149
9.5	The total energy projections of both CeBr_3 (red, dot) and Clover (blue, solid) obtained from $\text{CeBr}_3\text{-CeBr}_3\text{-Clover}$ and $\text{Clover-Clover-CeBr}_3$ triple coincidence data, respectively, have been shown. The strong photopeaks from ^{122}I and ^{124}I are marked with \star and $\#$ signs, respectively. The $\$$ sign has been used to mark photopeaks which may be new transitions or may come from other nuclei that have been also produced in the same fusion reaction.	150
9.6	The CeBr_3 (red) and Clover (blue) gated energy spectrums from $\text{CeBr}_3\text{-CeBr}_3\text{-Clover}$ and $\text{Clover-Clover-CeBr}_3$ triple coincidence data, respectively, are shown. (a) The 143 keV energy has been projected in both Clover and CeBr_3 with the double gate at 379 keV in Clover and at 302 keV in CeBr_3 and (b) The 302 keV energy has been projected in both Clover and CeBr_3 with the double gate at 379 keV in Clover and at 143 keV in CeBr_3	151
9.7	The CeBr_3 (red) and Clover (blue) gated energy spectrums from $\text{CeBr}_3\text{-CeBr}_3\text{-Clover}$ and $\text{Clover-Clover-CeBr}_3$ triple coincidence data, respectively, are shown. (a) The 379 keV energy has been projected in both Clover and CeBr_3 with the double gate at 143 keV in Clover and at 302 keV in CeBr_3 and (b) The 302 keV energy has been projected in both Clover and CeBr_3 with the double gate at 143 keV in Clover and at 379 keV in CeBr_3	152
9.8	The delayed and anti-delayed TAC spectra of cascade (302-143) and (379-302) keV of ^{124}I , used for the lifetime measurement in GCD method, are shown. The red solid line corresponds to the delayed time distribution and the blue dotted line correspond to the anti-delayed time distribution.	153
10.1	The design of the second phase of the VENTURE has been shown. The figure (a) represents the front view along with the beam line and figure (b) represents the top view of the array.	158

List of Tables

3.1	Relation between transition probability $\mathcal{T}(\sigma\mathcal{L})$ and reduced transition probability $\mathcal{B}(\sigma\mathcal{L})$. The units of $\mathcal{B}(\mathcal{E}\mathcal{L})$, $\mathcal{B}(\mathcal{M}\mathcal{L})$, $\mathcal{T}(\sigma\mathcal{L})$ and \mathcal{E} are given in $e^2fm^{2\mathcal{L}}$, $\mu_N^2fm^{2\mathcal{L}-2}$, sec^{-1} and MeV, respectively [MOR76].	23
3.2	The Weisskopf estimate of transition probability $\mathcal{T}(\sigma\mathcal{L})$ and reduced transition probability $\mathcal{B}(\sigma\mathcal{L})$ upto multipolarity(\mathcal{L}) equals to 4 for both electric and magnetic transition. The units of $\mathcal{B}(\mathcal{E}\mathcal{L})$, $\mathcal{B}(\mathcal{M}\mathcal{L})$, $\mathcal{T}(\sigma\mathcal{L})$ and \mathcal{E} are given in $e^2fm^{2\mathcal{L}}$, $\mu_N^2fm^{2\mathcal{L}-2}$, sec^{-1} and MeV, respectively [MOR76].	23
3.3	The above Table represents the Comparison among different scintillator detectors. Only fast decay component of all the mentioned detectors and their associated properties have been compared. The size of the both mentioned $LaBr_3(Ce)$ and $CeBr_3$ detectors are $1'' \phi \times 1''$ thick whereas, $LaBr_3$ is doped with 5% $CeBr_3$. Only main properties are compared for those detectors where, the terms ' ρ ' refers to specific gravity of the material; ' λ_{max} ' refers to maximum spectral emission wavelength; ' τ_d ' refers decay time; 'LY' refers to Light Yield of the crystal and 'R' refers to Energy Resolution at 662 keV.	48
3.4	Summarized of the main properties of XP2020/URQ and R9779 PMT [PHOTO, HAM09, FRA13]. \star refers to the Total Transit Spread (TTS) in the PMT and the FWHM of this distribution is a measure of time jitter.	50
4.1	Different techniques with their range, timing accuracy, measuring techniques have been summarized.	52
4.2	FWHM values obtained for different energy cascades with the VENTURE array.	80
4.3	The measurement of level lifetime for different levels of ^{106}Pd and ^{133}Cs , using VENTURE array.	82

5.1	The above Table shows a comparison of angular correlation coefficient values obtained from experimental result and theoretical calculation for 1173-1332 keV cascade of ^{60}Ni . The geometrical correction factors for both A_2 and A_4 are also tabulated.	99
7.1	Levels of ^{132}Xe and ^{131}I , for which lifetime measurements have been carried out in the present work. The lifetimes are calculated by using the equation: $\tau = \frac{1}{2}(\Delta C_{FEP} - \text{PRD})$. The quoted errors in lifetime are calculated by considering the standard deviation, i.e., $2\sigma \sim 7$ ps, obtained in the generation of PRD curve and the errors estimated for the ΔC values. The lifetimes marked with \star have been considered for some systematic error as described in text. For the cases where the measured lifetimes are less than the estimated error, the upper limits of lifetimes are shown. The J^π values are taken as per the assignments shown in Table 7.2. The measured lifetimes have been compared to the known values obtained from literature [JAK02, KHA06, KHA05, NAV90, RAM01] whereas available and rest are the newly measured values.	115
7.2	The excitation energy, most dominant particle partitions and level lifetimes for the low lying levels in ^{132}Xe and ^{131}I , obtained from shell model calculation with NUSHELLX, are shown. The experimental values are also shown for comparison. (a) shows the % probability of coupling between a particular combination of I_π and I_ν . (b) represents the % probability of a specific partition for a particular coupling.	121
7.3	The B(E1) and B(E3) transition strengths for the decay of negative parity levels in ^{131}I . . .	128
8.1	The EFG values obtained for iodine in tellurium(Te) with known values of quadrupole frequencies and quadrupole moments (Row 1-3). (a) The EFG value is quoted as given in Ref. [OOM79]. (b) Represents the V_{zz} obtained with scaling the EFG of Row 4 with the latest value of quadrupole moment [PYY18]. See text for details.	136
8.2	The values for V_{zz} , ω_Q and Q-mom, obtained in the present work for the first excited levels of $^{131,132}\text{I}$. The sign of the EQM could not be determined in the present experiment and only magnitudes are shown.	140
9.1	The measurement of lifetime of different levels in ^{124}I in the present work using VENTURE array have been shown.	152

Chapter 10

Summary and outlook

10.1 Summary

In the present thesis work, the $\gamma - \gamma$ fast timing array, abbreviated as VENTURE, consisting of multiple states of the art ultra-fast CeBr₃ detectors, has been developed at VECC, Kolkata for the measurement of nuclear level lifetimes down to few ps. The VENTURE array is the first $\gamma - \gamma$ fast timing array in India and possibly, the first CeBr₃ array in the World. In the process of developing the present array, the CeBr₃ detector of dimension 1" $\phi \times 1$ " thick and coupled to a Hamamatsu R9779 PMT has been characterised for its spectroscopic properties like energy response, energy and time resolution, and absolute efficiency. The operational condition for the detectors at the bias voltage of -1200 V and a CF delay of 0.8 ns were found to be optimum on the basis of linear response and best time resolution of the detectors. The present thesis reports a time resolution of 144(1) ps and 109(1) ps for a single CeBr₃ detector using 622-512 keV (¹⁰⁶Ru) and 1173-1332 keV (⁶⁰Co) cascades, respectively, and an energy resolution of 4.5% at 622 keV (¹⁰⁶Ru). The present work also demonstrates, for the first time, the use of CeBr₃ detectors towards the measurement of nuclear level lifetime using recently developed GCD technique. The application of common start timing technique has also been implemented with the GCD method for the first time and the methodology has been successfully explored to measure nuclear level lifetime in both off-beam and in-beam arrangement of the VENTURE array. In case of off-beam setup of VENTURE array, the lifetimes of few levels of ¹⁰⁶Pd and ¹³³Cs have been measured successfully with the GCD method using the standard ¹⁰⁶Ru and ¹³³Ba sources, respectively, and compared with the available literature data. In case of in-beam testing of VENTURE array, the lifetimes of few low-lying levels in ¹²⁴I, populated directly with ^{nat}Sb(α , xn) reaction, have been

successfully measured for the first time. The present work, thus, displays the capability of the VENTURE array for precise measurements of nuclear level lifetimes in sub-nanosecond region in both case of off-beam and in-beam data.

After successful exploration of GCD method with the VENTURE array, the same has been implemented to study the structure of the neutron-rich nuclei around ^{132}Sn . For this purpose the lifetimes of a few low lying excited levels in ^{131}I and ^{132}Xe have been measured that was aimed at exploring the validity of double shell closure of ^{132}Sn . The excited levels of neutron-rich iodine and xenon isotopes have been populated from the β -decay of respective tellurium parents which have been produced with the α -induced fission reaction $^{nat}\text{U}(\alpha, f)$ experiment. The stacked foil irradiation technique has been used to perform the fission experiment and the radiochemical separation process has been performed to separate the tellurium isotopes from the other fission products. Irradiation and separation have been performed for a multiple times to gather more data required in the lifetime measurement with GCD method. To interpret the experimental result, a LBSM was performed using NUSHELLX code. The present calculation could well explain the excitation energies and level lifetimes measured for the low lying excited levels in ^{131}I and ^{132}Xe . In addition to that, the strong configuration mixing observed from the calculation represents the collective nature of these levels which is also supported by the energy ratios and $B(E2)$ strengths. The decrease in $B(E2)$ values with increase in neutron number up to $N = 82$, both in ^{131}I and ^{132}Xe , supports the validity of double shell closure of ^{132}Sn . The $E1$ decays of the negative parity levels in ^{131}I have been measured and compared with the systematics of similar decay patterns in the neighboring isotopes. The enhanced $B(E1)$ and $B(E3)$ rates characterize octupole excitation in the structure of a nuclear level and in case of the 1646 keV, $11/2^-$ level in ^{131}I , enhancement was observed in these transition rates. Therefore, the thesis conforms the possibility of octupole correlation in ^{131}I .

The angular correlation table has been developed that can house the stand alone setup of VENTURE array and the angular correlation setup was characterized with the unperturbed $\gamma - \gamma$ angular correlation measurement in ^{60}Ni and ^{132}I . The main aim of this development was to explore the future possibility of the quadrupole moment measurement using IPAC method. The present thesis also reports the exploration of TDPAC method towards the measurement of EQM in iodine nuclei with $\text{LaBr}_3(\text{Ce})$ detectors. In this regard, the EQMs for the $5/2_1^+$ level in ^{131}I and 3_1^+ level in ^{132}I have been successfully measured using the TDPAC method. Therefore, the present measurement provides the first experimental data for the EQM of the $5/2_1^+$ level in ^{131}I ($N = 78$) and the quadrupole moment of 3_1^+ level of ^{132}I has been measured with

TDPAC technique for the first time. It is found that a linear interpolation, using the present experimental data and few selected datasets, viz., at $N = 72$ and 76 , predicts the quadrupole moment for the $5/2_1^+$ level as lower than that for $7/2_1^+$ level at $N = 82$ iodine and this observation has solved an unresolved issue on the quadrupole moments of $5/2_1^+$ and $7/2_1^+$ levels in odd-A iodine. The experimental data on nuclear deformation for the $5/2_1^+$ levels in the odd-Z, odd-A nuclei close to ^{132}Sn show a monotonic decrease of deformation up to $N = 82$, corroborating with the double shell closure of ^{132}Sn . The quadrupole moment for the first excited levels of $^{131,132}\text{I}$ have also been calculated using LBSM and are found to closely reproduce the experimental data. It is realized that the experimental measurement at $N = 82$ and more involved LBSM calculations for the $N = 72 - 82$ iodine nuclei might be useful to understand the real scenario on the evolution of EQMs up to $N = 82$.

In totality, the facility development and experiments carried out in the present thesis work have helped in exploring nuclear structure around ^{132}Sn , through measurement of level lifetime and EQM. Both the experimental results obtained in the present work corroborates with the doubly shell closed phenomenon at $Z = 50$ and $N = 82$. So, new and important experimental data has been contributed to the existing literature that will add to the understanding the nuclear structure around double shell closure at ^{132}Sn .

10.2 Future outlook

It was understood that, in order to measure the sub-nanosecond order level lifetime, particularly, in case of in-beam gamma spectroscopy, a larger array having more number of detectors is required. Therefore, a modification of the VENTURE array setup is necessary and hence, the second phase of the VENTURE array will be developed by adding more number of CeBr_3 detectors in the array for efficient $\gamma-\gamma$ fast timing measurement. The new design of the second phase of the VENTURE array is proposed where 54 CeBr_3 detectors along with 6 Clover HPGe detectors can be accommodated (see Fig. 10.1). The fabrication of the array will be done at VECC, Kolkata and therefore, the modified array will be used for lifetime measurements in other nuclei, systematically, around ^{132}Sn to get more information in this region.

The present work added the value of QM of $5/2^+$ state for $N = 78$, ^{131}I nucleus and tried to solve an unresolved problem on the quadrupole moments in odd-A iodine. However, there is no information of QM at $N = 82$ for $7/2^+$ state; and at $N = 80, 82$ for $5/2^+$ state; of iodine nuclei. All the data will help to predict, the actual picture of the evolution of the structure of these two states more accurately. Therefore,

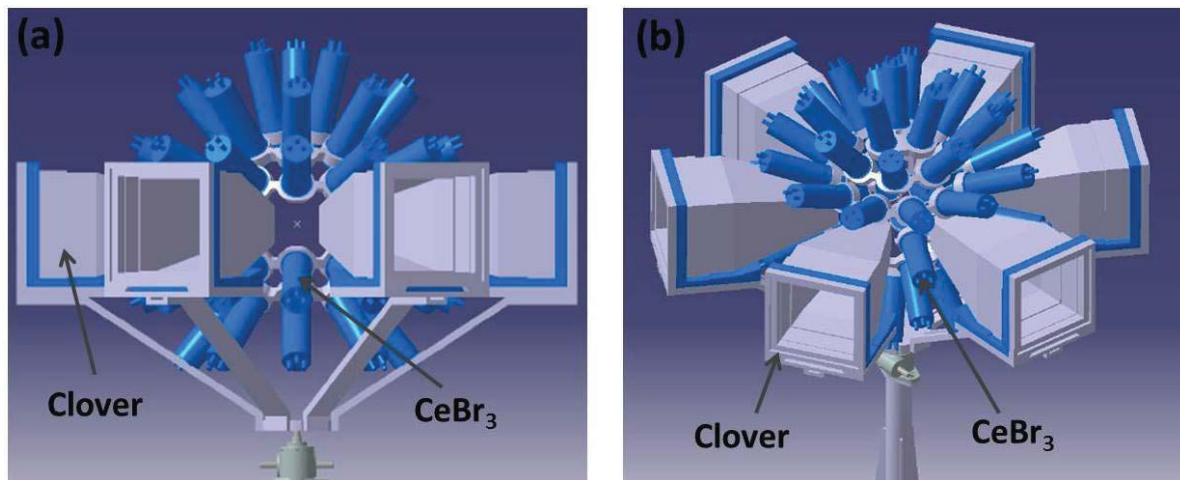


Figure 10.1: The design of the second phase of the VENTURE has been shown. The figure (a) represents the front view along with the beam line and figure (b) represents the top view of the array.

to enrich the knowledge in this region, the quadrupole moment measurement will be performed for other iodine nuclei up to $N = 82$. The Shell model calculation has been planned for all these odd- A isotopes to understand the role of configuration mixing in the EQMs.

Also, the angular correlation table, developed in the thesis work, will be utilized for the quadrupole moment measurement with the IPAC technique for different neutron-rich nuclei in this region and simultaneously, the Shell Model calculation will also be performed to interpret all the experimental results.

Synopsis

Nuclei around double shell closure, consisting few valence particles or holes compared to the closed shell, are important as they provide essential information in nuclear structure study. Particularly, the neutron-rich nuclei, around doubly magic nucleus ^{132}Sn ($Z = 50$, $N = 82$), lies far away from the β stability line and are difficult to access experimentally. So, nuclear structure study of these nuclei gives an unique opportunity to explore the validity of doubly closed phenomenons in this poorly studied region along with the changes of nuclear properties. More specifically, the nucleon-nucleon (n-n) interaction, effective charges, evolution of single particle or multi-particles wave functions etc. can be explored as a function of increasing neutron numbers. Therefore, the systematic study of these nuclei are necessary to understand the possible modification of nuclear shell structure as a function of increasing N/Z ; and these information are very much important not only in nuclear physics but also in astrophysics [GRA07].

The measurement of electromagnetic transition rates, that can be derived from nuclear level lifetime, is one of the best method to probe inside the nuclear structure since, it gives direct information of the nucleon-nucleon interactions and the overlapping wave functions [ALL14, OMT95]. Therefore, lifetime measurement provides the opportunity to study evolution of collectivity around the ^{132}Sn shell closure [ILI16, VOG17] from the reduced quadrupole transition probability, $B(E2)$. The doubly closed ^{132}Sn [FOG94] and some other nuclei [MUE06, SEL15, MAS05] around it are also known to have octupole correlation from the knowledge of reduced transition probability, viz., $B(E1)$ and $B(E3)$ strengths. Hence, the measurement of lifetime of the low-lying excited states of the nuclei around ^{132}Sn is of extreme importance in order to explore and enrich the knowledge on nuclear structure around double shell closure at $Z = 50$ and $N = 82$.

In addition to level lifetime, the Electric Quadrupole Moment (EQM) provides the direct estimate on the deviation of the nuclear charge distribution from sphericity [DAF85, HIN91]. The EQM is also a sensitive

probe to examine the evolution of deformation. Thus, such measurements in neutron-rich nuclei below doubly closed ^{132}Sn are of substantial importance to explore the expected spherical character, in this exotic domain, as one approaches the $N = 82$ shell closure [ALL11, BLA05, SIF06].

However, the experimental knowledge, till now, for these nuclei around ^{132}Sn is very scanty and is also inadequate. Particularly, in case of EQM, most of the existing results are from measurements done during early 60s to late 80s [STO16]. The main reason for the scarcity of data lies in the experimental difficulty in accessing this region by compound nuclear or transfer reactions using the available target-projectile combinations. Taking the advantages of availability of advanced detectors combined with the fission reaction followed by radiochemical separation of the fission fragments, it is possible to explore the low lying states of these nuclei more accurately. Most importantly, development of a $\gamma - \gamma$ fast timing array is of utmost necessity to perform the proposed measurements on nuclear level lifetime and nuclear quadrupole moments through Perturbed $\gamma - \gamma$ Angular Correlation (PAC) methods. In this regard, the following works have been performed in the present thesis work:

- A. Development of $\gamma - \gamma$ fast timing array: VENTURE (VECC Array for Nuclear fast Timing and Angular Correlation Studies) at VECC,
- B. Lifetime measurement in ^{131}I and ^{132}Xe using VENTURE array, and
- C. Quadrupole moment measurement in $^{131,132}\text{I}$ with perturbed angular correlation - which are discussed in the following sections.

A. Development of $\gamma - \gamma$ fast timing array (VENTURE) at VECC:

The nuclear excited states may have lifetimes from a few femtoseconds (fs) to microseconds (μs) and most of them lie in the sub-nanosecond or picosecond ($\sim\text{ps}$) region. There are many techniques available in the literature for the measurement of a lifetime in the range of ps to nanoseconds (ns). These involve different type of detectors, viz., high energy resolution but low timing Ge as well as very fast timing but low energy resolution BaF_2 [MAC89, XIE96, REG13]. In recent times, some state of the art scintillation detectors, viz., $\text{LaBr}_3(\text{Ce})$, has been available which has better energy resolution but comparable time resolution with respect to BaF_2 detectors. With the help of improved timing techniques [REG10, REG13] using these detectors, direct measurement of nuclear level lifetime in the ps range has been possible, almost in all types of experimental setups. As the $\text{LaBr}_3(\text{Ce})$ detectors are limited by their higher hygroscopic nature and

self-activity, the CeBr_3 scintillator detectors, available in more recent time, that has slightly poor energy resolution compared to $\text{LaBr}_3(\text{Ce})$ and an improved time resolution [FRA13] could be considered as a possible alternative to $\text{LaBr}_3(\text{Ce})$.

In the present thesis work, the ultra-fast CeBr_3 scintillators have been used to explore the lifetime measurement in the ps range and to develop the $\gamma-\gamma$ fast timing array at VECC, Kolkata. Therefore, as the first step, several individual $1'' \phi \times 1''$ thick CeBr_3 detectors coupled to Hamamatsu R9779 photomultiplier tubes (PMT) have been characterised by measuring its energy response, energy resolution, timing resolution and detection efficiency. The detectors are found to have a non-linear energy response above -1100V which could be corrected with the use of a charge sensitive preamplifier. Energy resolution of the detector was measured as function of γ energy as well as bias voltage and the detector was found to have a resolution of $\sim 4.5\%$ at 622 keV for all bias voltages. The efficiency for a single CeBr_3 detector was measured with standard technique and it was found that each detector have 5% efficiency compared to a Clover HPGe detector at ~ 1 MeV. The time resolution for a single pair of CeBr_3 detectors has been measured at different energies. The time resolution of a single CeBr_3 detector at 1173-1332 keV and 622-512 keV energies was found to be 109(1) ps and 144(1) ps, respectively.

Following the basic characterisation of the CeBr_3 detectors, the fast timing array, VECC Array for Nuclear fast Timing and Angular Correlation Studies (VENTURE), consisting of eight such CeBr_3 detectors, has been developed at Variable Energy Cyclotron Centre (VECC), Kolkata. The array could be used in its stand alone mode as well as with the array of Clover HPGe detectors like VENUS [SAH18] or INGA [MUR10, ALA18] for the complete γ spectroscopic measurement (Fig. 1). This array has been tested and used in both off-beam and in-beam experiments [ALA16a, ALA19] coupled with VENUS array to explore the measurement of lifetimes of the excited states taking the advantages of the Generalised Centroid Difference (GCD) method based on Mirror Symmetric Centroid Difference (MSCD) method [REG10, REG13]).

In the present thesis work, both the MSCD and GCD method have been explored to measure the nuclear level lifetime using CeBr_3 detectors for the first time in the world to the best of our knowledge. For the timing correlation between the incident γ -rays, a common start timing technique in the coincidence electronic setup has also been implemented, for the first time, with this method. The known standard source ^{152}Eu has been used to generate Prompt Response Distribution (PRD) curve which is required for timing calibration. The lifetime of the 512 keV level of ^{106}Pd has been successfully measured with two CeBr_3 detectors (using MSCD methods) and with VENTURE array (using GCD method) and compared with the



(a) Off-beam setup of VENTURE Coupled to VENUS.

(b) In-beam setup of VENTURE Coupled to VENUS.

Figure 1: Setup of VENTURE array in different configuration.

available literature value. In case of GCD method, the average \overline{PRD} curve has been drawn from the ${}^8\text{C}_2$ combination of PRD curves generated from the combination of 8 detectors of VENTURE array and finally, the lifetimes of the excited levels of the ${}^{106}\text{Ru}$ and ${}^{133}\text{Ba}$ have been successfully measured and compared with the available literature values. The development of VENTURE along with the characterization of CeBr_3 detectors has been published in Ref. [ALA17]. The VENTURE array, the first $\gamma - \gamma$ fast timing array in India, made of with the CeBr_3 scintillators, has been subsequently used to measure the lifetime down to a few ps (~ 8 ps) in the present thesis work.

In order to test the VENTURE array in case of an in-beam experiment, the array with six CeBr_3 detectors coupled with VENUS array of six Clover detectors has been used to explore the possibility of in-beam lifetime measurement in ${}^{122,124}\text{I}$. In the experiment, the excited states of ${}^{122,124}\text{I}$ nuclei were populated by using ${}^{nat}\text{Sb}(\alpha, xn)$ reaction with 40 MeV α -beam from $K = 130$ cyclotron at VECC, Kolkata. The Lifetime of two excited levels in ${}^{124}\text{I}$ nucleus have been successfully measured, in the present work, for the first time with the GCD method. It is realized that more number of detectors are required for in-beam measurements in order to increase the output efficiency. A structure has been designed for use in in-beam experiments involving prompt γ -rays produced with nuclear reaction. The next phase of VENTURE array will be developed by adding more number of detectors.

B. Lifetime measurement in ${}^{131}\text{I}$ and ${}^{132}\text{Xe}$ nuclei using VENTURE:

${}^{131}\text{I}$ and ${}^{132}\text{Xe}$ has three and four proton particles, respectively, and four neutron holes compared to the ${}^{132}\text{Sn}$ shell closure. So, the lifetime measurement of the low lying levels in these two nuclei reveals the n-n

interaction among these involved proton and neutron single particle orbitals. Also, the reduced transition probability, $B(E2)$, gives the information on evolution of collectivity as a function of neutron number up to $N = 82$. The ^{131}I ($Z = 53$, $N = 78$) nucleus has many negative parity states with the involvement of intruder orbital $h_{11/2}$ which are surrounded by several positive parity states. Many γ -rays, in the decay scheme, exists which have involvement of both positive and negative parity states and some of them could be assigned as E1 transition in nature from the conversion electron measurement [BEY67]. The E1 multipolarity of the decaying γ -ray in this region can be explained only if the associated positive parity state has formed due to core excitation of particle from the $\pi g_{9/2}$ or $\nu g_{9/2}$ orbital. So, measurement of $B(E1)$ strength can provide the direct signature on the possibility of such structures in these nuclei. The existence of octupole correlation is also known in the doubly closed ^{132}Sn [FOG94], even-even Xe around $N = 82$ [MUE06] and in other neutron deficient nuclei in this mass region [SEL15, MAS05] and can be explored from the knowledge of $B(E1)$ and $B(E3)$ strengths. So, the lifetime measurements of the low-lying levels of the neutron-rich iodine and xenon nuclei is of extreme importance in order to explore and enrich the nuclear structure around double shell closure at $Z = 50$ and $N = 82$.

In the present thesis work, the lifetimes of the low lying excited states of odd-A ^{131}I and even-even ^{132}Xe have been measured using the VENTURE array and $\gamma - \gamma$ fast timing GCD method. The low lying excited states of ^{131}I and ^{132}Xe nuclei are populated as the β -decay daughter and granddaughter of the respective Te fission fragments which are produced with $^{nat}\text{U}(\alpha, f)$ reaction with 40 MeV α -beam from K-130 cyclotron at VECC, Kolkata and separated radiochemically. The VENTURE array coupled to Clover detectors were used to perform the $\gamma - \gamma$ fast timing measurement using GCD method. Appropriate background corrections for Compton events under the Full Energy Peak (FEP) have also been taken care of for both feeding and decaying γ -rays. The lifetimes of low lying levels in ^{131}I and ^{132}Xe have been measured successfully for the first time.

The Large Basis Shell Model (LBSM) calculation has been performed with NUSHELLX code [BRO14] considering ^{100}Sn ($Z = 50$, $N = 50$) as core and $(1g_{7/2}, 2d_{5/2}, 2d_{3/2}, 3s_{1/2}, 1h_{11/2})$ as single particle orbitals, for both protons and neutrons, distributed over the 50 - 82 subshell space. The calculations were carried out using proton-neutron formalism in full valence space without any truncation and using the *sn100pn* interaction file for information of n-n interactions. The calculated energy sequence has been compared with the experimental energy levels upto 2.0 MeV. The lifetimes of all the positive parity levels of interest in ^{131}I and ^{132}Xe , measured experimentally, are reasonably reproduced from the present calculation. Since,

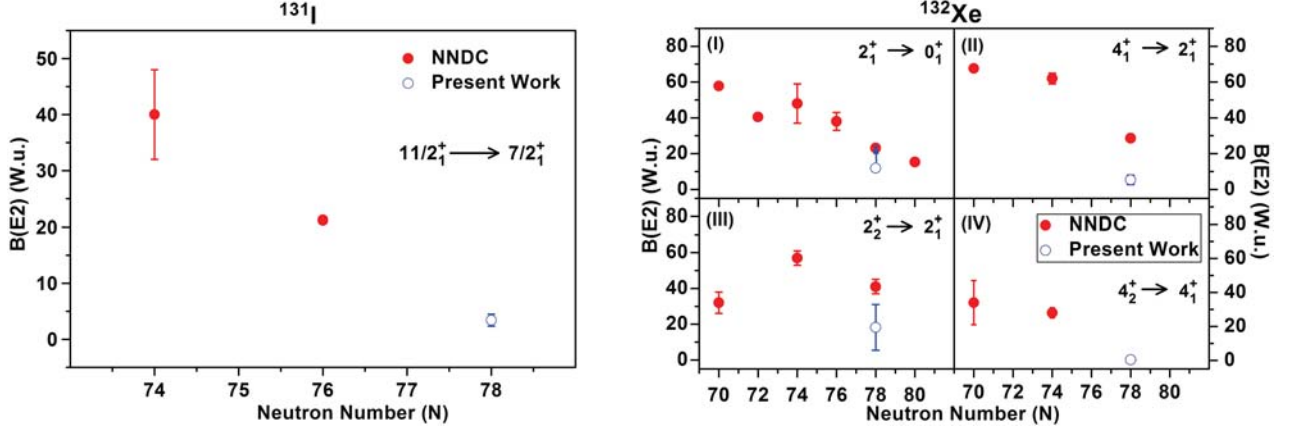
the single particle orbital available in the chosen model space do not allow E1 decay thus, lifetimes of the negative parity levels of ^{131}I could not be directly calculated with this present shell model calculation. Therefore, the lifetime of these states have been estimated by calculating the partial lifetime of the other known M1 or E2 transitions, decaying from the same states, and using their available branching ratios. The theoretically obtained lifetimes are well matched with the experimentally measured lifetimes. A substantial fragmentation of the wave functions, i.e., configuration mixing, in almost all the excited levels in both the nuclei have been observed, which conjectures the collective nature for the low lying levels in ^{131}I and ^{132}Xe .

The octupole correlation of the 1646 keV ($11/2^-$) level in ^{131}I has been conformed from the B(E1) and B(E3) strengths calculated from the measured lifetime and the B(E3) strength has been estimated to be 14 W.u. which is similar to that known for ^{132}Sn [FOG94], $^{124-134}\text{Xe}$ [VOG17], $^{132-138}\text{Ba}$ [BUR85], and in other nuclei [SPE89] and could also be well reproduced with the present shell model calculation. Collective nature of the levels in ^{131}I has been observed from B(E2) values calculated from the lifetime and these B(E2) values were found to decrease as a function of neutron number conforming shell closure at $N = 82$ (Fig. 2). In case of ^{132}Xe , the vibrational nature of the excited levels were conformed from the $E_{4_1^+}/E_{2_1^+}$ ratio, B(E2) values calculated from the lifetime and the fragmentation of wave function observed from shell model calculation. These B(E2) values for these levels were found to decrease as a function of neutron number conforming the shell closure at $N = 82$. The results from this work have been published in Ref. [ALA19].

C. Quadrupole moment measurement in $^{131,132}\text{I}$ with perturbed angular correlation:

In the iodine nuclei ($N \leq 82$), some anomalies are known regarding the quadrupole moments of $\pi d_{5/2}$ state at $N = 82$ among the theoretical prediction and experimentally measured values [HAF64]. The linear extrapolation of measured EQM at $N = 82$ for $7/2_1^+$ state agrees fairly well with the single particle estimate (spe) [HOR55]. However, the similar extrapolated value of measured EQM for $5/2_1^+$ state at $N = 82$ shows much larger value compared to $7/2_1^+$. In contrast to the experimental result, the theoretical calculations [HOR55, KIS63], performed at that time, predicted a larger absolute value of EQM for $7/2_1^+$ level compared to that for $5/2_1^+$ level in $N = 82$ iodine nucleus. Therefore, the systematic experimental determination of EQMs up to $N = 82$ iodine is of importance to understand the evolution of nuclear deformation of these two levels.

In the present thesis work, such initiative has been taken by measuring the EQMs of first excited levels



(a) The open circle (blue) represents the $B(E2)$ value calculated from the measured level lifetime, in the present work, for $11/2^+$ level in ^{131}I .

(b) The open circle (blue) represents the $B(E2)$ values calculated from the measured level lifetimes, in the present work, for ^{132}Xe .

Figure 2: The $B(E2)$ values for the decays of ^{131}I and ^{132}Xe levels in comparison to that in neighboring nuclei. The filled circles (red) represents the $B(E2)$ values calculated from the level lifetimes taken from NNDC database [NNDC].

of $^{131,132}\text{I}$ ($N = 78, 79$) by using Time Differential Perturbed Angular Correlation (TDPAC) technique. In addition, as the PAC techniques, viz., IPAC (Integral PAC) and TDPAC (Time Differential PAC), are also used for the measurement of EQMs, use of VENTURE array was explored to study angular correlation in ^{132}I . For this purpose, an angular correlation table was designed and fabricated to perform quadrupole moment measurement with PAC technique (Fig. 3). The geometry of the table was adjusted by measuring the angular correlation in ^{60}Ni and ^{132}I . The ^{132}I was produced from the decay of radiochemically separated ^{132}Te ($\sim 3d$) produced in the fission reaction $^{nat}\text{U}(\alpha, f)$ at $E_{beam} = 40$ MeV. The measured angular correlation values were compared with the theoretically calculated one using F_k coefficients [ALA17].

The EQMs of the $5/2_1^+$ state of ^{131}I and 3_1^+ state of ^{132}I have been measured by TDPAC technique using three $1'' \phi \times 1''$ thick $\text{LaBr}_3(\text{Ce})$ crystals coupled to XP2020URQ PM tubes. In this case, the radiochemically separated Te activity from the Al catcher foils were doped into the Te metal matrix and then, the metallic Te was annealed for 3h at the temperature of 573 K in an Argon atmosphere to provide the necessary Electric Field Gradient (EFG) required for TDPAC measurement. The Te activity was also counted with a BGO suppressed CLOVER HPGe detectors to identify the γ lines of interest. The time differential perturbation in the $\gamma-\gamma$ angular correlation was measured to estimate the quadrupole moments. The LBSM calculation as well as single particle estimates have been performed to interpret the experimental results.

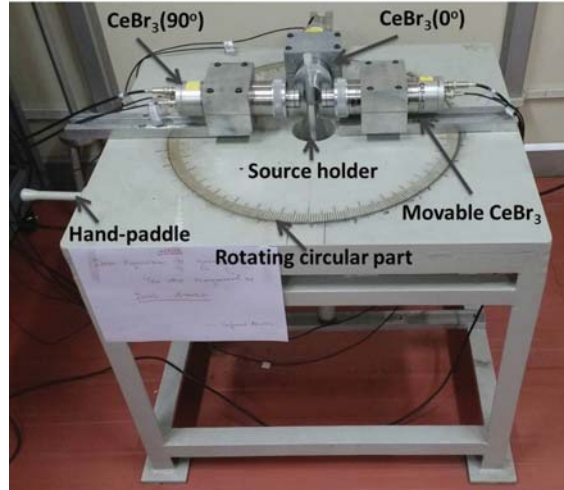


Figure 3: Illustration of the manufactured angular correlation setup.

The present measurement provides the first experimental data, beyond $N = 76$ iodine, for the EQM of the $5/2_1^+$ level in $N = 78$ iodine isotope. It is found that a linear interpolation, using the present experimental data and selected datasets at $N = 72$ and 76 is able to predict the quadrupole moment for the $5/2_1^+$ lower than that for $7/2_1^+$ level of $N = 82$ iodine (Fig. 4). The interpolated values also corroborate with the systematics shown by single particle estimates. To understand the evolution of collectivity for the $5/2_1^+$ states, the deformation parameter has also been calculated for the first $5/2^+$ levels in the odd-Z, odd-A nuclei around ^{132}Sn from the measured quadrupole moments and found a monotonic but nonlinear decrease of deformation up to $N = 82$, corroborating with the double shell closure of ^{132}Sn . The quadrupole moment for the first excited levels of $^{131,132}\text{I}$ have also been calculated with LBSM using the default effective charges ($e^p = 1.35$, $e^n = 0.35$) and are found to be reproducing the experimental data for $5/2_1^+$ of ^{131}I and 3_1^+ of ^{132}I though, it predicts a lower value for $7/2_1^+$ level of ^{131}I which do not corroborate with the available experimental data [STO16, IAEA]. It was, however, observed that the effective charge of ($e^p = 1.35$, $e^n = 1.3$) could reproduce the experimental value for the $7/2_1^+$ level of ^{131}I .

The increase in quadrupole moment for the $5/2_1^+$ levels is observed with the increase in number of neutron hole pairs compared to $N = 82$ shell closure. However, a similar contribution from the $\pi d_{5/2}$ orbital was observed from the almost constant spectroscopic factors for the $5/2_1^+$ levels of $^{125-131}\text{I}$ obtained from the result of proton transfer reactions [AUB68, TOL79]. Involved shell model calculations are planned, as a future perspective to the present work, in order to explore the configuration mixing in iodine isotopes as

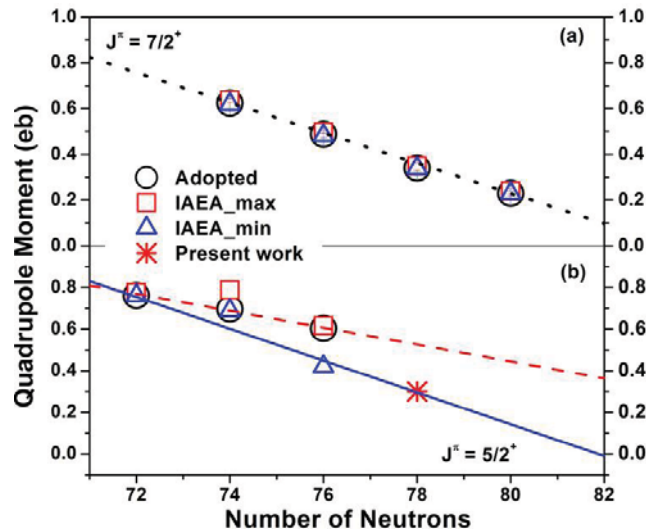


Figure 4: Experimental quadrupole moments (magnitude) for the (a) $7/2_1^+$ and (b) $5/2_1^+$ levels of odd-A I are shown as function of neutron number. The adopted values of quadrupole moments have been taken from Ref. [STO16], the maximum and minimum values, known for a particular isotope, have been taken from the IAEA compilation [IAEA]. The value at $N = 78$ for the $5/2_1^+$ level of ^{131}I is measured in the present work and is shown. Linear extrapolations up to $N = 82$ are shown for $7/2_1^+$ level (black dotted line) and $5/2_1^+$ level (red dashed and blue solid lines) with different data sets.

a function of neutron number.

The deformation of the $5/2_1^+$ levels have been estimated from the measured quadrupole moments which shows a monotonic but not so linear decrease up to $N = 82$. This also corroborates with the spherical character of the $5/2_1^+$ level of iodine at $N = 82$. The results on quadrupole moment measurement in iodine nuclei has been reported [ALA20].

Therefore, the present thesis can be sum up as follows:

In the present thesis work, the $\gamma - \gamma$ fast timing array (VENTURE) has been developed at VECC, Kolkata. The Lifetime measurement through GCD method has been performed using this array in ^{131}I and ^{132}Xe . The transition probabilities, calculated from the experimentally measured lifetimes, corroborate with double shell closure of ^{132}Sn and also establishes the presence of octupole correlation in ^{131}I . The angular correlation table has been developed and characterized with the unperturbed $\gamma - \gamma$ angular correlation measurement in ^{60}Ni and ^{132}I . The quadrupole moment of 3_1^+ level of ^{132}I and $5/2_1^+$ level of ^{131}I have been measured using TDPAC technique. The deformation and quadrupole moment corroborates the shell closure at $N = 82$ and also solve the $\pi d_{5/2}$ anomaly in this region. All the experimental results have been interpreted with Shell model calculations using NuShellX code.

Chapter 1

Introduction

1.1 Preface

The study of nuclear structure is one of the very important tools in nuclear physics to understand the basic characteristics and properties of the atomic nucleus, the many-body quantum mechanical system. The atomic nucleus exhibits a variety of structural properties with the change of nucleon (proton and neutron) numbers and provides a unique aspect of the strong nuclear force in case of extreme nucleon numbers [DOB94, OTS01, BAS07, DOB07]. Therefore, the properties of nuclei near the ‘valley of stability’ can not be extrapolated uniformly to the nuclei near the drip lines. In addition to that, the change of neutron-proton interaction in these exotic nuclei, due to change in the central potential, leads to a fascinating variety in the structure information, viz., shape deformation from spherical structure [MAH92], appearance of proton or neutron skin on the surface of nucleus [TAN92], migration of single particle states [OTS05], disappearance of shell and subshell closure and appearance of new shell closure, i.e., new magic number [WAR04, JAN05, STEP13], so forth and so on. Therefore, the nuclei lying far from the ‘valley of stability’ becomes one of the major topics of interest in nuclear structure physics. This is basically, to understand the possible modification of the shell structure as a function of increasing neutron or proton numbers. In particular, the neutron-rich nuclei, around double shell closure of ^{132}Sn ($Z = 50$, $N = 82$), with few valence particle and/or holes are of extreme contemporary importance to understand the evolution of nuclear structure around the well known double shell closure at $Z = 50$ and $N = 82$.

While almost all the structural properties of stable as well as near stable nuclei have been studied immensely but the structure of the nuclei lying far from the ‘valley of stability’ are not well explored, till today.

Particularly, the exotic nuclei towards the neutron drip line are very less studied in comparison to the nuclei lying around the stability line or in the proton-rich region. The main reason is that, unlike the neutron-rich nuclei, the stable nuclei or proton-rich nuclei can be easily produced using fusion evaporation reaction with stable target-projectile combination. However, to populate the neutron-rich nuclei, the light/heavy-ion induced fission reaction with stable projectile or deep-inelastic reaction with unstable exotic neutron-rich projectile has to be performed. Moreover, the low production yield of a particular fission fragment as well as so many simultaneously produced fragments, in the fission process, enhance difficulties and challenges.

In the present thesis work, the neutron-rich nuclei that are lying in the south-west of ^{132}Sn and that can be produced from β -decay of fission fragments were studied. In absence of a mass spectrometer, the radiochemical separation was employed through which a very clean elemental separation can be achieved.

The measurement of transition probabilities and Electric Quadrupole Moments (EQMs) are the direct indicators for the evolution of collectivity in a nucleus. So, measurements of these quantities in isotopes of neutron-rich iodine and xenon could be used to explore the validity of the shell closure at $N = 82$ with few extra protons compared to $Z = 50$. So, the present thesis aimed at the measurement of nuclear level lifetimes, to deduce the transition probabilities (^{131}I and ^{132}Xe), and EQMs ($^{131,132}\text{I}$) around ^{132}Sn . More details on the existing problems and standing interests in the structures of $^{131,132}\text{I}$ and ^{132}Xe are given in Chapters 7 and 8.

Also, since, the present thesis work mainly focuses on the measurement of nuclear level lifetime (in the sub-nanosecond or picosecond range) and EQM, thus, a dedicated and appropriate detecting system along with a suitable measurement technique is required. Therefore, in the present thesis, a fast timing array, VECC Array for Nuclear fast Timing and AngUlar CorRelation Studies (VENTURE), using several ultra-fast CeBr_3 scintillator detectors has been developed at VECC, Kolkata. For this purpose, the individual CeBr_3 detectors have been characterized for spectroscopic properties like energy response, energy resolution, timing resolution and detection efficiency. The Generalised Centroid Difference (GCD) method [REG16a], based on the Mirror Symmetric Centroid Difference (MSCD) method [REG10], has been explored with the VENTURE array for the sub-nanosecond order of lifetime measurement in both off-beam and in-beam experiments. To access the neutron-rich region around ^{132}Sn , the α -induced fission reaction on natural uranium (^{nat}U) target followed by radiochemical separation process has been performed. The Te fission products have been separated from the rest of the fission products using the radiochemical separation method. The low-lying states of iodine and xenon nuclei have been studied from the β -delayed γ -decay.

The VENTURE array has been utilized for detection of γ -rays and GCD method has been used to measure the lifetime of low-lying states in ^{131}I and ^{132}Xe nuclei. For the purpose of measurement of nuclear transition moment, in the present thesis work, an angular correlation table was designed and fabricated at VECC, Kolkata. The possibility of quadrupole moment measurement with Perturbed $\gamma - \gamma$ Angular Correlation (PAC) technique has been explored using the fabricated angular correlation setup. The Time Differential Perturbed Angular Correlation (TDPAC) measurement was performed to measure the EQM for first excited states of $^{131,132}\text{I}$, populated from the β -delayed decay of the radiochemically separated Te fission fragments. To provide the necessary Electric Field Gradient (EFG), required in this method, the separated Te fission fragments were doped into the tellurium metal during the radiochemical separation and doping process. The Large Basis Shell Model (LBSM) calculations using the ‘NUSHELLX’ code have been performed to interpret all the experimental results in the present thesis work.

1.2 Outline

The major activities carried out in the present thesis work can be listed as follows:

- (1) The development of $\gamma - \gamma$ fast timing array (VENTURE) with fast CeBr_3 detectors.
- (2) Characterization and testing of the array for off-beam and in-beam measurements and exploration on $\gamma - \gamma$ fast timing techniques, viz., MSCD and GCD.
- (3) Measurement of nuclear level lifetimes in ^{131}I and ^{132}Xe using VENTURE array.
- (4) Fabrication, setup and testing of a $\gamma - \gamma$ angular correlation table for its use in PAC measurement.
- (5) Measurement of EQM in $^{131,132}\text{I}$.

Presentation of these works along with the (i) introduction, (ii) summary, (iii) relevant nuclear models and (iv) discussion on relevant experimental techniques are completed using ten chapters in total, as discussed below.

A brief overview of general theories of nuclear structure along with the basic phenomena of LBSM code, NuShellX, have been discussed in Chapter 2. Chapter 3 covers the discussion on the basic theory of γ -ray spectroscopy, γ -rays’ interaction with matter along with important observables like detector response, energy and timing resolution and detection efficiency used in γ -ray spectroscopy. This chapter also includes discussions on different properties and usefulness of various types of detectors used in the present thesis work. In Chapter 4, the $\gamma - \gamma$ fast-timing GCD technique for the lifetime measurement in the sub-nanosecond order

region has been discussed. This chapter also covers the discussion about characterization of the individual ultra-fast CeBr₃ scintillator detectors along with the development and establishment of VENTURE array towards the lifetime measurement in picosecond region. Chapter 5 includes the development of an angular correlation setup along with a brief discussion on PAC measurement technique to measure the EQM. In Chapter 6, the difficulties of production of the neutron-rich nuclei have been discussed together with the discussion on experimental procedure used for their production in the present thesis work. Chapter 7 covers the measurement of lifetime in low lying states in neutron-rich ¹³¹I and ¹³²Xe nuclei using VENTURE array, developed under the present thesis work. The measurement corroborates the validity of double shell closure at ¹³²Sn and also establishes the presence of octupole correlation in ¹³¹I. In Chapter 8, the measurement of EQM in neutron-rich ^{131,132}I nuclei using TDPAC technique has been discussed. The results from this measurement also corroborates with the shell closure at N = 82 and also solve the anomaly among the quadrupole moments of 5/2₁⁺ and 7/2₁⁺ levels in iodine nuclei. Chapter 9 covers the in-beam testing of VENTURE array for measurement of sub-nanosecond order lifetime with the GCD method. The successful measurement of level lifetimes in few low lying states of ¹²⁴I, performed during the testing, has also been discussed in this chapter. Finally, in Chapter 10, conclusion and future perspective of the present thesis has been discussed.

Chapter 2

Nuclear structure and models

2.0.1 Introduction

The atomic nucleus, the complex many body quantum system containing mainly several number of fermions (protons and neutrons), is confined within a tiny spacial volume having diameter $\sim 10^{-14}$ to 10^{-15} m and forms a stable system through the strong attractive nucleon-nucleon (n-n) interaction and the proton-proton repulsive force. In order to understand the properties of nucleus, an adequate knowledge about the nature of n-n interaction is necessary. But, the exact mathematical form of the strong short range force that acts between the nucleons is still not known. From the very first day, various nuclear models have been developed to understand the structure and properties of the nuclei. However, each of these models can explain only few properties of the nucleus to some extent but none of these models can completely describe all the properties. Among several various proposed models, the different collective models (e.g., liquid drop model) and shell models with different types of coupling- are two mostly used theoretical models in nuclear physics.

The liquid drop model was the first successful model that has the capability to describe the macroscopic properties of the nucleus. The saturation properties of nuclear force, low compressibility of nuclear matter, well defined nuclear surface etc. - the macroscopic properties of nucleus are very similar to a liquid droplet. The nucleus as a liquid drop was first proposed in 1937 by N. Bohr and F. Kalckar [BOH37] and meanwhile, Weizscker and Bethe developed the historical semi-empirical mass formula [BET36, WEI35] for the binding energy of the nucleus. The fission process could also be nicely explained qualitatively with this model. The semi-empirical mass formula was very successful to explain the binding energy of the nucleus except few

nuclei having proton and/or neutron numbers equal to 2, 8, 20, 28, 50, 82, 126 etc. - which are known as magic numbers. This problem could be solved after development of independent particle model or shell model by Mayer and Jensen in 1949 [MAY49]. This model is a single particle model, i.e., each nucleon is considered to move independently in a mean field created by the rest of the nucleons and they assumed the potential as a spherical harmonic oscillator potential with a perturbation of nuclear spin-orbit coupling. This model nicely reproduces the magic shell gap at magic numbers and also spin-parity, magnetic moment, nuclear isomerism, stripping reaction etc. of the nuclei.

In the present thesis, the shell model has been used for interpretation of experimental data on lifetime and quadrupole moment in nuclei around double shell closure of ^{132}Sn . So, the topics relevant to nuclear shell model have been discussed briefly with microscopic approach from the basic interaction between the nucleons.

2.0.2 Microscopic approach: Independent particle model or Shell model

In case of the independent particle model, it is assumed that the nucleons are free within the nucleus and moves independently of each other within an average central potential. Thus, the nuclear n-body problem can be reduced to a simpler two-body system and the Hamiltonian can be expressed as:

$$\mathcal{H} = T + V = \sum_{i=1}^A \frac{\vec{P}_i^2}{2m_i} + \sum_{i>j=1}^A V_{ij} \quad (2.1)$$

where, V_{ij} is the two body n-n potential. On the first step, to transform the many body n-n interaction to a mean or average potential, a one-body potential U_i is added and subtracted with the Eq. (2.1):

$$\mathcal{H} = \sum_{i=1}^A \left[\frac{\vec{P}_i^2}{2m_i} + U_i \right] + \sum_{i>j=1}^A [V_{ij} - U_i] = \mathcal{H}_o + \mathcal{H}_{res} \quad (2.2)$$

where, $\mathcal{H}_o = \sum_{i=1}^A \left[\frac{\vec{P}_i^2}{2m_i} + U_i \right]$ is the Hamiltonian which describes the independent movement of nucleons

in a mean field potential and,

$$\mathcal{H}_{res} = \sum_{i>j=1}^A [V_{ij} - U_i] \quad (2.3)$$

is the 2-body residual interaction which can be considered as a small perturbation on the 1-body Hamiltonian \mathcal{H}_0 .

Microscopically, one can construct the mean or average field potential for a nucleus starting from a two body force to a many body force. The shape of this ad hoc potential should follow the following criteria:

(a) At the center or close to the center of the nucleus a nucleon will feel uniform nuclear force, i.e., net nuclear force on it will be zero:

$$\left. \frac{\delta V(r)}{\delta r} \right|_{r=0} = 0 \quad (2.4)$$

(b) The nuclear forces will be stronger when one moves from the surface ($r = R_0$) to the interior of the nucleus:

$$\left. \frac{\delta V(r)}{\delta r} \right|_{r < R_0} > 0 \quad (2.5)$$

(c) Due to finite range of the nuclear forces, outside the surface of the nucleus, it will become weaker, i.e.,

$$V(r) \simeq 0 \text{ for } r > R_0 \quad (2.6)$$

An analytic approach which satisfies the above conditions quite well is the Woods-Saxon potential:

$$V^{W.S}(r) = -\frac{V_0}{\left[1 + \frac{\exp(r-R_0)}{a}\right]} \quad (2.7)$$

where, $R_0 = r_0 A^{1/3}$, $V_0 \simeq 50$ [MeV], $a \simeq 0.5$ [fm] and $r_0 \simeq 1.2$ [fm].

The main problem is that the Schrödinger equation can not be solved analytically with this potential and thus, for simplicity in calculations, the following two approximations are generally used for qualitative

considerations: (a) Harmonic Oscillator:

$$V(r) = -V_0 \left[1 - \left(\frac{r}{R_0} \right)^2 \right] = \frac{1}{2} m \omega_0^2 (r^2 - R_0^2) \quad (2.8)$$

(b) Square Well:

$$V(r) = \begin{cases} -V_0 & \text{for } r \leq R_0 \\ \infty & \text{for } r > R_0 \end{cases} \quad (2.9)$$

In case of harmonic oscillator potential given in Eq. (2.8), the solution results equidistant energy levels -

$$\varepsilon_N = \left(N + \frac{3}{2} \right) \hbar \omega_0 - V_0 \quad (2.10)$$

with, $N = 2(n - 1) + \ell$, is known as the number of quanta in the oscillator or *principal quantum number*; where $n = 1, 2, \dots$, is the *radial quantum number*; $\ell = 0, 1, 2, \dots$, is the *angular momentum quantum number* and ω_0 is the oscillator frequency. The obtained energy levels are $\mathcal{D}(N)$ -fold degenerate:

$$\mathcal{D}(N) = \frac{(N+1)(N+2)}{2} \quad (2.11)$$

Thus, the levels with different n and ℓ but same N are degenerate. These unwanted degeneracies are removed if one chooses square-well potential. The true energies lie in between the two limits set by these two potentials. But both of two potentials are far from reality and could able to reproduce the magic numbers only up to 20.

2.0.3 Spin-orbit coupling: Spherical single particle shell model

Till now, in the above calculations, the spin of the nucleons are not taken into account. As the nuclear forces are spin dependent thus, a strong influence from nucleon spin must be incorporated in the calculations. In atomic physics, a small correction is considered for spin-orbit coupling which arises due to interaction between the orbital angular momentum and spin angular momentum. However, in the case of nuclear physics, the effect of this coupling is more effective and it comes as an additional term $(\vec{\ell} \cdot \vec{s})$, as suggested by M. G. Mayer [MAY50], in the expression of potential, i.e.,

$$V(r) = V'(r) + f(r) \vec{\ell} \cdot \vec{s} \quad (2.12)$$

where,

$$f(r) = \frac{b}{r} \frac{\partial v}{\partial r} \quad (2.13)$$

where, ‘ b ’ is a constant and $f(r)$ is a function of ‘ r ’ and corresponds to the spherically symmetric function $v(r)$.

The incorporation of this strong spin-orbit coupling term ($\vec{\ell} \cdot \vec{s}$) leads to splitting of the doubly degenerate levels with total angular momentum $j = \ell \pm \frac{1}{2}$ and shift the decoupled levels in energy proportional to $j(j+1) - \ell(\ell+1) - s(s+1)$, i.e., $\Delta E \sim 2\ell + 1$ where, $s = 1/2$. Thus, the split increases with ℓ . Mathematically, this is similar to a jj-coupling scheme of atomic physics, since $\vec{\ell} \cdot \vec{s}$ term commutes with s^2 , ℓ^2 , j^2 , j_z but not commute with ℓ_z and s_z . But unlike atomic physics the decoupled states with higher $j = \ell + \frac{1}{2}$ will have lower energy compared to its other branch, i.e., lower $j = \ell - \frac{1}{2}$. After inclusion of spin-orbit coupling term to the expression of potential, the model is now able to reproduce all the magic numbers accurately (see Fig. 2.1). The sequence of the energy levels within the different shells actually depends on the choice of $f(r)$. The shells, above magic number 20, contain mixed parity states in which among a branch of same parity states an opposite parity state coming from the next high- j level is included following the spin-orbit interaction. This opposite parity orbitals are called intruder orbitals (see Fig. 2.1). This unique parity orbital plays a significant role in nuclear structure because it does not mix with its neighbouring opposite (positive) parity orbitals in the multiplet and also far from the similar (negative) parity states. Therefore, the configurations that originate from these orbits are very pure with insignificant mixing from other configurations. This model was very successful to reproduce magic numbers after incorporating the spin-orbit term into the spherical harmonic potential and hence, the model was introduced as the spherical single particle shell model.

The shape of the nuclei having number of protons and/or neutrons equal to magic numbers normally appear as spherical and nucleons outside a core shell are considered as valence particles which are only incorporated in this single particle shell model calculations. The ground state properties, e.g., spin, parity, magnetic moment, quadrupole moment etc. of many nuclei very close to magic numbers, i.e., for almost all spherical nuclei can be nicely explained by this model. However, if the number of protons and neutrons departs from the magic numbers then the nuclei are no longer in spherical shapes and the residual part of the Hamiltonian of Eq. (2.3) becomes more significant. Thus, to describe the nuclear properties having

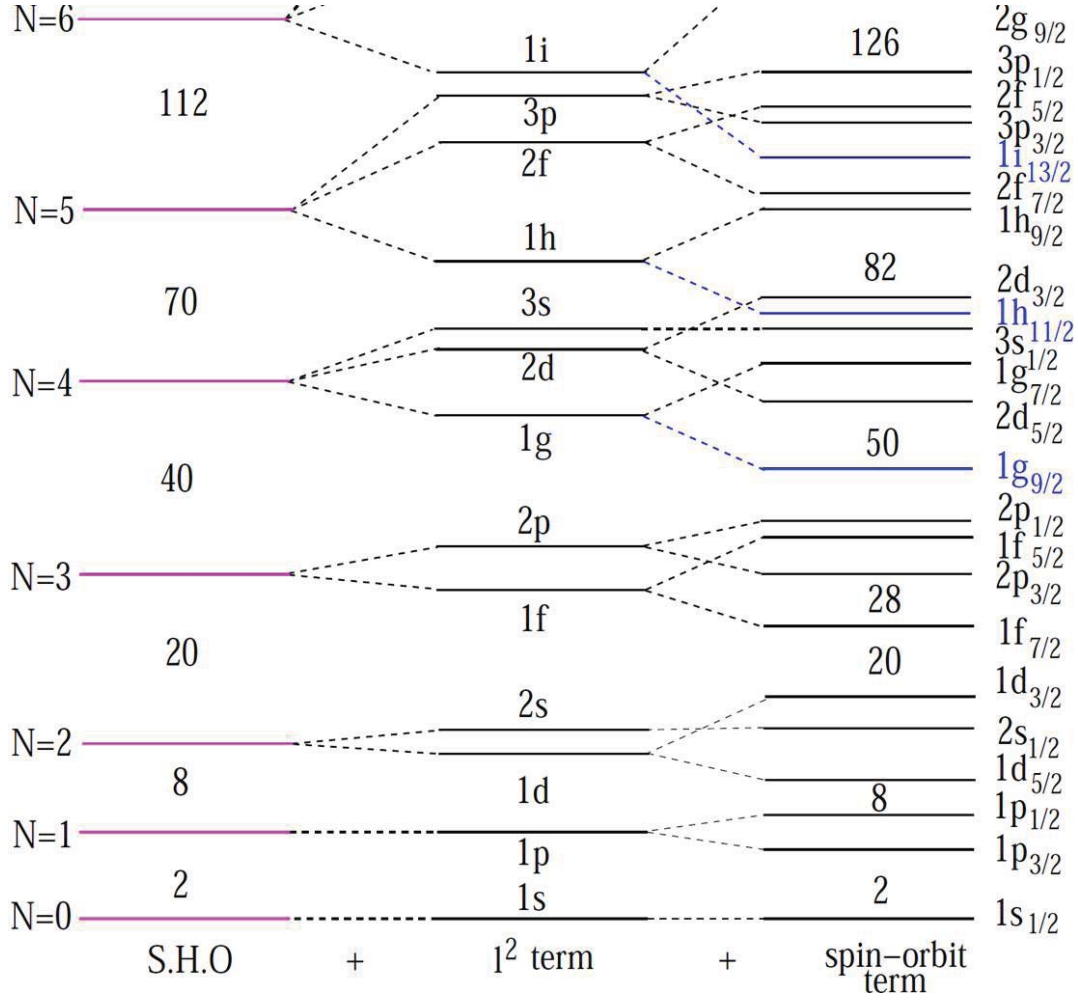


Figure 2.1: The evolution of shell structure with the addition of l^2 and spin-orbit term to the simple harmonic oscillator potential. The figure has been taken from Ref. [SAH18a]. Blue lines represent the intruder orbital.

many valence nucleons outside the core, a modification in the shell model calculation is required. These difficulties were overcome by Nilsson who introduced deformed shell model with a modified potential.

2.0.4 Deformed nuclear shapes: Nilsson model

The shape of the deformed nucleus can be described using its surface coordinates which is given by a general multipole expansion as follows:

$$\mathcal{R}(\theta, \phi) = \mathcal{R}_0 \left\{ 1 + \sum_{\lambda=0}^{\infty} \sum_{\mu=-\lambda}^{\lambda} \alpha_{\lambda\mu} Y_{\mu}^{\lambda}(\theta, \phi) \right\} \quad (2.14)$$

where, \mathcal{R}_0 is equal to the radius of the nucleus corresponding to its equilibrium spherical shape and Y_μ^λ represent the usual spherical harmonics of order λ, μ . The expansion parameter $\alpha_{\lambda\mu}$ are considered as collective variable and represents the amplitude of each spherical harmonic component. The term λ denotes the multipolarity of the shape oscillation whereas, μ is the projection of λ . $\lambda = 0$ is called monopole term corresponds to breathing mode of nucleus and in case of low-lying excited states of a nucleus this type of monopole oscillation does not occur due to the almost incompressible nature of its volume. $\lambda = 1$ is known as dipole term corresponds to displacement of center of mass, i.e., gives translation to the nucleus and also does not correspond to any kind of oscillation or shape deformation. For a deformation, only the terms $\lambda \geq 2$ are considered, whereas, the term $\lambda = 2$ is called quadrupole deformation of a nucleus, $\lambda = 3$ is octupole deformation and so on. If one considers that shape of a nucleus is invariant with respect to the symmetry planes and chooses the axis of the coordinate system corresponding to the body-fixed frame, then for $\lambda = 2$ one can write $a_{2,1} = a_{2,-1} = 0$ and $a_{2,2} = a_{2,-2}$. Therefore, the five components of $\alpha_{2\mu}$ reduces to only two real independent parameters $a_{2,0}$ and $a_{2,2} = a_{2,-2}$ which can be expressed in Hill-Wheeler [HIL53] coordinates β_2 and γ :

$$\begin{aligned} a_{2,0} &= \beta_2 \cos \gamma \\ a_{2,2} &= \frac{1}{\sqrt{2}} \beta_2 \sin \gamma \end{aligned} \quad (2.15)$$

so that,

$$\sum_{\mu} |\alpha_{2,\mu}|^2 = a_{2,0}^2 + 2a_{2,2}^2 = \beta_2^2 \quad (2.16)$$

where, β_2 is the measure of the magnitude of the quadrupole deformation and γ determines the deviation of the shape from axial symmetry. Thus, Eq. (2.14) can be expressed in a very simplified form:

$$\mathcal{R}_k = \mathcal{R}_0 \left[1 + \sqrt{\frac{5}{4\pi}} \beta_2 \cos(\gamma + 2\pi k/3) \right] \quad (2.17)$$

where, k varies from 1 to 3 and $\gamma = 0$ corresponds to pure prolate shape while, $\gamma = \pi/3$ represents pure oblate shape and in between triaxial shapes exist. The increment of γ by an integral multiple of $2\pi/3$ leads a simple permutation of the axis labels. This permutation of axis labels, therefore, differentiates between collective and non-collective rotation for a given direction of rotation. Taking the advantages of

these permutations in the Lund parametrization one can present both collective and non-collective rotation by changing γ range only from $-2\pi/3$ to $\pi/3$ as shown in Fig. 2.2. The $0^\circ \leq \gamma \leq 60^\circ$ range is sufficient to describe all the quadrupole shapes. The nuclear shape is said to be triaxial if the γ is not equal to the multiple of 60° . The mathematical form of intrinsic quadrupole moment (Q_0) can be expressed in terms of deformation parameter (β_2) [CAS90]:

$$Q_0 = \frac{3}{\sqrt{5\pi}} Z R_0^2 \beta_2 (1 + 0.16\beta_2) \quad (2.18)$$

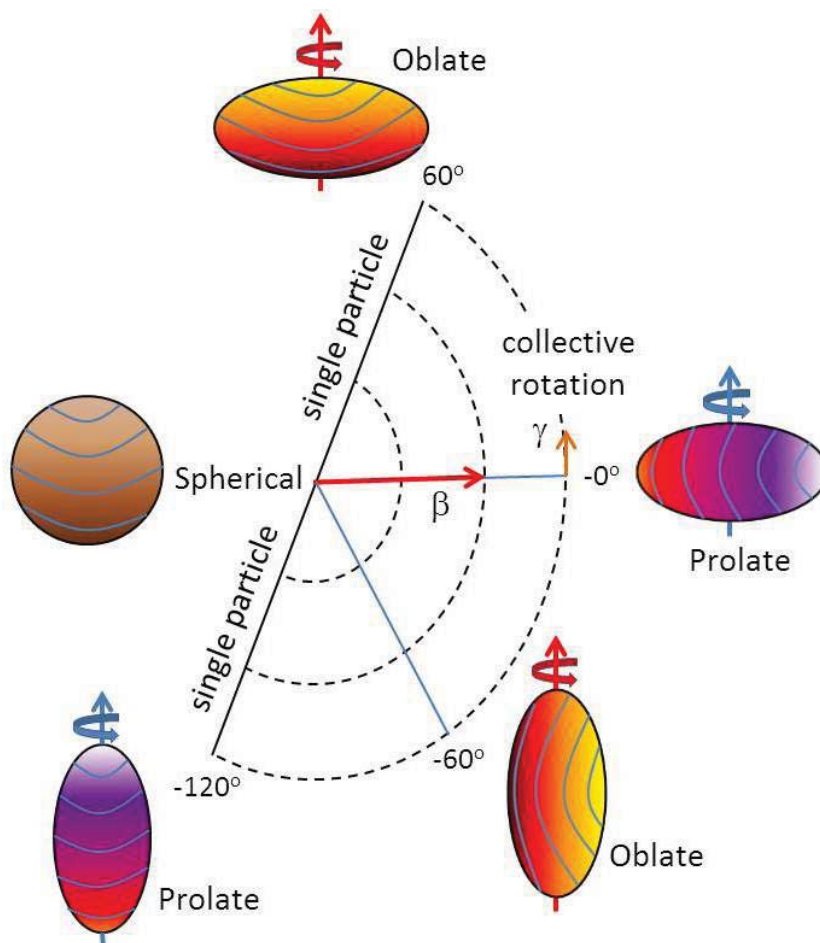


Figure 2.2: An illustration of various nuclear shapes in $(\beta - \gamma)$ plane using Lunds conventions [AND76].

Nilsson model

The properties of the deformed nuclei can be described using the Nilsson model which is a modified shell model, first proposed by Nilsson [NIL55, NIL69]. To describe the deformed nucleus, Nilsson used a non-spherical harmonic oscillator as a mean field along with a spin-orbit coupling ($\vec{\ell} \cdot \vec{s}$) term and a centripetal ($\vec{\ell} \cdot \vec{\ell}$) term and assumed that the nucleons move independently in that deformed potential. Therefore, the single particle Hamiltonian or so called Nilsson Hamiltonian, assuming z-axis axial symmetry of potential, can be expressed as:

$$\mathcal{H}_{Nilsson} = \frac{p^2}{2m} + \frac{1}{2}m[\omega_{\perp}^2(x^2 + y^2) + \omega_z^2 z^2] + C\vec{\ell} \cdot \vec{s} + D\vec{\ell} \cdot \vec{\ell} \quad (2.19)$$

where, ‘ C ’ and ‘ D ’ are the parameters containing the information about the strength of the spin-orbit interaction and centripetal effect, respectively. The spin-orbit term was added to the Hamiltonian $\mathcal{H}_{Nilsson}$ to reproduce the magic numbers. On the other hand, the centripetal term was added to $\mathcal{H}_{Nilsson}$ to produce a more realistic potential because, the nucleons with high ℓ -values, i.e., the nucleons at the surface of heavy nucleus feel a deeper average potential as compared to spherical harmonic oscillator potential and the energy levels are shifted down in energy. In the above Eq. (2.19), the $\omega_{\perp} = \omega_x = \omega_y$ and ω_z are the one dimensional oscillator frequencies which are function of parameter of deformation (δ):

$$\begin{aligned} \omega_{\perp}^2 &= \omega_0^2 \left(1 + \frac{2}{3}\delta\right) \\ \text{and } \omega_z^2 &= \omega_0^2 \left(1 - \frac{4}{3}\delta\right) \end{aligned} \quad (2.20)$$

where, ω_0 is the oscillator frequency in the spherical potential with $\delta = 0$. The parameter, δ , is the measure of elongation of the potential along the z-axis and is related to deformation parameter (β_2) as follows:

$$\delta = \frac{3}{4}\sqrt{\frac{5}{\pi}}\beta_2 \simeq 0.95\beta_2 \quad (2.21)$$

For a positive (negative) value of δ the shape of the deformation will be prolate (oblate). Now as the core is not a spherical one rather deformed axially, thus, j is no more a good quantum number and it splits up to $2j + 1$ sublevels and the splits can be described as the projection of symmetry axis, Ω . Here, Ω

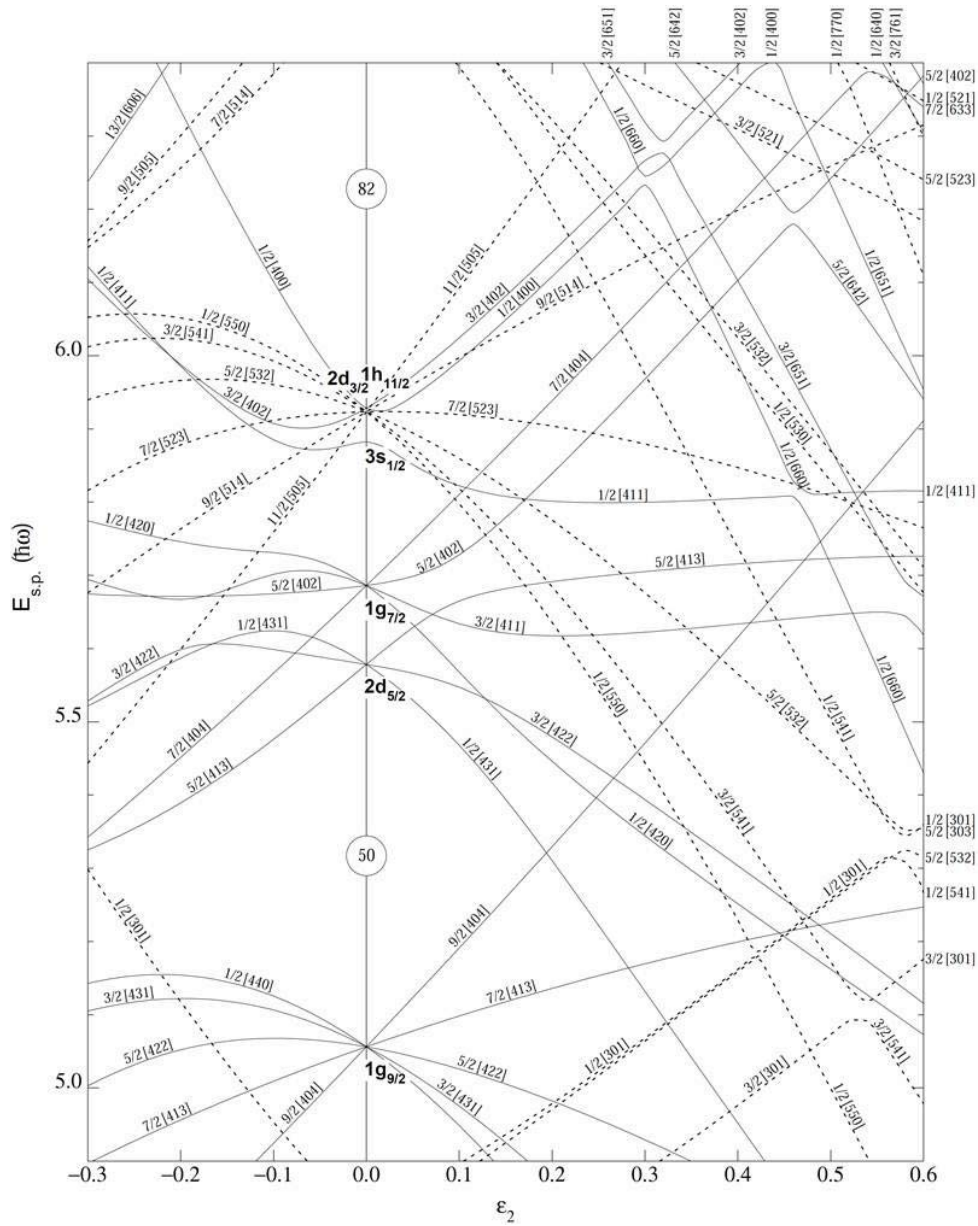


Figure 2.3: The Nilsson diagram for Z or $N = 50 - 82$ shell is shown. The diagram has been taken from Ref. [NIL55].

becomes a good quantum number and only time reversed orbits corresponding to $\pm\Omega$ are degenerate. As an example, a Nilsson diagram is given in Fig. 2.3 where, the diagram describes the evolution of single particle energies as a function of deformation parameter ϵ_2 ($= \delta$). The different levels in the diagram are

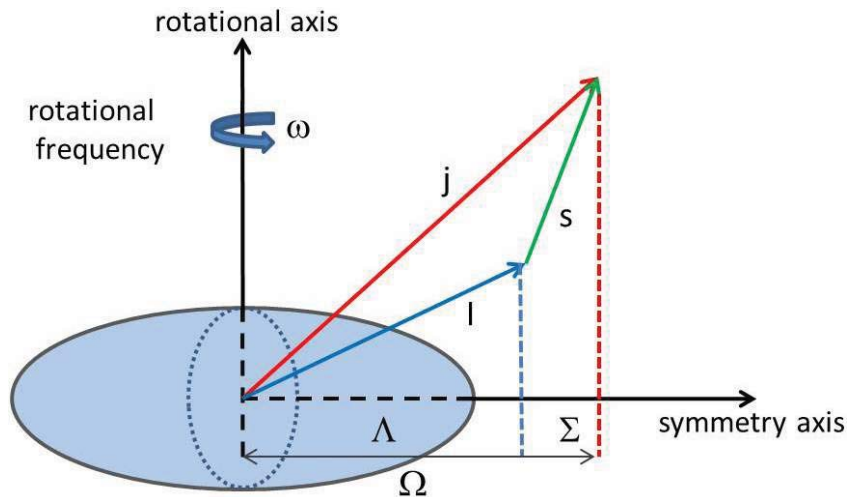


Figure 2.4: Asymptotic quantum numbers of axially deformed nucleus are shown.

labeled by a set of asymptotic quantum numbers

$$\Omega^\pi [N n_z \Lambda] \quad (2.22)$$

where, $\Omega = \Lambda + \Sigma$ is the projection of the angular momentum on the symmetry axis along with parity π such that

$$\pi = (-1)^N \quad (2.23)$$

where, N is the principal quantum number of the major shell while, n_z is its projection on symmetry axis. Λ and Σ are the projections of the orbital angular momentum (ℓ) and spin (s) on the symmetry axis, respectively, as described in Fig. 2.4. From the Nilsson diagram, it is clear that the m-substates, for a particular state, having lower Ω values are shifted downwards for prolate shapes and upwards for oblate shapes and vice versa for increasing Ω values. Two levels, with same quantum numbers, cannot cross each other; and with same Ω and π approach close to each other; and also repel due to Pauli Exclusion principle.

In order to predict different properties of a nucleus one need a suitable shell model code that has the ability to handle large number of nucleons and also give a reliable result.

Large basis shell model

There are many models in nuclear physics, though, modern large basis shell model calculation is very attractive as it gives the most accurate output of the nuclei close to the line of stability as well as far from stability [FEN73, NAV98, SAR01, HOR13]. Besides the predictions of low lying energy levels, it also can calculate different properties of nuclei, e.g., magnetic moment, g-factor, quadrupole moment, reduced transition probability etc. of very exotic nuclei also. In this model calculations, one does not need to calculate the total energy of the system considering the full dimension of valence nucleons 'A', rather one can calculate the total energy with respect to a closed core considering only the valence nucleons outside the core. Thus, one does not need to handle the full space dimension of matrix elements and the complexity of the calculation and time elapsed will also be less. The main parts on which the shell model is built are namely known as effective interaction, model space and diagonalization code of matrices. The main problems that appear in the calculation are: (a) The availability of model space and corresponding effective interaction. It is very difficult to get the effective interaction from the bare n-n force while, this effective interaction can not be used directly in the present state of SM calculations without any phenomenological corrections. (b) The calculation also depends on the capability of computer system because with the increase of the number of particles or holes and/or size of the valence space the dimension of the matrices tremendously blew up. (c) One has to set single particle energies for both protons and neutrons orbital of the configuration space or model space as an input parameter.

Configuration space or Model space

The configuration space or model space is the region of the single particle levels that can be /is occupied by the valence nucleons outside the inert core. The inert core and the model space can be similar or different for the protons and neutrons depending on their total numbers. In the shell model calculation, it is assumed that the whole properties of a nucleus are determined by the valence nucleons thus, the inert cores are kept to remain unchanged and the valence nucleons are played to occupy the different orbital in a permutation mode keeping in mind the Pauli Exclusion principle. The best results are obtained when the model space can be made as large as possible but with the increase of the size the computational time is increased a lot and the empirical Hamiltonians are also difficult to determine for the large space. Thus, one has to compromise to choose an optimum model space. In the present thesis, the calculations have been done using ^{100}Sn ($Z = 50$, $N = 50$) as core and 50 - 82 subshell shape as the models spaces for both proton and

neutron valence particles .

Effective interaction

For shell model calculation a suitable effective interaction between the valence nucleons is required. This many body interaction matrix can be given in a form of two body matrix elements. The value of the elements mainly depends on the single particle wave function and residual interaction. It depends on the total spin and isospin of the two body system.

Nowadays, there are many codes available (e.g., OXBASH, NuShell, NuShellX@MSU, Antoine etc.) to perform the LBSM calculation. In the present thesis work, the NuShellX@MSU code has been explored to interpret the experimental results.

Present work: NuShellX@MSU code

NuShellX is a computer based code originally written by Bill Rae [RAE] to perform the LBSM calculation. This code has capability to predict the exact energies, spin-parity of the states, spectroscopic factors, nuclear moments etc. for the low lying states. The code uses a J-coupled proton-neutron basis and the dimensions of up to order of 100 million of J-scheme matrix can be considered and is based on the previous NuShell code developed by Alex Brown. Later on, the NuShellX code was also modified by Alex Brown from MSU with a name ‘NuShellX@MSU’ [BRO, BRO14]. It is a set of wrapper codes that use the data files for model spaces and Hamiltonian to generate input for NuShellX. The NuShell code generates basis states in the m-scheme and after that, it computes the matrix elements in the j-scheme. Therefore, it can bypass the complication of the analysis and can also avoid the large matrix dimension created during m-scheme. Another advantage is that the matrix elements of Hamiltonian are calculated ‘on-the-fly’, therefore, the amount of storage is relatively less. The size of the model space should be optimized as calculations can not be performed with infinite space. Sometimes, truncations are required depending on the computational capability. In general, the most complete and appropriate results are obtained with the larger model space but at the same time, the computation time also increases exponentially with the size of model space. On the other hand, the empirical interactions are normally better determined if the size of the model space is small.

The low-lying spectra of iodine ($Z = 53$) and xenon ($Z = 54$) nuclei around ^{132}Sn ($Z = 50, N = 82$) have been performed using large scale shell model NuShellX code. The ^{100}Sn ($Z = 50, N = 50$) has been considered

as a core. The $jj55pn$ model space is considered for both the valence protons and neutrons where the particles are distributed over the single particle states $1g_{7/2}$, $2d_{5/2}$, $2d_{3/2}$, $3s_{1/2}$ and $1h_{11/2}$ with single particle energies of 0.80720 ($\pi 1g_{7/2}$), 1.56230 ($\pi 2d_{5/2}$), 3.31600 ($\pi 2d_{3/2}$), 3.22380 ($\pi 3s_{1/2}$), 3.60510 ($\pi 1h_{11/2}$), -10.60890 ($\nu 1g_{7/2}$), -10.28930 ($\nu 2d_{5/2}$), -8.71670 ($\nu 2d_{3/2}$), -8.69440 ($\nu 3s_{1/2}$), and -8.81520 ($\nu 1h_{11/2}$) MeV, respectively. For the effective interaction, the two body matrix elements named as $sn100pn$ has been used which is actually obtained from a realistic interaction calculated by Brown et al. [BRO05] using the G matrix derived from CD Bonn n-n interaction [MAC96]. The said potential is a charge dependent n-n potential. As protons are charged particles thus Coulomb interaction was also included in the interaction between protons. Therefore, the Hamiltonian consists of three parts of interaction: the proton-proton (pp) interactions, neutron-neutron (nn) interactions, and proton-neutron (pn) interactions, i.e., $H = H_{nn} + H_{pp} + H_{pn}$. For the single particle wave function, the harmonic oscillator was used. This method is an iterative procedure and the lowest energy states are calculated first. The one-body transition densities obtained from the output of the program can be used to calculate the matrix elements for $\mathcal{E}\lambda$ and $\mathcal{M}\lambda$ and hence, nuclear moments, e.g., magnetic moments, quadrupole moments etc.

Chapter 3

Gamma-ray spectroscopy

3.1 Introduction

The γ -ray spectroscopy, an important branch of experimental nuclear structure studies, provides one of the standard research tools to study the properties of the nuclei. As electromagnetic radiation is a well understood phenomenon compared to nuclear forces, a vast part of nuclear properties can be understood from the study of the electromagnetic transitions. A nucleus, in general, can be excited through different nuclear reactions and it de-excites to the ground state by successive emission of γ -rays, i.e., electromagnetic transitions, if the excited nucleus has not enough energy for emission of a particle. These successively emitted γ -rays carry important information of the nuclear excited states which are involved in the emission process. The richness of knowledge of nuclear structure depends on what one knows about the excited states and thus, the detection of the emitted γ -rays from the excited states become one of the standard technique of nuclear spectroscopy. The emitted γ -rays are collected using suitable gamma detectors on the basis of the properties of γ -rays' interaction with detector material and, thereby, the information carried by the γ -rays are extracted. This spectroscopy is related to the direct or indirect measurement of γ -ray transition energies, transition rates, angular correlations, linear polarisations, transition branching ratios, mixing ratios etc. and thus provides the information of nuclear level structure, spin and parity of the states, levels lifetimes, quadrupole moment, magnetic moment, associated wavefunctions and transition matrix elements etc. This method, therefore, has been applied immensely to probe various aspects of the nuclear structure and explore the nuclei with respect to nuclear models to know whether it behaves like single particle nature or shows a collective behavior or others.

For the development of ultra-fast scintillator detectors (e.g., LaBr₃(Ce) or CeBr₃) in recent times, as well as the availability of high energy resolution semiconductor detectors (e.g., Clover HPGe) nowadays, it is possible to access the nuclear transitions and hence to study the nuclear structure with great accuracy and variety. With the development of HPGe detectors in different form the high resolution spectroscopy has evolved to a great extent by now [ROS98, AKK12, MUR10, ALA18]. In addition, the development of ultra-fast scintillator detectors (viz., LaBr₃(Ce) and CeBr₃), it has been possible to perform $\gamma - \gamma$ fast timing spectroscopy with direct measurement of nuclear level lifetimes with high precision and accuracy [MAJ09, MAR10, DEL10, REGA12, ROB14, WIE16, FRA17]. The present thesis is based on the $\gamma - \gamma$ fast timing spectroscopy with the development of a $\gamma - \gamma$ fast timing array with CeBr₃ detectors.

As an integral part of gamma spectroscopic measurement, understanding the electromagnetic transitions and its properties are of importance. The same has been discussed in the following subsections, along with the other parameters that have been used in the present thesis work.

3.1.1 Electromagnetic transition probabilities

When a nucleus is produced in an excited state then it normally decays through the emission of photons (γ -rays) to reach it's ground state, in case the excitation energy is below its particle emission threshold. Consider a nucleus that decays from an initial state of energy \mathcal{E}_i , angular momentum \mathcal{I}_i and parity π_i to a final state of energy \mathcal{E}_f , angular momentum \mathcal{I}_f and parity π_f by emitting a γ -ray of energy ($\mathcal{E}_\gamma = \mathcal{E}_i - \mathcal{E}_f$). The conservation of angular momentum states that the total initial angular momentum should be equal to total final angular momentum, thus [KRA87],

$$\mathcal{I}_i = \mathcal{L} + \mathcal{I}_f \tag{3.1}$$

where \mathcal{L} , is the angular momentum that is carried out by the emitted gamma radiation, is known as multipolarity. The emitted radiation follows a set of selection rules depending upon the angular momentum and parity of the initial and final states. As Eq. (3.1) forms a closed triangle the possible values of \mathcal{L} are restricted to:

$$| \mathcal{I}_i - \mathcal{I}_f | \leq \mathcal{L} \leq | \mathcal{I}_i + \mathcal{I}_f | \tag{3.2}$$

Thus, the emitted radiations have only positive angular momentum $\mathcal{L} > 0$ (i.e., 1, 2, 3, ...). $\mathcal{L} = 0$ is the monopole term and is forbidden as the intrinsic spin of a radiation which is equal to $1\hbar$ implies that 0^+ to 0^+ transition (i.e., $\mathcal{L} = 0$) is forbidden. The higher values, i.e., $\mathcal{L} = 1$ is called dipole term, $\mathcal{L} = 2$ is called quadrupole term and so on. Whether an emitted radiation is of electric type or magnetic type that depends on selection rules of parity:

for purely electric multipole radiation: $\pi_f = (-1)^\mathcal{L} \pi_i$ and

for purely magnetic multipole radiation: $\pi_f = (-1)^{\mathcal{L}+1} \pi_i = -(-1)^\mathcal{L} \pi_i$.

Thus, if a transition of γ photon takes place with no change in parity then the transition would be either even electric or odd magnetic type and if the parity is changed then it would be odd electric or even magnetic. The lowest multipoles usually dominate, i.e., emission of multipole \mathcal{L} is more probable than emission of multipole $\mathcal{L} + 1$. Also, the emission of electric multipole is more dominant than the emission of same magnetic multipole. It is important to note that if the lowest order multipole radiation is electric type then other multipolarities can be avoided due to their negligible strength and if the lowest order is magnetic type then the next higher order electric multipole should be taken into account due to its non-negligible strength.

The radiated power in electric and magnetic transition of order \mathcal{L} can be described by [KRA87]:

$$\mathcal{P}(\sigma\mathcal{L}) = \frac{2(\mathcal{L} + 1)c}{\varepsilon_0 \mathcal{L} \{(2\mathcal{L} + 1)!!\}^2} \left(\frac{\omega}{c}\right)^{2\mathcal{L}+2} |\mathcal{Q}_{fi}(\sigma\mathcal{L})|^2 \quad (3.3)$$

It is an expression of energy radiated per unit time in the form of photon. The σ stands for Electric (\mathcal{E}) or Magnetic (\mathcal{M}) multipole character. The term $\mathcal{Q}_{fi}(\sigma\mathcal{L})$ is transition matrix element between the initial state of wave function ψ_i and final state of wave function ψ_f and according to Quantum mechanics, it can be defined by Multipole operator $\mathcal{Q}(\sigma\mathcal{L})$ where,

$$\mathcal{Q}_{fi}(\sigma\mathcal{L}) = \langle f | \mathcal{Q}(\sigma\mathcal{L}) | i \rangle = \int \psi_f^* \mathcal{Q}(\sigma\mathcal{L}) \psi_i dv \quad (3.4)$$

Therefore, the number of photons, each of energy $\hbar\omega$, emitted per unit time, i.e., transition probability can

be expressed by [MOR76]:

$$\mathcal{T}(\sigma\mathcal{L}) = \frac{8\pi(\mathcal{L} + 1)}{\hbar\mathcal{L}\{(2\mathcal{L} + 1)!!\}^2} \left(\frac{\omega}{c}\right)^{2\mathcal{L}+1} |\mathcal{Q}_{fi}(\sigma\mathcal{L})|^2 \quad (3.5)$$

The above equation represents the transition probability for one sub-process $\mu = m_i - m_f$, where m_i and m_f are substates of initial and final states, respectively. In order to get total transition probability, i.e., information of lifetime (inverse of total transition probability) associated to the initial state, one has to take sum over all possible substates μ and m_f :

$$\begin{aligned} \mathcal{T}(\sigma\mathcal{L}; j_i \rightarrow j_f) &= \sum_{\mu, m_f} \mathcal{T}(\sigma\mathcal{L}, \mu; j_i m_i \rightarrow j_f m_f) \\ &= \frac{8\pi(\mathcal{L} + 1)}{\hbar\mathcal{L}\{(2\mathcal{L} + 1)!!\}^2} \left(\frac{\omega}{c}\right)^{2\mathcal{L}+1} \sum_{\mu, m_f} |\langle j_f m_f | \mathcal{Q}(\sigma\mathcal{L}) | j_i m_i \rangle|^2 \\ &= \frac{8\pi(\mathcal{L} + 1)}{\hbar\mathcal{L}\{(2\mathcal{L} + 1)!!\}^2} \left(\frac{\omega}{c}\right)^{2\mathcal{L}+1} \mathcal{B}(\mathcal{L}, j_i \rightarrow j_f) \end{aligned} \quad (3.6)$$

where, the term $\mathcal{B}(\mathcal{L}, j_i \rightarrow j_f) \equiv \sum_{\mu, m_f} |\langle j_f m_f | \mathcal{Q}(\sigma\mathcal{L}) | j_i m_i \rangle|^2$ is known as ‘reduced transition probability’.

With the help of the Wigner-Eckart theorem and orthonormality relation of Clebsch-Gordan coefficient the reduced transition matrix can be expressed as [MOR76]:

$$\mathcal{B}(\mathcal{L}, j_i \rightarrow j_f) = \frac{1}{2j_i + 1} |\langle j_f | \mathcal{Q}(\sigma\mathcal{L}) | j_i \rangle|^2 \quad (3.7)$$

which ensures that the lifetime of a state does not depend on its orientation (i.e., rotational invariance).

The relation between the excitation $\mathcal{B}(\mathcal{L}) \uparrow$ and decay $\mathcal{B}(\mathcal{L}) \downarrow$ of a nuclear state is:

$$\mathcal{B}(\mathcal{L}, j_i \rightarrow j_f) = \left(\frac{2j_f + 1}{2j_i + 1}\right) \mathcal{B}(\mathcal{L}, j_f \rightarrow j_i) \quad (3.8)$$

The relation between transition probability $\mathcal{T}(\sigma\mathcal{L})$ and reduced transition probability $\mathcal{B}(\sigma\mathcal{L})$ according to Eq. (3.6) is tabulated in Table 3.1.

Using Weisskopf single-particle estimates [WEI51], one can theoretically calculate the reduced transition probabilities for \mathcal{EL} and \mathcal{ML} transitions. In this estimate the nuclear transition is considered as single particle transitions, i.e., a nucleon transits from one single particle orbit to another without effecting other nucleons in the nucleus which experience a constant central potential. The equations of Weisskopf single-

Table 3.1: Relation between transition probability $\mathcal{T}(\sigma\mathcal{L})$ and reduced transition probability $\mathcal{B}(\sigma\mathcal{L})$. The units of $\mathcal{B}(\mathcal{E}\mathcal{L})$, $\mathcal{B}(\mathcal{M}\mathcal{L})$, $\mathcal{T}(\sigma\mathcal{L})$ and \mathcal{E} are given in $e^2 fm^{2\mathcal{L}}$, $\mu_N^2 fm^{2\mathcal{L}-2}$, sec^{-1} and MeV, respectively [MOR76].

$\mathcal{T}(\mathcal{E}1)$	=	1.59×10^{15}	\mathcal{E}^3	$\mathcal{B}(\mathcal{E}1)$
$\mathcal{T}(\mathcal{E}2)$	=	1.22×10^9	\mathcal{E}^5	$\mathcal{B}(\mathcal{E}2)$
$\mathcal{T}(\mathcal{E}3)$	=	5.67×10^2	\mathcal{E}^7	$\mathcal{B}(\mathcal{E}3)$
$\mathcal{T}(\mathcal{E}4)$	=	1.69×10^{-4}	\mathcal{E}^9	$\mathcal{B}(\mathcal{E}4)$
$\mathcal{T}(\mathcal{M}1)$	=	1.76×10^{13}	\mathcal{E}^3	$\mathcal{B}(\mathcal{M}1)$
$\mathcal{T}(\mathcal{M}2)$	=	1.35×10^7	\mathcal{E}^5	$\mathcal{B}(\mathcal{M}2)$
$\mathcal{T}(\mathcal{M}3)$	=	6.28×10^0	\mathcal{E}^7	$\mathcal{B}(\mathcal{M}3)$
$\mathcal{T}(\mathcal{M}4)$	=	1.87×10^{-6}	\mathcal{E}^9	$\mathcal{B}(\mathcal{M}4)$

particle estimates derived from Eq. (3.7) can be expressed in the following simple forms as [MOR76]:

$$\mathcal{B}(\mathcal{E}\mathcal{L}) = \frac{1.2^{2\mathcal{L}}}{4\pi} \left(\frac{3}{\mathcal{L}+3} \right)^2 A^{2\mathcal{L}/3} \quad [\text{in } e^2 fm^{2\mathcal{L}}] \quad (3.9)$$

$$\mathcal{B}(\mathcal{M}\mathcal{L}) = \frac{10}{\pi} (1.2)^{2\mathcal{L}-2} \left(\frac{3}{\mathcal{L}+3} \right)^2 A^{(2\mathcal{L}-2)/3} \quad [\text{in } \mu_N^2 fm^{2\mathcal{L}-2}] \quad (3.10)$$

The above equations give approximate values and would be expected to match with the experimental results in case of extreme single-particle spectra. The Weisskopf estimate is especially useful to compare the order of experimentally observed values with the theoretically calculated values. If the observed transition rate is smaller than Weisskopf estimate by several orders then it results a poor overlapping between initial and final wave functions whereas, a larger decay rate by several orders refers to a result of collective behavior of multiple nucleons. A comparative study of Weisskopf estimate for different multipolarity of electric and magnetic transition is tabulated in Table 3.2.

Table 3.2: The Weisskopf estimate of transition probability $\mathcal{T}(\sigma\mathcal{L})$ and reduced transition probability $\mathcal{B}(\sigma\mathcal{L})$ upto multipolarity(\mathcal{L}) equals to 4 for both electric and magnetic transition. The units of $\mathcal{B}(\mathcal{E}\mathcal{L})$, $\mathcal{B}(\mathcal{M}\mathcal{L})$, $\mathcal{T}(\sigma\mathcal{L})$ and \mathcal{E} are given in $e^2 fm^{2\mathcal{L}}$, $\mu_N^2 fm^{2\mathcal{L}-2}$, sec^{-1} and MeV, respectively [MOR76].

$\sigma\mathcal{L}$	$\mathcal{B}(\sigma\mathcal{L})$	$\mathcal{T}(\sigma\mathcal{L})$
$\mathcal{E}1$	$6.45 \times 10^{-2} A^{2/3}$	$1.02 \times 10^{14} A^{2/3} \mathcal{E}^3$
$\mathcal{E}2$	$5.94 \times 10^{-2} A^{4/3}$	$7.23 \times 10^7 A^{4/3} \mathcal{E}^5$
$\mathcal{E}3$	$5.94 \times 10^{-2} A^2$	$3.37 \times 10^1 A^2 \mathcal{E}^7$
$\mathcal{E}4$	$6.29 \times 10^{-2} A^{8/3}$	$1.06 \times 10^{-5} A^{8/3} \mathcal{E}^9$
$\mathcal{M}1$	1.79	$3.12 \times 10^{13} \mathcal{E}^3$
$\mathcal{M}2$	$1.65 A^{2/3}$	$2.21 \times 10^7 A^{2/3} \mathcal{E}^5$
$\mathcal{M}3$	$1.65 A^{4/3}$	$1.03 \times 10^1 A^{4/3} \mathcal{E}^7$
$\mathcal{M}4$	$1.75 A^2$	$3.25 \times 10^{-6} A^2 \mathcal{E}^9$

3.1.2 Internal conversion

For low energy γ -ray transition, internal electron conversion is an important phenomenon because a nucleus in an excited state decays to lower energy state of the same nucleus not only by emitting γ -ray but also by non-radiative process like internal electron conversion. As the radius of orbital (Bohr orbits) is inversely proportional to atomic number (Z), thus, the electrons in atomic orbitals of a heavy nucleus have a finite probability to penetrate into the nucleus and come under the influence of multiple fields. The nucleus can make a transition from higher to lower energy state after transferring energy to the electron by direct coupling. The vacancy created by emission of the electron from the inner shell due to this process is rapidly filled up by an electron from a higher orbit, leading to the emission of characteristic X-rays. The ratio of the probability of nuclear transition by internal conversion (\mathcal{T}_e) and by γ -decay (\mathcal{T}_γ) is a measure of internal conversion coefficient [KRA87] : $\alpha = \mathcal{T}_e/\mathcal{T}_\gamma$ and the total transition probability (\mathcal{T}_{total}) is :

$$\mathcal{T}_{total} = \mathcal{T}_\gamma + \mathcal{T}_e = \mathcal{T}_\gamma(1 + \alpha) \quad (3.11)$$

The probability of internal conversion is largest for innermost K-shell electrons and decreases rapidly towards the outermost layers: $\alpha_K > \alpha_L > \alpha_M > \dots$ and the total internal conversion coefficient is given by:

$$\alpha = \alpha_K + \alpha_L + \alpha_M + \dots \quad (3.12)$$

The value of α depends on atomic number (Z), transition energy (E) and multipolarity (\mathcal{L}) of the transition. According to Dancoff and Morrison [DAN39]: (1) The internal conversion increases with atomic number ($\alpha \propto Z^3$) and decreases with principle quantum number. (2) The coefficient is larger for transition of low energy and dominates over γ -ray emission for transition of energy (≤ 200 keV). (3) Probability of γ -decay decreases with higher multipolarity (\mathcal{L}) whereas, internal conversion probability increases. In case of $0^+ \rightarrow 0^+$ nuclear transition, for which γ -ray decay is forbidden, the only possible transition is internal conversion.

Thus, the low energy and high-multipolarity transition in heavy nuclei increases the rate of electron conversion and hence, conversion coefficient. Therefore, the actual or experimental decay rates of γ -ray will be altered and hence, measured lifetime of the decaying state.

3.1.3 Nuclear level lifetime

The lifetime (τ) or mean life (τ_{mean}) of an excited state is defined as the average time it takes to decay from a higher excited state to a lower excited or ground state of a radioactive nucleus and is equal to inverse of total transition rate between the two states and can be expressed as [KRA87]:

$$\tau = \tau_{mean} = \frac{1}{\mathcal{T}_{total}} = \frac{1}{\mathcal{T}_{\gamma}(1 + \alpha)} = \frac{t_{1/2}}{\ln 2} \quad (3.13)$$

where, $t_{1/2}$ is known as half-life which is the representation of decay constant of a radionuclide and can be defined by the time required to decrease of activity to one-half of its initial activity.

If a given excited state decays to more than one final state via different decay paths then the total transition probability will be the sum over all individual transition probability. If $\mathcal{T}(i)$ is the transition probability of a i^{th} decay path then total transition probability will be:

$$\mathcal{T}_{total} = \sum_i \mathcal{T}(i) \quad (3.14)$$

The partial half-life for each decay path can be calculated from its partial transition probability,

$$t_{1/2}(i) = \frac{\ln 2}{\mathcal{T}(i)} \quad (3.15)$$

and thus, the actual half-life of the given excited state will be the sum of all partial half-life:

$$t_{1/2} = \sum_i t_{1/2}(i) \quad (3.16)$$

On the other hand, from the measured experimental half-life $t_{1/2}$ of a state one can find out partial half-life $t_{1/2}(i)$ for a particular i^{th} decay path if the state has a branch of decay path and hence, partial transition probability $\mathcal{T}(i)$ of that particular path can be calculated. Therefore, the reduced transition probability $\mathcal{B}(i)$ calculated from that partial transition probability using Eq. (3.6) can be compared with the theoretically calculated Weisskopf estimate as given in Table 3.2.

3.1.4 Mixing ratio

In case of mixed nature, e.g., $\mathcal{E}(\mathcal{L}) + \mathcal{M}(\mathcal{L} + 1)$ or $\mathcal{M}(\mathcal{L}) + \mathcal{E}(\mathcal{L} + 1)$, for a allowed transition, the mixing ratio (δ) can be calculated by the ratio of their respective transition probability from the initial state to final state and can be expressed as:

$$\text{for } \mathcal{E}(\mathcal{L}) + \mathcal{M}(\mathcal{L} + 1) \text{ mixed transition : } \delta^2 = \frac{\mathcal{T}(\mathcal{M}(\mathcal{L} + 1))}{\mathcal{T}(\mathcal{E}(\mathcal{L}))} \quad (3.17)$$

$$\text{for } \mathcal{M}(\mathcal{L}) + \mathcal{E}(\mathcal{L} + 1) \text{ mixed transition : } \delta^2 = \frac{\mathcal{T}(\mathcal{E}(\mathcal{L} + 1))}{\mathcal{T}(\mathcal{M}(\mathcal{L}))} \quad (3.18)$$

Again, for a given mixed transition, the fraction of a particular type of multipolarity decay, so called branching fraction (b) is related to mixing ratio δ and can be expressed as (e.g., $\mathcal{M}(\mathcal{L}) + \mathcal{E}(\mathcal{L} + 1)$):

$$\text{branching fraction of } \mathcal{E}(\mathcal{L} + 1) : b(\mathcal{E}) = \frac{\mathcal{T}(\mathcal{E}(\mathcal{L} + 1))}{\mathcal{T}(\mathcal{M}(\mathcal{L})) + \mathcal{T}(\mathcal{E}(\mathcal{L} + 1))} = \frac{\delta^2}{1 + \delta^2} \quad (3.19)$$

$$\text{and branching fraction of } \mathcal{M}(\mathcal{L}) : b(\mathcal{M}) = \frac{\mathcal{T}(\mathcal{M}(\mathcal{L}))}{\mathcal{T}(\mathcal{M}(\mathcal{L})) + \mathcal{T}(\mathcal{E}(\mathcal{L} + 1))} = \frac{1}{1 + \delta^2} \quad (3.20)$$

3.1.5 $\gamma - \gamma$ angular correlation

The idea of angular correlation originates from the basic physics which suggests that the probability of emission of radiation or quantum by a radioactive nucleus depends on the angle between the direction of emission of the radiation and the nuclear spin axis. However, the radioactive nuclei in a sample or source are, in general, randomly oriented and thus, an isotropic nature of distribution of the emitted radiations is normally observed. For an anisotropic distribution, photons emitted by nuclei which are not randomly oriented, i.e., having common spin orientation need to be examined [FRA55, MUH08].

This type of situation can be obtained in a number of ways, e.g., if the radioactive sample is kept at a very low temperature under a strong electric or magnetic field so that the nuclei are aligned according to the field and thus, gives an angular distribution of the emitted radiation with respect to the direction of the applied field. Another simple way is that if one can select an ensemble of nuclei whose spins happen to lie in a preferred direction then the successive radiations emitted from the nuclei will have definite angular correlation with respect to one another provided that the emissions must be in coincidence and emitted from the same nucleus. For example, in a fusion evaporation reaction, the angular momentum of the compound

nucleus is directed perpendicular to the beam direction and the γ -rays are emitted from the ensemble of the oriented nuclei. Moreover, under an electric or magnetic field, the interaction of aligned spins with the field makes a precession of the nuclear spins around the symmetric axis of the field and as a result the anisotropy of the correlation also changes. Therefore, one can divide this method into two types of phenomena depending on the measurement environment: perturbed angular correlation and unperturbed angular correlation [FRA55]. If the system is not affected by any environmental or external field that means if the nuclei are not affected by any extranuclear field during the measurement time then it is called an unperturbed angular correlation while, if the system is perturbed by sufficient extranuclear field then it is called perturbed angular correlation.

The angular correlation can also be studied between different type of radiations, e.g., $\alpha - \gamma$, $\beta - \gamma$, $\gamma - \gamma$, $e^- - e^-$ etc depending upon the physics of interest. It is a very important tool to study the dynamic characteristics, e.g., β , γ transition between levels as well as static properties such as angular momenta (spin), parity, magnetic moment, EQM etc. of ground state as well as few first excited states of the nuclei. In the present work, both perturbed and unperturbed angular correlation has been studied and EQM is measured for excited states of iodine isotopes. The detail theory of both perturbed and unperturbed angular correlation along with development of angular correlation setup have been discussed in Chapter 5.

3.2 Detection of γ -rays: Interaction with matter

Whenever a γ -ray moves through matter, it interacts with the material by an indirect process. It deposits its kinetic energy to the medium giving rise to some kind of effects like ionization, excitation etc. The γ -ray interacts with matter via three major interaction process namely, photoelectric absorption, Compton scattering and pair production.

3.2.1 Photoelectric absorption

This process states that if a γ -ray interacts with an absorber atom then it transfers full energy of it to an electron of the atom. So an energetic photoelectron is ejected from the bound states of the atom. This process can't take place with a free electron because in that case energy-momentum conservation does not hold. Only bound electrons, thus, can take part in this process and absorb the incident photons (see Fig. 3.1).

If the γ -ray has sufficient energy ($h\nu$) then the photoelectron is ejected from the tightly bound inner orbit like K shell, L shell etc. The energy of the ejected electron will be $E_e = h\nu - E_b$, where E_b is the binding energy of the electron in that particular shell. In addition, the vacancy created by the ejected electron in the atomic shell may be filled by an electron from the outer orbital of the atom. As a result, it emits characteristic X-ray which is usually reabsorbed by the detector itself via some photoelectric absorption involving less tightly bound shells. So this process results full energy deposition of the incident γ -ray to the detecting system. This absorption process predominates with the γ -rays of relatively low energy (≤ 200 keV) and the absorber material with a relatively high atomic number (Z). The absorption cross-section per atom varies as:

$$\sigma_{photo} = Z^n / E_\gamma^{3.5} \quad (3.21)$$

where, n varies between 4 to 5.

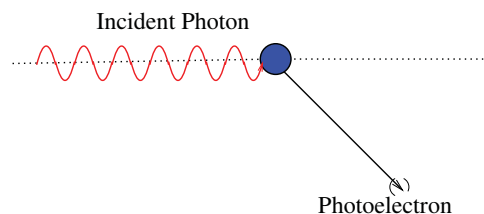


Figure 3.1: An illustration of photoelectric effect.

3.2.2 Compton scattering

If an incident γ -ray is elastically scattered from a loosely bound electron of an atom then it is known as Compton scattering (see Fig. 3.2). In this interaction, the photon imparts a part of its energy to the loosely bound electron, assumed to be at rest. The electron, therefore, recoils at some angle, say ϕ with respect to the initial incident photon direction and the γ -ray scatters away at angle θ (say) with reduced energy. The energy difference between the incident photon and the scattered photon is carried away by the recoil electron. According to energy-momentum conservation relation, the reduced energy of the scattered γ -ray

is given by:

$$h\nu' = \frac{h\nu}{1 + \gamma(1 - \cos\theta)} \quad (3.22)$$

where, $\gamma = h\nu/m_0c^2$ and m_0c^2 is the rest mass energy of the electron. Therefore, according to the conservation, the kinetic energy of the recoil electron will be:

$$E_e = h\nu - h\nu' = h\nu \frac{\gamma(1 - \cos\theta)}{1 + \gamma(1 - \cos\theta)} \quad (3.23)$$

$$\text{and } \cot \frac{\theta}{2} = (1 + \gamma) \tan \phi \quad (3.24)$$

The photon can be scattered in any direction from $\theta = 0^\circ$ to its maximum value $\theta = 180^\circ$. So the energy distribution of electron shows a continuum starting from zero to the maximum value, known as the Compton continuum and contributes to the background in the spectra below the photopeak as shown in Fig. 3.5. This interaction is predominant in the intermediate energy range (0.1 MeV to 1.5 MeV). The probability of the interaction per atom depends on the number of electrons available in the target and hence, it increases linearly with atomic number Z .

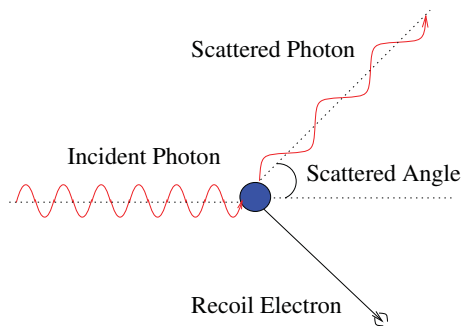


Figure 3.2: An illustration of Compton scattering process.

3.2.3 Pair production

This process occurs when the incident γ -ray energy exceeds twice the rest mass energy of an electron (i.e., $E_\gamma \geq 2m_0c^2 = 1.02 \text{ MeV}$) and passes near the Coulomb field of an atomic nucleus. The γ -ray completely disappears and is converted into a pair of electron-positron ($e^+ - e^-$) (see Fig. 3.3). The excess energy

of the photon above 1.02 MeV (the minimum energy required to create a $e^+ - e^-$ pair) is shared as the kinetic energy of the two particles. The positron is slowed down in the absorbing medium and afterward annihilates with one of the electrons from the surrounding material and produce two annihilation photons, each with energy 511 keV. The probability of cross-section of this interaction varies approx. as the square of the atomic number Z of the absorbing material.

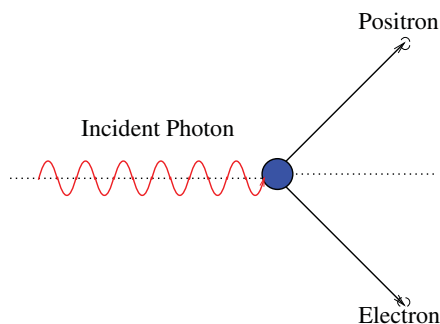


Figure 3.3: An illustration of pair production process.

The Fig. 3.4 shows a comparative representation of variation of absorption cross-section of these three interaction depending on the energy of the γ -ray energy.

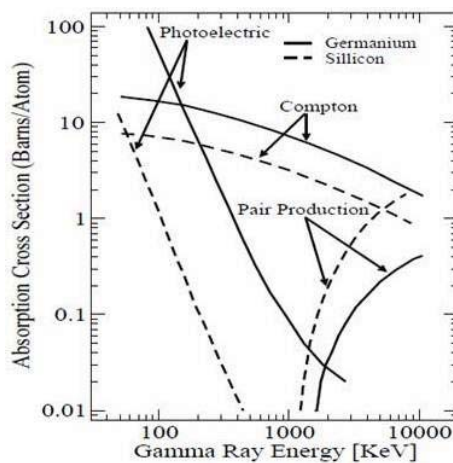


Figure 3.4: Representation of relative probability (absorption cross-section) of the three types of interactions in Ge ($Z = 32$) and Si ($Z = 14$) as a function of the γ -ray energy has been shown. Image taken from Experiments in Nuclear Science published by EG & G Ortec.

A typical energy spectrum has been shown in the following Fig. 3.5.

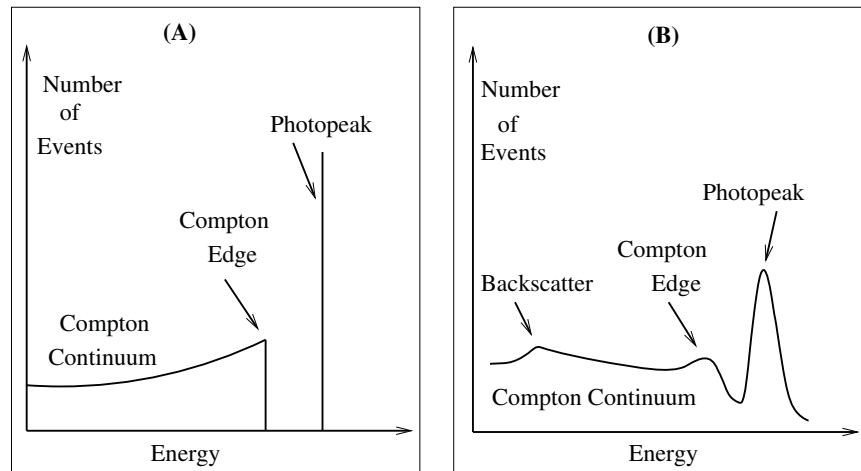


Figure 3.5: A typical energy spectrum due to Compton and photopeak effect of a gamma detector: (A) shows an ideal γ -ray spectrum and (B) shows a real γ -ray spectrum.

3.3 Important observables used in γ -ray spectroscopy

Following the detection of the γ radiation, it is necessary to characterise the transition for extracting the associated information on the nuclear level from which the transition is emitted. Now, the capability of producing a usable signal for a given type of radiation and energy is referred to as sensitivity of a detector. Any one particular detector can not be sensitive to all types of radiation at any energy. They are actually sensitive to certain types of radiation in a given energy range. Outside this range they are less sensitive producing unusable signal or their detecting efficiency is greatly decreased. Thus depending on the physics interest, a particular type of detector or an array with several detectors is chosen for the experiment. Before choosing the detectors one has to keep in mind the common observables of a detector, e.g., its response, energy resolution, detecting efficiency, timing resolution etc. for a wide range of energy. These observables are defined from the parameters of a photopeak in the spectrum which is Gaussian in shape (see Fig. 3.5 (B)) or from the time of detection required by the γ photon from the time of its incidence on the detector.

3.3.1 Detector response

The output signal of radiation detectors, in general, is in the form of a current or voltage pulse. The integral of pulse with respect to time reflects the amount of ionization or excitation taking place inside the detecting material. The integral can be assumed directly proportional to the amplitude or pulse height of

the signal. The relation between the radiation energy and the pulse height of the final output signal is called the response of the detector. The response may be linear or non-linear over a wide energy range depending upon the types of incident radiation, types of detector and its signal processing accessories etc.

3.3.2 Energy resolution of a detector

The energy resolution of a detector evaluates how well it distinguishes between two γ -rays with close energies, i.e., it is the ability of a detector to separate two pulses generated by the γ -rays of closely spaced energies. It is defined as the Full Width at Half Maximum (FWHM) (ΔE) of the Full Energy Peak (FEP) divided by the energy value (E) at the peak position. Ideally, a delta function type FEP is expected but in reality, the FEP with finite width has appeared. The width reflects the random statistical fluctuations that originate in the process of charge creation and collection even though exactly same amount of energy is deposited in the detector. Thus, if, in total, n number of charge carriers are created on an average then according to Poisson distribution the inherent statistical distribution equal to the standard deviation (σ) of \sqrt{n} is observed in that number n [KNO10]. For larger n , the Poisson distribution leads to Gaussian shape and the resolution due to only statistical fluctuation in the number of charge carriers can be expressed as:

$$\text{Resolution}(R) = \frac{\text{FWHM}(\Delta E)}{\text{Peak Energy } (E)} = \frac{2.35k\sqrt{n}}{kn} = \frac{2.35}{\sqrt{n}} \quad (3.25)$$

where, average energy $E = kn$ and $\text{FWHM} = 2.35\sigma = 2.35k\sqrt{n}$, k is a proportionality constant. Thus, the resolution (R) will be improved if the number of charge carriers (n) are increased. In case of gas detector ~ 35 eV is required to create one ion pair, whereas for scintillator detector it is almost ~ 100 eV to create photoelectron and for semiconductor (germanium) detector it is only ~ 3 eV to create one electron-hole pair. As, for same incident energy, the number of carriers (n) is larger in germanium detector, thus, it provides better energy resolution over the other scintillator or gas detectors. A correction term known as Fano factor (F) is added in standard deviation ($\sigma = k\sqrt{Fn}$). The factor is actually the function of all various fundamental processes to transfer energy in the detector and the correction is required as all reactions do not participate to ionize the medium, e.g., phonon excitations, etc. [LEO94]. For scintillator detector the Fano factor (F) is equal to unity, thus, no correction is required for it, whereas, in case of semiconductor detector or gas detector it is less than unity and hence, improves the resolution.

Besides the fluctuation in ionization, a number of other factors may affect the actual resolution of a

detector. Those may be noise, drift etc. from both the detector and its associated electronics. In the total FWHM, therefore, all the factors should be incorporated:

$$FWHM_{total} = \sqrt{(FWHM_{statistical})^2 + (FWHM_{noise})^2 + (FWHM_{drift})^2 + \dots} \quad (3.26)$$

3.3.3 Gamma detection efficiency

The efficiency of a detector is defined as the probability that an emitted particle or radiation will interact with the detector's material and produce a significant count. In case of γ detection, the photopeak efficiency is of concern as the photopeak only provides complete information about the emitted radiation. The absolute photopeak efficiency is known as the total efficiency of a detector and is defined as that fraction of radiation quanta emitted by the source which is actually recorded by the detector as photopeak events:

$$\textit{Absolute Efficiency: } \varepsilon_{abs} = \frac{\textit{Number of events registered}}{\textit{Number of events emitted by the source}} \quad (3.27)$$

The absolute efficiency depends not only on the detector properties but also on the distance from the source to a detector. Thus, it can then be factored into two parts: intrinsic efficiency (ε_{int}) and geometric efficiency (ε_{geo}). The intrinsic efficiency can be defined as:

$$\textit{Intrinsic Efficiency: } \varepsilon_{int} = \frac{\textit{Number of events registered}}{\textit{Number of events impinging on the detector}} \quad (3.28)$$

The probability of this type of efficiency depends on the interaction cross-sections of the incident radiation on the detector medium. The efficiency, thus, is a function of several parameters, e.g., type of radiation and its energy, detector material and its thickness in the direction of incident radiation etc. For the charged particles like α or β , the probability of capture cross-section is so high that the interaction takes place immediately in the form of ionization after traveling a small distance in the detector volume. But, in the case of an uncharged particle like neutron or gamma radiation, the probability of capture cross-section is not so high as they rarely interact with the detector medium and travel a large distance between interactions through the material. Actually, they first interact with the medium to create secondary energetic charged particles and that charged particles are then absorbed by the detecting material in the form of ionization.

On the other hand, the geometric efficiency depends on the fraction of source radiation which is geo-

metrically intercepted by the opening area of the detector, i.e., on the solid angle subtended by the detector on the source position. It may also depend on the size of the source and angular distribution of the emitted radiation. The geometric efficiency can be defined as:

$$\textbf{Geometric Efficiency: } \varepsilon_{geo} = \frac{\text{Number of events impinging on the detector}}{\text{Number of events emitted by the source}} \quad (3.29)$$

It is equal to $\Omega/4\pi$ for isotropic emission of radiation from the source where, Ω is the solid angle made by the detector at the source position. Thus, to measure the absolute efficiency of a detector for a given source of radiation placed at a certain distance from the detector, the information of both the intrinsic (ε_{int}) and geometric (ε_{geo}) efficiency of the detector are necessary and can be expressed by the product of them using standard formulation:

$$\varepsilon_{abs} = \varepsilon_{int} \varepsilon_{geo} = \frac{\Omega}{4\pi} \varepsilon_{int} = \frac{cps}{dps \times I} \quad (3.30)$$

where, cps is the ‘count per second’ of the detector, dps stands for ‘disintegration per second’ of the source and I is the abundances for the particular γ -ray transitions. Experimentally, cps can be determined as the area under a full energy peak per unit time.

3.3.4 Time resolution of a detector

The time resolution of a detector means that how accurately the interaction times of radiations with the material of a detector can be measured. To get a profile of timing distribution, a two detectors combination can be used in coincidence mode. As the probability of generation of photoelectrons or pair of electron-holes from incident radiation can be described as the statistical Poisson distribution thus, for incident prompt events the shape of the coincidence timing distribution normally appears as a Gaussian-like shape for two identical detectors. The FWHM (Full Width at Half Maximum) of the Gaussian distribution refers to the combined time resolution ΔT_c of the two detectors. The FWHM contains all the timing uncertainty from the detectors and their associated electronics. It includes all timing uncertainty that exists inside the detector crystal’s volume ($\Delta T_{crystal}$) due to photoelectrons or electron-holes or exciton creation and collection process. If there is a photodetector like photomultiplier tube (PMT) connected with the crystal, in case of scintillator detector, to enhance the light output then, time dispersion arising from the PMT (ΔT_{PMT}) due to photoelectrons conversion, transit time jitter etc. appears in the observed width

of FWHM. Another major timing dispersion appears in that width is due to time walk or time jitter of Constant Fraction Discriminator (CFD) (ΔT_{CFD}), due to amplitude of light output of PMT, used in the electronic circuit in both the timing branches. Thus, the actual time resolution of a single detector ΔT_s can be expressed as:

$$\Delta T_s = \frac{\Delta T_c}{\sqrt{2}} = \frac{FWHM}{\sqrt{2}} \propto \sqrt{(\Delta T_{Crystal})^2 + (\Delta T_{PMT})^2 + (\Delta T_{CFD})^2} \quad (3.31)$$

For a better time resolution of a detector, a high light output, as well as short decay and rise time, are also required. The light output refers to the number of photoelectrons that are generated in the photodetector and actually depends on the light output of the scintillator crystal and the properties of photodetector, i.e., its light extraction efficiency and quantum efficiency etc. The rise time of the signal plays an important role as it consists of the timing information at a very early stage but it is affected by many factors like rise time of scintillation process itself, fluctuations due to photon transmit from emission point to photocathode, fluctuations occur in the multiplication process etc.

According to the Ref. [HYM64] the time resolution of a scintillator detector can be expressed as:

$$\Delta T \propto \frac{\sqrt{\tau_d}}{\frac{N_{phe}}{ENF}} \quad (3.32)$$

where, τ_d is the decay time of scintillator, N_{phe} is the number of photoelectrons and ENF is the excess noise factor of the photodetector.

3.4 γ -ray fast timing spectroscopy: Detectors and their uses

With the increase of nucleon numbers, the discrete energy states of a nucleus and emitted γ -ray energies from the excited states also become closer and closer. Thus, the energy spectrum obtained from the collection of the emitted γ -rays looks more and more complex and the complexity increases with the increase of accessible higher angular momentum states. On the other hand, if the parent nucleus is unstable in its ground state then the daughter nucleus, in general, is produced in its one of the excited states after β or Electron Capture (EC) decay and hence, it cools down towards respective ground state by emitting successive gamma radiations. The above chain is continued until a stable daughter nucleus is obtained. Thus in the decay spectroscopy, all the gamma energies of parent nuclei and its respective daughter nuclei

may present and thus, the order of complexity of the energy spectrum depends on the order of simplification of the experimental method and on the detecting system used in that experiment. Therefore, a suitable detector or an array of detectors is required which has very good energy resolution, i.e., a capability to identify all the individual gamma in that energy spectrum. On the other hand, as most of the excited nuclear states have lifetime in the picosecond (ps) region thus, in order to measure these lifetimes of ps width, the detectors with very good timing resolution are required for the $\gamma - \gamma$ fast timing measurement. Again, the detector should have reasonable intrinsic detection efficiency for a wide range of energy and also should have reasonable density and volume so that probability of interaction cross-section of photoelectric effect increases. In the next section, the working principle of semiconductor and scintillator detectors, mostly used in the nuclear spectroscopy have been discussed along with the recent development of advanced detectors with their advantages and limitations.

3.4.1 Semiconductor detector

The semiconductor detector, made of crystalline semiconductor materials (mostly silicon or germanium), has a moderate bandgap between conduction band and valence band with respect to metal and insulator. The basic operating principle of such detector is that when an energetic radiation is passed through the material, a number of electron-hole pairs are created inside the material. Then these charge carriers are collected by an applied electric field to produce an electrical signal and, hence, the information about the incident radiation is extracted. The semiconductor detector made of High-Purity Germanium (HPGe) crystal, mostly used in γ -ray spectroscopy, has been discussed below.

High-Purity Germanium (HPGe) detectors

Basically, the HPGe detector is a reverse biased semiconductor (pn-junction) diode. The depletion region, between pn-junction, which is a measure of the active volume of the detector plays an important role. Only immobile ionized atoms are present in the depletion region and no carriers (free electrons and holes) are available there. When an energetic radiation is passed through the depletion region electron-hole pairs are created and these mobile charge carriers are swept out of the depletion region under the influence of the applied electric field and drift towards the respective collector ends. Their motion gives rise to electrical pulse which contains the information of energy and timing of the incident radiation. The depletion depth of a semiconductor detector is given by [KNO10]:

$$d = \left(\frac{2\epsilon V}{eN} \right)^{1/2} \quad (3.33)$$

where, ϵ is the dielectric constant of the material, V is the applied reverse bias voltage, e is the electric charge and N is the net impurity concentration in the initial semiconductor material. In case of normal germanium semiconductor the maximum achievable depletion depth is a few mm only, even at close to breakdown voltage. In the High-Purity Germanium (HPGe) detector the impurity concentration can be reduced to very low ($\sim 10^9$ atoms/cm³) as a result of advances in manufacturing techniques and thus, a depletion depth of several cm can be achieved. As the band gap of germanium crystal is small (~ 0.7 eV) this detector can not be operated at room temperature due to large thermally induced leakage current. The detectors are thus cooled at liquid nitrogen temperature (77 K) through thermal contact when it is operated. This detector offers an excellent energy resolution (~ 2 keV at 1 MeV) and thus is used for high energy resolution spectroscopy. The timing resolution of this detector, however, is poor (~ 10 ns) in comparison to the scintillator detectors that are majorly used in fast timing spectroscopy.

Clover HPGe detector

The clover detector consists of four HPGe crystals (as shown in Fig. 3.6) placed in four quadrants of a square, arranged like a four-leaf clover. Each detector has a square front face and round edges which is obtained by tapering it on two adjacent faces with an angle 7.1° starting at round the half of the length and by cutting the two remaining faces parallel to the axis of crystal and along its whole length. This enables a closed packing of the crystals with a small gap of 0.2 mm. The Clover detector is encapsulated in a vacuum cryostat attached to a liquid nitrogen dewar to cool the detector around 77° K. The diameters and lengths of each individual crystal of the Clover HPGe detector used in the present work are 50 mm and 70 mm, respectively. The total volume of four tapered crystals is ~ 470 cm³ which is about 89% of the original crystal volume. Each of the crystals behaves as an independent detector and has two separate output signals that can be used to extract energy and timing information.

If the γ -ray undergoes photoelectric interaction in any one of the individual crystals of the clover then the total energy will be absorbed by that crystal, while if it undergoes Compton scattering from one crystal to the next, then the coincidence events can be added back together, in offline analysis. This is known as

add-back method by which the overall peak-to-total is increased by getting back the lost photopeak events. The add-back efficiency, therefore, is increased and greater than the sum of the individual efficiency of the four crystals. The add-back mode provides a great advantage for measuring high energy γ -rays with clover detectors. Also, as a consequence of its design, there is a number of advantages of a clover detector: (1) As the effective solid angle is reduced for individual crystals, thereby energy resolution is improved. (2) The crystal size is small, thus, timing resolution is much better than that of single large HPGe crystal of the same volume. (3) Due to the smaller opening angle of the clover detector in comparison to a large volume HPGe detector, the effect of Doppler broadening on the resulting spectra is reduced. (4) Linear polarization of the γ -ray can also be measured with these detectors by studying the direction of Compton scattering.

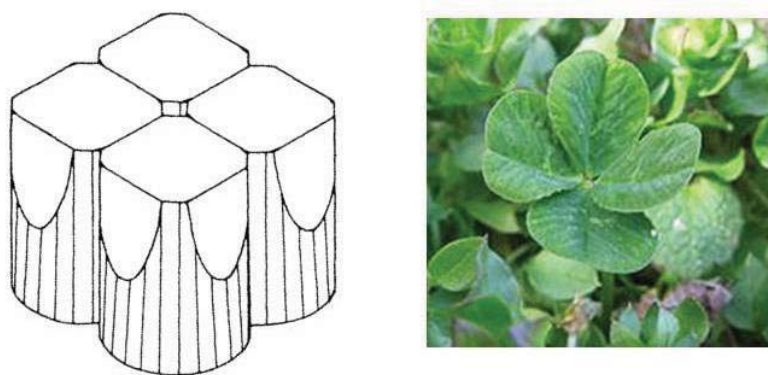


Figure 3.6: A schematic geometry of the crystals of a clover detector. The crystals are arranged like a four leaf clover.

The clover detector can be surrounded by an anti-Compton shield made by scintillating material Bismuth Germanate ($Bi_4Ge_3O_{12}$), abbreviated as BGO to further reduce the Compton background in the γ -ray spectrum. This surrounding BGO detector is used to detect the escaped Compton scattered γ -rays from the clover volume and is kept as a veto to that scattered γ -rays. Thus, Compton background in the total energy spectra is reduced and hence peak-to-background ratio is improved.

3.4.2 Scintillator detector

Scintillation materials have a property known as luminescence. The phenomena of luminescence are the process of re-emission of the excited energy in the form of electromagnetic radiation in the visible region. Luminescence can be classified into two types: fluorescence, phosphorescence. If the re-emission occurs immediately or within 10^{-8} sec after absorption, the process is usually called fluorescence. If the decay time is

larger compared to fluorescence due to the involvement of excited meta-stable state then the luminescence is called phosphorescence (or afterglow). This decay time may be sustained from a few microseconds to hours depending on the material. Due to several processes like mechanical strain, heating, chemical reaction and absorption of light etc. the excitation of the material may also occur. If the process occurs due to radiations then the phenomenon of emission of light is called scintillation and the material is called scintillator [KNO10, LEO94]. The scintillator materials are mainly of two types - organic and inorganic scintillator. The difference between these two types of scintillators mainly belongs to their different mechanism of the scintillation process. In the case of the organic scintillator, instead of the physical state of the material, the scintillation process depends only on single molecular process whereas in the case of an inorganic scintillator the crystal lattice is involved.

Organic scintillator detector

The organic scintillator is generally formed by aromatic hydrocarbons in the form of solid or liquid. This type of scintillator has a very rapid decay time on the order of ns or even less. Scintillation light arises due to the transition of free valence electrons which occupy the n-molecular orbital but not any particular atom. The following Fig. 3.7 represents the energy level diagram of molecules where, the symbol S_0 denotes the ground states, i.e., singlet state. The excited singlet states in the figure are represented by S^* , S^{**} , \dots and so on above the singlet state. The lowest triplet state is referred to as T_0 and excited levels are represented by T^* , $T^{*,*}$, \dots and so on. Each of the electronic levels is further subdivided into fine structure configuration corresponding to various vibrational states. The energy spacing between electron levels is of the order of a few eV whereas the spacing between the vibrational states is of the order of 0.15 eV.

The molecular singlet states which are excited by incident radiation generally decay immediately (few ps) by internal degradation to the S^* state without emitting any radiation. The actual EM radiation occurs when S^* state decays to one of the vibrational states of the ground state S_0 . The lifetime of such decay is typically in the low ns region. In case of triply excited states, similar degradation brings the system to the T_0 triplet state which is forbidden to decay to the singlet states due to multiple selection rules. The relaxation occurs due to $T_0 - T_0$ interaction and produces the delayed or slow component of scintillation light.

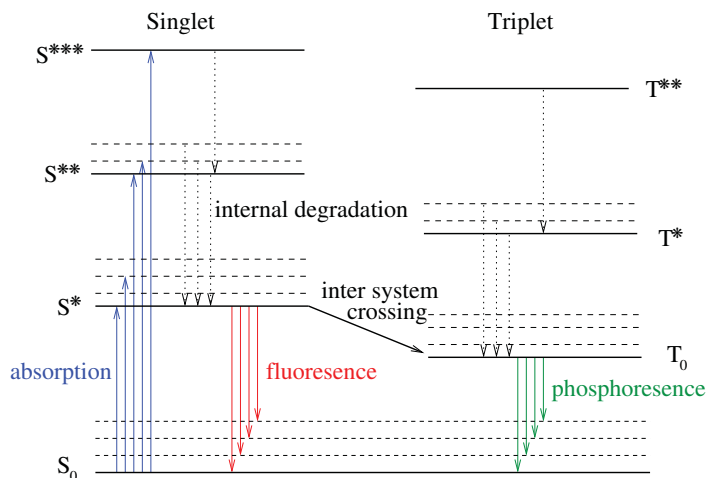


Figure 3.7: An illustration of the energy level of organic scintillator molecule. ‘S’ denotes the single state and ‘T’ denotes the triplet state.

Inorganic scintillator detector

The scintillation mechanism in inorganic scintillators can be characterized using an electronic band structure found in an insulator. Here, two mechanisms can take place when a nuclear particle is incident on the crystal. The electrons may be excited from the valence band to conduction band leaving the corresponding hole in the valence band or an exciton (weakly bound electron-hole pair) may be created into the exciton band located just below the conduction band. The exciton moves freely through the crystal until they de-excite. In the intrinsic crystal, the emission of photon due to transition of an electron from the conduction band to valence band is an insufficient process. Now if impurities are added to the crystal by doping, energy states in the forbidden gap between valence and exciton band are created. These energy states which behave like de-excitation sites are known as recombination centers through which electrons can de-excite to the valence band. A schematic diagram of this mechanism is shown in Fig. 3.8.

The probability of recombination is widely increased with the number of recombination centers, i.e., with the impurity added to the crystal. Now if a succeeding electron comes and recombines with the migrating free hole or hole from an exciton pair then it may allow a transition from the excited state to ground state by emitting radiation. Sometimes, the excited state is a meta-stable state and de-excitation takes time (from a few microseconds to hours depending upon the material) enhancing a slow decay component. If the transition band gap of the crystal is such that the energy of the emitted radiation falls in the visible to

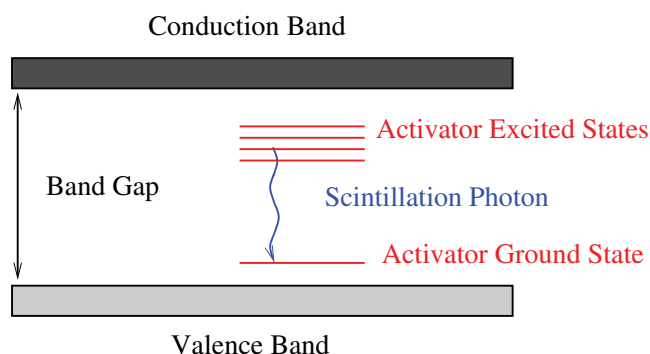


Figure 3.8: An illustration of energy band structure along with activator sites of an inorganic scintillation crystal.

ultraviolet range of EM spectrum, then a scintillation photon is produced.

Photomultiplier tube (PMT)

As the light output from the scintillator is very low and is not sufficient for extracting information therefrom, thus, photomultiplier tubes are normally coupled to the scintillator to convert the light output into an enhanced electronic signal. A typical PMT consists of a photocathode made of photosensitive material, an electron collection system, a dynode chain or electron multiplier section and an anode. When a scintillation photon from the scintillator falls on the photocathode an electron is emitted through photoelectric effect. The emitted primary photoelectron is accelerated towards the first dynode of the electron multiplier section by the voltage applied between cathode and anode; and invokes the release of secondary electrons upon striking from the first dynode. All the electrons from the first dynode, then, are accelerated towards the next dynode where more electrons are emitted and further accelerated and so on as shown in Fig. 3.9. Thus, depending upon the number and type of dynodes and applied voltage between them, a gain of 10^7 to 10^{10} secondary electrons per a typical scintillation event can be obtained [KNO10, LEO94].

To increase the sensitivity or quantum efficiency of the photocathode for a wide range of wavelength of scintillation photon the material and thickness of photocathode are adjusted by compromising between semi-transparency (thick enough to stop most of the photon) and potential barrier (work function) for the photoelectrons. But a lower potential barrier may increase the emission of thermal electrons which increases noise in the final signal. On the other hand, the statistical noise and variation in the transit time of electrons are the two most important factors which affect the time resolution and response of a PMT. The generation of statistical noise due to the statistical nature of the photoelectric effect and the secondary

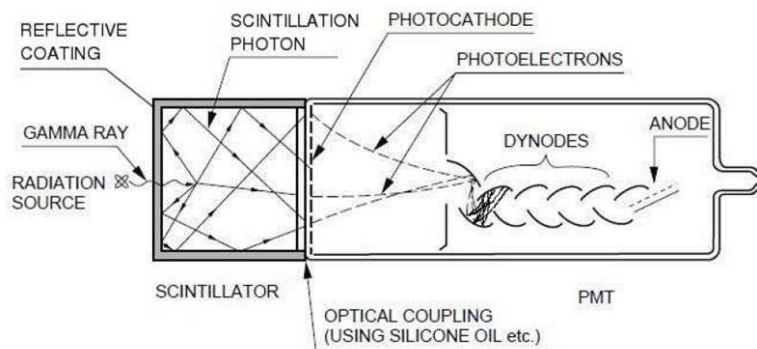


Figure 3.9: A schematic design of scintillator detector with PM tube.

emission process of electrons can be reduced by increasing the quantum efficiency of the photocathode and increasing the secondary emission of the multiplier. The different velocity of photoelectrons emitted from the photocathode and their path length traversed from photocathode to the first dynode gives rise to a time spread in the final signal out of a PMT. The time spread is mostly dependent on the geometry of the photocathode and the focusing electrodes. The time spread due to the distribution of velocity can be reduced by increasing the voltages between the cathode and first dynode and between other dynodes of the electron multiplier. But higher voltage increases the gain of the PMT and leads it into a saturation effect which results in a non-linear response of the PMT output and, thus, deteriorates the energy resolution. To minimize all the noises as much as possible, a suitable configuration of the PMT and an optimum voltage supply is used for a particular type of scintillator. As the total transition time is very small, thus, the typical scintillator is very fast compared to the semiconductor and hence provides a good time resolution.

In general photocathode, dynodes and anode of PMT are connected with stabilized voltage source through voltage divider circuit which may consist of a chain of fixed or variable resistances in such a way so that all the dynodes get desired voltage and make sure that the first dynode held positive voltage with respect to photocathode but negative with respect to second dynode and second dynode is negative with respect to third and so on thus, electrons will be attracted and gives an anode signal. The polarity of the power supply may be two types: positive polarity and negative polarity. In case of positive polarity, the anode is connected with a high positive potential with the cathode grounded as shown in Fig. 3.10 (a) while, in the negative polarity, the cathode is connected with a high negative potential with the anode grounded as shown in Fig. 3.10 (b). The choice of polarity depends on the type of application but in both the cases the photocathode must have always lower potential with respect to anode.

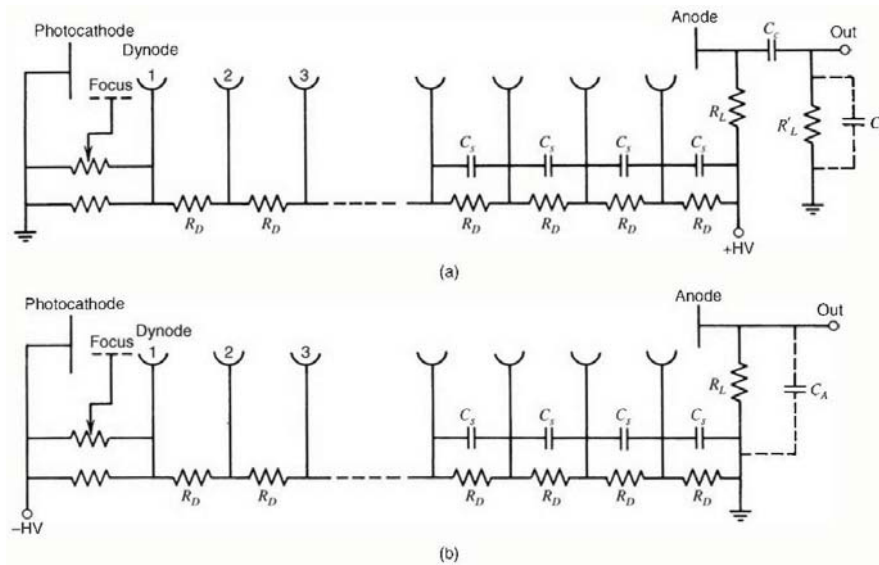


Figure 3.10: An illustration of schematic design biasing supply in PMT (a): refers to the positive polarity biasing supply at anode and photocathode is grounded while, (b): refers to the negative polarity biasing supply at photocathode which must be isolated from the ground and anode is kept at ground potential. Both the diagram are taken from [KNO10] where the other specifications of resistances and capacitors used in the diagram have been given. Only, in case of positive polarity, an extra coupling capacitor C_c must be connected with the anode output to block the anode high voltage but transmit only the signal pulse to the associated electronic circuit at ground potential.

In the case of positive polarity, if the cathode is not connected with the ground potential then spurious discharges may occur from cathode to scintillator or outer envelope of the detector. The grounded photocathode also minimizes noise occurring in the actual signal. Since, the anode is kept at a constant high positive potential thus, the anode output must be connected with the associated electronic circuit through a coupling capacitor (as shown in Fig. 3.10 (a)) so that it blocks the anode high voltage but transmit only the signal pulse to the electronics at ground potential. That coupling capacitor in between the anode and the electronic circuit, however, reshapes the anode pulse and thus, the timing information of that pulse may be interrupted and delayed. In the pulse counting system where timing information is not so crucial, this type of polarity is usually preferred but in the case of a fast timing experiment where timing information is very important, positive bias supply is not suitable. These problems can be overcome if the negative bias supply is used where the anode is kept at ground potential thus the signal pulses can be connected directly with the electronics without any coupling capacitor as shown in Fig. 3.10 (b). Another advantage is that instead of photocathode now the anode is at ground potential and high voltage is supplied to the cathode instead of anode thus, any ripple originates due to fluctuation of the high voltage supply is not capacitively

coupled directly onto the signal output therefore, the energy resolution will be less deteriorated. Thus for the fast timing experiment where timing information is very crucial, negative polarity is used in the PMT module. Since in case of negative polarity, the photocathode is kept at a high negative voltage thus, extra care should be taken so that no leakage currents generates from PMT to grounded material and no unwanted ‘dark current’ pulses may arise to affect the operation.

In some special experiments both energy and timing information are very important therefore, two alternative signal outputs from PMT are required for that information. Thus, some times, a second alternative signal may be taken from one of the dynode (especially from the last dynode) which gives a net positive voltage pulse (with a smaller amplitude than negative anode pulse) due to a net positive charge induced in the dynode as a larger amount of electrons leave the dynode than were initially arrived.

3.5 Development and use of fast timing array: Literature survey

In the present thesis, the main aim is to measure the nuclear level lifetime and transition moments which carry an utmost importance in understanding the structure of the atomic nucleus, as they provide a direct access to the transition rates associated with the de-population of the nuclear levels. For this purpose, a literature survey has been made for finding the suitable detector to develop a fast timing array along with the fast timing techniques that will be appropriate for measurement of level lifetimes in nuclei around the doubly closed ^{132}Sn .

Timing measurement techniques have been explored in different ranges from nanoseconds (ns) to picoseconds (ps) [PET06, DEW89, SCH68, MAC89], which are appropriate for in-beam prompt spectroscopy or off-beam decay spectroscopy. Such measurement involves different types of γ detectors, viz., high resolution Ge as well as fast timing BaF_2 . With the availability of the scintillation detectors like $\text{LaBr}_3(\text{Ce})$, in recent times, having energy resolution much better than the BaF_2 detectors along with a comparable time resolution, the exploration and application of an improved fast timing technique in ps range could be found in several literatures [REG10, REG13, RUD15, REG14, BHA13].

Recently, another scintillator detector, viz., CeBr_3 which is also highly hygroscopic as LaBr_3 , has been reported to have slightly poorer energy resolution compared to $\text{LaBr}_3(\text{Ce})$ [BIL11] but a similar time resolution [FRA13, DOL13]. These detectors are being explored as a viable alternative to $\text{LaBr}_3(\text{Ce})$ detectors which are limited by their self-activity [BIL11, LUT13]. The measurement of energy response,

energy resolution, time resolution and the efficiency of the CeBr₃ detectors of various sizes and coupled to different types of PMTs is found in several literatures [BIL11, FRA13, DOL13, GAU08, ACK15]. The efficiency measurement for an 1" ϕ \times 1" thick CeBr₃ detector was performed by comparing with the known efficiency of a LaCl₃ detector by the authors of Ref. [BIL11]. However, to the best of our knowledge, the measurement of absolute detection efficiency for these detectors is absent till date.

The non-proportionality in the response of a scintillator is found below 100 keV which is the intrinsic characteristic of all scintillators [LEC14]. The effect of this non-proportionality was found to contribute to the energy resolution of the CeBr₃ detectors by $\sim 2.8\%$ [QUA13, QUA14]. Also, as the high voltage in the PMT is increased to obtain better time resolution of the detector, the nonlinearity in the overall energy response of the detector is found in the PMT and/or amplifier outputs. This is basically related to the saturation effect of a particular PMT and its voltage divider circuit when coupled to a fast scintillator like LaBr₃ or CeBr₃ having fast and bright scintillation process [QUA11, DOR04]. Hence, it is also important to explore the effect of the applied bias voltage of the PMT on the energy response and energy resolution of the CeBr₃ detectors along with their time resolution.

3.5.1 Detectors and PMTs used in the present thesis

The Clover HPGe detectors along with BGO shields have been used in the present thesis for high resolution detection of gamma radiations. This was useful to understand the complete γ -ray profile as well as to clean and select gamma energy gates in fast timing scintillators by comparing the spectrum from these detectors to that obtained with the scintillators.

Two types of inorganic scintillator detectors (LaBr₃(Ce) and CeBr₃) have been used for γ -ray fast timing spectroscopic studies. The Hamamatsu R9779 and XP2020/URQ PMTs have been used along with CeBr₃ and LaBr₃(Ce), respectively, in the present work. A comparison of the properties and limitations of the used scintillators and PMTs used in the present thesis have been discussed below:

A brief comparison between LaBr₃(Ce) and CeBr₃ detectors:

The used LaBr₃:5%Ce crystal is made by a solid solution of 95% LaBr₃ with a doping of 5% CeBr₃. The lattice structure of both LaBr₃ and CeBr₃ crystals is uranium tri-chloride (UCl_3) type with an asymmetrical hexagonal crystal structure. The doped CeBr₃ element in LaBr₃ solution creates an activator state in between the conduction band and valence band of LaBr₃ crystal where the Ce³⁺ ion acts as a luminescence

center due to its allowed 5d to 4f transition [KNO10] and thus, scintillation light is generated when an effective incident energy is deposited in the crystal (see Fig. 3.11). The principle decay time (≤ 25 ns [SHA03]) of cerium luminescence in the host LaBr_3 material offers an attractive ultra-fast response of this scintillator detector.

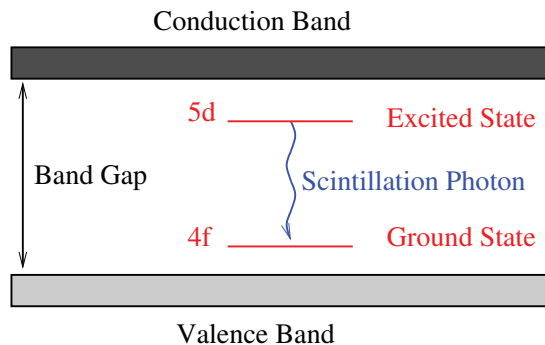


Figure 3.11: A schematic sketch of band structure of LaBr_3 crystal doped with Ce^{3+} ion.

The scintillation characteristic of CeBr_3 is very similar to $\text{LaBr}_3(\text{Ce})$. Here, Ce^{3+} behaves itself as an intrinsic constituent and luminescence center for producing scintillation light [SHA05]. As mentioned above, the similar luminescence in this crystal occurs due to transition from the lowest 5d level to the spin orbit split 4f ($^2F_{5/2}$ and $^2F_{7/2}$) ground state indicating a characteristic double emission band [QUA13, DRO08]. The main drawback in this detector is the apparent overlap of cerium absorption and emission band which is responsible for self-absorption in CeBr_3 crystal. As the short wavelength side of the Ce^{3+} emission band, which may be absorbed by other Ce^{3+} ions, may be re-emitted as a double band emission, i.e., re-distributed over the entire double band spectrum therefore, the fast decay time constant is being prolonged. The effect of self-absorption or so called ‘radiation trapping’ depends on the concentration of cerium ion and the size of the detector. The probability of loss of photons, which is a measure of decreasing the light yield of a scintillator, mainly depends on the distance traveled by photons inside the crystal and the presence of impurities that may absorb the photons. Thus, if the cycle of absorption occurs many time it will increase inhomogeneous performance of the detector and hence, degrade the energy resolution of the detector [QUA13]. It is seen that larger probability of photon loss makes the average light yield of CeBr_3 as approximate 68% of that typically achievable with $\text{LaBr}_3:5\%\text{Ce}$ [QUA13].

The main drawback associated with $\text{LaBr}_3(\text{Ce})$ scintillator is due to intrinsic radioactivity from ^{138}La isotope of Lanthanum element (0.09% naturally abundant) and ^{227}Ac (actinium is a chemical analogue to

lanthanum) [KNO10]. These radio-nuclei comes from the raw material, used to prepare detecting crystal, as Ac, La and Ce are chemically homologous elements and those are extremely difficult to separate one from the other. The radioisotope ^{138}La ($t_{\frac{1}{2}} = 1.03 \times 10^{11} \text{ y}$) has two primary decay mode: ^{138}La to ^{138}Ba (66.4%) via electron capture and ^{138}La to ^{138}Ce (33.6%) via β -decay. In the electron capture process a 1436 keV γ -ray emits in coincidence with a 32 keV Ba X-ray and may also produce a sum-peak at 1468 keV; while in case of β -decay, 789 keV γ -ray decays in coincident with a 255 keV endpoint energy and thus, a trapezoid-shaped continuum from just above 750 keV to just beyond 1000 keV may be observed. On the other hand, in the energy range of 1750 keV to 3500 keV, intrinsic γ -ray contributes due to α -decays associated with the ^{227}Ac decay chain. In a recently published paper the profile of intrinsic radioactivity of $\text{LaBr}_3(5\%\text{Ce})$ crystal coupled with Hamamatsu R2083 PMT has been experimentally studied and discussed (see Fig. 3.12) [CHA20].

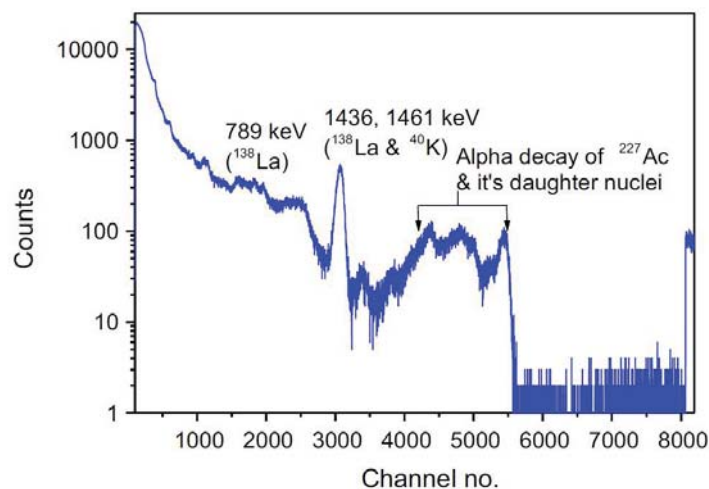


Figure 3.12: The figure shows the background spectrum of a $1'' \phi \times 1''$ thick $\text{LaBr}_3(5\%\text{Ce})$ crystal coupled with 8-stage Hamamatsu R2083 PMT. The emission energy peaks of intrinsic activity are clearly visible [CHA20].

It is worthy to mention that the ^{227}Ac isotopes can be significantly reduced from the impurities with the increasing manufacturing experience of growing the crystal [KNO10]. In the CeBr_3 crystal, the Ce and Br elements do not have any naturally occurring radioactive isotope and a small amount of intrinsic activities mainly due to ^{227}Ac present in the raw material. Thus, below $\sim 1.7 \text{ MeV}$ energy, there is no significant background effect due to the present of intrinsic activities in the CeBr_3 detector.

Besides the less intrinsic activities present in CeBr_3 with respect to LaBr_3 , the smaller ionic radius

Table 3.3: The above Table represents the Comparison among different scintillator detectors. Only fast decay component of all the mentioned detectors and their associated properties have been compared. The size of the both mentioned $\text{LaBr}_3(\text{Ce})$ and CeBr_3 detectors are $1'' \phi \times 1''$ thick whereas, LaBr_3 is doped with 5% CeBr_3 . Only main properties are compared for those detectors where, the terms ‘ ρ ’ refers to specific gravity of the material; ‘ λ_{max} ’ refers to maximum spectral emission wavelength; ‘ τ_d ’ refers decay time; ‘LY’ refers to Light Yield of the crystal and ‘R’ refers to Energy Resolution at 662 keV.

Detector	ρ	λ_{max} (nm)	τ_d (ns)	LY (Photons/MeV)	R (%)	Ref.
NaI(Tl)	3.67	415	230	38000	7	[KNO10]
BaF ₂	4.89	220	0.6	1400	10	[KNO10, LAV83]
BGO	7.13	480	300	8200	20	[KNO10]
$\text{LaBr}_3(\text{Ce})$	5.07	380	26	66000	3.1	[KNO10, QUA13]
CeBr_3	5.18	380	19	40000-47000	4.2-4.7	[QUA13]

of Ce (120 picometres) than that of La (122 picometres) and the larger effective atomic number Z_{eff} of CeBr_3 (45.9) than that of $\text{LaBr}_3:5\%\text{Ce}$ (45.3) makes the density of CeBr_3 (5.18 gm/cm³) larger than that of $\text{LaBr}_3:5\%\text{Ce}$ (5.07 gm/cm³) [QUA13]. Therefore, the detection efficiency of the CeBr_3 detector in terms of pair production at a given energy is expected to have a slightly larger value than that of the $\text{LaBr}_3:5\%\text{Ce}$ detector.

The basic descriptions of these detectors in comparison with other three mostly used inorganic scintillator detectors, viz., NaI(Tl), BaF₂ and BGO, have been shown in Table 3.3.

The PMTs used in the present work

The $\text{LaBr}_3(\text{Ce})$ scintillators are coupled with a very fast response 12-stage XP2020/URQ PMT while, the CeBr_3 scintillators are coupled with 8-stage R9779 PMTs which have also very fast response. Each of the PMTs has a well designed voltage divider circuits used for negative polarity bias supply to provide voltage to the respective photocathode, dynodes and anode. For an illustration, a schematic design of a circuit diagram of a R9779 PMT has been shown in Fig. 3.13. Among the two output signals of that PMT, in the present work, the anode output is directly used for timing signal and the last dynode signal is used for energy information. Both types of PMTs have a very fast rise time with a small transit time spread. The few main features of them are tabulated in Table 3.4.

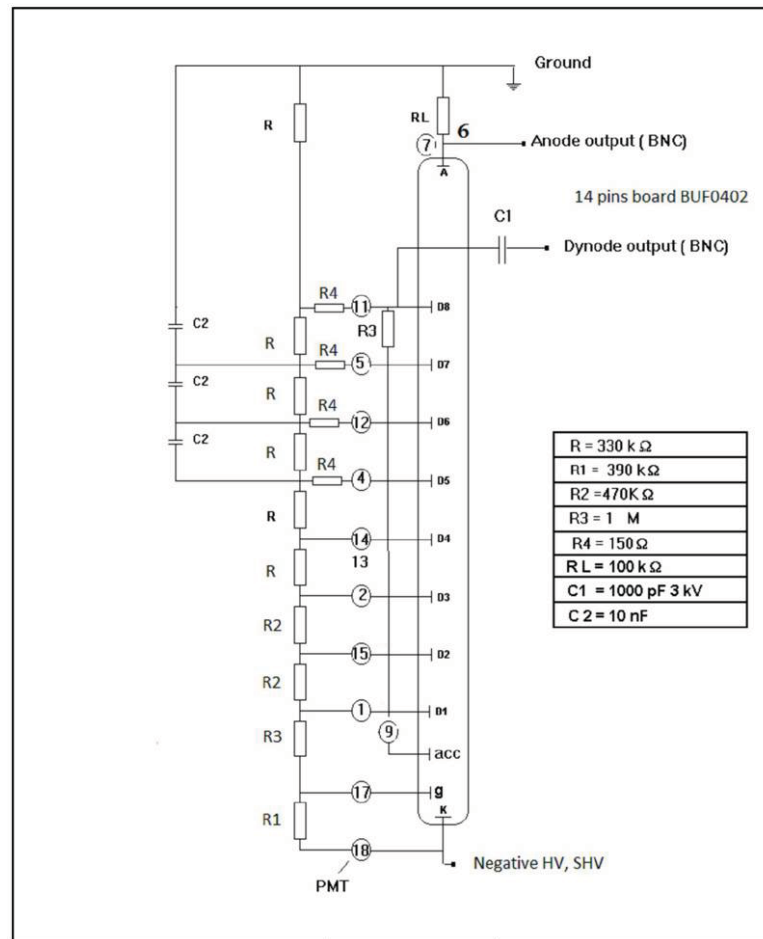


Figure 3.13: A schematic design of a Hamamatsu R9779 PMT and its biasing system [HAM09].

3.5.2 Testing and development in present thesis work

In the present work, prior to the development of the fast timing array, the characterization of an $1'' \phi \times 1''$ thick CeBr₃ detector, coupled to Hamamatsu R9779 PMT, has been performed by measuring its energy response, energy resolution, time resolution and detection efficiency for the γ -rays in a range of 80 keV to 1.4 MeV. The efficiency of one such CeBr₃ detector has been compared to that of a Clover HPGe detector and corroborated with a Monte Carlo simulation using GEANT3 package. This has been discussed in Subsection 4.4.1 of Chapter 4.

Following the basic characterization of the CeBr₃ detectors, an array consisting of such multiple CeBr₃ detectors has been set up at Variable Energy Cyclotron Centre (VECC), Kolkata. This array has been named as VECC Array for Nuclear fast Timing and Angular CorRElation Studies (VENTURE) and could

be used in its stand alone mode as well as with the array of Clover HPGe detectors like VENUS [SAH18] for complete γ spectroscopic measurement. The array will be used for the measurement of nuclear level lifetime down to few ps and the quadrupole moment [ALA16a, ALA16b]. The in-beam and off-beam setups of the array and an angular correlation table, designed and fabricated at VECC, Kolkata, are discussed in Chapter 4.

Table 3.4: Summarized of the main properties of XP2020/URQ and R9779 PMT [PHOTO, HAM09, FRA13]. \star refers to the Total Transit Spread (TTS) in the PMT and the FWHM of this distribution is a measure of time jitter.

PMT	Max. supply volt.(V)	Max. spectral response (nm)	Anode pulse rise time (ns)	FWHM TTS* (ps)	dark current (nA)	total gain
XP2020/URQ	3200	380	1.4	350	20	$\sim 3 \times 10^7$
R9779	1750	380	1.8	250	15	$\sim 5 \times 10^5$

The present work reports the exploration of the Mirror Symmetric Centroid Difference (MSCD) method [REG10] and Generalized Centroid Difference (GCD) method [REG13] with the $\gamma - \gamma$ time difference spectra, for the first time with CeBr₃ detectors. In addition to the lifetime measurement, the angular correlation measurement has been performed for few cascades of ⁶⁰Co and ¹³²I, respectively, with a setup of three such CeBr₃ detectors on the angular correlation table. The measurements are discussed in Chapter 5.

Chapter 4

Development of VECC Array for Nuclear fast Timing and AngUlar CorRelation Studies (VENTURE): $\gamma - \gamma$ fast timing measurement

4.1 Importance of lifetime measurement in nuclear structure study

To understand nuclear structure of the atomic nuclei, the knowledge of lifetimes of discrete and quantized nuclear states are of extreme importance. The information on level lifetime, i.e., the inverse of transition probability from initial state to final state, provides direct insight into the overlapping of the wave functions of those states. More fundamentally it provides the electromagnetic transition matrix elements which is very important to understand the structure of a particular nuclear level [FOS74]. So the measurement of lifetime gives crucial information regarding fundamental properties of nuclei and thus, becomes a useful tool for testing various existing models. Lifetime measurements have, thus, been employed for understanding the basics of nuclear structure in different mass regions on the segrè chart. Nuclear levels have a wide range of lifetimes from 10^{-15} seconds to 10^{15} years and thus different timing measurement techniques have been established to cover such a wide dynamic range. In the following subsection, a number of techniques for measurement of a nuclear level lifetime have been discussed.

4.2 Techniques for nuclear lifetime measurement

Table 4.1: Different techniques with their range, timing accuracy, measuring techniques have been summarized.

Methods		Timing region (sec)	Timing accuracies	Procedure of measurement	Condition on level lifetime
Electronic method (delayed coincidence)	Slope method	$10^{-10} < \tau < 10^{-6}$	$\sim 1\%$	Directly measured from time distribution spectrum	Lifetime larger than Full Width at Half Maxima (FWHM) of Prompt Response Function (PRF) by at least 30%
	Deconvolution method				Lifetime larger than FWHM of PRF
	Centroid shift method	$10^{-12} < \tau < 10^{-9}$			Lifetime comparable or below the FWHM of PRF
Doppler shift methods	RDM	$10^{-12} < \tau < 10^{-9}$	$\sim 5\%$	Fitting energy curve	
	DSAM	$10^{-14} < \tau < 10^{-12}$	$\sim 10\%$		

Different techniques are available for measurement of nuclear level lifetimes and they are limited by their own advantages and disadvantages depending on the methods of measurement. Among those different measurement techniques, the electronic method and the Doppler shift method are the basic and widely applicable ones to directly determine the lifetimes of the nuclear states. Depending on the measurement methodology, the electronic method can be further divided into three types; named as slope method, deconvolution method and centroid shift method, respectively, as tabulated in Table 4.1. Moreover, the centroid shift method has been recently improved, thereby proposing the Mirror Symmetric Centroid Difference (MSCD) method or widely known as Generalized Centroid Difference (GCD) technique, when extended to a setup of N detectors. Similar to the electronic method, the Doppler shift method can also be subdivided into the two techniques named as Recoil Distance Method (RDM) and Doppler Shift Attenuation Method (DSAM). The lifetime ranges covered by these different techniques are different and have been summarized, along with their timing accuracy, measurement methodology and restrictions on lifetime width, etc., in Table 4.1 .

4.2.1 Doppler shift method

The RDM and DSAM, two commonly used techniques for measuring lifetime, depend on the Doppler shift mechanism. They are based on the fact that a moving source (an excited nucleus) emitting γ -rays in flight shows a Doppler effect and a change or shift in the γ -ray's energy can be observed. In both methods, the Doppler shift of the γ -rays depends on the velocity β ($= \frac{v}{c} \ll 1$) of the moving nucleus and the shifted energy can be framed as (up to first order approximation) :

$$\mathcal{E}_\gamma = \mathcal{E}_\gamma^0 [1 + \beta(t) \cos(\theta)] \quad (4.1)$$

where, θ is the angle between the direction of the moving nucleus and the emitted γ -ray and \mathcal{E}_γ^0 is the energy of the γ -ray when the nucleus is at rest. At $\theta = 0^\circ$ the shift will be maximum, i.e., when the γ -rays are detected in the direction of the recoil nucleus and there will be no shift in the energy of the γ -ray if $\theta = 90^\circ$.

✠ In case of RDM, an energetic ion beam is allowed to fall on a thin target and the γ -rays emitted from the nuclei, in flight and at rest, are counted with high purity Ge detectors. The preparation of the target stopper assembly is very crucial for this method. The whole setup is designed in such a way that uniform vacuum space is kept in between the target and stopper material so that the recoil nucleus can move freely towards the beam direction and then is stopped by the stopper. For holding the target - stopper assembly and maintaining variable distance between them, the plunger device is very useful. The whole plunger assembly contains a cylindrical vacuum chamber made by aluminium housing and a motor assembly is attached with it to maintain various known distances (d) between target and stopper. The stopper is made of a material which has a high stopping power (e.g., Au, Ta etc.).

Normally, an excited nuclear state decays according to the following relation [FOS74] :

$$\frac{d\mathcal{I}}{dt} = -\lambda \mathcal{I}_0 e^{-\lambda t} \quad (4.2)$$

where, \mathcal{I}_0 refers to the initial number of nuclei present at the decaying state at initial time $t = 0$ and \mathcal{I} is the number of nuclei that depopulate the state after time t . λ is the transition rate or decay constant which involves the lifetime of the state of interest. Let us consider, the recoil nuclei produced in a reaction have velocity v and take time \mathcal{T} ($= d/v$) to travel from target to stopper through vacuum. Now, if there is \mathcal{I}_0

number of nuclei in an excited state, then a fraction of nuclei radiates before time \mathcal{T} , i.e., before they are stopped by stopper and rest of them decays after time \mathcal{T} while they are fully stopped. The γ -rays which are emitted in flight from the recoil nuclei, their corresponding energy will be shifted by Doppler effect according to Eq. (4.1). Similarly, the nuclei which emits γ -rays within the stopper, while are in rest, their corresponding energy will be unshifted. The ratio \mathcal{R} of the unshifted intensity to the total intensity (shifted and unshifted) is an exponential function of traveling time \mathcal{T} :

$$\mathcal{R} = e^{-\lambda\mathcal{T}} \quad (4.3)$$

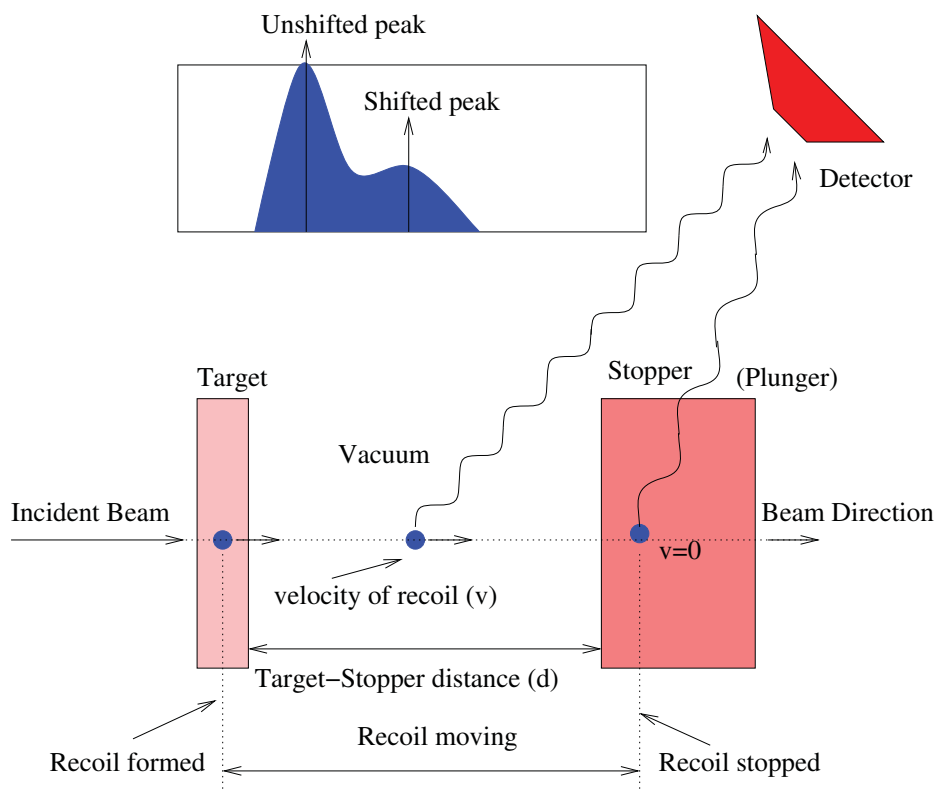


Figure 4.1: A schematic design of RDM method.

Thus, by fitting the slope of the $\ln \mathcal{R}$ vs \mathcal{T} graph one can determine the decay constant λ and hence lifetime τ of the state of interest. The range of applicability of this method can be estimated by the available velocities of the recoils and the traveling distance between target and stopper. The measurable lowest lifetime is limited by the minimum distance that can be maintained between target and stopper. A

schematic design of this method is shown in Fig. 4.1.

✠ In case of DSAM technique, a thick target or a thin target backed by a thick foil is used. The difference from the RDM technics is that the recoiling nuclei move through the medium in which they slow down and finally are stopped by atomic and nuclear collisions. For large recoil velocities, the total slowing-down time is of the order of few picoseconds. If the lifetime of the excited states is of the order of this magnitude, then the recoiling nuclei will decay in flight and due to recoiling within the material the energy of the nuclei decreases continuously. Thus, the emitted γ -rays will have typical lineshape resulting from the continuous change in the Doppler shift due to variation of velocity of the recoils. A schematic design of such an arrangement of the DSAM technique is shown in Fig. 4.2.

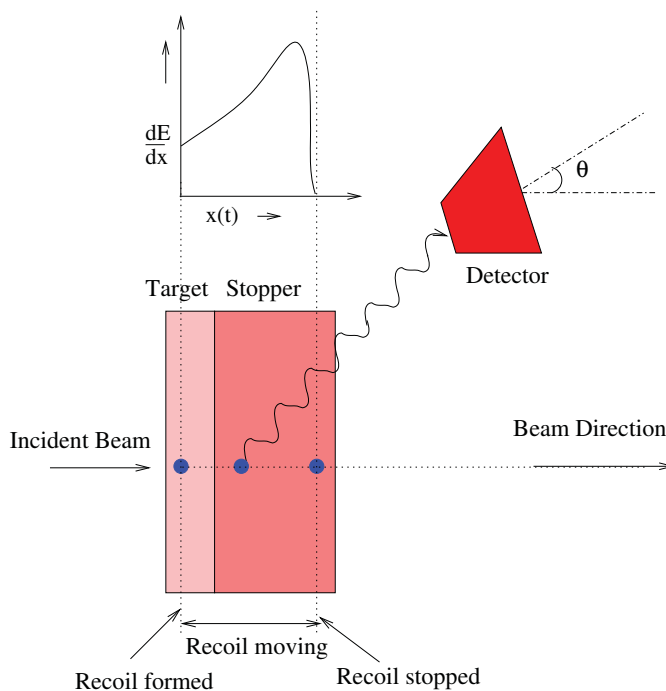


Figure 4.2: A schematic design of DSAM method.

To obtain the lifetimes in this technique, the exact knowledge of recoil velocity of the nuclei along with the electronic stopping power is required. It is also important to know the relative population of the states of interest and the angular distribution of the emitted γ -rays as well as recoiling nuclei. Thus if at a certain time t , the population of a level having lifetime τ is $n = n(t, \tau)$ then the intensity distribution [BAR68] of emitted γ -ray energy due to its decay will be :

$$\frac{dn(\mathcal{E}_\gamma(v(t)))}{d\mathcal{E}_\gamma} = \frac{dn(t, \tau)}{dt} \frac{dt}{dv(t)} \frac{dv(t)}{d\mathcal{E}_\gamma} \quad (4.4)$$

The value of the last term $\frac{dv(t)}{d\mathcal{E}_\gamma}$ can be determined using Eq. (4.1) but the value of the middle term $\frac{dt}{dv(t)}$ depends on the energy loss of the recoils and can be expressed as:

$$\frac{dt}{dv(t)} = \frac{1}{m} \frac{d(\mathcal{E}_{recoil}(t))}{dx} \quad (4.5)$$

where, m is the mass of the recoil nuclei. Thus using the known values of population and recoil energy loss, the emitted γ -ray energy distribution, known as lineshape, can be generated using the above Eq. (4.4). The experimental lineshape is then compared to the simulated one and lifetime τ can be determined from the fitting parameter.

The two above discussed methods have a wide application to measure lifetimes in the range of few 10^{-9} sec to few 10^{-12} sec but they have some limitations also. For both the cases, sensitivity of the measurement depends on the good energy resolution of the detector because, small recoil velocities result a small Doppler effect thus, the shifted and unshifted peaks can't be resolved. Both the methods are limited to measure the lifetimes in low-lying levels, having well known decay and feeding pattern, to avoid the effect of complex transitions decaying from the higher excited states. The other limitations are:

In case of RDM: (1) The target should be uniform and thin enough so that the recoil nucleus can easily penetrate the target material otherwise, the distribution of velocities of the recoiled nuclei will be broadened and differ from considered uniform velocity. Thus, uncertainties in the measured lifetimes will be increased; (2) The penetrating time has to be much shorter than the lifetime τ to be measured; (3) The slowing down time of the recoil in the stopper should be shorter than the nuclear lifetime, otherwise, shape of the unshifted energy distribution will be broadened as all nuclei don't decay at rest and make the analysis difficult, etc.

Whereas, **In case of DSAM:** (1) The sensitivity depends on the well-defined instrumental line shape; (2) The population of the excited states depends on other parameters like lifetime of the feeders and also their rate of population etc.; (3) The side feeding pattern should be taken into account carefully because, relatively short effective side feeding times comparable to stopping time of the recoil can produce

perturbation in the results of lifetime determinations, etc.

The above said two methods are highly dependent on the energy spectrum of the emitted γ -rays and finally lifetimes are determined from the fitting parameters of the energy spectrum. Thus, though the errors quoted in the value of lifetimes are very small compared to other methods (electronic method) in this lifetime region but the uncertainty in the lifetime increases drastically for both RDM ($\sim 5\%$) and DSAM ($\sim 10\%$). In contrast, the lifetimes are extracted by measuring the time difference of the nuclear decay events with a earlier time reference. This method will be discussed more elaborately as in the present thesis, the lifetimes of nuclear states have been determined by electronic method.

4.2.2 Electronic method

The electronic method or so-called delayed coincidence technique is a widely applicable technique for measurement of short lifetimes ($\sim 10^{-12}$ to 10^6 sec) of nuclear level. The technique involves measurement of time delays between the formation and succeeding decay of the state, the latter of which takes place according to Eq. (4.2). To know the formation time of a state, the particle detection from a nuclear reaction or the radiations populating the state or the pulsed beam timing can be used. While, the detection of γ -rays or conversion electrons is considered as the time of decay from the state.

In the present work, $\gamma - \gamma$ timing correlation has been used for this purpose. That means the time of formation and the time of decay are considered when a γ -ray populates a state and the other depopulates that state, respectively. The lifetime of the state has been derived by electronic method while using the time correlation between two electronic signals generated by the two coincidence γ -rays. This electronic method involves different fast timing techniques which depend on the nature of their measurement procedures and also lifetimes of the states of interest. In the following subsection, the different $\gamma - \gamma$ fast timing techniques will be discussed in detail.

4.2.3 The $\gamma - \gamma$ fast-timing technique

In $\gamma - \gamma$ fast-timing technique, the time resolution of a given setup is very crucial. The time resolution for a setup of two detectors can be measured using prompt events or by measuring a lifetime shorter than the resolving time of the setup [FOS74]. For very fast timing detector setup, as obtained with fast scintillator detectors, the two γ -rays connecting a nuclear state with lifetime, $\tau \leq 1$ ps can be considered as prompt events. The time difference distribution between two such γ detection events is known as Prompt Response

Function (PRF) which describes timing characteristic of the setup. The shape of the PRF depends on the nature of incident radiations and the type of detectors used in the setup. If the time response of the two detectors are similar, then the obtained PRF would be a symmetric Gaussian Distribution due to statistical nature of nuclear decay. Otherwise, an asymmetric Gaussian Distribution will be observed if the time responses of two detectors are not similar. The Full Width at Half Maxima (FWHM) of the time distribution peak of PRF provides an estimate about the Time Resolution (TR) of the setup.

The FWHM of prompt events includes all timing uncertainty obtained from the total electronic setup, viz., the uncertainties arising from the scintillation process of light collection inside the scintillator crystal, conversion of those scintillation light to electrons at photocathode of PMT; successive multiplication of electrons by PMT dynodes and also due to CFDs and other electronic modules used in the timing circuit.

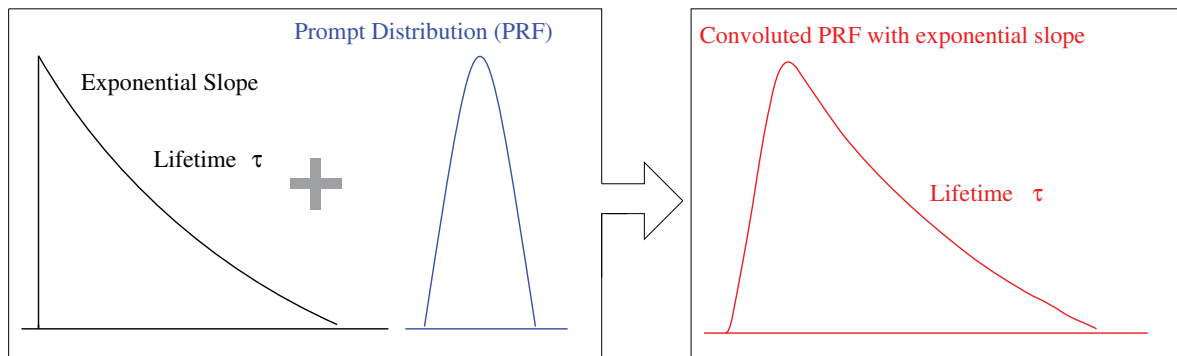


Figure 4.3: Illustration of a time spectra due to convolution of prompt time peak (PRF) with the exponential decay slope.

The time distribution $D(t)$ for directly measurable lifetime τ ($= 1/\lambda$) shows asymmetric shape and can be represented by the convolution integral of the normalized PRF $P(t)$ with an exponential decay as shown in Fig. 4.3. The mathematical form of the distribution can be expressed as:

$$D(t) = n\lambda \int_{-\infty}^t P(t' - t_0) e^{-\lambda(t' - t_0)} dt' \quad (4.6)$$

where, $P(t' - t_0)$ is the PRF having peak at t_0 and n is the number of counts in the time distribution spectrum, known as the normalization factor. In ideal case, the time distribution $D(t)$ shows asymmetric shape where no background of any kind contributes. If only random background (not time correlated events or constant time background) contributes Eq. (4.6) needs to be extended by a constant. If the mean-lifetime of the level of interest is long enough so that it is significantly larger than the FWHM of corresponding

PRF, then a notable decay slope appears on the delayed part of the time difference distribution, as shown in Fig. 4.3. The logarithmic slope of this distribution can be written as

$$\frac{d}{dt}[\ln D(t)] = -\lambda \left[1 - \frac{P(t)}{D(t)} \right] \quad (4.7)$$

For $P(t) \ll D(t)$, the logarithmic slope is simply proportional to the decay constant λ and thus the mean lifetime can be determined from the exponential fitting. This can be achieved by two methods namely, slope method and deconvolution method [MAC89].

✂ The slope method is a very simple technique, can be used to determine lifetime directly by fitting only the delayed slope of the time difference distribution after the prompt contribution with an exponential function $e^{-\lambda t}$. The selected part of fitting is very sensitive and thus one has to choose it carefully. The accuracy of this method increases with the lifetime of the state of interest as higher lifetime gives larger delayed slope beyond the PRF. Thus, selected part becomes less sensitive and gives more accurate result. If the lifetime of level of interest is greater than the FWHM of PRF (i.e., the time resolution of the experimental setup) by at least 30 percent, the slope method can be applied to measure the lifetime [FOS74].

✂ The deconvolution method can be applied for measuring the lifetime even below the limit of the slope method. If the slope of the time distribution is larger than the ‘apparent slope’ of the corresponding PRF, normally a Gaussian distribution, then this method is capable to determine lifetime [MAC89]. The fitting of the spectrum is carried out by deconvoluting the known prompt peak and slope part (the reverse process of the one shown in Fig. 4.3) and the lifetime is determined by minimizing the fitting χ^2 parameter as much as possible. The deconvolution method yields more precise result over slope method as in this method the whole time distribution is considered instead of only slope part of the delayed time distribution.

✂ Now if the lifetime τ is smaller even than the time resolution of the experimental setup, then no slope is seen beyond the PRF distribution and it results in a time difference distribution that is approximately same as the Gaussian distribution of PRF itself. The slope method or deconvolution method can not be applied and in that case, the centroid shift method is very useful to determine the lifetime of the level directly. The method has been experimentally developed and successively applied to $\beta - \gamma - \gamma$ experiment by H. Mach and Moszyński [MAC89, MOS89] to measure the lifetime.

The analytical method to determine decay times was first reported by Z. Bay in 1950 [BAY50]. The first moment of a distribution of time delay i.e., ‘center of gravity’ according to Z. Bay, normally known as

‘centroid’, can be defined as:

$$\mathcal{C}_{exp} = \langle t \rangle = \frac{\int_{t_{min}}^{t_{max}} tn(t)dt}{\int_{t_{min}}^{t_{max}} n(t)dt} \quad (4.8)$$

where, $n(t)$ is the number of counts in time t and related to $D(t)$, the time distribution according to Eq. (4.6). The variance of $D(t)$ is a measure of statistical error in the determination of the centroid. Eq. (4.8) is valid for the ideal case, where no background of any kind contributes. The limits of integration, t_{min} (just at the beginning of the peak of the time difference distribution) and t_{max} (just at the end of the peak of the time difference distribution), have to be chosen appropriately so that possible large systematic errors which is related to the random background (bkg) distributed on the left and right of the time peak can be avoided.

The standard deviation of measured centroid can be defined as:

$$\delta\mathcal{C} = \sqrt{\text{var}(D(t))} = \sqrt{\langle t^2 \rangle - \langle t \rangle^2} \quad (4.9)$$

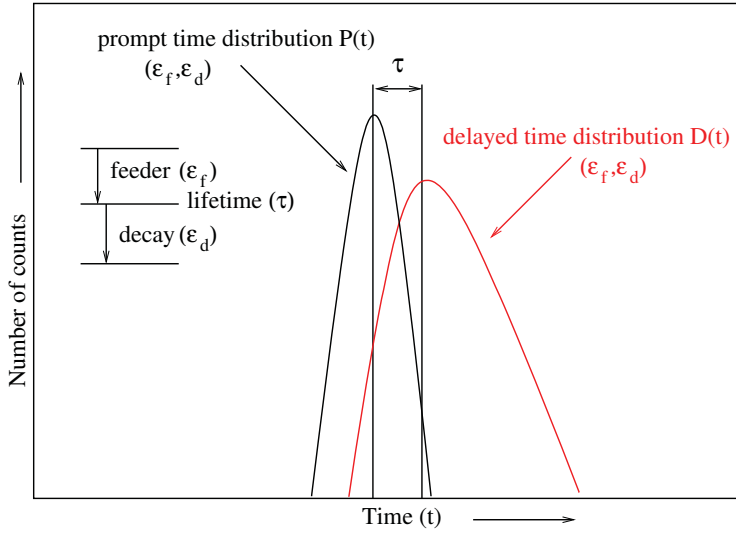


Figure 4.4: An illustration of prompt and delayed time distributions for a fast-timing setup.

As shown in Fig. 4.4, the centroid of the delayed time distribution \mathcal{C}^D is shifted from the centroid of the PRF \mathcal{C}^P by the mean lifetime τ . Thus for a particular γ -ray cascade of energies \mathcal{E}_f (feeding gamma) and

\mathcal{E}_d (decaying gamma), the lifetime of state of interest can be extracted from the delayed time distribution using the following equation:

$$\tau = C^D(\mathcal{E}_f, \mathcal{E}_d) - C^P(\mathcal{E}_f, \mathcal{E}_d) \quad (4.10)$$

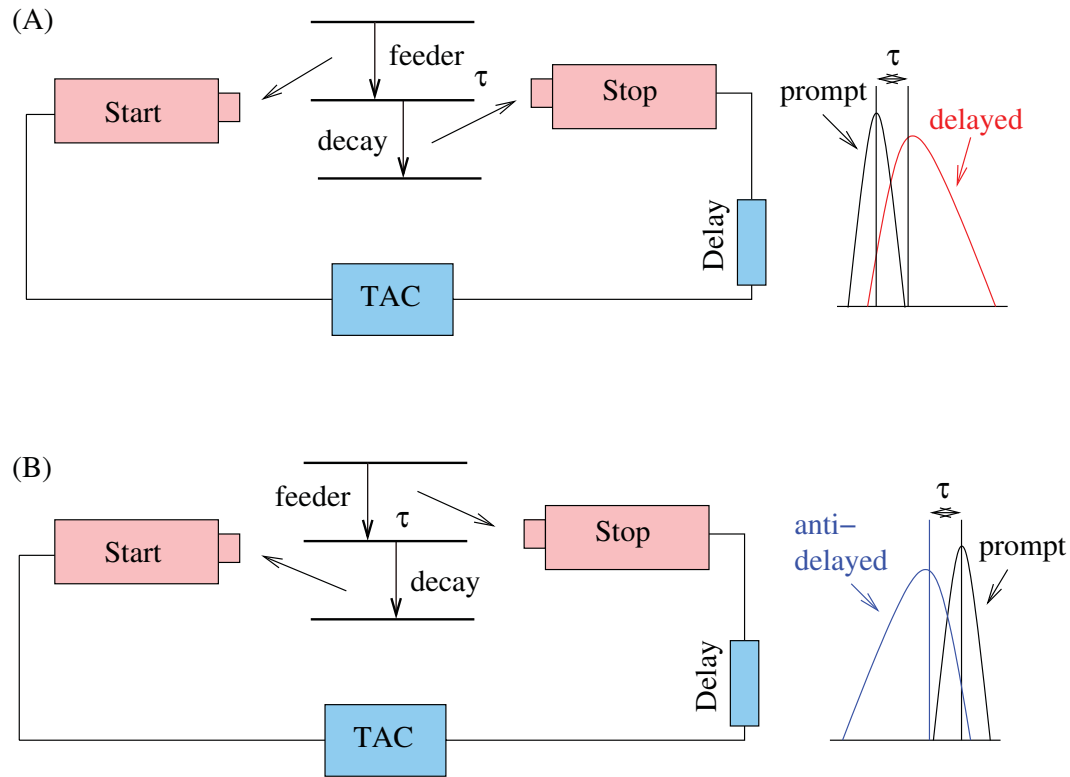


Figure 4.5: A simple design of two detector assembly to illustrate delayed and anti-delayed time distribution with prompt response function.

Depending on the detection procedure as shown in Fig. 4.5 of γ -rays of a cascade by the detectors, two types of delayed time distribution can be generated. They are known as delayed or anti-delayed time distribution and can be demonstrated by a two detector setup. Among the two detectors, if one is called start detector and other is called stop detector, then, when the start detector detects the feeding γ -ray and stop detector detects the decaying γ -ray then the produced time distribution is generally called delayed time distribution and lifetime can be determined using Eq. (4.10). And for the inverse case, i.e., when the feeding gamma is detected by stop detector and decaying gamma is detected by start detector then the time distribution is called anti-delayed time distribution and lifetime can be measured by the following Eq.

(4.11). The delayed and anti-delayed time difference distribution along with the respective prompt time distributions are illustrated in Fig. 4.6.

$$\tau = C^P(\mathcal{E}_d, \mathcal{E}_f) - C^{AD}(\mathcal{E}_d, \mathcal{E}_f) \quad (4.11)$$

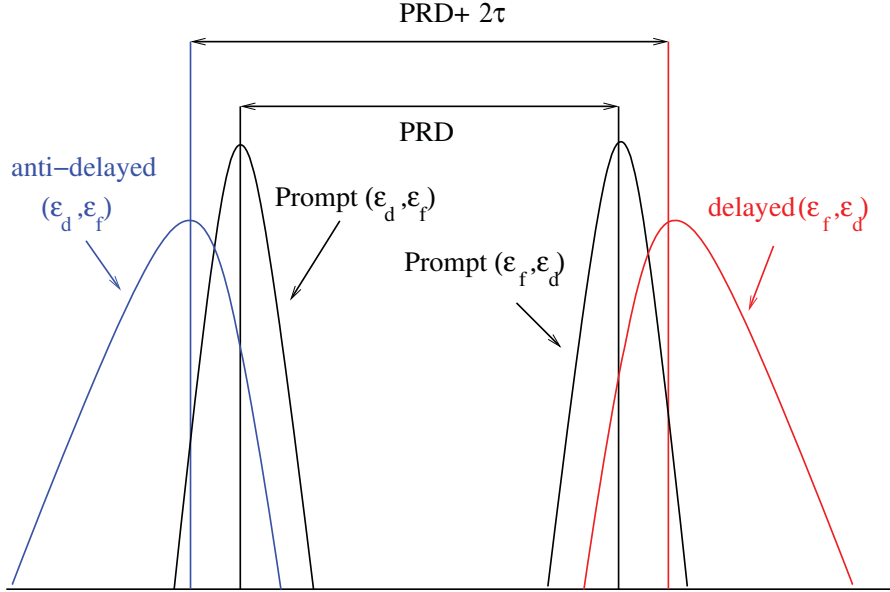


Figure 4.6: The delayed and anti-delayed time distribution with respective prompt response function. The difference between both the prompt response function gives the PRD whereas, difference between time distribution of delayed and anti-delayed is a measure of PRD with two times of level mean lifetime.

However, in real cases, the centroid of the prompt events PRF is a function of energy. This is because the timing signal information generated by CFD module used in the electronic setup depends on the energy of the incident γ -ray, output pulse shape of the detector and the definition of zero crossover time of the CFD. This dependency is known as time walk characteristic of the CFD and the characteristics can be described by non-linear function of energy [REG12] as follows:

$$\delta t(\mathcal{E}_\gamma) = \frac{a}{\sqrt{\mathcal{E}_\gamma + b}} + c\mathcal{E}_\gamma + d \quad (4.12)$$

where a , b , c and d are free parameters obtained by least square fitting of the experimental data. Thus the energy dependency of prompt centroid $C^P(\mathcal{E})$ makes the analysis very difficult and the final result depends on the accuracy of the time walk characteristic, known as ‘prompt curve’ which sets the limit of

this method. The main challenge, thus, is to calibrate the prompt curve with energy dependent centroid position of prompt decay and to interpolate it for a required energy.

Therefore, to measure the lifetime of an excited state using this method, the prompt curve as a function of energy has to be generated from the $\gamma - \gamma$ cascades of prompt coincidence or having precisely known lifetimes. So for this purpose, one can make a two detector setup in such a way that one detector (say, start detector or stop detector) detects constantly the reference γ -ray (\mathcal{E}_{ref}) and other detector detects the coincident γ -rays (\mathcal{E}_γ) for a wide range of energy. Thus two prompt curve, $\mathcal{C}^P(\mathcal{E}_\gamma, \mathcal{E}_{ref})$ and $\mathcal{C}^P(\mathcal{E}_{ref}, \mathcal{E}_\gamma)$, corresponding to the same reference energy will be generated [REG10]. In ideal case, the two curves will be crossed by each other at the reference energy. Thus ideally, for the equal energy gates, both the timing branch give same centroid value which is known as true prompt centroid ($\mathcal{C}^P(\Delta\mathcal{E}_\gamma = 0)$). However, the two timing branches in case of real setup are not symmetric and the time difference between each prompt curve and ideal true prompt line along the energy axis is not matched [REG10]. Therefore, for different reference energies, the resulting prompt curves differ from one another and their timing asymmetry make complexity to determine an overall centroid curves for a wide range of energy and hence centroid of PRF for an energy combination of interest.

The proposed of Mirror Symmetric Centroid Difference (MSCD) method [REG10] or in general, Generalized Centroid Method (GCD) [REG13] by J.-M. Régis, as an extension of Centroid Shift method, overcomes this problem. For two detector setup this extended method is called MSCD whereas, for more than two detectors setup or for an array with several detectors it is known as GCD method. In the following section, a brief discussion has been done about the methodologies of these two methods.

4.2.4 MSCD technique

In this method, the centroid difference of the two timing branch which are mirror symmetric (in ideal case) with respect to the energy difference is considered as a physical observable. Thus, the branch timing characteristic, i.e., asymmetry in the setup for non-equal time response is canceled out by defining the Centroid difference ($\Delta\mathcal{C}$) (4.13) between the delayed and anti-delayed time distributions [REG10] as both the branches have similar timing asymmetry effect due to electronic setup.

$$\Delta\mathcal{C}(\mathcal{E}_f, \mathcal{E}_d) = \mathcal{C}^D(\mathcal{E}_f, \mathcal{E}_d) - \mathcal{C}^{AD}(\mathcal{E}_f, \mathcal{E}_d) \quad (4.13)$$

For an ideal case, the delayed centroid curve $\mathcal{C}^D(\mathcal{E}_f, \mathcal{E}_d)$ is shifted in parallel by $+\tau$ from the corresponding prompt $\mathcal{C}^P(\mathcal{E}_f, \mathcal{E}_d)$ curve if the stop detector makes gate on the reference decay transition according to Eq. (4.10). Similarly, the anti-delayed curve $\mathcal{C}^{AD}(\mathcal{E}_d, \mathcal{E}_f)$ is shifted in parallel by $-\tau$ from the prompt curve $\mathcal{C}^P(\mathcal{E}_d, \mathcal{E}_f)$ if the decay transition is gated by the start detector according to Eq. (4.11). The illustration of this mechanism has been shown in Fig. 4.7.

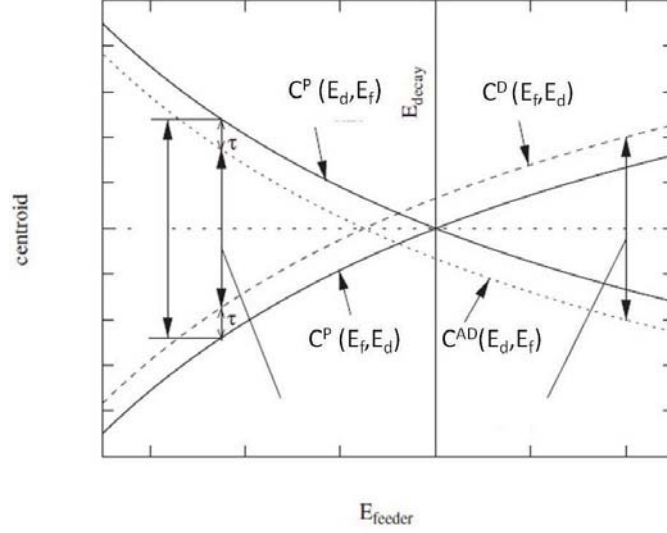


Figure 4.7: Two prompt timing branches corresponding to detection procedures of feeding and decaying γ -rays by start and stop detector of an ideal setup and also the delayed timing branches having lifetime τ have been shown by the solid curve and dashed curve, respectively. The figure is taken from Ref. [REG10] and is modified slightly.

Thus, the linearly combined centroid difference can be given by the following equation:

$$\begin{aligned}
 \Delta\mathcal{C}(\mathcal{E}_f, \mathcal{E}_d) &= \mathcal{C}^D(\mathcal{E}_f, \mathcal{E}_d) - \mathcal{C}^{AD}(\mathcal{E}_f, \mathcal{E}_d) \\
 &= \{\mathcal{C}^P(\mathcal{E}_f, \mathcal{E}_d) + \tau\} - \{\mathcal{C}^P(\mathcal{E}_d, \mathcal{E}_f) - \tau\} \\
 &= \{\mathcal{C}^P(\mathcal{E}_f, \mathcal{E}_d) - \mathcal{C}^P(\mathcal{E}_d, \mathcal{E}_f)\} + 2\tau \\
 &= PRD(\mathcal{E}_f, \mathcal{E}_d) + 2\tau
 \end{aligned} \tag{4.14}$$

where,

$$PRD(\mathcal{E}_f, \mathcal{E}_d) = \mathcal{C}^P(\mathcal{E}_f, \mathcal{E}_d) - \mathcal{C}^P(\mathcal{E}_d, \mathcal{E}_f) \tag{4.15}$$

is the Prompt Response Difference (PRD) describes the combined prompt $\gamma-\gamma$ time walk of the two timing branch of the setup and is independent of the single timing branch as well as all timing asymmetry arising from electronic setup are canceled out. Thus the linearly combined centroid shift difference between delayed and anti-delayed is shifted by $+2\tau$ from the corresponding PRD curve as shown in Fig. 4.8.

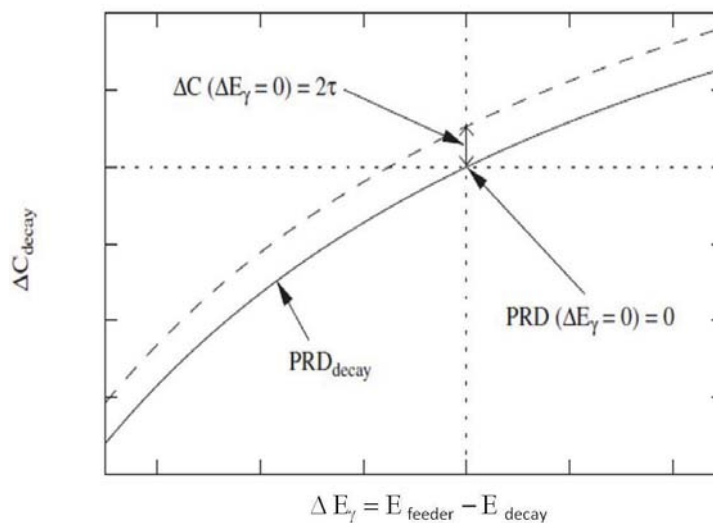


Figure 4.8: The linearly combined centroid difference ΔC curve (dashed line) related to lifetime τ is shifted by $+2\tau$ from the PRD curve [REG10].

With respect to inversion of start-stop detectors or detection of feeding-decaying γ -ray, the centroid difference is mirror symmetric which is independent of the timing of the detector and can be represented as:

$$\Delta C(\mathcal{E}_f, \mathcal{E}_d) = -\Delta C(\mathcal{E}_d, \mathcal{E}_f) \quad (4.16)$$

$$\text{and } PRD(\mathcal{E}_f, \mathcal{E}_d) = -PRD(\mathcal{E}_d, \mathcal{E}_f) \quad (4.17)$$

The PRD curve still depends on incident photon energy in case of a real setup due to CFD time walk. The time walk can be reduced by setting proper zero-crossover in CFD. For a theoretical case of $\mathcal{E}_f = \mathcal{E}_d$, i.e., $\Delta\mathcal{E}_\gamma = (\mathcal{E}_f - \mathcal{E}_d) = 0$ (see Fig. 4.8), the above Eq. (4.15) gives :

$$PRD(\mathcal{E}_f, \mathcal{E}_d) = \mathcal{C}^P(\mathcal{E}_f, \mathcal{E}_f) - \mathcal{C}^P(\mathcal{E}_d, \mathcal{E}_d) = PRD(\Delta\mathcal{E}_\gamma = 0) = 0 \quad (4.18)$$

and thus,

$$\Delta\mathcal{C}(\Delta\mathcal{E}_\gamma = 0) = 2\tau \quad (4.19)$$

This means the linearly combined centroid difference $\Delta\mathcal{C}$ curve related to lifetime τ is shifted by $+2\tau$ from the PRD curve and at $\Delta\mathcal{E}_\gamma = 0$ the PRD value should be zero and hence lifetime can be determined using the above Eq. (4.19) directly.

As PRD is a function of energy thus, one can write:

$$PRD(\mathcal{E}_f, \mathcal{E}_d) = PRD_{\mathcal{E}_d}(\mathcal{E}_f) \quad (4.20)$$

where, \mathcal{E}_f represents different feeding transitions of a state and \mathcal{E}_d represents the fixed reference decay transitions from the same state.

For any arbitrary cascade, the PRD value according to Eq. (4.20) can be calculated by:

$$PRD(\mathcal{E}_f, \mathcal{E}_d) = PRD(\mathcal{E}_f) - PRD(\mathcal{E}_d) \quad (4.21)$$

To draw a well defined PRD curve for a wide range of energy, data points for different reference energies are required. According to Eqs. (4.18) and (4.20), PRD should be zero at the reference energy \mathcal{E}_f or \mathcal{E}_d that means the PRD curve crosses the energy axis at that reference energy. Thus, different reference energy gives different prompt curves which are parallelly shifted from each other. Finally, the respective prompt curves have to be shifted in parallel in order to draw one smooth PRD. The shape of the PRD curve mainly depends on the CFD shaping delay time, adjustment of CFD baseline and PMT gain variance [REG16a] and can be fitted by the following non-linear function [ALA17].

$$PRD(\mathcal{E}_\gamma) = \frac{a}{\sqrt{\mathcal{E}_\gamma + b}} + c \mathcal{E}_\gamma + d \quad (4.22)$$

which basically represents the energy dependent time walk as expressed in Eq. (4.22). The parameters a , b , c and d are the constant/free parameters obtained by least square fitting of the experimental data points. The error in the PRD value (δPRD) can be determined from the standard deviations of the data points from the fitting curve.

In Eq. (4.14), it is assumed that the distributions in the time spectrum are generated from the time response of the FEPs and there is no contribution from background. However, in the real experiment contribution of background, especially from Compton events, can not be avoided as the experimental $\Delta\mathcal{C}(\mathcal{E}_f, \mathcal{E}_d)$ i.e. ($\Delta\mathcal{C}_{exp}$) for any cascade is determined by taking the energy gates on the two FEPs energies \mathcal{E}_f and \mathcal{E}_d and thus includes underlying background contribution. A correction, hence, related to that underlying background is essential and this can be achieved by applying the following set of equations:

$$\begin{aligned}
t_{corr}(feeder) &= \left[\frac{\Delta\mathcal{C}_{exp} - \Delta\mathcal{C}_{Compton}}{\pi} \right]_{feeder} \\
t_{corr}(decay) &= \left[\frac{\Delta\mathcal{C}_{exp} - \Delta\mathcal{C}_{Compton}}{\pi} \right]_{decay} \\
t_{corr} &= \frac{1}{2} [t_{corr}(feeder) + t_{corr}(decay)] \\
\Delta\mathcal{C}_{FEP} &= \Delta\mathcal{C}_{exp} + t_{corr}
\end{aligned} \tag{4.23}$$

where, π is the peak to background (ptb) ratio and t_{corr} represents the total background correction which is necessary to determine the background corrected centroid difference ($\Delta\mathcal{C}_{FEP}$) for the FEP from the obtained experimental centroid difference ($\Delta\mathcal{C}_{exp}$). $\Delta\mathcal{C}_{Compton}$ is the measure of centroid difference of the time response of the background underlying both the photopeaks (feeder and decay) [REG10]. As the background is under the photo peaks, it is not possible to measure the same at the point of FEP. Thus, the $\Delta\mathcal{C}_{Compton}$ values for both the γ -rays are obtained by fitting the bkg pattern at different points before and after the FEP while taking the centroid differences corresponding to the coincidences among the photopeak of feeder (decay) and the Compton background neighboring to decay (feeder) γ -rays in a particular cascade. Hence, in Eq. (4.14), $\Delta\mathcal{C}(\mathcal{E}_f, \mathcal{E}_d)$, i.e., $\Delta\mathcal{C}_{exp}$ has to be replaced by $\Delta\mathcal{C}_{FEP}$ and Eq. (4.14) becomes:

$$\tau = \frac{1}{2} [\Delta\mathcal{C}_{FEP} - PRD] \tag{4.24}$$

The error in the measured lifetime can be determined using the following equation:

$$\delta\tau = \frac{1}{2} \sqrt{(\delta\Delta\mathcal{C}_{exp})^2 + (\delta t_{corr})^2 + (\delta PRD)^2} \tag{4.25}$$

This method has few major advantages over Centroid Shift method, viz.,

1. All the timing asymmetries of the time walk characteristic can be canceled out. Any possible shift in time, whatever be the source and if the shift is not dependent on energy, will be nullified as the effect will be same for both the timing branch. Thus this method is independent of the setup geometry.
2. The respective prompt curves for different reference energies can be shifted in parallel and the centroid of the time spectra of reference energy can also be used while the curve is fitted. Hence, the number of data points increases in the plot, thus, can be calibrated more accurately and hence a general PRD curve can be determined for a wide range of any energy combination. The PRD value for any energy can be determined from the fitting parameter.
3. At the point where PRD value is zero, the lifetime can be determined from directly measured centroid difference value using Eq. (4.19) without calibrating the PRD curve, as at that point the measurement is independent of prompt energy and also all possible timing asymmetries.
4. As timing uncertainty is less, thus, the total error in the measured lifetime value is reduced in this method. etc.

4.2.5 GCD technique

The GCD method [REG16a] is applicable for a setup with \mathcal{N} number of detectors, where delayed and anti-delayed time distributions are generated from the superposition of time spectra which are obtained from all possible combinations of the timing setup. So, the MSCD technique is considered as a special case of GCD technique with $\mathcal{N} = 2$.

If there is \mathcal{N} number of detectors in an array with similar timing response, then total $\mathcal{N}C_2$ or $\frac{\mathcal{N}(\mathcal{N}-1)}{2}$ unique detector-detector combination (mn) is possible. Here, the index m is associated to start detectors varied from $m = 1, 2, 3, \dots, (\mathcal{N} - 1)$ and index n corresponds to stop detectors varied from $n = (m + 1), (m + 2), \dots, \mathcal{N}$; with $m \neq n$. As each detector-detector combination gives individual PRD_{mn} ($m \neq n \in \mathcal{N}$) thus, total $\mathcal{N}C_2$ or $\frac{\mathcal{N}(\mathcal{N}-1)}{2}$ individual PRD_{mn} can be constructed. So one has to combine all the PRD_{mn} to construct a general average PRD for the setup of the array.

According to Eq. (4.14), the linear combination of the centroid difference ΔC_{mn} and the PRD_{mn} can be reformed as following:

$$\sum_{m=1}^{\mathcal{N}-1} \sum_{n=m+1}^{\mathcal{N}} \Delta C_{mn} = \sum_{m=1}^{\mathcal{N}-1} \sum_{n=m+1}^{\mathcal{N}} PRD_{mn} + {}^{\mathcal{N}}C_2 2\tau$$

$$\overline{\Delta C} = \overline{PRD} + 2\overline{\tau} \quad (4.26)$$

where, $\overline{\Delta C} = \frac{2}{\mathcal{N}(\mathcal{N}-1)} \sum_{m=1}^{\mathcal{N}-1} \sum_{n=m+1}^{\mathcal{N}} \Delta C_{mn}$, the mean centroid difference and $\overline{PRD} = \frac{2}{\mathcal{N}(\mathcal{N}-1)} \sum_{m=1}^{\mathcal{N}-1} \sum_{n=m+1}^{\mathcal{N}} PRD_{mn}$, the mean PRD refers that the time difference between delayed and anti-delayed information are distributed around their mean value and independent on the individual detector-detector combinations.

If the number of detectors (\mathcal{N}) increases the whole analysis becomes more and more complex. The difficulties of the analysis can be reduced by superimposing the data of the individual detector-detector combinations. This is done during the off-line analysis, using a well written program, where event-by-event coincidence data are sorted and stored as separate event files. While sorting the data event-by-event, it is ensured that, in case of a particular coincident event any one detector out of the \mathcal{N} number of detectors of an array must be a start detector and any one detector from the rest $\mathcal{N} - 1$ detectors must be a stop detector and all the coincidence events have been superimposed in such a way that (i) the total array with \mathcal{N} number of detectors behave like two detector setup where one set of detectors will start and other set of detectors will stop the event, irrespective of the detector combination and (ii) the data are written in the format of $(\mathcal{E}_{start}, \mathcal{E}_{stop}, \Delta t_{start-stop})$. Thus, the \mathcal{N} number of detectors are reduced to two detectors of MSCD method. The only difference from the normal MSCD method is that in this case mean $\overline{\Delta C}$ and \overline{PRD} will be generated. It is important to mention that Eq. (4.26) is valid only for the FEP events, i.e., there is no contribution from background side. As the background coming from underlying of FEP can not be avoided in a real setup thus the required corrections in centroid difference are to be accounted for and this can be done in the similar way of MSCD method following Eq. (4.23). Therefore, the background corrected actual mean centroid difference $\overline{\Delta C}_{FEP}$ can be determined and thus the lifetime of an excited state using the following equation:

$$\tau = \frac{1}{2} [\overline{\Delta C}_{FEP} - \overline{PRD}] \quad (4.27)$$

Similar to MSCD method, in GCD method also, the mirror symmetric nature of centroid reduces the

possible systematic errors in the result of final lifetime. In addition, the degradation of time walk decreases with the increasing number of detectors. This is because the small degradation induced in case of a real setup due to slightly different time walk characteristics in individual two detector combination is redeemed by the statistics obtained by superimposed of $\gamma - \gamma$ time spectra of all the combination, provided that the timing asymmetry in prompt centroid is small compared to the FWHM of PRF. The later suggests the use of the same size of detectors in the fast timing array is beneficial for more precise results.

The time precision of such an \mathcal{N} detector setup can be defined as [MACH]:

$$\mathcal{T}_{tp} = \frac{\mathcal{T}_{TR}}{\sqrt{N_{count}}} \quad (4.28)$$

where, \mathcal{T}_{TR} is the equivalent to full width at half maxima of the timing response, i.e., the timing resolution of the \mathcal{N} detectors setup and N_{count} is the total number of coincidence counts in the timing distribution spectrum which strictly depends on the geometrical coverage of the array having \mathcal{N} number of detectors and their total intrinsic detection efficiency. The timing resolution of the \mathcal{N} detectors setup is the convolution of the timing response of the ${}^{\mathcal{N}}C_2$ individual pairs. Thus an array will have a good timing response if all the individual pairs provides good timing resolution and therefore, a sufficient number of coincidence counts will give a very precise measurement of level lifetime according to Eq. (4.28).

In the present work, the GCD technique has been explored to measure the nuclear level lifetimes \sim few ps and more, following the development of the VENTURE array having eight numbers of CeBr₃ detectors. Prior to this, the PRD curve was generated by using a setup of two CeBr₃ detectors of the array. In both the cases, the ¹⁵²Eu source has been used to generate the PRD curve and as a test case, the ¹⁰⁶Ru and ¹³³Ba sources were used to measure the known level lifetimes of the 512 keV level of ¹⁰⁶Pd, and 161 keV and 384 keV levels of ¹³³Cs. The results obtained from these measurements, while developing the first phase of the VENTURE array under the present thesis, have been described in the following sections.

4.3 Experimental setup for characterization of CeBr₃ detectors, Development of VENTURE array, MSCD and GCD measurements

The experiment was carried out in two different configurations for the CeBr₃ detectors. In those configurations, the standard NIM based coincidence electronics and VME based data acquisition system (consisting of Mesytec MADC-32 and LAMPS data acquisition system [LAMPS]) were used. All the subsequent data

4.3. EXPERIMENTAL SETUP FOR CHARACTERIZATION OF $CeBr_3$ DETECTORS, DEVELOPMENT OF

analyses were done with the software program LAMPS.

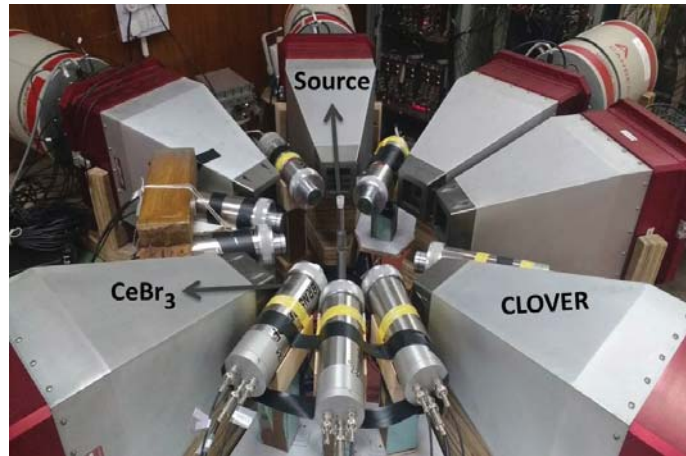


Figure 4.9: The VENTURE array of eight $CeBr_3$ detectors coupled to the VENUS array of six clover HPGe detectors is shown.

In the first configuration, consisting of one $CeBr_3$ detector, the measurements of energy response, energy resolution and detection efficiency were performed. For the measurement of efficiency, the source to detector distance was kept at 16 cm.

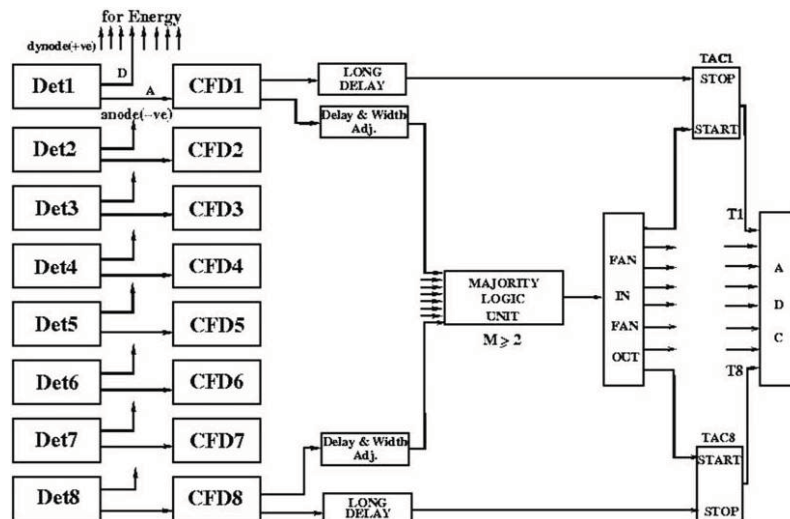


Figure 4.10: The timing electronics setup used for the signal processing with the VENTURE array.

The second configuration consists of two $CeBr_3$ detectors kept at 150° . This setup was used to measure the time resolution (Subsection 4.4.3) and the $\gamma - \gamma$ time walk characteristics using the MSCD method (Section 4.5). As an extension of the second configuration, the VENTURE array was set up with eight

such CeBr_3 detectors, as shown in Fig. 4.9, to explore the possibility of lifetime measurement using GCD method (Section 4.6). The VENTURE array can also be used in stand alone mode as shown in Fig. 4.11.



Figure 4.11: Stand alone setup of VENTURE array with six CeBr_3 detectors which are arranged on angular correlation table (discussed in Section 5.3 of Chapter 5).

In both these measurements, the ORTEC 584 CFD modules were used to generate the time pulses in Constant Fraction (CF) mode and with the use of CF delay, as and when required. In case of MSCD measurement with two detectors, one of the two CFD pulses was used as start and the other as stop, respectively, and fed to a Time to Amplitude Converter (TAC) module. The ‘.AND.’ of these two signals were used as the trigger for acquiring data. In case of the VENTURE array, the signal processing was done by following a common start timing technique as described in Fig. 4.10. This is different from the timing electronics used in the previous works where centroid difference measurements have been done by using LaBr_3 detectors [REG13, MAR10, REG16a] and from those where GCD technique has been proposed and explored [REG13, REG16a]. Hence, the present work also reports, for the first time, the use of common start timing electronics in combination with the GCD method. This method, however, requires more numbers of TAC modules compared to the method adopted in Ref. [REG16a]. In the present work, a MASTER logic signal with $M_\gamma \geq 2$ was generated by using a majority logic unit and the width and delay matched timing outputs of the individual CeBr_3 detectors. This was used as the trigger to ADC and fed to the start of the TACs corresponding to all the detectors of the array. The CFD signals, appropriately delayed from start, was given to stop of the individual TACs used in the VENTURE electronics. The coincidence data was gathered for the TAC signals corresponding to all the detectors along with their energy signals. Hence, each of these TACs (say, TAC_i) measured the time difference between the detector i and the MASTER

trigger generated from the two detectors hit (say, i and j). In the same event, TAC_j will also have data that corresponds to the time difference between the detector j and the MASTER trigger. During analysis, all the energy and time parameters were gain matched to correct for the drifts observed as a function of time. The details of data sorting and the method of generating the total $\gamma - \gamma$ time difference spectra (TDS) has been discussed in the Section 4.6.

4.4 Characterization of CeBr_3 detectors

4.4.1 Energy response, resolution and linearity

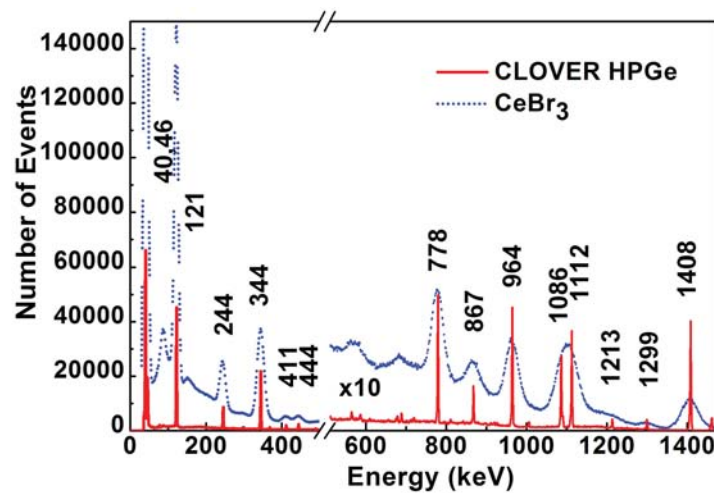


Figure 4.12: The energy spectra obtained with CeBr_3 detector and Clover HPGe detector using a ^{152}Eu source.

The energy spectrum obtained with a CeBr_3 detector is shown in Fig. 4.12 and compared with that for a Clover HPGe detector. In Fig. 4.13, the experimental γ energy spectrum for a CeBr_3 detector obtained with a ^{60}Co source has been compared with that generated by a Monte Carlo simulation with GEANT3 package [BRU86]. In the simulation, the different possible interaction processes of γ -rays along with the exact geometrical condition of the CeBr_3 crystal including its window material were considered for reconstructing the γ energy spectrum. The experimental spectrum is found to be well reproduced by the simulation except for the deviation observed at low energy region. This deviation could be attributed to the inherent background and the backscattered peak. However, it has been found from the existing literature that the detection of low-energy ‘scattered’ γ -rays (e.g., the backscatter peak) is mainly responsible for the higher

background level compared to the net Compton background level [REG16b].

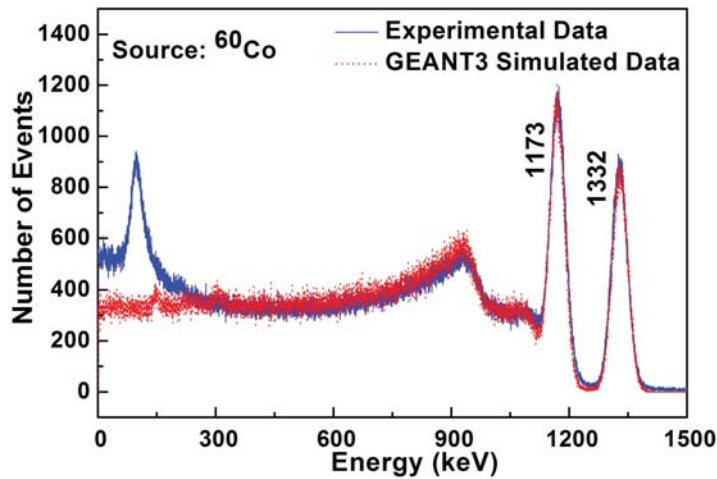


Figure 4.13: The experimental and simulated γ spectra for the CeBr_3 detector using ^{60}Co source.

The energy response of the CeBr_3 detectors was measured at different bias voltages of the PMT using the dynode signal while directly coupling it with a spectroscopy amplifier. The energy response was also measured by coupling the dynode output with the amplifier by introducing a preamplifier in between for all the bias voltages from -1000 V to -1700 V at an interval of 100 V. The representative results have been displayed in Fig. 4.14 and it is observed that the energy response becomes nonlinear after a bias voltage of -1100 V while using the direct dynode pulse. However, the response seems to become linear with the use of the preamplifier at all the bias voltages. The nonlinear response may come from the saturation effect of the PMT originated due to the bright scintillation light of CeBr_3 detectors [QUA11, DOR04]. As the biasing of the PMT is provided with a simple voltage divider circuit (VDC), the PMT appears to be entering into increased current amplification/saturation region(s) due to the high light intensity. The value of the decoupling capacitor connected at the dynode stage may not be sufficient to maintain the linearity when spectroscopy amplifier was connected directly. Nonetheless, it appears that the additional capacitor connected at the input stage of the preamplifier modifies the value of the decoupling capacitor at the last dynode stage of the PMT and thus, maintaining a linear response for the entire range of the anode current.

The energy resolution of the detectors has been measured as a function of bias voltage of the PMT while using the preamplifier and shown in Fig. 4.15 (a) for the 622 keV transition. A similar measurement has also been performed at different energy values for a fixed bias of -1200 V and is shown in Fig. 4.15 (b). It is observed that the energy resolution of the detector remains almost constant with different bias

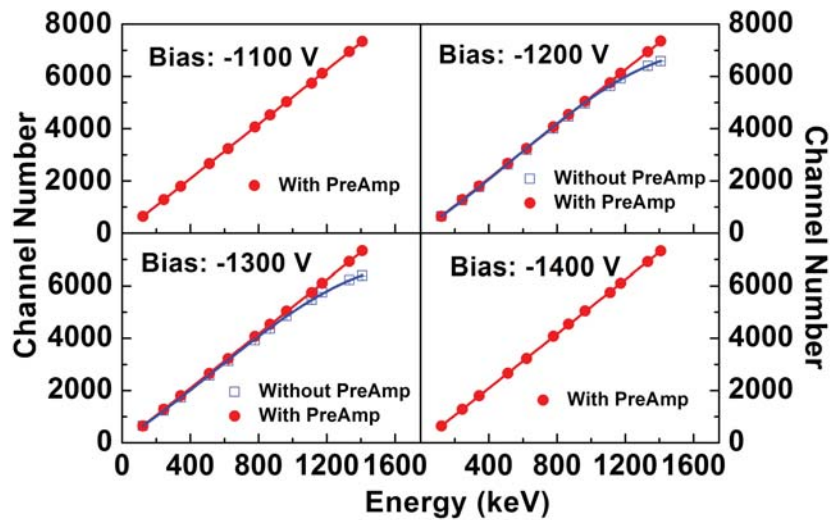


Figure 4.14: Few representative energy response curves at different bias voltages.

voltages. The observed improvement in the energy resolution compared to that obtained earlier [FRA13] is possibly because of the effect of the linearity in the response function as suggested in several studies [QUA13, QUA14].

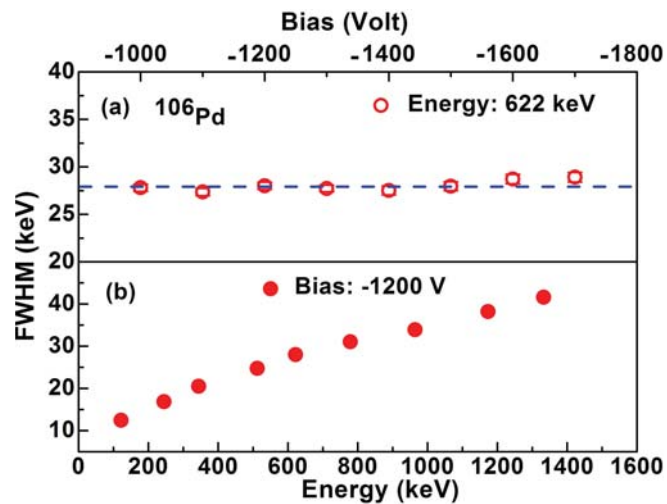


Figure 4.15: (a) Variation of FWHM obtained at 622 keV is shown with the applied bias voltages. (b) Variation of FWHM with γ energy at a fixed bias voltage.

4.4.2 Absolute efficiency

The efficiency measurement of a single CeBr_3 detector has been performed by using standard point sources, viz., ^{152}Eu , ^{133}Ba and ^{60}Co , of known disintegration per second (dps) which were kept at a distance of 16 cm from the detector. The absolute detection efficiency, which depends both on the intrinsic efficiency of the detector and the solid angle (geometric efficiency), has been extracted by using Eq. (3.30). The obtained efficiency has been plotted as a function of γ energy in Fig. 4.16. In the same plot, the absolute efficiency of the CeBr_3 detector determined from a Monte Carlo simulation with GEANT3 simulation package [BRU86] and the efficiency of a Clover HPGe detector have also been shown. The simulation was performed as described in Subsection 4.4.1 and the result is found to be in good agreement with the experimental data. The efficiency of a Clover HPGe detector was obtained by using the add-back technique as described in Ref. [DUC99]. It is found that the efficiency of the $1'' \phi \times 1''$ thick CeBr_3 detector comes about 5% of the efficiency of a Clover HPGe detector at ~ 1 MeV.

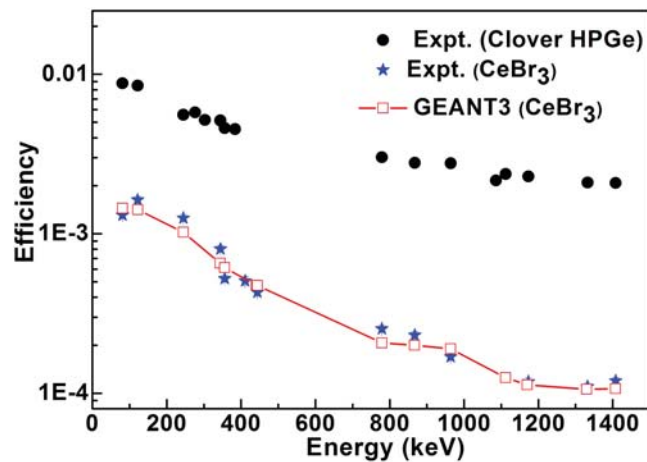


Figure 4.16: The measured efficiency of the CeBr_3 detector at 16 cm is compared with GEANT3 simulation and add-back efficiency of a Clover HPGe detector.

4.4.3 Time resolution

The timing measurement has been performed with two CeBr_3 detectors at different bias voltages and with different CF delay. In order to determine the time resolution, energy gated time peaks were generated by using a TAC module, as described in Section 4.3. A range of 50 ns was used in the TAC and the total time spectrum was displayed on an 8K spectrum. In the present work, the time resolution for the set of two

CeBr_3 detectors was studied while varying the CF delay from 0.5 ns to 10 ns. During this measurement, the bias voltage of the PMT was set at -1700 V.

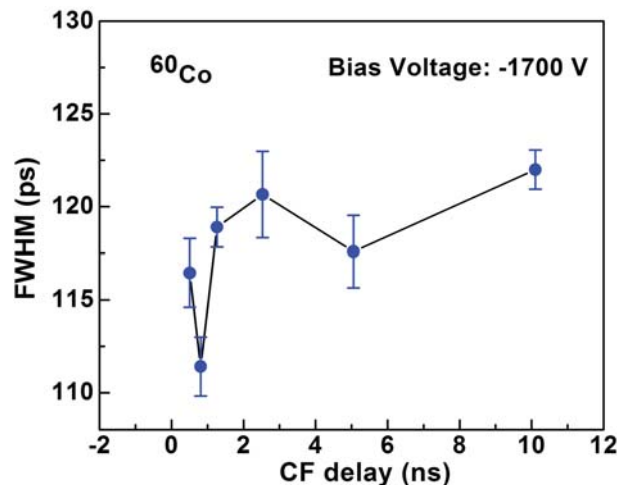


Figure 4.17: The time resolution is shown as a function of CF delay.

It has been observed that the best time resolution is obtained with 0.8 ns CF delay, as shown in Fig. 4.17. The time resolution was also measured by varying the bias voltage of the PMT from -700 V to -1700 V by fixing the CF delay at ~ 0.8 ns and the results are shown in Fig. 4.18 for two different cascades of 622-512 keV and 1173-1332 keV. It is concluded from the above measurements, that the detectors can be operated at -1200 V bias voltage of the PMT and with a 0.8 ns CF delay for obtaining the best time resolution. The best TAC spectra obtained with a ^{60}Co and a ^{106}Ru sources are shown in Fig. 4.19 in which the FWHM corresponds to the time resolution obtained with two CeBr_3 detectors. This gives rise to the time resolution of a single CeBr_3 detector at ^{60}Ni and ^{106}Pd energies to be 109(1) ps and 144(1) ps, respectively.

The time resolution for an $1'' \phi \times 1''$ thick CeBr_3 coupled to a R9779 fast PMT, obtained earlier [FRA13] at ^{60}Ni energies and ^{22}Na annihilation γ energies, are ~ 120 ps and ~ 164 ps, respectively. An improvement of time resolution by ~ 10 ps in the present work compared to Ref. [FRA13] could be attributed to the difference in measurement techniques followed in the two works. In Ref. [FRA13], time resolution has been measured with a combination of BaF_2 - CeBr_3 detectors compared to the CeBr_3 - CeBr_3 detectors used in the present case.

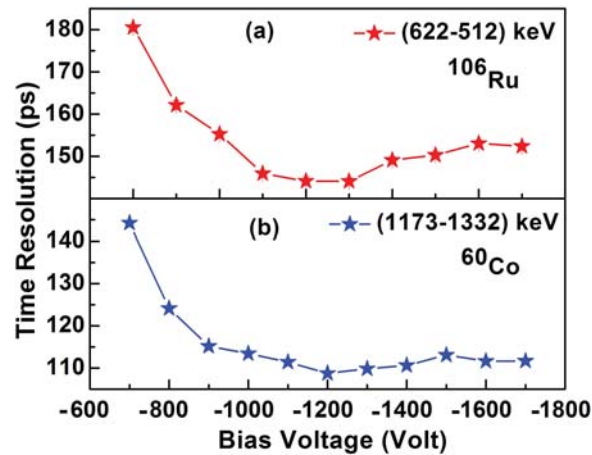


Figure 4.18: The time resolution is shown as a function of bias voltage of the PMT.

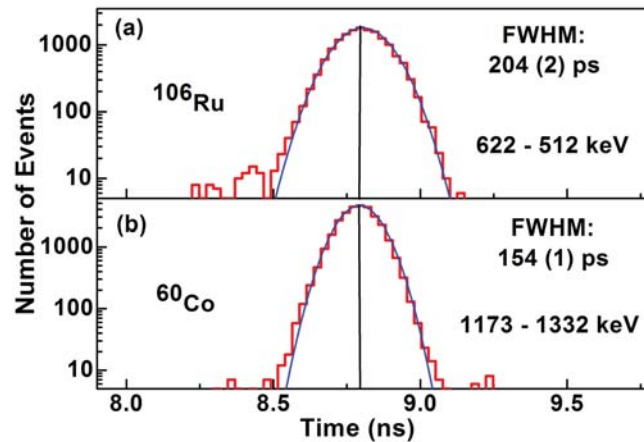


Figure 4.19: The TAC spectra obtained with two CeBr_3 detectors while using the ^{60}Co and ^{106}Ru source. The obtained FWHM values are indicated in the corresponding plot.

4.5 Applications of MSCD technique with 2 detectors

In this measurement, the PRD curve was generated as described above and the PRD calibration was done by following the procedures given in Ref. [REG16a, REG12]. The relevant gated spectra are shown in Fig. 4.20, obtained from ^{152}Eu source as well as ^{106}Ru source.

The latter has been used to measure the lifetime of the 512 keV level in ^{106}Pd , as described below. During this measurement, the CF delay was set at 0.8 ns and the PMT bias voltage was set at -1700 V. The delayed and anti-delayed time spectra obtained for few of the associated cascades are shown in Fig. 4.21. The data points for the PRD curve were generated by following the MSCD technique, as described

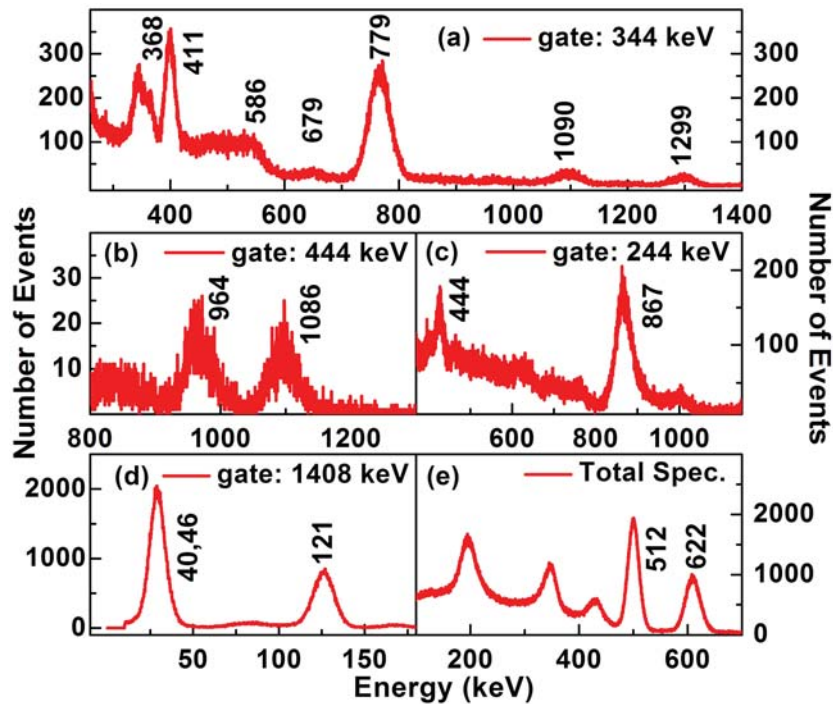


Figure 4.20: The energy spectra obtained by gating on different reference energies, viz., (a) 344 keV, (b) 444 keV, (c) 244 keV and (d) 1408 keV transitions, by using the ^{152}Eu source. (e) The energy spectrum obtained with ^{106}Ru source is shown.

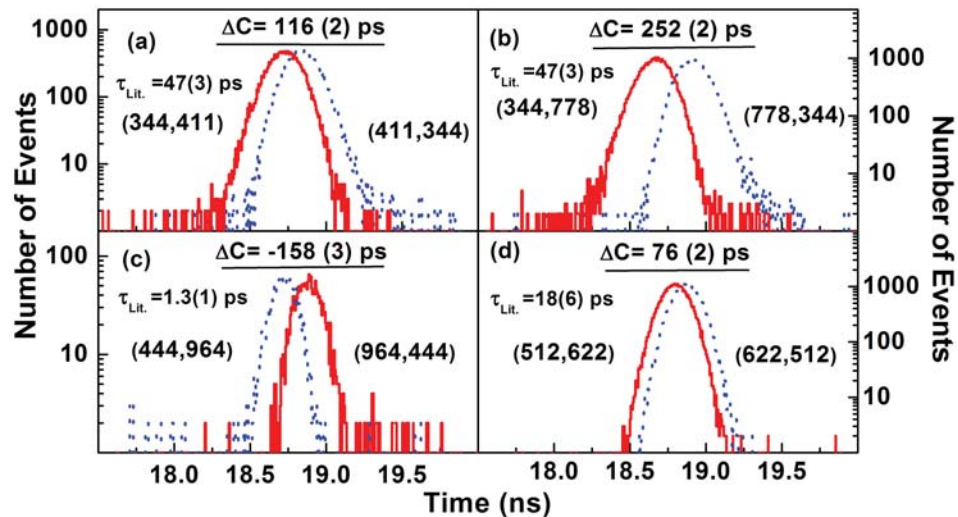


Figure 4.21: Few delayed and anti-delayed time spectra obtained with the two CeBr_3 detector setup using cascades of ^{152}Gd (a,b), ^{152}Sm (c) and ^{106}Pd (d) are shown. The delayed time distributions are shown with blue (dotted) and the anti-delayed with red (solid) line. (For interpretation of the references to colour in this figure legend, the reader is referred to the web version of this article.)

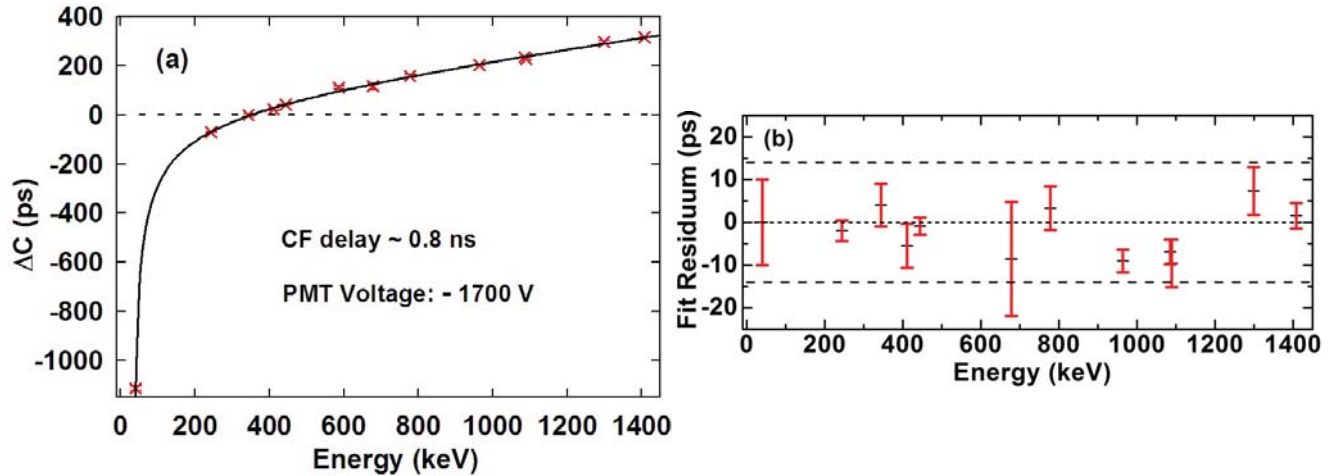


Figure 4.22: (a) The PRD curve obtained with two CeBr₃ detectors. The solid line shows the fit to these data points by using the function described in Eq. (4.22). (b) The fit residuum is shown for the data points with respect to a 3σ deviation for the PRD curve.

above, and are shown in Fig. 4.22 (a). The error value corresponding to each data point was determined by considering the statistical error for the determination of the centroid as well as the errors in the lifetime values with the associated $\gamma - \gamma$ cascades.

The data points have been fitted to generate the PRD calibration function using Eq. (4.22). The error in the PRD curve was estimated by calculating the standard deviation (σ) of the experimental data points from the fitted PRD curve and the fit residuum for the data points are shown in Fig. 4.22 (b) with respect to 3σ value (14 ps). Following the generation of calibration curve, the Centroid difference for the 622 keV cascade of ¹⁰⁶Pd has been determined and shown in Fig. 4.21 (d). Using this centroid difference and the PRD values at 512 and 622 keV γ energies, the level lifetime of the 512 keV level of ¹⁰⁶Pd was measured to be 19(10) ps which closely matches with the literature value [FRE08]. The error in the measured lifetime has been estimated by using both the errors in the centroid difference and the PRD.

Table 4.2: FWHM values obtained for different energy cascades with the VENTURE array.

Cascade (keV)	FWHM (ps)	
	2-det.	VENTURE
344-778	227(1)	276(4)
444-964	190(4)	235(5)
512-622	204(2)	250(5)
1173-1332	154(8)	188(3)

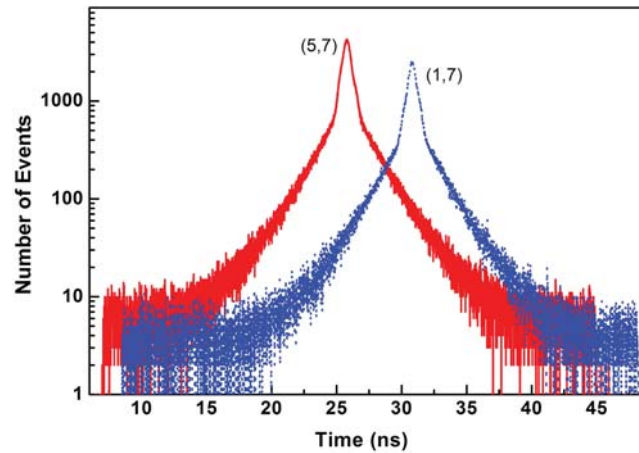


Figure 4.23: The time difference spectra obtained with different combinations of CeBr_3 detectors of the VENTURE array.

4.6 Applications of GCD technique with VENTURE array

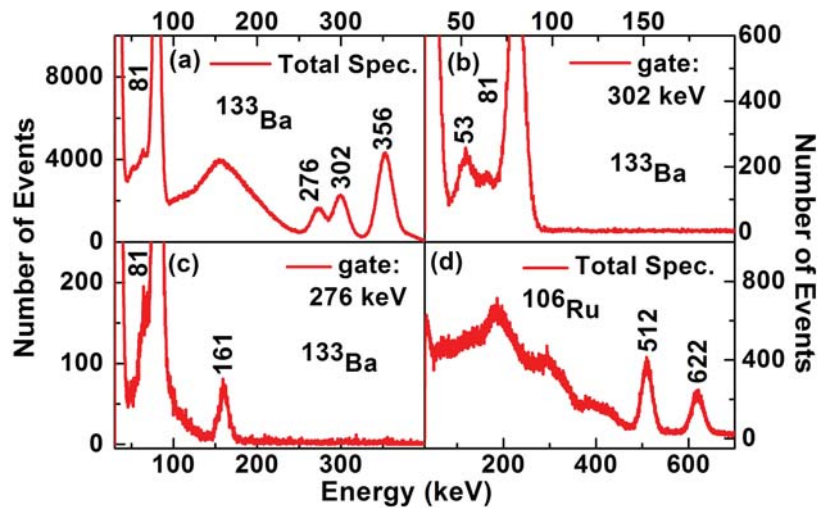


Figure 4.24: The total spectrum (a) obtained from ^{133}Ba source along with the 302 keV gate (b), 276 keV gate (c) and total spectrum from ^{106}Ru source (d) have been shown.

In order to generate the \overline{PRD} curve with the VENTURE array, the GCD technique was used in combination with common start timing technique while operating the detectors at -1700 V bias. The data were gathered with ^{152}Eu , ^{133}Ba and ^{106}Ru sources. During offline analysis, the list mode data were sorted event by event where a valid event was considered only when the ADCs corresponding to the energy of the two detectors (E_i and E_j) and the corresponding TACs (TAC_i and TAC_j) have valid data, decided by the

Table 4.3: The measurement of level lifetime for different levels of ^{106}Pd and ^{133}Cs , using VENTURE array.

Nucleus	Level	Cascade (keV)	$\overline{\Delta C}$	\overline{PRD}	τ (ps)	
					pres. work	Lit.
^{106}Pd	511.9 keV 2^+	622-512	91(6)	58(14)	17(8)	18(6) [FRE08]
^{133}Cs	160.6 keV $\frac{5^+}{2}$	276-161	551(24)	103(14)	224(14)	248(6) [KHA11]
^{133}Cs	383.8 keV $\frac{3^+}{2}$	53-302	-214(7)	-342(14)	64(8)	63(16) [KHA11]

thresholds. For all these events TAC_i and TAC_j were subtracted to generate the time difference spectra, TAC_{ij} ($i > j$), between any two detectors of the array, as shown in Fig. 4.23.

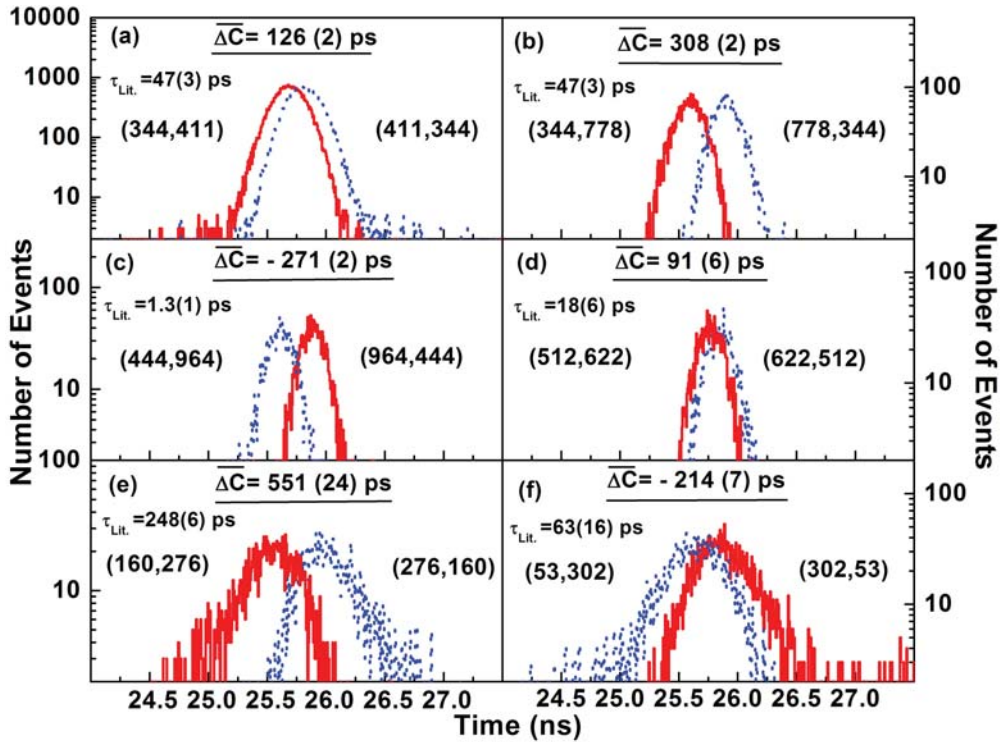


Figure 4.25: The delayed and anti-delayed time spectra obtained with the cascades of ^{152}Eu , ^{106}Ru and ^{133}Ba sources using VENTURE array. The delayed time distributions are shown with blue (dotted) and the anti-delayed with red (solid) line.

These time distribution spectra are equivalent to the ones reported in Ref. [REG16a] and thus, confirms that the electronics used in the present work have the ability to be used with GCD technique. Twenty eight

combinations were thus generated which were time calibrated before generating the total TDS by adding these individual TAC_{ij} s. While doing so, the gain matched energy of the detector i and detector j from each event were kept in two energy parameters. These two energy parameters and the total TDS represented the VENTURE array as equivalent to a two detector set up. The energy gates were put in these two final energy parameters to project the total TDS in order to generate the delayed and anti-delayed time spectra followed by the generation of the \overline{PRD} curve of the array. The FWHM values have been determined from the time distribution curves obtained for the VENTURE array for several cascades as shown in Table 4.2. The FWHM values show a maximum degradation $\sim 25\%$ compared to the ones obtained with two detector measurements and this was observed to be mainly contributed by the worst combination of the detectors present in the array. The centroid differences were measured for different cascades in ^{152}Sm , ^{152}Gd , ^{106}Pd and ^{133}Cs nuclei. Some representative energy spectra are shown in Fig. 4.24 and the representative delayed and anti-delayed time spectra are given in Fig. 4.25.

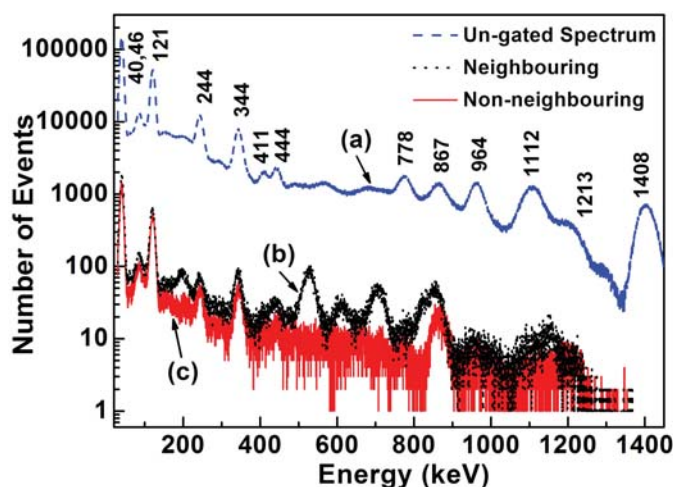


Figure 4.26: (a) The un-gated energy spectrum. (b) The 244 keV gated spectrum using neighbouring detectors showing ‘ghost peaks’ (c) The 244 keV gated spectrum using non-neighbouring detectors which show clean peaks.

While generating the delayed and anti-delayed time spectra for PRD determination, those combinations were not considered which displayed false coincidence due to back-scattered γ -rays coming from the Compton scattered events at some other neighboring detectors. This was understood from the appearance of ‘ghost peak’ in 244 keV gated spectrum shown in Fig. 4.26, which is similar to the observation with an array of LaBr_3 detectors [REG14].

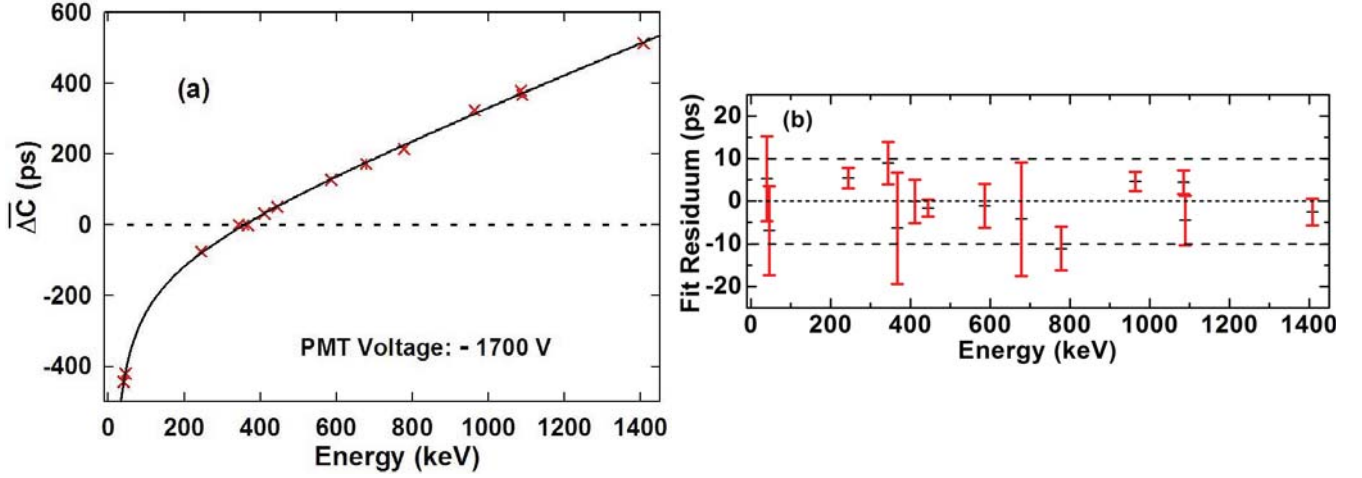


Figure 4.27: (a) The \overline{PRD} curve obtained with the VENTURE array is shown. The solid line shows the fit to these data points by using the function described in Eq. (4.22). (b) The fit residuum is shown for the data points with respect to a 3σ deviation for the PRD curve.

The \overline{PRD} curve, generated from the centroid differences obtained with the ^{152}Eu source and by fitting the data points with Eq. (4.22) is shown in Fig. 4.27 (a). The fit residuum has been displayed in Fig. 4.27 (b) by showing the data points with respect to the 3σ standard deviation (~ 10 ps), obtained as the error in PRD determination.

The obtained standard deviation (σ) ~ 3 ps shows the possibility of the measurement of nuclear level lifetime down to few ps. Table 4.3 shows the centroid differences obtained for the 512 keV level in ^{106}Pd , and the 161 and 384 keV levels in ^{133}Cs , obtained from the decay of ^{106}Ru and ^{133}Ba sources, respectively. The level lifetimes obtained for these levels by using the above \overline{PRD} calibration function have also been displayed in the Table 4.3. The background correction was made, as described in Eq. (4.23), whenever required. The errors in the final lifetime value have been calculated by considering all possible errors present in the measurement which are the standard error in \overline{PRD} and also the error in the centroid shifts calculated with required background correction. All the lifetimes could be reproduced in the present measurement with the VENTURE array. The level lifetime obtained for the 160.6 keV level of ^{133}Cs shows a small deviation from the literature value when measured following the GCD method. The lifetime of this level was also determined by using slope and convolution techniques which resulted in the lifetime values of 247(37) ps and 232(10) ps, respectively. The lifetime value obtained for the 160.6 keV level by using the GCD method is similar to the one obtained in earlier works with LaBr_3 detectors [REG12]. The observed deviation might be due to low statistics gathered for the relevant cascade and the related error in the centroid determination.

Chapter 5

VENTURE array for $\gamma - \gamma$ angular correlation measurement

5.1 Introduction:

The $\gamma - \gamma$ angular correlation was described theoretically for the first time by Hamilton in 1940 [HAM40]. In the succeeding years, many experiments were performed but those were unsuccessful to verify Hamilton's theorem due to a lack of detectors and experimental techniques. The first successful experiment was carried out in 1947 by Brady and Deutsch [BRA47] using Geiger counter detectors. The introduction of scintillator detector in 1948 [BRA48] in place of ultra-slow Geiger counter helped a rapid development of the field of angular correlation.

The effect of extranuclear field on the angular correlation, i.e., the perturbed angular correlation was first mentioned by Goertzel in 1946 [GOE46]. A few years later, the effect was first successively observed experimentally by Frauenfelder [FRA51] in 1951. A lot of studies, theoretically as well as experimentally on the early days dealing with both perturbed and unperturbed angular correlation, were performed to give a completeness of this method by many scientists, viz., Racah (1951), Alder (1952), Fano (1953), Abragam and Pound (1953), Coester (1954), Devons and Goldfarb (1957), Biedenharn (1962), Paul and Brunner (1963), Karlsson (1964), Frauenfelder and Steffen (1966) and so on. Now, this method has become a very important and necessary technique to study the structure of a nucleus. With the rapid development of modern detectors and its electronic accessories as well as experimental techniques, the important properties of low lying states can be studied nowadays more precisely using these methods.

The general term, angular correlation, can be characterized on the basis of general properties of radiations emitted successively in coincidence and those are known as directional angular correlation and polarization angular correlation. The directional angular correlation involves the measurement of relative emission probability of the second radiation as a function of the angle relative to the first emission while, the polarization angular correlation involves the measurement of linear or circular polarization of the radiations on the basis of their relative probability of emissions as a function of the included angle.

In the present work, we are interested with the $\gamma - \gamma$ directional angular correlation and the physics outcome from it, thus, we will focus on this method only. At first, the $\gamma - \gamma$ directional angular correlation will be discussed for the decaying nuclei which are free, i.e., no extranuclear fields are acted on the nucleus and then, the influence of the extranuclear fields on the angular correlation will be discussed.

5.1.1 $\gamma - \gamma$ directional unperturbed angular correlation:

The theoretical formula of $\gamma - \gamma$ directional angular correlation for the free nuclei can be derived in a very simplified way. Consider a single γ -ray with angular momentum \vec{L} traveling in a direction \vec{k} decays from initial state of spin I_i to final state of spin I_f of a cascade. According to quantum mechanics, the spin (I) of any state are being quantized by m substates ($m = -I, \dots, +I = 2I + 1$) along the quantization axis and the emitted γ -ray of angular momentum \vec{L} can be characterized in terms of angular quantum number or multipolarity L , magnetic quantum number M and propagation vector \vec{k} . The multipolarity (L) is defined as $\vec{L}^2 = \hbar L(L + 1)$ and $L_z = M\hbar$ where, L_z is the projection of \vec{L} along quantization axis (say, z-axis). The magnetic quantum number ($M = m_i - m_f$) of the transition depends on the quantum number m_i and m_f of the initial and final substates, respectively.

In general, the statistical distribution of intensity of one radiation alone will be isotropic because of random orientation of the nuclear spin of the emitting nuclear states. However, anisotropic radiation results when some orientations of nuclear angular momentum (L) are favorable with respect to some reference axis or one can say, when magnetic sublevels (m) of the emitting nuclear level are unequally populated.

To understand this phenomena now, consider a three level system through which a collection of identical nuclei in an excited initial state (A) decaying to a final state (C) via intermediate state (B) by emission of two successive γ -rays γ_1 (A \rightarrow B) with quantum number $L_1, M_1 (= m_a - m_b)$ and γ_2 (B \rightarrow C) with quantum number $L_2, M_2 (= m_b - m_c)$ as shown in Fig. 5.1. Also consider the propagation vector of the two γ -rays γ_1 and γ_2 are \vec{k}_1 and \vec{k}_2 , respectively.

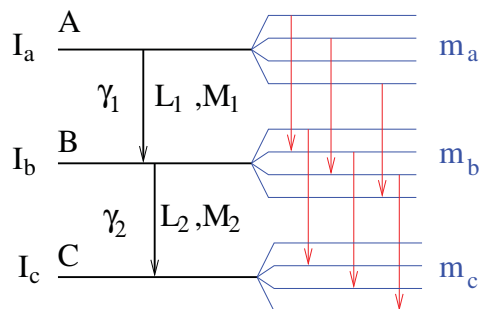


Figure 5.1: A schematic diagram of a three level cascade emitting two successive γ -rays along with sublevel splitting and transition between them is shown.

Since, the probability of emission of a radiation in a particular direction is dependent on the angle between the direction of propagation of the γ -ray and the spin axis of the nucleus, thus, to observe the correlation between two successive γ -rays it is necessary to select an ensemble of nuclei emitting photons (γ_1) in a fixed direction (\vec{k}_1) and to measure the intensity of successive emitted photons (γ_2) in other direction (\vec{k}_2) as a function of angle θ (\vec{k}_1, \vec{k}_2) with respect to direction (\vec{k}_1). Practically, it can be achieved by the setup of two detectors: ‘Detector 1’ and ‘Detector 2’ as shown in Fig. 5.2, where the ‘Detector 1’, fixed at a certain position, registers γ_1 and another movable ‘Detector 2’ registers γ_2 as a function of angle θ (\vec{k}_1, \vec{k}_2) with respect to ‘Detector 1’. To ensure both the emission are from the same nucleus a fast coincidence between the detectors are required depending on the intermediate level lifetime. It is also important to note that an anisotropic angular correlation is being found if some unequal population of m -substates in the intermediate level is preserved until the second photon is emitted, i.e., population of magnetic sublevels does not change for a duration equal to lifetime of the intermediate state. The intermediate state having lifetime $\tau \leq 10^{-10}$ sec, normally, fulfill the required condition and thus, the directional correlation will be undisturbed or unperturbed.

The excited initial levels may be populated from a radioactive nucleus by α - or β -decay or electron capture or due to isomeric transition. For a mathematical derivation, it can be assumed that all magnetic substates (m_a) in the initial states are equally populated during the emission of photon γ_1 . The relative population $P(m_b)$ of each sublevel in the intermediate state depends on the initial transition and can be expressed as Eq. (5.1) [ADL78]:

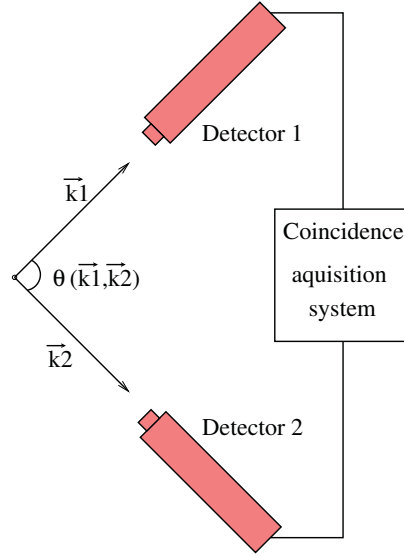


Figure 5.2: A schematic diagram of arrangement of two detectors for measuring angular correlation has been shown.

$$P(m_b) \propto \sum_{m_a} [CG(m_a m_b)]^2 F_{L_1}^{M_1}(\theta) \quad (5.1)$$

where, the term in the square bracket is the Clebsch-Gordan coefficient and square of it denotes the relative transition probability from m_a to m_b transition:

$$CG(m_a m_b) = \langle I_b m_b L_1 M_1 | I_a m_a \rangle \quad (5.2)$$

The term $F_{L_1}^{M_1}(\theta)$ is known as characteristic directional distribution for each ($m_a \rightarrow m_b$) transition where θ is the angle between emitted γ -ray and the z-axis. Practically, it is not possible to separate individual transition components $m_a \rightarrow m_b$ thus, the unresolved total distribution from $A \rightarrow B$ is always observed.

One simplification can be made by choosing γ_1 (\vec{k}_1) along the quantization axis (z-axis) which will make the angle $\theta = 0^\circ$ between emitted first γ -ray (γ_1) and the z-axis. This special choice restrict M_1 to ± 1 since, in a definite direction a photon can have angular momentum only $\pm \hbar$ along its propagation direction.

Thus, Eq. (5.1) becomes,

$$P(m_b) \propto \sum_{m_a} \langle I_b m_b L_1 \pm 1 | I_a m_a \rangle^2 F_{L_1}^{\pm 1}(0) \quad (5.3)$$

Similarly, to calculate the total directional distribution for transition $B \rightarrow C$ one must know the relative population $p(m_b)$ for each substate (m_b) of the intermediate state, relative transition probability for each transition between $m_b \rightarrow m_c$ and the directional distribution $F_{L_2}^{M_2}(\theta)$. Therefore, the total angular correlation function $\mathcal{W}'(\theta)$, the probability of emission of γ_2 at an angle θ with respect to γ_1 , i.e., z-axis can be expressed by:

$$\begin{aligned} \mathcal{W}'(\theta) &\propto \sum_{m_c m_b} P(m_b) [CG(m_b m_c)]^2 F_{L_2}^{M_2}(\theta) \\ &\propto \sum_{m_c m_b m_a} \langle I_b m_b L_1 \pm 1 | I_a m_a \rangle^2 F_{L_1}^{\pm 1}(0) \langle I_c m_c L_2 M_2 | I_b m_b \rangle^2 F_{L_2}^{M_2}(\theta) \end{aligned} \quad (5.4)$$

The directional distribution term ($F_{L_2}^{M_2}(\theta)$) can be usually expressed as Legendre Polynomials ($P(\cos\theta)$) and all other terms can be reduced to coefficients only. Thus, the correlation function can be reduced in a simplified form as:

$$\mathcal{W}'(\theta) = \sum_{k=0}^{k_{max}} A'_k P_k(\cos\theta) \quad (5.5)$$

where, the term A'_k is known as angular correlation coefficients which depend upon the previously mentioned dynamics and static properties of the nuclear states and can be separated into two factors: $A'_k = A_k^1 A_k^2$. The factor A_k^1 depends only upon the transition $A \rightarrow B$ and the second factor A_k^2 depends only upon the transition $B \rightarrow C$. The k are integer numbers and define the degree of correlation. The highest value of k , i.e., k_{max} can be calculated from the selection rule [FRA55]:

$$0 \leq k \leq \text{Min}(2I_b, 2L_1, 2L_2) \quad (5.6)$$

For most of the cascade $k_{max} \leq 4$ has been considered since, the change of angular momentum larger than $\Delta I = 2$ in the second transition implies a too long half-life of the intermediate state and thus, the angular correlation experiment will not be sensible. As the parity is conserved for a γ transition in a cascade thus,

only even value of k is possible. Therefore, Eq. (5.5) can be written in a reformed structure:

$$\begin{aligned}\mathcal{W}'(\theta) &= A_0' P_0(\cos \theta) + A_2' P_2(\cos \theta) + A_4' P_4(\cos \theta) \\ \mathcal{W}(\theta) &= 1 + A_2 P_2(\cos \theta) + A_4 P_4(\cos \theta)\end{aligned}\quad (5.7)$$

where, $A_2 = A_2'/A_0'$ and $A_4 = A_4'/A_0'$ and the term first $P_0(\cos \theta)$ of Legendre Polynomial is equal to one. The term $\mathcal{W}(\theta)$ is the normalized total angular correlation function.

The coefficients A_2 and A_4 are the functions of the spins and multiplicities of the states involved and can be calculated theoretically using F-coefficient [FEREN]. In case of a pure $\gamma - \gamma$ cascade, e.g., $I_a \xrightarrow{L_1} I_b \xrightarrow{L_2} I_c$ as shown in Fig. 5.3 (a), the coefficient of the first and second transition can be expressed as $A_k^1 = F_k(L_1 L_1 I_a I_b)$ and $A_k^2 = F_k(L_2 L_2 I_b I_c)$, respectively. But for a mixed $\gamma - \gamma$ cascade, e.g., $I_a \xrightarrow{L_1, L_1'} I_b \xrightarrow{L_2, L_2'} I_c$ as shown in Fig. 5.3 (b), they can be expressed as:

$$\begin{aligned}A_k^1 &= \frac{1}{1 + \delta_1^2} [F_k(L_1 L_1' I_a I_b) + 2\delta_1 F_k(L_1 L_1' I_a I_b) + \delta_1^2 F_k(L_1 L_1' I_a I_b)] \\ \text{and } A_k^2 &= \frac{1}{1 + \delta_2^2} [F_k(L_2 L_2' I_b I_c) + 2\delta_2 F_k(L_2 L_2' I_b I_c) + \delta_2^2 F_k(L_2 L_2' I_b I_c)]\end{aligned}\quad (5.8)$$

where, δ_1 is the mixing ratio between multiplicities L_1 and $L_1' = L_1 + 1$ for the first transition from I_a to I_b and δ_2 is the mixing ratio between multiplicities L_2 and $L_2' = L_2 + 1$ for the second transition from I_b to I_c .

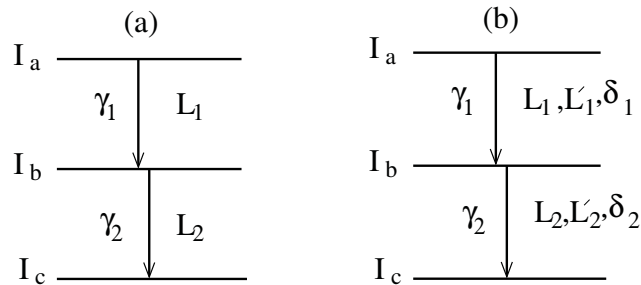


Figure 5.3: A schematic diagram of (a) a pure γ - γ transition and (b) a mixed γ - γ transition.

The Eq. (5.7) is valid only when the probe nucleus is free from any extranuclear fields. However, if the nucleus is doped in an environment where the extranuclear fields are present then the population of

sublevel of intermediate state can change due to interaction with the field and hence, the $\gamma - \gamma$ angular correlation becomes perturb.

5.1.2 $\gamma - \gamma$ directional perturbed angular correlation:

In the unperturbed case, the population of the hyperfine m-states in the intermediate level was not altered within the duration of its population by γ_1 and depopulation by γ_2 . Now if the time interval between emission of γ_1 and γ_2 , i.e., lifetime of the intermediate state is long enough and sufficient to interact with the extranuclear field then the nuclei in the intermediate state feels a torque. Therefore, the population of m-states may be altered either due to the interaction of Magnetic Dipole Moment (MDM) of the nucleus to the extranuclear magnetic field or due to interaction of EQM to the extranuclear electric field. This technique, therefore, can be used to determine the MDMs or/and EQMs of the nuclear states using the known extranuclear field. Reversely, the extranuclear fields of a sample can be determined using the nuclei with known moments.

In the perturbed angular correlation technique, the nuclei are doped as a probe in the host nuclei. The extranuclear fields present at the host nuclear site interact with the moment of probe nuclei. Semi-classically, these interactions produce a precession of angular momentum of the intermediate state around the symmetry axis of the field. Thus, the orientation of the spin I_b of intermediate level is changed in the time interval between emission of γ_1 and γ_2 and the angular correlation, therefore, altered. Quantum mechanically, the interactions can lead to transitions among m_b states. Thus, the γ_2 emits from a hyperfine state with an altered population density $P(m_b)$ and therefore, the angular correlation attenuates. The angular correlation, thus, is no more constant over time elapsed rather, it becomes a function of time. The dependency of correlation over the time interval between the emission of γ_1 and γ_2 is said to be perturbed angular correlation and the correlation function changes to:

$$\mathcal{W}'(\theta) = \sum_k^{k_{max}} A'_k G'_k(t) P_k(\cos \theta) \quad (5.9)$$

and the normalized function is:

$$\mathcal{W}(\theta) = 1 + \sum_k^{k_{max}} A_k G_k(t) P_k(\cos \theta) \quad (5.10)$$

where, $G_k(t)$ is a function of time and is known as perturbation factor which contains the information of the nature of the interaction and how the population of the intermediate state has been altered. The factor $G_k(t)$ is equal to unity at the time $t = 0$ when the initial orientation occurs that means it is the time when the initial m_b -state is populated by the emission of γ_1 . The time dependency of G_k results a periodic or monotonic decrease of the angular correlation. In case of monotonically decreased angular correlation, finally, $G_k(t)$ reaches zero and the correlation vanishes that means the angular distribution becomes completely isotropic.

The crucial parameter is the lifetime τ , of the intermediate state, the time needs to feel the torque due to perturbation. The extranuclear field also must be strong so that it exerts a sufficient precessional torque. In addition, the resolving time τ_r of the coincidence circuit, used for the collection of the feeding (γ_1) and decaying (γ_2) γ -rays of a cascade in coincidence, is an important parameter to determine the perturbed angular correlation experimentally. Since, the angular correlation is now time-dependent and if the measurements start at a time t_s after the initial orientation occurs ($t = 0$), then the angular correlation function can be expressed as [HEER]:

$$\mathcal{W}(\theta) = \frac{\int_{t_s - \tau_r}^{t_s + \tau_r} \mathcal{W}(\theta, t) e^{-t/\tau} dt}{\int_{t_s - \tau_r}^{t_s + \tau_r} e^{-t/\tau} dt} \quad (5.11)$$

The situation can be understood by following two cases:

Case I: Integral Perturbed Angular Correlation (IPAC) : This method can be applied when $\tau_r \gg \tau$, i.e., time resolution of the coincidence analyzer is much larger than the intermediate level lifetime. The obtained coincident time distribution, thus, appears as a statistical Gaussian like shape. In this case, the measurement is not affected due to the resolving time of the analyzer and one can take average over the total radiation independently of the time at which the successive γ -rays are emitted. Thus, a time integrated

correlation is observed and it can be expressed as [ADL78]:

$$\mathcal{W}(\theta, \infty) = \frac{1}{\tau} \int_{t=0}^{t=\infty} \mathcal{W}(\theta, t) e^{-t/\tau} dt \quad (5.12)$$

Therefore, the weight averages $\overline{\mathcal{W}(\theta, \infty)}$ can be deduced in the interval between $t = 0$ and $t = \infty$ using the following relation [ADL78]:

$$\overline{\mathcal{W}(\theta, \infty)} = \sum_k^{k_{max}=4} A_k \overline{G_k(\infty)} \quad (5.13)$$

and finally, the product $A_2 \overline{G_2(\infty)}$ can be deduced easily if the term A_4 is negligibly small. If the perturbed field is very large or time resolution is poor then IPAC is the ideal method to apply.

Case II: Time Differential Perturbed Angular Correlation (TDPAC) : This method can be applied when $\tau_r \ll \tau$, i.e., the resolving time of the analyzer is much lower than the lifetime of the level of interest. An asymmetric Gaussian shape with clearly visible slope, therefore, appears in the timing distribution spectrum depending on the level lifetime (τ). In this method, the attenuation factor $G_k(t)$ can be experimentally determined easily using the following equation if the $\gamma - \gamma$ coincidence pattern is known for at least two different angles (viz., 90° and 180°).

$$A_2 G_2(t) = 2 \times \frac{\mathcal{W}(180^\circ, t) - \mathcal{W}(90^\circ, t)}{\mathcal{W}(180^\circ, t) + 2\mathcal{W}(90^\circ, t)} \quad (5.14)$$

The perturbation may be static or dynamic and it depends on whether the extranuclear field is constant or changing with time. For the case of dynamic perturbations, the magnitude as well as direction of the external field varies with time whereas, in case of static interactions the field is independent of time elapsed, i.e., both magnitude and direction of the field does not change with time. The ultimate aim of the present work is based on the measurement of quadrupole moments of nuclear states using the TDPAC technique by probing the nuclei of interest in the field of static extranuclear electric field. In addition, explorations have been made for the measurement of quadrupole moments through IPAC technique. For the later purpose, the VENTURE array has been tested for its use in measurement of $\gamma - \gamma$ angular correlation with known and unknown cascades.

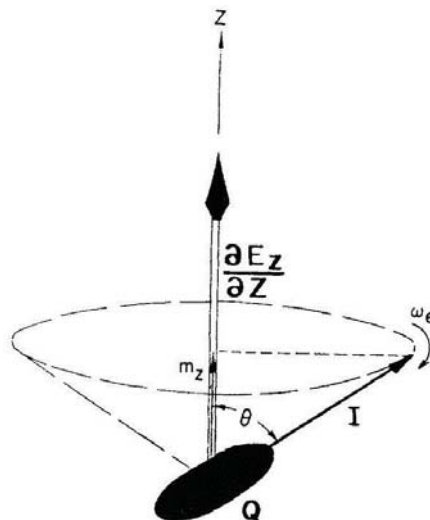


Figure 5.4: The figure shows an illustration of the precession of nuclear angular momentum I around the symmetry axis of an EFG [STE55].

5.2 TDPAC method: Measurement technique of Electric Quadrupole Moment (EQM)

For an effective hyperfine interaction, the external electric field must be strong enough ($\sim 10^{21}$ V/cm²) to produce a measurable effect on the interaction. This large amount of strong field can not be produced artificially at the lattice site using an external electric field from outside of the material. The electric field present at the lattice site due to electron-proton interaction has that much strength. Therefore, a non-cubic shape of the crystal structure is required to provide an effective electric field in a preferred direction since, the gradient of electric field [$\vec{\nabla}E(x, y, z)$] is essential for interaction with Quadrupole moment of the probed nucleus. The gradient of electric field or electric field gradient (EFG) is a second order tensor quantity and nine component values, in general, are required to specify it. With a proper choice of principle axis and applying the electric field's properties, more specifically Laplace law, the components can be reduced from nine to two. Furthermore, if one assumes axial symmetry of the field (say, around z-axis), it can be specified only by one component alone, i.e., $\frac{\delta E_z}{\delta z}$ or $\frac{\delta^2 V}{\delta z^2}$ or V_{zz} . If the fields are non-axial (viz., rhombic or orthorhombic), then the EFG can be described by its main component V_{zz} and by introducing an asymmetry parameter (η) [STE55]:

$$\eta = \frac{|V_{xx} - V_{yy}|}{V_{zz}} \quad (5.15)$$

The values of η lie between 0 (minimum value) to 1 (maximum value) and it is a measure of the deviation from the axially symmetric form $V_{xx} = V_{yy}$. The transition frequencies are now η dependent and deviate from its harmonic behavior. Thus, the asymmetry parameter η is a measure of loss of periodicity and distortion effect present in the perturbation factor $G_k(t)$.

A proper crystal structure (non-cubic) can be used as a host material to provide an effective EFG on the probed nuclei. The EQM, Q , of the nuclear state interacts with the present EFG and feels a torque for which the spin I of the state starts precession around the symmetric axis of the field gradient as shown in Fig. 5.4. That interaction leads to the splitting of the sublevels (m) of the intermediate state (see Fig. 5.5) and each of the sublevels can be described by the following equation of interaction energy [ADL78]:

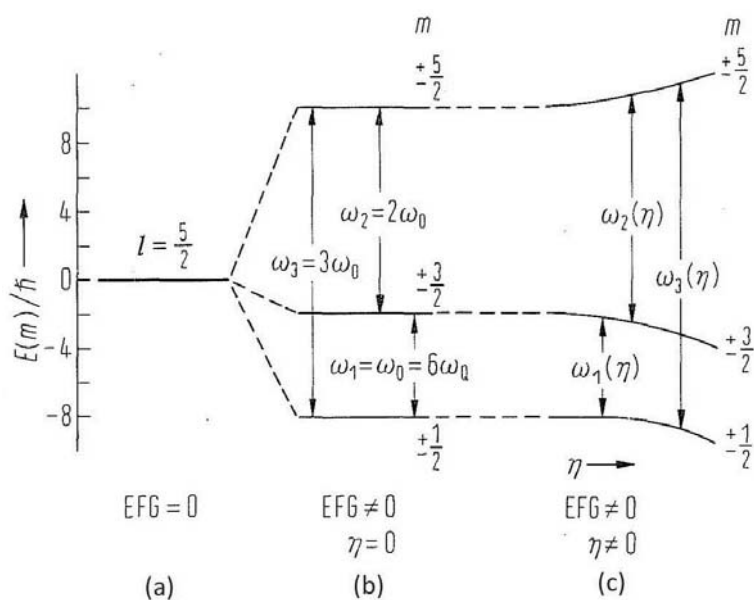


Figure 5.5: Splitting of a $I = 5/2$ state due to interaction of static EFG: (a) when EFG = 0; (b) when EFG $\neq 0$ but $\eta = 0$; (c) when EFG and η both are $\neq 0$ [ADL78]. The shift in the levels due to η are not to scale.

$$\begin{aligned}\mathcal{E}_Q(m) &= \frac{3m^2 - I(I+1)}{4I(2I-1)} eQV_{zz} \\ &= [3m^2 - I(I+1)]\omega_Q\hbar\end{aligned}\quad (5.16)$$

where, V_{zz} is the principal component of the EFG along the symmetric z-axis and ω_Q is the quadrupole frequency:

$$\omega_Q = \frac{eQV_{zz}}{4I(2I-1)} \quad (5.17)$$

The spin independent quadrupole interaction frequency coupling constant (ν_Q) can be derived as

$$\nu_Q = \frac{eQV_{zz}}{h} \quad (5.18)$$

The precession frequencies or so called characteristic frequencies (ω_n) correspond to the differences of level energy between neighbouring substates:

$$\omega_n = \frac{\mathcal{E}_Q(m) - \mathcal{E}_Q(m')}{\hbar} = n\omega_0 \quad (5.19)$$

where, n is any integer value and ω_0 is called the fundamental precession frequency which is the frequency obtained from the smallest non-zero energy difference:

$$\begin{aligned}\omega_0 &= \frac{3eQV_{zz}}{4I(2I-1)} = 3\omega_Q \text{ for integer spin(I)} \\ &= \frac{3eQV_{zz}}{2I(2I-1)} = 6\omega_Q \text{ for half-integer spin(I)}\end{aligned}\quad (5.20)$$

The allowed transitions between m -states leads to the attenuation of the angular correlation by an amount [ADL78]:

$$G_k(t) = \sum_n S_{kn} \cos(n\omega_0 t) \quad (5.21)$$

where, the terms n in the summation are restricted by the combination of the allowed m values:

$$\begin{aligned} \text{If spin } I \text{ is integer: } n &= (m^2 - m'^2) \\ \text{and, If spin } I \text{ is half-integer: } n &= \frac{1}{2}(m^2 - m'^2) \end{aligned}$$

and the term S_{kn} is known as geometrical coefficients and is proportional to square of Clebsch Gordon coefficients. Since, A_4 terms are negligible in most cases thus, only up to $k = 2$ is sufficient to give an illustration of angular correlation. The theoretical shape of the perturbation factor $G_k(t)$ for $k = 2$ can be defined by the following equation:

$$G_2(t) = \sum_n a_n e^{(-\omega_n \delta t)} \times e^{(-\frac{1}{2}\omega_n^2 \tau_R^2)} \times \cos(\omega_n t) \quad (5.22)$$

The summation index n can assume all positive integer values (including zero) and its maximum value depends on the number of hyperfine split levels. The exponential damping terms given in Eq. (5.22) attribute to (i) the finite resolving time (τ_R) of the measurement setup, characterized by a Gaussian distribution and (ii) the inhomogeneity introduced during sample preparation, expressed with the Lorentzian frequency distribution having relative width parameter δ . The coefficients a_n have dependence on the nuclear radiation parameters and the electric field asymmetry parameter η (Eq. (5.15)).

As evident from the above equation, the theoretical shape of the perturbation function is significantly affected by instrumentation, asymmetry of EFG and quality of the sample along with the population mode of the $\gamma - \gamma$ cascade, as follows:

(1) Firstly, because of the intrinsic time resolution of the coincidence circuit and with the approximation that the resolution function is a Gaussian distribution of width τ_R , a correction factor $e^{(-\frac{1}{2}\omega_n^2 \tau_R^2)}$ is introduced into the expression given in Eq. (5.22). The multiplication with this correction factor attenuates the amplitude of oscillations and shifts the zero time from its true value. (2) The second effect arises from a situation where the EFG has no axial symmetry ($\eta \neq 0$), i.e., from the asymmetry η of EFG. The eigen values of the m -states are approximated by power series of η and the transition frequencies become η -dependent with the loss of harmonic nature of quadrupole frequency (with exception for $\eta = 1$). (3) The third effect originates from the inhomogeneity of polycrystalline solid and defects present in that sample. This effect may result in situations where the crystalline fields experienced by the nucleus in its intermediate

state vary considerably from nucleus to nucleus. So, the experimental curve is fitted with a distribution of frequencies.

Experimentally, the $\gamma - \gamma$ coincidence histograms, mentioned in Eq. (5.10), are recorded as a function of time elapsed between the emission of feeding and decaying γ -rays, at least at two different angles (viz., 90° and 180°). The experimental perturbation function $G_2(t)$, obtained from Eq. (5.14), is least-square fitted with the theoretical expression to get the hyperfine parameters ω_Q and η . As the quadrupole frequency, ν_Q (Eq. (5.18)), is proportional to the EQM (Q) and EFG (V_{zz}), EQM is directly obtained from the known value of EFG. The measurement of EQM in iodine nuclei using the TDPAC technique has been discussed in Chapter 8.

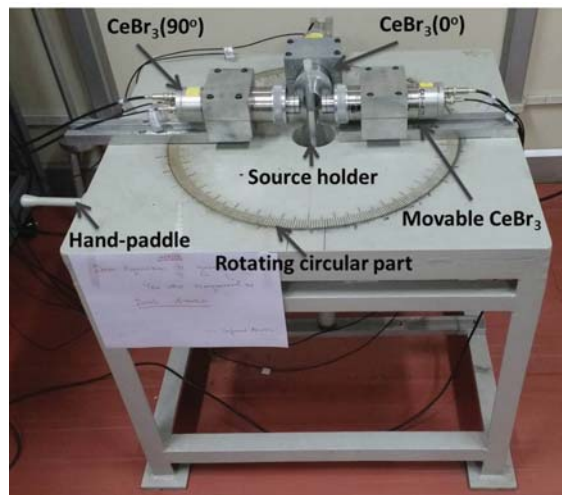


Figure 5.6: Illustration and brief descriptions of the manufactured angular correlation setup.

5.3 Development of an angular correlation setup

An angular correlation table has been designed and manufactured at VECC for measurement of angular correlation as shown in Fig. 5.6. The table has been designed in such a way that it consists of a movable concentric circular part, in the top plane, which can be rotated 360° easily with the help of a hand-paddle. A source holder can be placed at the center of the table as well as it can be adjusted vertically easily to keep the source at the same height to the center of the detectors. The movable circular part is scaled with 2π angles with a spacing of 1° and the adjusted fixed portion of the table is also scaled to measure the amount of rotation of the movable part. The table has capability to house three detectors ($\text{LaBr}_3(\text{Ce})$ or

CeBr₃) at three different specified angles. Two detectors among the three are fixed at an angle of 90° with respect to each other using a special holder setup which is fixed with the unmovable portion of the square table and the rest is attached with the movable circular portion using an appropriate holder. Therefore, the last detector can be moved at different angular positions using the hand-paddle without disturbing the other two fixed detectors. The distance between target and detectors can be adjusted up to a distance of 20 cm, while, the relative rotational angles can be varied with an accuracy of 1°.

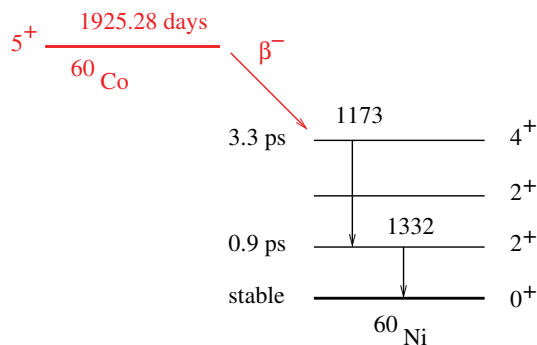


Figure 5.7: The simplified decay scheme of ${}^{60}\text{Ni}$, as populated from the decay of ${}^{60}\text{Co}$ source.

Table 5.1: The above Table shows a comparison of angular correlation coefficient values obtained from experimental result and theoretical calculation for 1173-1332 keV cascade of ${}^{60}\text{Ni}$. The geometrical correction factors for both A_2 and A_4 are also tabulated.

${}^{60}\text{Co} \rightarrow {}^{60}\text{Ni}$ cascade (keV)	Experimental Result		Theoretical calculation		Geometrical correction factor	
	A_2	A_4	A_2	A_4	A_2	A_4
1173-1332	0.095(13)	0.011(16)	0.102	0.009	1.07	0.81

This table can also be used for the stand alone configuration of the VENTURE setup using several CeBr₃ detectors as shown in Fig. 4.11. The advantages of this type of setup are that the detectors can be kept in a very close configuration with the source and the relative angular positions of the detectors can be adjusted and measured precisely which is very important while performing the experiment with angular correlation measurement. This stand alone VENTURE setup with a combination of this table can also be widely used for any off-beam decay experiment.

In the present study, a standard ${}^{60}\text{Co}$ source in diluted form has been used to perform a precise un-

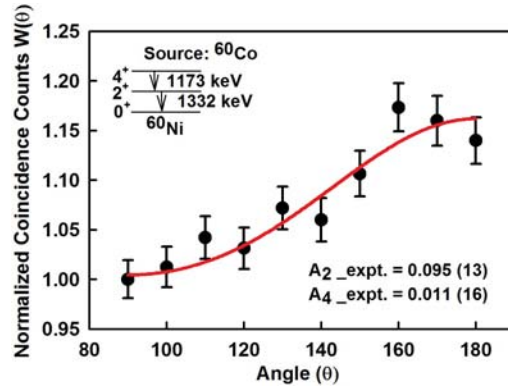


Figure 5.8: The figure shows the distribution of normalized angular correlation $W(\theta)$ as a function of θ for 1173-1332 keV cascade of ^{60}Ni and the obtained experimental angular correlation coefficient, A_2 and A_4 , from the fitting parameters.

perturbed angular correlation measurement placing three $1'' \phi \times 1''$ thick CeBr_3 detectors coupled with 8-stage fast R9779 PMTs. Two CeBr_3 detectors are placed and fixed at an angle of 90° with respect to each other and the angular correlation measurement was performed by varying the angular position of the third detector starting from 90° to 180° at an interval of 10° . The information of angular correlation has been collected in coincidence for the γ -rays of 1173-1332 keV cascade of ^{60}Ni which is produced after β -decay of ^{60}Co (see Fig. 5.7). The obtained anisotropy histogram of angular correlation between 1173 and 1332 keV at each angle was plotted as a function of angle as shown in Fig. 5.8. The data points were fitted using the equation of angular correlation function (Eq. (5.7)). From the fitting parameter the experimental angular correlation coefficients $A_2 = 0.095(13)$ and $A_4 = 0.011(16)$ were obtained.

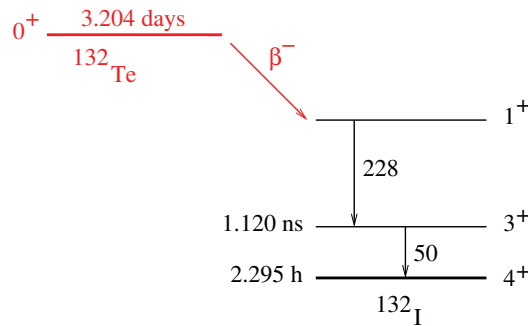


Figure 5.9: The simplified decay scheme of ^{132}I , as populated from the decay of ^{132}Te source.

For a comparison of the experimental results with the theoretical one, the angular correlation coefficients were also calculated using the F_k coefficient (Eq. (5.8)). The transition of 1173 keV ($4^+ \rightarrow 2^+$) and 1332

keV ($2^+ \rightarrow 0^+$) are well known pure E2 transitions with zero mixing ($\delta = 0$) from higher multipolarity. From the theoretical calculations the values of 0.102 and 0.009 for A_2 and A_4 , respectively, were obtained. The theoretical results of angular correlation coefficients are very close to experimental one. The small deviation occurs due to geometrical effects arising from both detector's solid angle coverage and also source volume. Since the detectors were kept in very close configurations and also instead of point-drop, an extended source was used in diluted liquid form thus, a geometrical correction factor is essential to get the actual angular correlation. Both the above results (experimental and theoretical) suggest the required solid angle correction factors in A_2 and A_4 to be 1.07 and 0.81, respectively (see Table 5.1).

5.4 $\gamma - \gamma$ angular correlation measurement in ^{132}I

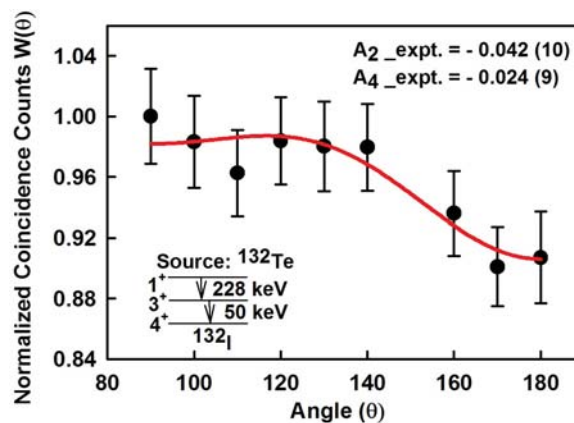


Figure 5.10: The figure shows the distribution of normalized angular correlation $\mathcal{W}(\theta)$ as a function of θ for 228-50 keV cascade of ^{132}I and the obtained experimental angular correlation coefficient, A_2 and A_4 , from the fitting parameters, after incorporating the geometrical correction factor.

The unperturbed angular correlation measurement was also performed for the 228-50 keV cascade in ^{132}I (see Fig. 5.9) produced from the decay of ^{132}Te ($\tau \sim 3$ d). The Te isotopes were obtained as one of the fission fragments produced from the $^{238}\text{U}(\alpha, f)$ reaction (discussed in details in the next chapter) by using α -beam from $K = 130$ cyclotron at VECC, Kolkata. The Te isotopes were separated from the other fission products by radiochemical separation method and thus it was a challenge to gather sufficient statistics required for the angular correlation measurement. The angular correlation result has been displayed in Fig. 5.10 and the A_2 and A_4 coefficients were obtained from the least square fitting of the data points using Eq. (5.7) followed by the solid angle corrections. From the fitting parameter the experimental angular correlation

coefficients $A_2 = -0.042(10)$ and $A_4 = -0.024(9)$ were obtained. The A_2 value is found to be close to the theoretical value -0.0714 , calculated by considering the multipolarity of the 1-E2-3-M1-4 cascade of ^{132}I as obtained from the Ref. [KHA05]. The deviation from the theoretical unperturbed angular correlation coefficients could be due to even very small mixing of higher multipoles in the associated γ transitions. It was found that an E2 mixing of $\sim 0.16\%$ in the 50 keV transition ($\delta_m = -0.04$, δ_m is mixing ratio) and a pure E2 nature of 228 keV transition explains the observed anisotropy in the present work.

Chapter 6

Production of neutron-rich nuclei

Most of the stable nuclei, in the lower mass region, have an equal number of proton and neutron but as one goes to heavier stable nuclei, the neutron number increases drastically with respect to proton numbers to compensate for the effect of Coulomb force between positively charged protons. From the nuclear landscape (Fig. 6.1), it can be easily seen that for a given neutron (N), proton (Z) or mass number (A), the number of stable nuclei is fairly small and the lifetime of unstable nuclei around the stable nuclei decreases rapidly as one moves away from the stable region. In the proton-rich side, the nuclei decay mainly via electron capture (ε) decay or β^+ decay whereas, in the neutron-rich side they decay via β^- decay. In the upper side (large Z and N) of the landscape, particle emission (α -decay) and fission takes place due to large number of nucleon compared to the stable nuclei in the same region.

However, most of the knowledge of nuclear properties has been obtained, till now, from the study of nuclei lying in the valley of beta stability and in the proton-rich side of the stability line. The main reason is that the stable nuclei or proton-rich nuclei can be easily produced using fusion evaporation reaction with stable target-projectile combination. However, the nuclei in the neutron-rich side can't be produced with this usual fusion evaporation reaction with stable target-projectile combination. Therefore, to produce them, one may use fusion evaporation reaction with unstable exotic neutron-rich projectile or Radioactive Ion Beam (RIB). The energetic short-lived unstable neutron-rich or RIB can be produced either via the Isotope Separation On-Line (ISOL) technique [KHAL06] or via the in-flight separation technique [HAR00]. Both the methods are limited by the lower production cross-section and decay half-lives of radioactive fission fragments and also, by the unwanted contaminants during separation. The separated fission fragments are transported away from their place of production to explore their purity or properties and prepare them

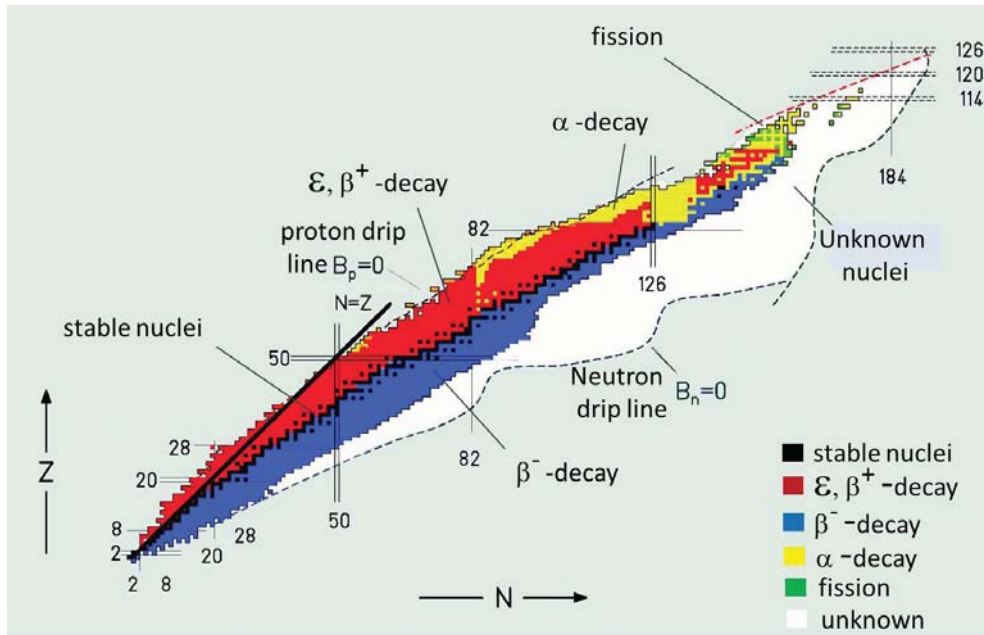


Figure 6.1: The figure shows the chart of nuclides within the border line of proton and neutron drip lines along with $N = Z$ line. The stable nuclei are shown in black squares whereas, the nuclei, already studied or observed, are shown in different grades of color depending on the different decay modes. The white area shows the unknown nuclei which remain mostly on the neutron-rich side. The horizontal and vertical lines represent the number of magic nucleons. The figure taken from [KHAL04] has been modified slightly.

for secondary acceleration, as and when required. The said fragments may also be used to study nuclear structure of themselves or their daughters through decay spectroscopy.

In case of ISOL techniques, the radioactive isotopes, using a primary beam, are produced in a target and then thermalized in a catcher which may consist of the material made with solid, liquid or gas. The target and the catcher may be the same material/object. The radioactive isotopes are extracted and transported from the catcher/target and ionized in the ionization chamber. Therefore, the radioactive ionized nuclei are mass analyzed and extracted from the ion source using a dipole magnet and then, again, transported and subsequently post-accelerated to the required energy.

In case of the in-flight separation technique, a primary heavy ion beam of several tens of MeV per nucleon is fragmented in a primary target and the resulting particles are sent to experimental side after electromagnetic separation. The main challenge is to separate and transport the secondary beam through the transport system after suppressing the highly intense primary beam transmitted through the primary target. This method is able to provide isotopes close to stability without the limitations due to their

lifetimes or chemical properties. Though, the disadvantages come from the low beam quality and lower production of ion species.

The above two methods were mainly about the techniques of the in-beam experiments and online analysis to study the neutron-rich nuclei with fusion evaporation reaction using radioactive ion beam. Now, there exists another alternate method to study these exotic neutron-rich nuclei in a well manner. In this process, one may perform an induced fission reaction with a heavy mass target and then, perform off-beam radiochemical separation process to separate the particular nuclei of interest from the rest of the fission fragments and therefore, the low-energy excited states of the successive β -delayed daughter isotopes can be studied [DIK74, DAS99]. This method is one of the best methods to peak up the nuclei of interest with sufficient purity. As the unstable individual fragments decay exponentially with time thus, the elapsed time between the end of irradiation of the target and the beginning of counting of the sample is very important. Thus, the time required for the separation should be short as much as possible so that an efficient fission yield remains at the end of the separation. Thus, the half-life of the parent nucleus plays a crucial role in the successful performance of this process. In the present thesis work, this radiochemical separation technique has been used to study the neutron-rich iodine and xenon isotopes around ^{132}Sn . Therefore, this radiochemical separation process including fission reaction, selection of target-projectile combination, irradiation technique etc. will be discussed briefly in the following subsections.

6.0.1 Nuclear fission

Nuclear fission is a special type of process where a heavy mass nucleus or an excited compound nucleus disintegrates into two daughter nuclei of comparable atomic numbers and mass numbers. This process was first successfully discovered by Otto Hahn and Fritz Strassmann and by Lise Meitner and Otto Frisch in 1939 [KRA87]. The nuclei having mass $A > 200$ are normally deformed in their ground state due to the significant repulsive effect of Coulomb force which exists between positively charged protons. On the other side, the attractive nuclear force which is actually analogous to surface tension of the nucleus opposes this Columbic instability. As a result, the fission process observed in the heavier nuclei may have two types of fission mode: one is spontaneous fission and another is particle induced fission reaction. The parent nucleus having $A > 240$ (e.g., ^{240}Pu , ^{252}Cf etc.) generally break spontaneously into two smaller daughter nuclei without any externally supplied excitation energy. Whereas, in the later case, a threshold energy is required to overcome the Coulomb barrier which is arisen due to mutual coulomb effect of the target and projectile

combination. Therefore, an excited compound nucleus is formed and finally, it splits due to the vibration occurred in that system. This excitation energy comes from the kinetic energy and binding energy of the projectile. The expression of coulomb barrier for a given target and projectile combination can be written as:

$$V_c = \frac{1}{4\pi\epsilon_0} \frac{Z_p Z_t e^2}{R_0(A_p^{1/3} + A_t^{1/3})} \quad (6.1)$$

where, A_p and Z_p are the mass number and atomic number of the projectile, respectively, and A_t and Z_t are the mass number and atomic number of the target, respectively, and R_0 is a constant known as nuclear radius parameter. In case of α (^4He) projectile and ^{238}U target, the coulomb barrier comes out to 28 MeV. Thus, the α -beam having kinetic energy more than 28 MeV is required for the induced fission of ^{238}U . However, as there is a certain probability of sub-barrier fusion cross-section to occur, there may be very low fission cross-sections observed below the barrier as well. According to Fig. 6.2, it can be easily seen that the α -induced fission cross-section of ^{238}U becomes saturated at and after 40 MeV beam energy. Therefore, the 40 MeV α -beam is sufficient to get the maximum fission yield for this particular target projectile combination.

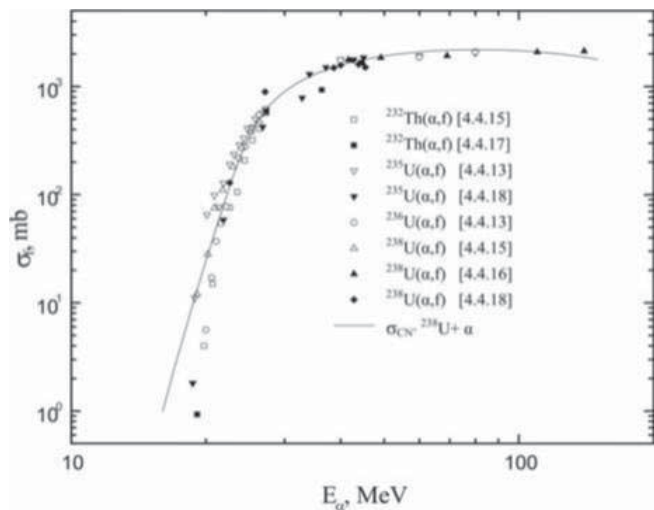


Figure 6.2: Experimentally observed α -induced fission cross-section of different thorium and uranium isotopes as a function of beam energy.

Now, the two fission products are lying in a highly excited state while fission occurs and move in opposite directions due to repulsion effect of mutual Coulombic force. The product nuclei may be unstable in nature

and thus, by emitting one or more neutrons or by emission of β -particles followed by γ emission, these may produce exciting daughter isotopes and the decay chain is continued until a stable nucleus is obtained. In the fission process, the most striking feature is the asymmetric feature of mass distribution of fission fragments. In case of ^{235}U , due to the thermal neutron induced fission, the lighter fission products have mass number distribution between $A = 85$ to 105 whereas, the heavier products have distribution between $A = 130$ to 150 [KRA87] (see Fig. 6.3). The yield curve is also symmetric about the central minimum of the curve, since for every heavy fission fragment there must be a corresponding light fission fragment with equal percentage yield. In the fission reaction, when a compound nucleus is split into two fission fragments then, ~ 200 MeV energy has been released. Thus, a huge heat is also produced in this reaction.

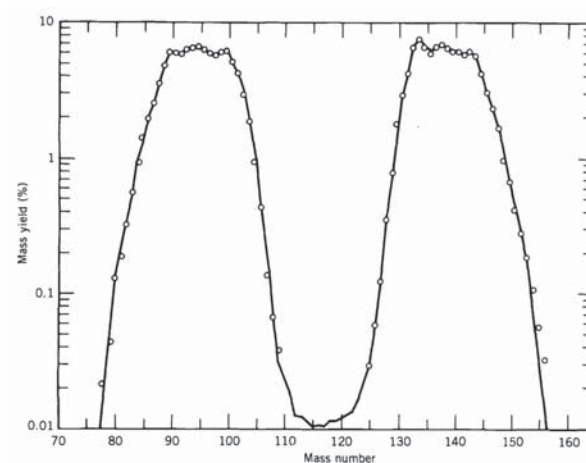


Figure 6.3: Mass distribution of fission fragments from thermal neutron induced fission [KRA87].

6.0.2 Experimental procedure: Present work

In the present thesis work, the fission reaction has been performed by bombarding the energetic α -particle with ^{nat}U target which consists 99.3% ^{238}U , 0.7% ^{235}U and a small amount of ^{234}U . The experimental details, preparation of targets along with the radiochemical separation of nuclei of interest from the other fission fragments have been discussed briefly in the following paragraphs.

Preparation of target:

In the present work, the electrodeposition technique has been used to prepare the ^{nat}U targets. The electrodeposition technique is one type of electrolysis process which uses electric current to reduce the

cations of dissolved metal so that a coherent coating of the desired metal can be formed on a conductive electrode. In the present case, uranyl nitrate ($UO_2(NO_3)_2$) in liquid form was used for the electrodeposition and the uranium target was deposited on a $25\ \mu\text{m}$ thick and $15\ \text{mm} \times 15\ \text{mm}$ square ^{nat}Al foil. Here, the Al foil also behaves as a backing foil to support the uranium target since, the prepared uranium target is not a self-supported target. The voltage and current of the electrodeposition system were controlled in such a way so that the target ions are deposited uniformly on the Al backing foil. The weight of the target was measured with the weight difference method. The setup used for the preparation of targets is shown in Fig. 6.4. In the present experiment, $\sim 1\text{mg}/\text{cm}^2$ ^{nat}U targets of 8 mm diameter was prepared on the square ^{nat}Al foils with $25\ \mu\text{m}$ thickness. The duration of preparation of each target, in general, was $\sim 2 - 3$ h. The prepared targets were dried under the IR lamp and finally, stored safely inside a vacuum desiccator.



Figure 6.4: The experimental setup of electrodeposition technique used, in the present thesis work, for preparation of targets is shown. The figure has been taken from Ref. [SAH18a].

Irradiation technique:

Since, the yield of the Te fission isotopes of interest is very low, thus, in the present work, the stacked foil irradiation technique was used to increase the total yield of the desired radionuclide. In this irradiation method, a number of thin targets and catcher foils are kept in an alternate position. In the present work, as shown in Fig. 6.5, the $25\ \mu\text{m}$ thick ^{nat}Al foils were used as catcher foils behind every ^{nat}U target to collect the recoiling fission fragments coming out from the target foils. The setup of stacked foils was built on a flange, as shown in Fig. 6.6, which was made of stainless steel and was equipped with a beam dump as well

as a cooling system. As high-Z beam stopper, a 2 mm thick and 15 mm \times 15 mm square Tantalum (Ta) sheet was also kept at the very end of the stacked foil to stop the beam coming out of the last catcher foil. Few Al spacers with 0.5 mm thin along with a circular hole of 6 mm diameter were used to separate each targets and catchers of the stacked foils so that one can easily de-assemble all the targets and catcher foils after end of irradiation. A collimator of 6 mm diameter was used before the target to define the circular area exposed for beam irradiation. The stacked foil setup on the flange was such that the beam will face the target first, then catcher, then again target, then again catcher and so on. Finally, the remaining projectiles will be stopped at the Ta beam dump, as shown in Fig. 6.5. Before irradiation, the target chamber was evacuated up to $\sim 10^{-2}$ torr through the rotary pump and then, the gate valve was opened to connect the target chamber with the main beam line which was maintained at $\sim 10^{-7}$ torr pressure.

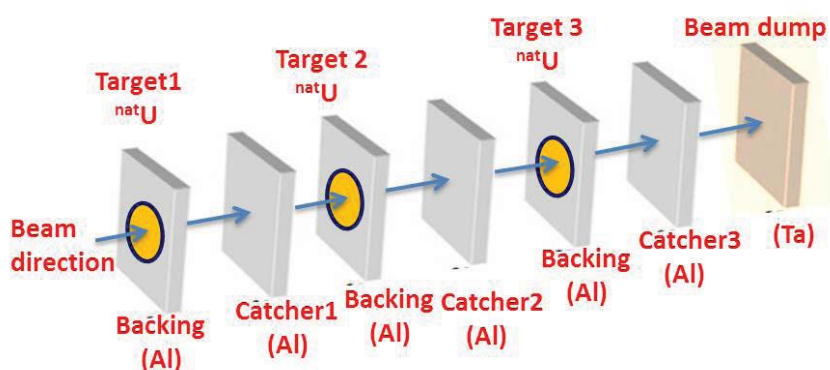


Figure 6.5: An illustration of Stacked foil arrangement.



Figure 6.6: The snapshot of the flange and the preparation of stacked foil on it.

In the present work, the 40 MeV α -beam with ~ 500 nA beam current from K-130 cyclotron at VECC, Kolkata was used to perform the fission ${}^{nat}\text{U}(\alpha, f)$ reaction (see Fig. 6.7). As ${}^{238}\text{U}$ is present in 99.3% in ${}^{nat}\text{U}$, the primary compound nucleus formed in this reaction is ${}^{242}\text{Pu}^*$. The unstable compound nucleus will be broken into two fragments after emission of 2 - 3 prompt fast neutrons. The produced fragments will be recoiled with kinetic energy in opposite direction to each other. In the present work, it was observed that the fission products present in target foils and the catcher foils were almost equal in population.

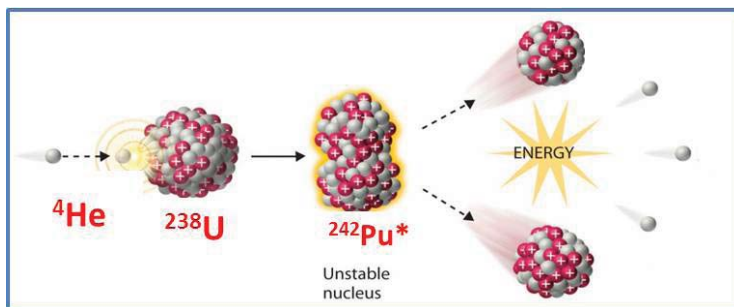


Figure 6.7: The illustration of the fission reaction on ${}^{nat}\text{U}$ target with α -beam.

Irradiation was carried out for a duration of ~ 48 h in order to have a negligible relative yield of the short lived Te nuclei and to produce the sufficient relative yield of the parent ${}^{131m}\text{Te}$ ($\tau \sim 33$ h) and ${}^{132}\text{Te}$ ($\tau \sim 3$ d) nuclei. After 2 - 3 h cooling period, the irradiated stack foil was brought to the radiochemistry laboratory for further processing. With proper safety, the setup was de-assembled and catcher foils containing the recoiling fission products were collected to perform the radiochemical separation of the active Te nuclei from rest of the fission products. The total time which was required to complete the radiochemical separation process up to this was in general 30 - 45 minutes. In case of fast processing, when required in case of smaller half-life of the radionuclide of interest, within 20 minutes the catcher foils can be made ready for performing radiochemical separation of fission products with proper safety precautions.

Radiochemical separation:

At first, the collected catcher foils were dissolved in concentrated hydrochloric acid. The inactive tellurium carrier in the form of Te(VI) and a small amount of Hydrazine Sulfate were added to the solution. Then, the radioactive tellurium along with the tellurium carrier were reduced to metallic Te(0) by chemical method. Using centrifugation technique, the metallic Te(0), deposited as a black precipitate at the lower part of the centrifuge tube, has been separated from the rest of the solution, known as supernatant. The precipitate

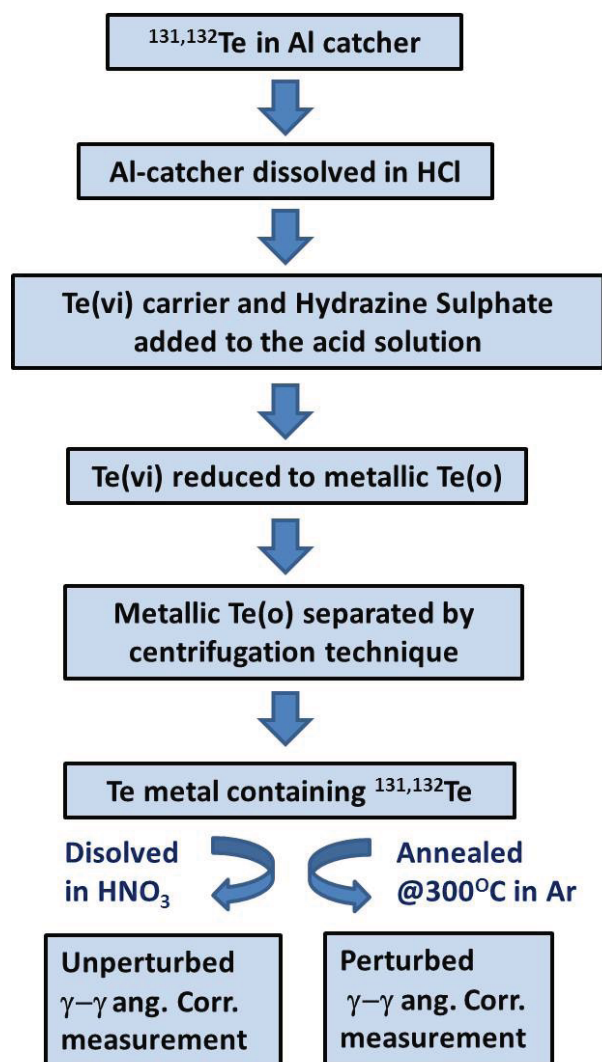


Figure 6.8: The procedure of radiochemical separation technique for separation of tellurium isotopes from fission products is shown.

was then washed with dilute HCl followed by distilled water several times. Almost 90% of total fission activity was removed in this technique as the supernatant and the remaining 10% activity was actually contained the pure metallic Te(0) isotopes. After washing, the separated black precipitate was dissolved in concentrated nitric acid and the solution was transferred to counting tube. The volume of the prepared sample was $\sim 200 \mu\text{L}$. The sample containing the inactive Te isotopes along with active Te was used as a radioactive source during the subsequent $\gamma - \gamma$ coincidence measurements. In the present thesis work, the low lying excited states of ^{131}I and ^{132}Xe nuclei have been studied, which were populated as the β -

decay daughter and grand-daughter of the respective separated Te isotopes. To increase the statistics of the data, required for lifetime (Chapter 7) as well as EQM (Chapter 8), the similar irradiation technique, radiochemical separation and subsequent counting were done multiple times.

Now, in case of PAC measurement (discussed in Chapter 8), the separated solid Te(0) metal powder was annealed in argon (Ar) atmosphere at 573 K for 3 h. Therefore, a continuous flow of the Ar gas was maintained inside the heating chamber during the annealing process. After the end of the heating process, the sample was slowly cooled down to room temperature and placed in front of detectors for the subsequent measurement. In case of PAC measurement performed in the present thesis work, the trigonal crystal structure of the Te metallic powder, consisting of both active and inactive Te isotopes, provides the necessary EFG to the active nuclear site.

Chapter 7

Lifetimes and transition probabilities for the low lying states in ^{131}I and ^{132}Xe

7.1 Introduction

The ^{131}I and ^{132}Xe have three and four extra proton particles compared to $Z = 50$ shell closure, respectively, and four extra neutron holes for each of them compared to $N = 82$ shell closure around ^{132}Sn . The negative parity intruder orbital $1h_{11/2}$ plays a very important role in the region between 50 - 82 shell gap since, it is surrounded by the other positive parity orbital $1g_{7/2}$, $2d_{5/2}$, $2d_{3/2}$ and $3s_{1/2}$ which have low angular momentum compared to $1h_{11/2}$ intruder orbital.

Existence of octupole correlation is known in the doubly closed ^{132}Sn [FOG94], even-even Xe around $N = 82$ [MUE06] and in other neutron deficient nuclei in this mass region [SEL15, MAS05] from the knowledge of $B(E1)$ and $B(E3)$ strengths. So, the lifetime measurements of the low lying levels of the neutron-rich iodine and xenon nuclei is of extreme importance in order to explore and enrich the nuclear structure around double shell closure at $Z = 50$ and $N = 82$ which is difficult to access experimentally.

In the present work, we focus on the lifetime measurement using $\gamma - \gamma$ fast timing technique for the low lying levels of odd-A ^{131}I and even-even ^{132}Xe nuclei populated through the decay of radiochemically separated Te fission fragments. The Generalized Centroid Difference (GCD) method [REG16a] has been used to analyse the experimental $\gamma - \gamma$ time difference distribution obtained with VENTURE array [ALA17]. The LBSM calculations using NushellX code [BRO14] have been performed to understand the excitation energies, dominant particle partitions and level lifetimes for the low lying levels in ^{131}I and ^{132}Xe . The

transition strengths have been calculated from the measured level lifetime and discussed in the light of the systematics in the neighboring nuclei.

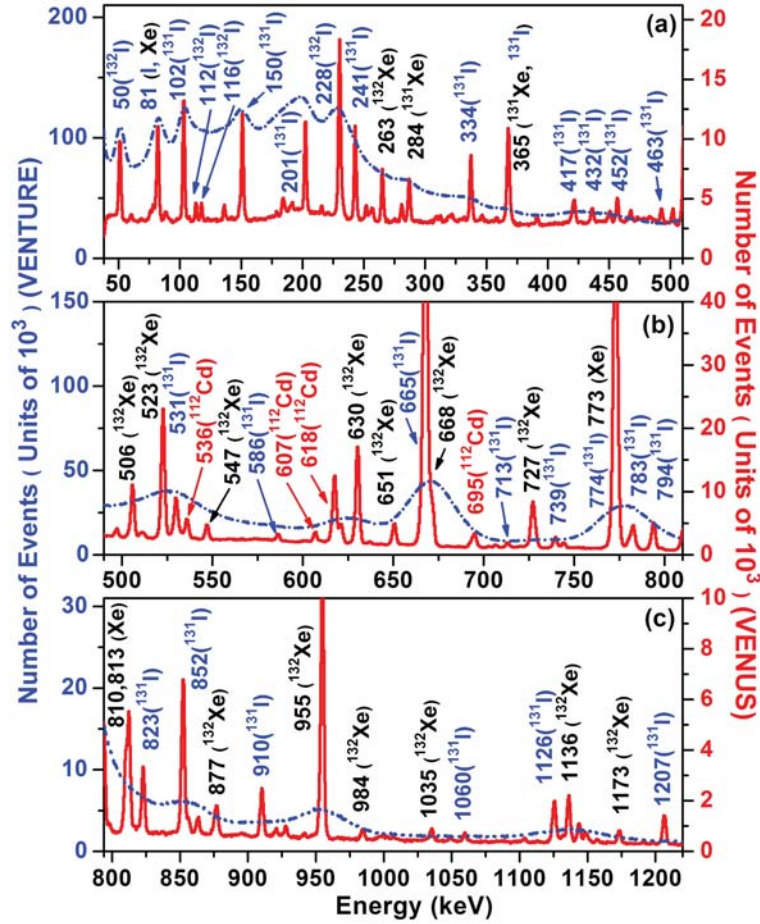


Figure 7.1: The total projections (without any background subtraction) obtained from the CeBr₃ (blue dash-dotted line) and Clover detectors (red solid line) are shown from CeBr₃-CeBr₃ and CeBr₃-Clover coincidences, respectively. The γ -rays from different isotopes are identified and marked with different colours of text for I(blue), Xe(black) and Cd (red) (contamination).

7.2 Experimental details

The excited states of ^{131}I and ^{132}Xe nuclei are populated as the β -decay daughter and grand-daughter of the respective ^{131m}Te ($\tau \sim 33$ h) and ^{132}Te ($\tau \sim 3$ d) fission fragments which are produced with $^{nat}\text{U}(\alpha, f)$ reaction with 40 MeV α -beam from K-130 cyclotron at VECC, Kolkata, as discussed in Chapter 6. The radiochemically separated Te activity from the other fission fragments are kept in a liquid medium during

Table 7.1: Levels of ^{132}Xe and ^{131}I , for which lifetime measurements have been carried out in the present work. The lifetimes are calculated by using the equation: $\tau = \frac{1}{2}(\Delta C_{FEP} - \text{PRD})$. The quoted errors in lifetime are calculated by considering the standard deviation, i.e., $2\sigma \sim 7$ ps, obtained in the generation of PRD curve and the errors estimated for the ΔC values. The lifetimes marked with \star have been considered for some systematic error as described in text. For the cases where the measured lifetimes are less than the estimated error, the upper limits of lifetimes are shown. The J^π values are taken as per the assignments shown in Table 7.2. The measured lifetimes have been compared to the known values obtained from literature [JAK02, KHA06, KHA05, NAV90, RAM01] whereas available and rest are the newly measured values.

Nucleus	E_x (keV)	J^π	cascade (keV)	ΔC_{exp} (ps)	ΔC_{BG} (ps)	p/b	ΔC_{BG} (ps)	p/b	t_{corr} (ps)	ΔC_{FEP} (ps)	PRD (ps)	Lifetime (τ) (ps)	
												(feeder)	(decay)
^{131}I	774	$11/2_1^+$	1126-774	203(3)	211(3)	1.66(6)	164(1)	2.78(4)	5(2)	208(4)	165	22(5)	-
	852	$9/2_1^+$	794-852	-10(4)	-22(8)	1.1(2)	5(2)	1.22(2)	-1(4)	-11(6)	-28	9(5)	-
	1646	$11/2_1^-$	334-794	-228(2)	-267(5)	1.04(1)	-249(5)	1.86(3)	25(3)	-203(4)	-248	23(5)	-
	1797	$15/2_1^-$	102-241							-	-	8.4(7)ns	8.5(3)ns
	1899	$13/2^-$	81-1126	-692(5)	-814(2)	1.14(1)	-784(14)	1.58(5)	83(6)	-609(8)	-676	34(6)	-
^{132}Xe	668 \star	2_1^+	630-668	-14(2)	-21(3)	1.50(2)	-39(1)	2.68(3)	7(2)	-7(3)	-19	≤ 8	6.1(5) - 9.7(30)
	1298 \star	2_2^+	506-630	-48(2)	-42(2)	1.23(1)	-58(3)	1.60(2)	1(1)	-47(2)	-66	10(8)	4.4(4)
	1440	4_1^+	955-773	109(1)	102(4)	1.55(4)	95(3)	2.44(3)	6(2)	115(2)	87	14(5)	2.6(2)
	1963	4_2^+	877-523	186(4)	185(2)	1.04(2)	163(1)	1.30(1)	10(3)	196(5)	177	10(5)	-

the subsequent $\gamma - \gamma$ coincidence measurements with VENTURE [ALA17] and VENUS [SAH18] arrays. The VENTURE array with eight $1'' \phi \times 1''$ thick fast CeBr₃ detectors has been used to detect the de-excited γ transitions for lifetime measurement and was setup along with the VENUS array of six Compton suppressed Clover HPGe detectors.

The GCD technique has been used for the analysis of $\gamma - \gamma$ fast timing data in which a PRD curve is generated that represents the prompt time characteristics of the array. The prompt response depends on the PMT voltages, CFD settings, detector geometry, etc. along with other long-term effects. In the present work, the PRD curve shown in Fig. 4.27 in Chapter 4 has been used, as the data has been acquired with the same experimental setup. Also, the prompt response was checked time to time with source data in order to check for any major deviation. The details on the generation of PRD curve for the VENTURE array and the determination of the PRD value for a particular $\gamma - \gamma$ cascade can also be found in Chapter 4 and Ref. [ALA17].

7.3 Results

The CeBr₃ total projection from the CeBr₃-CeBr₃ coincidences is shown in Fig. 7.1 and is compared with the Clover total projection from CeBr₃-Clover coincidence. These total projections are obtained without any subtraction of the underlying background. The spectrum from Clover detectors depicts the clean separation

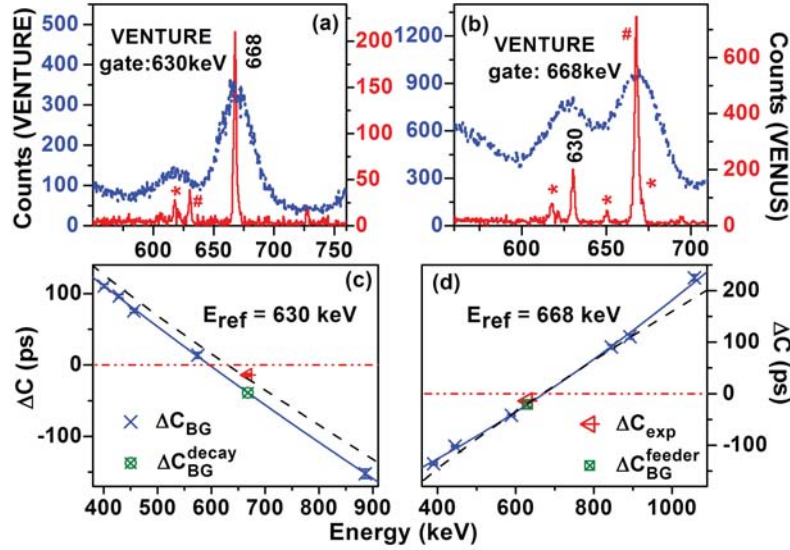


Figure 7.2: The CeBr_3 energy gated projections of CeBr_3 (blue dash-dotted lines) and Clover (red solid lines) detectors are shown with gate on (a) feeder (630 keV) and (b) decay (668 keV) γ -rays of 630-668 keV cascade of ^{132}Xe . The photopeaks observed in (a) and (b) are marked with \star and $\#$, respectively, in case they arise from known γ - γ coincidences or from the coincidence with the Compton background under the gating transition. The background analysis for this cascade are shown in panels (c) and (d) where ΔC_{BG} values are shown with respect to PRD = 0 at E_{ref} . The PRD curve is also shown with black dashed line by making PRD = 0 at E_{ref} . The red dash-dotted line is drawn to guide the eye for ΔC or PRD = 0.

of Te isotopes from rest of the fission fragments with a little contamination from the Ag isotopes that gives rise to the γ lines from ^{112}Cd . The lifetimes measured in the present work are listed in Table 7.1 with some of the relevant information. The measured lifetimes are compared with earlier results, wherever available.

During the lifetime measurement using GCD method, the delayed and anti-delayed time distributions for different γ - γ cascades are analyzed to determine the experimental centroid difference (ΔC_{exp}). Appropriate background corrections, following similar methods as described in Subsection 4.2.4 of Chapter 4 and Ref. [REG17], are employed in the present work for determining the background corrected centroid differences for the FEP (ΔC_{FEP}). The PRD is determined from the calibrated prompt time curve of the VENTURE array as described in Section 4.6 of Chapter 4. Two standard deviation ($2\sigma \sim 7$ ps), obtained in the prompt time calibration, was considered while calculating the error in measured lifetime following Eq. (4.25).

Figs. 7.2 and 7.3 demonstrate the above analysis procedure of lifetime measurement, considering two selective cascades of 630-688 keV of ^{132}Xe and 1126-774 keV of ^{131}I , respectively. In both of these figures, the gated projections from CeBr_3 - CeBr_3 and CeBr_3 -Clover coincidences are shown which are obtained by

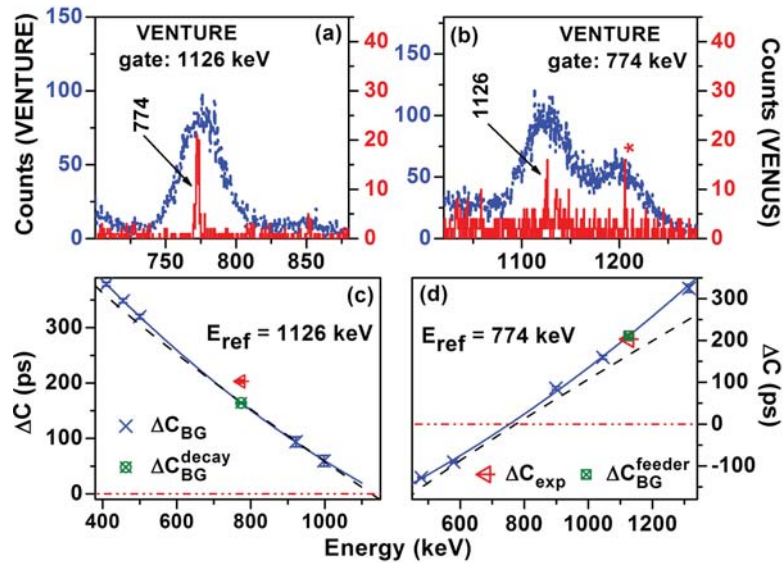


Figure 7.3: The CeBr_3 energy gated projections of CeBr_3 (blue dash-dotted lines) and Clover (red solid lines) detectors are shown with gate on (a) feeder (1126 keV) and (b) decay (774 keV) γ -rays of 1126-774 keV cascade of ^{131}I . The background analysis for this cascade are shown in panels (c) and (d) where ΔC_{BG} values are shown with respect to $\text{PRD} = 0$ at E_{ref} . The PRD curve is also shown with black dashed line by making $\text{PRD} = 0$ at E_{ref} . The red dash-dotted line is drawn to guide the eye for ΔC or $\text{PRD} = 0$.

setting the CeBr_3 gate for (a) E_{feeder} and (b) E_{decay} , respectively. The comparison of these two projections was helpful in selecting the energy gate for lifetime measurement and to identify if there is any unresolved photopeak around the energy of interest. Such peaks are marked with \star , if arises due to known $\gamma - \gamma$ coincidences and with an $\#$ if it is due to coincidences with the Compton background underlying the gated photopeak. An extra systematic error has been added to the measured lifetime of the level in case the photopeak neighboring to the transition of interest was found to be disturbing the measurement and such levels are indicated by \star in Table 7.1. The background analysis is also demonstrated in Figs. 7.2 and 7.3, both around (c) E_{decay} and (d) E_{feeder} , respectively. The background corrections are shown with respect to $\text{PRD} = 0$ at the reference energy value. The value of ΔC_{expt} is also indicated on the figures and the same is taken from the separation between the delayed and anti-delayed TAC projections shown in Fig. 7.4 for all the cascades listed in Table 7.1. All kinds of centroid difference (ΔC) values obtained from this analysis and required for the determination of level lifetime are listed in Table 7.1.

The lifetimes measured with GCD method are shown in Table 7.1 in comparison to the earlier works, wherever available. Only the upper limit of lifetime is shown when the measured value is found to be less than the error obtained in the measurement. Prior to the present measurement, the level lifetimes for

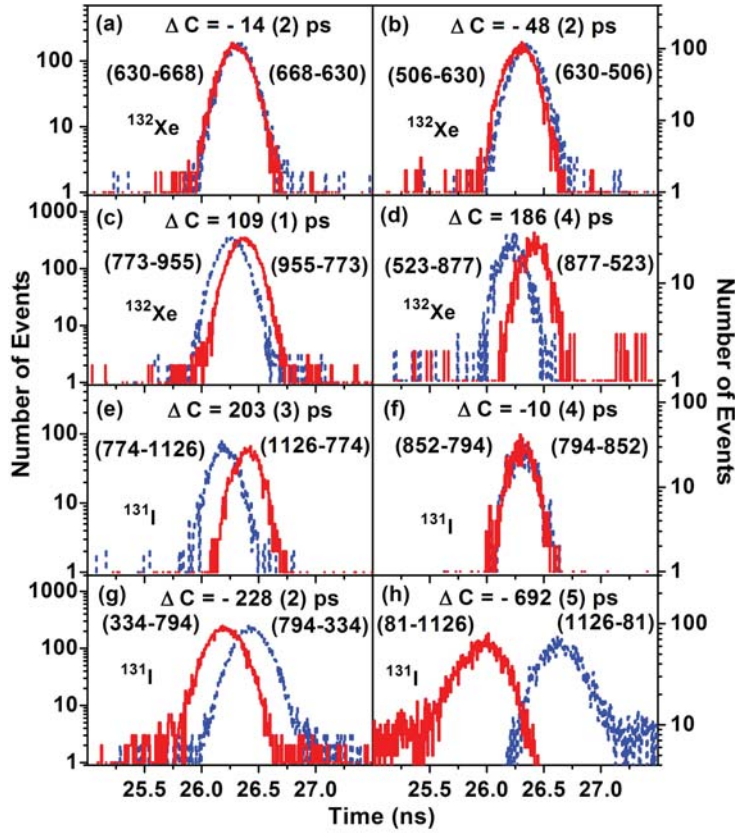


Figure 7.4: The delayed and anti-delayed TAC spectra for few cascades of ^{132}Xe (a - d) and ^{131}I (e - h) nuclei, used for the lifetime measurement with GCD method. The delayed and anti-delayed time distributions are shown with red (solid) and blue (dotted) lines, respectively.

the 511.9 keV level of ^{106}Pd and the 160.6 and 383.8 keV levels of ^{133}Cs were reproduced from the same experimental setup, as described in Ref. [ALA17]. In the present measurement, a systematic error was required to be added to the lifetimes of the levels marked with \star in Table 7.1. Among these, the 621 keV peak was found to be contaminating both the 630-668 (668 keV, 2_1^+ level of ^{132}Xe) and 506-630 (1298 keV, 2_2^+ level of ^{132}Xe) cascades. As the lifetime of the decaying and feeding levels of the 621 keV transition is not known, an error of 3 ps ($\sim 1\sigma$) was added to the lifetimes of these two levels. No contaminations were found, however, that can be considered as disturbing transitions for the remaining levels listed in Table 7.1.

The present measurement could yield the lifetimes of the 774 keV ($11/2_1^+$), 852 keV ($9/2_1^+$), 1646 keV ($11/2_1^-$) and 1899 keV ($13/2_1^-$) levels of ^{131}I with GCD method. None of these lifetimes are known in literature and thus the present work provides these data for the first time. Along with ^{131}I , the lifetime measurement was also explored for the first few excited levels in ^{132}Xe which was yielded from the decay

of ^{132}I . However, according to the data available for the Xe nuclei around $N = 82$ [NNDC], the lifetimes for most of these levels in ^{132}Xe are expected to be below the standard deviation of the PRD. So, the precise determination of lifetimes for these levels in ^{132}Xe are difficult as the values are at the limits of the capability of the present experiment. Among these, the lifetime of the 2_1^+ level was measured, prior to the present work, with different techniques and the corresponding values vary among themselves between 6.1(5) - 9.7(30) ps [NAV90, RAM01]. Considering this variation for the 2_1^+ level, it is observed that the present measurement could reasonably reproduce the level lifetime of the first two excited levels in ^{132}Xe . In case of next excited level (4_1^+), however, the lifetime value yielded with the present GCD analysis is in the higher side in comparison to the earlier Coulomb excitation experiments [JAK02, NAV90, RAM01]. In addition, the level lifetime for the 4_2^+ level in ^{132}Xe could also be measured for the first time in the present work. Along with the lifetime measurement with GCD method, the lifetime of the 1797 keV ($15/2_1^-$) level of ^{131}I was also measured with slope method. This was done by using the time distribution spectrum for the 102-241 keV cascade. The time distribution spectra and the slope fit for the 102-241 keV cascade is shown in Fig. 7.5 and the present measurement yielded a level lifetime of 8.4(7) ns which is in agreement with the earlier measurements [KHA06] and listed in Table 7.1.

The known experimental level sequences and the level lifetimes obtained for ^{131}I and ^{132}Xe have been interpreted from LBSM calculations as described in Section 7.4 and the structure associated to different excited levels in these two nuclei are discussed in Section 7.5.

7.4 Shell model calculation

The LBSM calculations were carried out using proton-neutron formalism in full valence space without any truncation available with the code NuShellX as discussed in Subsection 2.0.4 of Chapter 2. The calculations were performed using the *jj55pn* model space and *sn100pn* interaction file available with the code considering ^{100}Sn as a core. In Table 7.2, the calculated excitation energies are compared with the experimental energies of the low lying levels, mostly below 2.0 MeV, in the iodine and xenon nuclei under study.

The decomposition of angular momentum of proton and neutron ($I_\pi \otimes I_\nu$) for each level is listed in Table 7.2 along with the dominant particle partitions contributing to the configuration mixed (J^π) states. Only those $I_\pi - I_\nu$ combinations are listed which have contribution of greater than 10% in the total wavefunction.

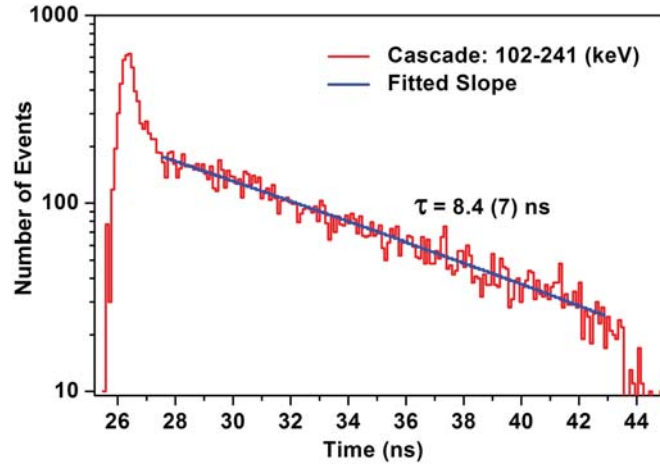


Figure 7.5: The time distribution obtained for the 102-241 keV cascade with an appropriate background subtraction is shown.

Different partitions obtained for a particular coupling are also listed in Table 7.2. In general, all those partitions having probability $>5\%$ are listed, wherever available. However, there are some cases where all the partitions are of less than 5% strength and in such situation the partition having the maximum probability is only listed. It is important to mention that the corresponding partitions, listed in the Table 7.2, however, account only for about not more than 25% of the total partitions involved in constituting the state. This indicates a tremendous fragmentation of the wave functions, i.e., configuration mixing, in almost all the levels in ^{131}I and ^{132}Xe .

The transition probabilities, corresponding to the decay of excited levels in ^{131}I and ^{132}Xe , have been calculated using effective charges ($e^p = 1.35$, $e^n = 0.35$) and g-factors ($g_l^p = 1.0$, $g_s^p = 5.586$, $g_l^n = 0.0$ and $g_s^n = -3.826$). The lifetimes have been calculated from these transition probabilities by considering the theoretical branching and experimental γ energy values. The conversion coefficient for a particular transition was calculated from the BrIcc code [KIB08]. The lifetime values obtained from the calculation have been compared with the experimental results for the positive parity levels, as shown in Table 7.2. The lifetimes of all the positive parity levels in ^{131}I and ^{132}Xe are reasonably reproduced from the calculation. However, using the above method, the level lifetimes could not be directly estimated for the negative parity levels of ^{131}I , viz., 1646 keV ($11/2_1^-$), 1797 keV ($15/2_1^-$) and 1899 keV ($13/2_1^-$). These levels are known to de-excite by strong E1 decays and the single particle orbitals available in the chosen model space of our calculation do not allow such E1 decay to occur. However, lifetime for two of these levels could be calculated

TABLE II: continued...

Nucleus	E _x		J ^π		I _π	I _ν	%	Major	%	Lifetime	
	(keV)						prob.	Partition	prob.	(ps)	
	Expt.	Calc.	Expt.	Calc.			(a)		(b)	Expt.	Calc.
¹³¹ I	2112	1976	6 ⁺	6 ⁺	4 ⁺	2 ⁺	20.72	$\pi(1g_{7/2}^2 2d_{5/2}^2) \otimes \nu(2d_{3/2}^{-2} 1h_{11/2}^{-2})$	1.71		
					4 ⁺	2 ⁺	11.64	$\pi(1g_{7/2}^2 2d_{5/2}^1) \otimes \nu(2d_{3/2}^{-2} 1h_{11/2}^{-2})$	1.57		
					6 ⁺	0 ⁺	53.17	$\pi(1g_{7/2}^3 2d_{5/2}^1) \otimes \nu(3s_{1/2}^{-2} 1h_{11/2}^{-2})$	5.10		
					6 ⁺	2 ⁺	10.31	$\pi(1g_{7/2}^3 2d_{5/2}^1) \otimes \nu(2d_{3/2}^{-2} 1h_{11/2}^{-2})$	14.62		
	0	0	7/2 ⁺	7/2 ⁺	5/2 ⁺	2 ⁺	10.02	$\pi(1g_{7/2}^3) \otimes \nu(2d_{3/2}^{-2} 1h_{11/2}^{-2})$	2.28		
					7/2 ⁺	0 ⁺	68.33	$\pi(1g_{7/2}^3) \otimes \nu(3s_{1/2}^{-2} 1h_{11/2}^{-2})$	5.92		
					7/2 ⁺	0 ⁺		$\pi(1g_{7/2}^3) \otimes \nu(2d_{3/2}^{-2} 1h_{11/2}^{-2})$	18.66		
	150	246	5/2 ⁺	5/2 ⁺	5/2 ⁺	0 ⁺	51.26	$\pi(1g_{7/2}^3) \otimes \nu(2d_{3/2}^{-2} 1h_{11/2}^{-2})$	10.46		
					5/2 ⁺	2 ⁺	11.95	$\pi(1g_{7/2}^3) \otimes \nu(2d_{3/2}^{-2} 1h_{11/2}^{-2})$	6.29		
					5/2 ⁺	2 ⁺	11.95	$\pi(1g_{7/2}^3) \otimes \nu(2d_{3/2}^{-1} 3s_{1/2}^{-1} 1h_{11/2}^{-2})$	1.52		
					7/2 ⁺	2 ⁺	24.74	$\pi(1g_{7/2}^3) \otimes \nu(2d_{3/2}^{-2} 1h_{11/2}^{-2})$	5.38		
	493	450	3/2 ⁺ , 5/2 ⁺	5/2 ⁺	5/2 ⁺	0 ⁺	58.24	$\pi(1g_{7/2}^2 2d_{5/2}^1) \otimes \nu(2d_{3/2}^{-2} 1h_{11/2}^{-2})$	12.94		
					5/2 ⁺	2 ⁺	13.64	$\pi(1g_{7/2}^2 2d_{5/2}^1) \otimes \nu(2d_{3/2}^{-2} 1h_{11/2}^{-2})$	2.91		
					7/2 ⁺	2 ⁺	12.33	$\pi(1g_{7/2}^3) \otimes \nu(2d_{3/2}^{-2} 1h_{11/2}^{-2})$	2.18		
	602	653	3/2 ⁺ , 5/2 ⁺	3/2 ⁺	3/2 ⁺	0 ⁺	42.53	$\pi(1g_{7/2}^3) \otimes \nu(2d_{3/2}^{-2} 1h_{11/2}^{-2})$	11.00		
					5/2 ⁺	2 ⁺	15.15	$\pi(1g_{7/2}^3) \otimes \nu(2d_{3/2}^{-2} 1h_{11/2}^{-2})$	4.66		
					7/2 ⁺	2 ⁺	29.68	$\pi(1g_{7/2}^3) \otimes \nu(2d_{3/2}^{-2} 1h_{11/2}^{-2})$	8.90		
	774	803	9/2 ⁺ , 11/2 ⁺	11/2 ⁺	7/2 ⁺	2 ⁺	44.33	$\pi(1g_{7/2}^3) \otimes \nu(2d_{3/2}^{-2} 1h_{11/2}^{-2})$	12.71	22(5)	11
					11/2 ⁺	0 ⁺	32.36	$\pi(1g_{7/2}^3) \otimes \nu(2d_{3/2}^{-2} 1h_{11/2}^{-2})$	10.18		
	852	872	9/2 ⁺	9/2 ⁺	7/2 ⁺	2 ⁺	49.46	$\pi(1g_{7/2}^3) \otimes \nu(2d_{3/2}^{-1} 3s_{1/2}^{-1} 1h_{11/2}^{-2})$	9.02	9(5)	4
					9/2 ⁺	0 ⁺	22.34	$\pi(1g_{7/2}^3) \otimes \nu(2d_{3/2}^{-2} 1h_{11/2}^{-2})$	9.36		
9/2 ⁺					0 ⁺		$\pi(1g_{7/2}^3) \otimes \nu(2d_{3/2}^{-2} 1h_{11/2}^{-2})$	6.15			
876	896	1/2 ⁺	1/2 ⁺	1/2 ⁺	0 ⁺	42.51	$\pi(1g_{7/2}^2 3s_{1/2}^1) \otimes \nu(2d_{3/2}^{-2} 1h_{11/2}^{-2})$	9.41			
				5/2 ⁺	2 ⁺	43.14	$\pi(1g_{7/2}^2 2d_{5/2}^1) \otimes \nu(2d_{3/2}^{-2} 1h_{11/2}^{-2})$	13.49			
1006	1040	—	7/2 ⁺	5/2 ⁺	2 ⁺	38.72	$\pi(1g_{7/2}^2 2d_{5/2}^1) \otimes \nu(2d_{3/2}^{-1} 3s_{1/2}^{-1} 1h_{11/2}^{-2})$	8.52			
				5/2 ⁺	2 ⁺		$\pi(1g_{7/2}^2 2d_{5/2}^1) \otimes \nu(2d_{5/2}^{-1} 3s_{1/2}^{-1} 1h_{11/2}^{-2})$	7.85			
				7/2 ⁺	0 ⁺	35.38	$\pi(1g_{7/2}^2 2d_{7/2}^1) \otimes \nu(2d_{3/2}^{-2} 1h_{11/2}^{-2})$	10.9			

TABLE II: continued...

Nucleus	E _x (keV)		J ^π		I _π	I _ν	% prob. (a)	Major Partition	% prob. (b)	Lifetime (ps) (Pres. work)	
	Expt.	Calc.	Expt.	Calc.						Expt.	Calc.
	1060	1169	9/2 ⁽⁺⁾	9/2 ⁺	5/2 ⁺	2 ⁺	33.56	$\pi(1g_{7/2}^2 2d_{5/2}^1) \otimes \nu(2d_{3/2}^{-2} 1h_{11/2}^{-2})$	10.09		
					9/2 ⁺	0 ⁺	34.07	$\pi(1g_{7/2}^2 2d_{5/2}^1) \otimes \nu(2d_{3/2}^{-2} 1h_{11/2}^{-2})$	10.31		
	1556	1554	+	15/2 ⁺	7/2 ⁺	4 ⁺	16.96	$\pi(1g_{7/2}^3) \otimes \nu(2d_{3/2}^{-2} 1h_{11/2}^{-2})$	5.25		
					11/2 ⁺	2 ⁺	29.89	$\pi(1g_{7/2}^3) \otimes \nu(2d_{3/2}^{-2} 1h_{11/2}^{-2})$	9.70		
					15/2 ⁺	0 ⁺	32.98	$\pi(1g_{7/2}^3) \otimes \nu(2d_{3/2}^{-2} 1h_{11/2}^{-2})$	9.96		
	1596	1649	+	13/2 ⁺	9/2 ⁺	2 ⁺	21.93	$\pi(1g_{7/2}^2 2d_{5/2}^1) \otimes \nu(2d_{3/2}^{-2} 1h_{11/2}^{-2})$	5.29		
					13/2 ⁺	0 ⁺	44.81	$\pi(1g_{7/2}^2 2d_{5/2}^1) \otimes \nu(2d_{3/2}^{-2} 1h_{11/2}^{-2})$	13.58		
	1646	1606	11/2 ⁻	11/2 ⁻	11/2 ⁻	0 ⁺	56.72	$\pi(1g_{7/2}^2 1h_{11/2}^1) \otimes \nu(3s_{1/2}^{-2} 1h_{11/2}^{-2})$	6.74	23(5)	-
								$\pi(1g_{7/2}^2 1h_{11/2}^1) \otimes \nu(2d_{3/2}^{-2} 1h_{11/2}^{-2})$	18.32		
					11/2 ⁻	2 ⁺	27.81	$\pi(1g_{7/2}^2 1h_{11/2}^1) \otimes \nu(2d_{3/2}^{-1} 3s_{1/2}^{-1} 1h_{11/2}^{-2})$	5.12		
								$\pi(1g_{7/2}^2 1h_{11/2}^1) \otimes \nu(2d_{3/2}^{-2} 1h_{11/2}^{-2})$	5.94		
	1797	1776	9/2 ⁻ , 11/2 ⁻ , 13/2 ⁻	15/2 ⁻	5/2 ⁺	5 ⁻	13.02	$\pi(1g_{7/2}^3) \otimes \nu(2d_{3/2}^{-2} 3s_{1/2}^{-1} 1h_{11/2}^{-1})$	4.68	8.4(7)ns	22ns
					5/2 ⁺	7 ⁻	10.02	$\pi(1g_{7/2}^3) \otimes \nu(2d_{3/2}^{-1} 3s_{1/2}^{-2} 1h_{11/2}^{-1})$	2.58		
					7/2 ⁺	5 ⁻	57.91	$\pi(1g_{7/2}^3) \otimes \nu(2d_{3/2}^{-2} 3s_{1/2}^{-1} 1h_{11/2}^{-1})$	21.25		
							$\pi(1g_{7/2}^3) \otimes \nu(2d_{3/2}^{-3} 1h_{11/2}^{-1})$	8.27			
	1899	1841	9/2 ⁻ , 11/2 ⁻ , 13/2 ⁻	13/2 ⁻	5/2 ⁺	5 ⁻	14.42	$\pi(1g_{7/2}^3) \otimes \nu(2d_{3/2}^{-2} 3s_{1/2}^{-1} 1h_{11/2}^{-1})$	5.88	34(6)	44
					7/2 ⁺	5 ⁻	42.33	$\pi(1g_{7/2}^3) \otimes \nu(2d_{3/2}^{-2} 3s_{1/2}^{-1} 1h_{11/2}^{-1})$	15.21		
								$\pi(1g_{7/2}^3) \otimes \nu(2d_{3/2}^{-3} 1h_{11/2}^{-1})$	6.17		
	1925	1916	11/2 ⁻	11/2 ⁻	5/2 ⁺	5 ⁻	17.28	$\pi(1g_{7/2}^3) \otimes \nu(2d_{3/2}^{-2} 3s_{1/2}^{-1} 1h_{11/2}^{-1})$	6.42		
					7/2 ⁺	5 ⁻	42.36	$\pi(1g_{7/2}^3) \otimes \nu(2d_{3/2}^{-2} 3s_{1/2}^{-1} 1h_{11/2}^{-1})$	15.07		
								$\pi(1g_{7/2}^3) \otimes \nu(2d_{3/2}^{-3} 1h_{11/2}^{-1})$	6.17		

7.5 Discussion

The level structures for the ¹³¹I and ¹³²Xe nuclei are discussed below based on the results of shell model calculations given above and comparison with systematics of the neighboring nuclei. The systematic comparison has been helpful in understanding the evolution of level structure in these nuclei as a func-

tion of neutron number. This has been done by comparing the level energies and the transition rates for individual levels. The reduced transition probabilities ($B(E\lambda)$) have been estimated, using the standard formulations [MOR76], from the measured level lifetimes and the known branching and mixing ratios [KHA06, KHA05].

7.5.1 ^{131}I

The level energies of ^{131}I up to 2.0 MeV could be well reproduced from present shell model calculation. However, in Table 7.2, only the low lying levels up to 1060 keV and a few higher lying levels those are relevant to the present measurements and discussions are shown. Both of the second and third excited levels in ^{131}I at 493 keV and 602 keV have experimental J^π assignment of $3/2^+$ or $5/2^+$ [KHA06]. The present calculation shows two such levels at 450 and 653 keV excitations which have J^π values of $5/2^+$ and $3/2^+$, respectively, and could be assigned accordingly. This is, however, in contrary to the earlier shell model work of Ref. [TER15] and the experimental level sequences in ^{127}I and ^{129}I , where the first $3/2^+$ level is below the second $5/2^+$. The 774 keV level has been known to have the J^π assignment of $9/2^+$ or $11/2^+$ [KHA06]. The present calculation predicts one $11/2^+$ level at 803 keV and accordingly the 774 keV level is suggested to have a $11/2^+$ assignment. Next four excited levels at 852, 876, 1006 and 1060 keV are also well reproduced in the present calculation. The 1006 keV level possibly has $7/2^+$ assignment as the 1040 keV ($7/2^+$) is the only level that was produced from the present calculation between the 896 ($1/2^+$) and 1169 ($9/2^+$) keV. The next two levels, shown in Table 7.2, at 1556 and 1596 keV are predicted at 1554 and 1649 keV from the present calculation. Our calculation could also reproduce all the negative parity levels up to 1925 keV ($11/2^-$) in ^{131}I . The J^π values of both the 1797 and 1899 keV levels were assigned to have ($9/2^-$, $11/2^-$, $13/2^-$) in NNDC [KHA06]. However, the angular correlation and nuclear orientation experiments [LHE75] suggested the spin-parity of $15/2^-$ and $13/2^-$, respectively, for the 1797 and 1899 keV levels. The said assignment of the 1797 keV level is also supported by the recent experimental observation from multi-nucleon transfer with ^{136}Xe [WAT09] and the M1 nature of the 102 keV transition connecting the 1899 keV and 1797 keV levels. In our present calculation, two negative parity levels of $15/2^-$ and $13/2^-$ are predicted at 1776 and 1841 keV, respectively, and are accordingly associated with the 1797 and 1899 keV levels. The recent experiment [WAT09] on ^{131}I also supports the spin assignments of the 1556 and 1596 keV levels as $15/2^+$ and $13/2^+$, respectively. The excitation energies for a few other levels observed in this multi-nucleon transfer experiment, viz., 1881 keV ($15/2^+$), 1885 keV ($17/2^-$) and 1918 keV ($19/2^-$)

are also reproduced from the present work at 1832, 2011 and 1956 keV, respectively, but are not listed in Table 7.2.

As mentioned in Section 7.4, a strong fragmentation of configuration was found for the excited levels in ^{131}I and $<1\%$ strength was found for 35 – 55% of the total partitions. Such strong fragmentation of configuration conjectures the collective nature for these levels in ^{131}I . Considering the major configurations, the structure of the positive parity levels in this nucleus was found to be dominated by $\pi g_{7/2}$, $\nu h_{11/2}$ and $\nu d_{3/2}$ orbitals. The $5/2^+$ levels in ^{131}I have mixed configurations involving both $\pi g_{7/2}$ and $\pi d_{5/2}$ orbitals. This is not in line with many of the earlier understanding regarding the pure $\pi d_{5/2}$ configuration of the first excited state in ^{131}I [MAC71, DEV65]. The negative parity levels in ^{131}I was found to be developed from multi-quasiparticle excitation involving both $\pi h_{11/2}^1$ particle and $\nu h_{11/2}^{-1}$ hole. From the present calculation, it was found that the lowest negative parity level at 1646 keV, $11/2^-$ has major contribution from the $\pi h_{11/2}^1$ particle in comparison to the other higher lying negative parity levels in ^{131}I , viz., 1797, 1899 and 1925 keV, where both protons and neutrons were found to be contributing in the major partitions.

Among the two positive parity levels in ^{131}I for which lifetime measurement has been done in the present work, the 774 keV, $11/2^+$ level decays mainly by a strong E2 transition to the $7/2^+$ ground state, indicating a collective nature for this level. The $B(E2)$ value for the decay of the lowest $11/2^+$ levels in ^{131}I and its neighboring nuclei up to the $N = 82$ shell closure is shown in Fig. 7.6. The $B(E2)$ value for $11/2_1^+ \rightarrow 7/2_1^+$ decay shows a decreasing trend as a function of neutron number supporting the loss of collectivity as one approaches the double shell closure of ^{132}Sn .

As discussed in Section 7.4, the E1 decays from the negative parity levels in ^{131}I could not be calculated in the chosen shell model valence space. The lifetime of the 1797 keV ($15/2^-$) level in ^{131}I was known from earlier works [DEV65] and is also measured in the present work (c.f. Table 7.1) as 8.4(7) ns. This level mainly decays by the 201 and 241 keV transitions, which are known to be of E1 nature from the conversion electron measurement [BEY67], and by considering these strong decays, no theoretical estimate of level lifetime was possible for this level. One 151 keV transition of very weak intensity is known from this level to the 1646 keV, $11/2^-$ level. Considering E2 multipolarity for this transition and by correcting for the branching ratios as available in NNDC [KHA06], the lifetime for this level comes out to be 21 ns from shell model calculation. The 1899 keV ($13/2_1^-$) level decays by two strong transitions, viz., 102 keV (M1) and 1126 keV (E1). The measured lifetime of this level comes out to be 34(6) ps (c.f. Table 7.1). The present calculation estimates a lifetime of 116 ps for the 1899 keV level by considering only the 102 keV M1 decay.

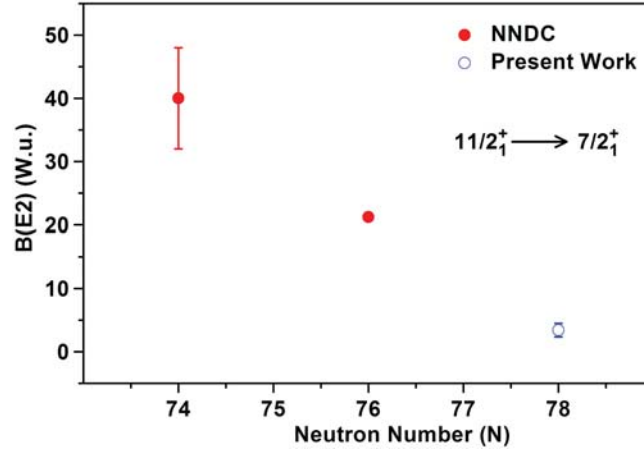


Figure 7.6: The $B(E2)$ values for the decay of 774 keV, $11/2^+$ level in ^{131}I in comparison to that in neighboring nuclei is shown. The filled circles (red) represent the values calculated from the level lifetimes taken from NNDC database [NNDC] and the open circle (blue) is for ^{131}I and is measured in the present work. The branching and mixing ratios are taken from NNDC database.

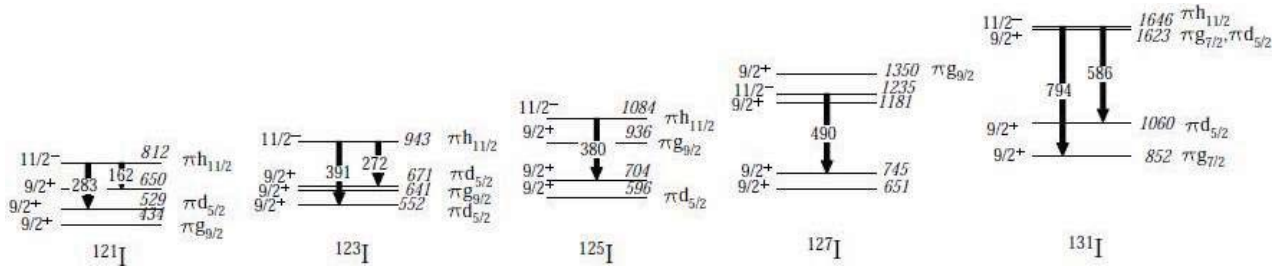


Figure 7.7: The systematics of E1 decays from the $11/2^-$ levels in the iodine nuclei around ^{132}Sn .

Considering this partial lifetime and the known branching of the 102 keV, the level lifetime of the 1899 keV level is estimated to be 44 ps which is close to the present measurement. The level lifetime of the 1646 keV, $11/2^-$ level was also measured for the first time in the present work (c.f. Table 7.1). However, no theoretical estimate could be made for this lifetime as the level is de-excited by two E1 transitions, viz., 586 and 794 keV, which carry the major share of decay out intensity and the nature of the other weak decays from this level are not available in literature. The E1 decays from these negative parity levels are discussed in comparison to the systematics observed in the neighboring nuclei.

The 1646 keV, $11/2^-$ level decays by the 794 keV E1 transition to the 852 keV, $9/2^+$ level. The presence of $\Delta J = 1$, $\Delta\pi = -1$ proton orbitals ($\pi h_{11/2}$, $\pi g_{9/2}$) are necessary in the configuration of the initial (1646 keV, $11/2^-$) and the final (852 keV, $9/2^+$) levels for this E1 decay to occur. However, the major configurations for the 852 keV level were found to involve $\pi g_{7/2}^3$ protons and to have the same neutron hole configuration

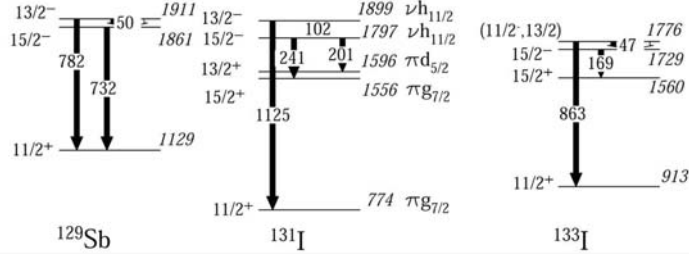


Figure 7.8: The systematics of E1 decays from the $13/2^-$ and $15/2^-$ levels in the I and Sb nuclei around ^{132}Sn .

as that of 1646 keV level. Also, the excitation energy of the 852 keV level was very well reproduced from the present calculation with such a configuration. Hence, the origin of E1 decay from the 1646 keV level could not be explained from the present shell model calculation. In order to understand this, the decays of such $11/2^-$ levels observed in the neighboring iodine nuclei have been studied and are shown in Fig. 7.7. It is found that, in all these nuclei, the E1 decays are observed from the $11/2^-$ ($\pi h_{11/2}^1$) level to the $9/2^+$ levels having configurations involving either $\pi d_{5/2}^1$ or $\pi g_{7/2}^1$. Also, no connection was found between these $11/2^-$ ($\pi h_{11/2}^1$) levels to the proposed $\pi g_{9/2}^{-1}$ levels, wherever known. In addition, the excitation energy of the lowest $\pi g_{9/2}^{-1}$ level, known in these nuclei, was found to increase as a function of neutron number; and at $N = 74$, it was observed at a higher excitation compared to the $11/2^-$ ($\pi h_{11/2}^1$) level. So, it may be conjectured that $\pi g_{9/2}^{-1}$ excitation in ^{131}I will be at higher excitation compared to the 1646 keV, $11/2^-$ level.

Both of the next two negative parity levels in ^{131}I , viz., 1797 keV ($15/2^-$) and 1899 keV ($13/2^-$), were found to have the involvement of $\nu h_{11/2}$ hole in the major configurations obtained from the present shell model calculation. As discussed above for 1646 keV level, the strong E1 decays from these levels, viz., (i) 1797 keV ($15/2^-$) \rightarrow 1556 keV ($15/2^+$), (ii) 1797 keV ($15/2^-$) \rightarrow 1596 keV ($13/2^+$) and (iii) 1899 keV ($13/2^-$) \rightarrow 773 keV ($11/2^+$), could be explained only if a $\nu g_{9/2}^{-1}$ configuration is involved in the configuration of the final levels, viz., 774, 1556 and 1596 keV. However, all these three levels could be well reproduced in the present calculation with the involvement of $\nu d_{3/2}^{-2} h_{11/2}^{-2}$ configurations and without any contribution from $\nu g_{9/2}$.

A systematic comparison of the $15/2^-$ and $13/2^-$ levels and their E1 decays neighboring to ^{131}I have also been shown in Fig. 7.8 where it is observed that these negative parity levels in ^{129}Sb and ^{133}I also show similar decays as observed in case of ^{131}I . However, neither the configurations of these levels in ^{129}Sb and ^{133}I are known nor the existence of any $\nu g_{9/2}^{-1}$ configuration is yet found in these nuclei. Such neutron core

excitation is, however, supposed to involve much higher excitation as predicted in ^{133}Cs [BIS16].

Table 7.3: The B(E1) and B(E3) transition strengths for the decay of negative parity levels in ^{131}I

E_i (keV)	J_i	E_f (keV)	J_f	E_γ (keV)	Multipole (λ)	Expt.	B(E λ) W.u.	
							$e^p = 3.0$	NushellX $e^p = 2.0$
1646	$11/2^-$	852	$9/2^+$	794	(E1)	$2.6(8) \times 10^{-5}$	11	5.5
		1060	$9/2^+$	586	(E1)	$1.0(3) \times 10^{-5}$		
		150	$5/2^+$	1496	(E3)	< 14		
1797	$15/2^-$	1556	$15/2^+$	241	E1	$1.6(2) \times 10^{-6}$		
		1596	$13/2^+$	201	E1	$2.8(3) \times 10^{-6}$		
1899	$13/2^-$	774	$11/2^+$	1126	(E1)	$4.3(1.0) \times 10^{-6}$		

Earlier, the possibility of an octupole excitation of the core, coupled to a single-quasiparticle state, was considered for the excitation of the 1797 keV level in ^{131}I (c.f. Ref. [BEY67]). In order to test such a conjecture, the B(E1) and B(E3) strengths obtained from the measured lifetimes are tabulated in Table 7.3 for the decay of the negative parity levels in ^{131}I . The B(E3) rate calculated from present shell model calculation are also shown in Table 7.3 for comparison.

The B(E1) rates from the 1646 keV ($11/2^-$) level to the 852 and 1060 keV ($9/2^+$) levels are found to be similar to that observed for the 3^- level in ^{114}Xe [ANG02] where octupole collectivity has been established. It is, however, observed that the B(E1) strengths from the 1797 and 1899 keV levels are not enhanced similar to the 1646 keV level. Moreover, by considering pure E3 nature for the 1496 keV γ -ray (1646 keV ($11/2^-$) \rightarrow 150 keV ($5/2^+$)), the limit for the corresponding B(E3) strength was estimated. This B(E3) strength was observed to be < 14 W.u. which is similar to that known for ^{132}Sn [FOG94], $^{124-134}\text{Xe}$ [MUE06], $^{132-138}\text{Ba}$ [BUR85] and in other nuclei [SPE89] in this mass region where octupole correlation has been observed. The octupole correlation around $Z = 56$ [BUC16] is expected from the interaction of the two $\Delta J = 3$ orbitals, viz., $d_{5/2}$ and $h_{11/2}$, in 50 - 82 subshell space. The experimental B(E3) value for the 1646 keV level was also reasonably reproduced from the present shell model calculation as evident from Table 7.3. It comes out to be 5.5 W.u. and 11.0 W.u., by considering effective proton charge (e^p) as 2.0 (c.f. Ref. [OMT95, SAR01]) and 3.0, respectively. Most importantly, it was found that the B(E3) value for this level, which was dominated by $\pi h_{11/2}$ configuration, is almost independent on the value of effective neutron charge (e^n). On the contrary, the calculated B(E3) value for the second $11/2^-$ level at 1925 keV, where both proton and neutron configurations have non-negligible role, is dependent on both e^p and e^n . Although this B(E3) value comes out to be very less and no γ -decay of $\Delta J = 3$ in nature is known from this 1925 keV

level, nonetheless, the present calculation and comparison clearly indicates the difference in contribution of proton and neutron in the structure of the first two $11/2^-$ levels in ^{131}I .

Among the $11/2^-$ levels in the neighboring iodine nuclei shown in Fig. 7.7, the level lifetimes or their limits are known in case of ^{121}I , ^{123}I and ^{125}I . Although pure E1 is known only for ^{123}I , the $B(E1)$ strengths known for the $11/2^- \rightarrow 9/2^+$ decays for all these cases are $1.65(21) \times 10^{-5}$ W.u. (^{121}I), $6(3) \times 10^{-5}$ W.u., $3.3(17) \times 10^{-6}$ W.u. (^{123}I) and $> 2.3 \times 10^{-5}$ W.u. (^{125}I), respectively [NNDC]. No E3 decay is known for these levels and it was not possible to compare $B(E3)$ strengths for the $11/2^-$ levels in the lighter iodine nuclei to that obtained for ^{131}I .

7.5.2 ^{132}Xe

The even-even Xe isotopes are known to have a transitional behaviour from γ -soft to vibrational, as one moves towards the $N = 82$ shell closure [NOM17, PUD80]. The $E_{4_1^+}/E_{2_1^+}$ ratio for ^{132}Xe comes out to be 2.16 which indicates a vibrational structure for this nucleus. From our present shell model calculation also, this ratio comes out to be 2.06 which is in good agreement with the experimental one. Very well agreement of experimental data and present calculation was also found for all other yrast levels in this nucleus. This indicates that the present calculation could nicely reproduce the structure of the collective low lying levels in ^{132}Xe . The approach towards vibrational nature for the Xe nuclei are also indicated in the very recent work by L. Kaya et.al. [KAY18] where shell model calculations with $sn100pn$ interaction was also performed. The present calculation was found to reproduce those results obtained for ^{132}Xe in full valence space by Kaya et al. However, in the present shell model calculation, the 3_1^+ level is predicted at a higher excitation compared to 4_2^+ , also the 2_3^+ level is predicted at a lower excitation compared to both the 4_2^+ and 3_1^+ levels. The earlier shell model calculation with $sn100pn$ interaction made similar predictions on the 3_1^+ level [VOG17] and none of the previous calculations [VOG17, TER15] showed the excitation energy of the 2_3^+ level which is, however, identified as a mixed symmetry state in Ref. [COQ10]. The level at 1850 keV is shown as 0^+ and 2^+ in NNDC [KHA05]. However, our calculation predicts a 0^+ level at 1697 keV, indicating that the level at 1850 keV might be a 0^+ .

The collective nature of the low lying levels in ^{132}Xe is also indicated from the strong configuration mixing observed for these levels as discussed in Section 7.4. In fact, almost $\sim 45\%$ of the partitions have strength $< 1\%$ for the 0^+ levels and this increases to almost 70% for other levels (2^+ , 3^+ and 4^+) in ^{132}Xe .

Fig. 7.9 shows the reduced E2 transition probabilities for the decay of few low lying levels in Xe nuclei

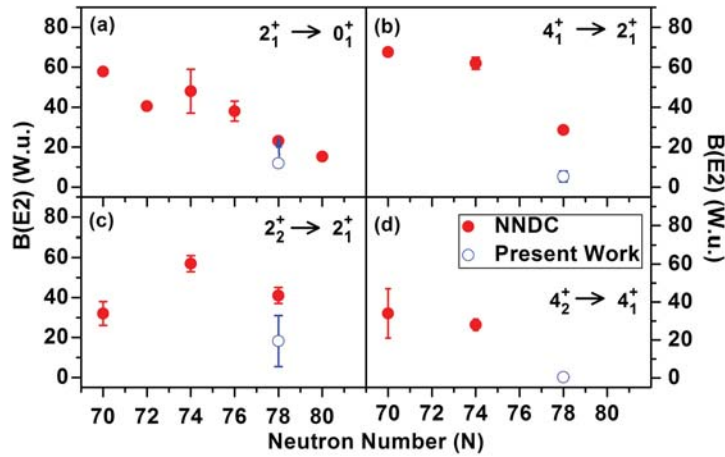


Figure 7.9: The $B(E2)$ values for the decays of ^{132}Xe levels in comparison to that in neighboring nuclei. The filled circles represent the values calculated from the level lifetimes taken from NNDC database [NNDC]. The open circles are for ^{132}Xe and are measured in the present work. The branching and mixing ratios are taken from NNDC database.

as a function of neutron number up to the shell closure at $N = 82$. The lifetime data obtained in the present work add the points at $N = 78$ for the 2_1^+ , 4_1^+ , 2_2^+ and 4_2^+ levels. The absolute $B(E2)$ values for these levels supports their collective nature and the decrease in $B(E2)$ values for all these low lying levels conjectures the validity of double shell closure at ^{132}Sn .

Chapter 8

Measurement of EQM in neutron-rich

$^{131,132}\text{I}$

8.1 Introduction

The measurement of EQM is important to estimate the deviation of the nuclear charge distribution from sphericity [DAF85, HIN91]. It is also a sensitive probe to indicate the evolution of shell structure. Thus, such measurements in neutron-rich nuclei below doubly closed ^{132}Sn are of substantial importance to probe the prevalence of expected spherical character as one approaches the $N = 82$ shell closure in this exotic domain [ALL11, BLA05, SIF06]. However, the availability of experimental data on EQM in this mass region are inadequate. Apart from a few, most of the existing results are from measurements done during early 60s to late 80s [STO16]. So, it is important to perform more measurements on EQM to enrich the understanding of the evolution of shell structure around ^{132}Sn .

In case of iodine nuclei, the systematic change of measured EQM for the $5/2_1^+$ and $7/2_1^+$ levels were studied in 1964 [HAF64]. It was found by the authors of Ref. [HAF64] that a linear extrapolation of the measured values to the closed neutron shell at $N = 82$ predicted a value of $Q = 0.11$ b for the $7/2_1^+$ state. However, the extrapolated value of EQM for $5/2_1^+$ state, obtained in a similar manner, is much larger. In contrast to the data, both the theoretical calculations performed at that time, (i) by Kisslinger and Sorensen [KIS63] and (ii) the single-particle estimates and the configuration mixing calculations by Horie and Arima [HOR55], predicted a larger absolute value of EQM for $7/2_1^+$ level compared to that for $5/2_1^+$ level in $N = 82$ iodine nucleus.

It is worth mentioning that in Ref. [HAF64], specifically for the $5/2_1^+$ level, the linear extrapolation was based on only three data points which are again significantly away from shell closure of $N = 82$. So, systematic experimental determination of quadrupole moments up to $N = 82$ iodine is of importance to understand the evolution of nuclear deformation of the $5/2_1^+$ and $7/2_1^+$ levels. Subsequent to the work of Ref. [HAF64], very few measurements of EQMs of iodine nuclei have been performed [ROB72, HAA73, OOM79, GRO87]. Till date, no experimental measurement exists on the EQM of $5/2_1^+$ levels in odd-A iodine with $N > 76$.

In the present work, the quadrupole moment for the $5/2_1^+$ level of $N = 78$ ^{131}I has been measured with latest generation $\text{LaBr}_3(\text{Ce})$ scintillator detectors using TDPAC spectroscopy [FRA65]. The TDPAC measurement was performed with iodine as PAC probe doped in metallic tellurium matrix. The active iodine isotopes were produced from the β -decay of respective tellurium parent isotopes. The neutron-rich tellurium isotopes were produced by the α -induced fission of ^{nat}U followed by their radiochemical separation from the rest of the fission products. The tellurium isotopes were doped into the tellurium metal during the radiochemical separation process to provide the necessary EFG to interact with the EQM of the nuclear states. The quadrupole moment of 3_1^+ level of ^{132}I produced from decay of ^{132}Te , which had sufficient activity in the prepared sample, was also measured. This is, however, was measured earlier [OOM79, IAEA] by IPAC technique that usually introduces larger uncertainties compared to the TDPAC method. So, the present work provides the first experimental result on the quadrupole moment of the $5/2_1^+$ level in odd-A iodine above $N = 76$ and that of the 3_1^+ level of ^{132}I using a different technique.

8.2 Methods and materials

The determination of EQM of an excited nuclear state relies on the direct or indirect measurement of its interaction with an EFG. The EFG produced at the site of the nucleus due to the presence of surrounding charges in an atomic or molecular environment could be sufficient to yield a measurable effect by interacting with the nuclear charge distribution. In case of a solid, an EFG $\sim 10^{21}$ V/m² can be obtained from the periodically arranged atomic or molecular charges present around the nucleus. The interaction between the EQM of an excited state of the nucleus and the EFG can be measured by a hyperfine technique, viz., TDPAC Spectroscopy [FRA65]. In a TDPAC experiment, the time differential perturbation in the $\gamma - \gamma$ angular correlation, arising due to such kind of electric quadrupole interaction, is measured to determine

the EQM of the nuclear excited state. More details of this technique have already been given in Chapter 5 of this thesis.

The following two subsections describe the production of neutron-rich iodine isotopes and the TDPAC measurement performed in the present work.

8.2.1 Production of $^{131,132}\text{I}$ and sample preparation

The excited states of $^{131,132}\text{I}$ have been populated from the β^- decay of ^{131m}Te ($t_{1/2} \sim 33$ h) and ^{132}Te ($t_{1/2} \sim 3$ d), respectively. The parent nuclei were produced via $^{nat}\text{U}(^4\text{He}, f)$ reaction followed by radiochemical separation. Stacks of ~ 1 mg/cm² thick ^{nat}U targets, prepared by electro-deposition on 25 μm thick aluminium backing foil, was irradiated with 40 MeV α -beam for 36 h at K = 130 AVF cyclotron of VECC, Kolkata. Each stack was prepared with four / five uranium targets separated by 25 μm thick aluminium catcher foils. The recoiling fission products were collected on the catcher foils which were subsequently used for the radiochemical separation and doping into tellurium metal matrix as discussed in Chapter 6. In order to separate the tellurium isotopes from rest of the fission products, the catcher foils were dissolved in concentrated nitric acid followed by the addition of inactive tellurium carrier. The radioactive tellurium along with the tellurium carrier were reduced to metallic Te(0) by chemical method. The metallic tellurium was then annealed at 573 K for 3 h in argon atmosphere. The crystalline phase of the metallic tellurium powder, prepared in this way, was of near spherical shape with ~ 5 mm diameter and was characterized by powder X-ray Diffraction (XRD) measurement. All the peaks, as shown in Fig. 8.1, obtained in XRD analysis could be assigned to the trigonal crystal structure of tellurium metal powder.

8.2.2 Experimental details

In the present experiment, performed at room temperature, the separated tellurium fission fragment activity doped in tellurium metal was counted using BGO suppressed Clover HPGe detectors prior to the TDPAC measurement in order to identify the γ lines of interest and their coincidence relationships with other observed γ -rays. The TDPAC spectrometer consisted of three 1" $\phi \times 1$ " thick cylindrical LaBr₃(Ce) crystals coupled to XP2020URQ photomultiplier tubes and kept in a planar geometry. One of the detectors was used as the 'START' detector and the other two as 'STOP-90' and 'STOP-180' detectors based on their angular position of 90° and 180°, respectively, with respect to the 'START' detector. The tellurium powder sample was kept at a distance of 5 cm from the detectors for counting. The distance was chosen in such a

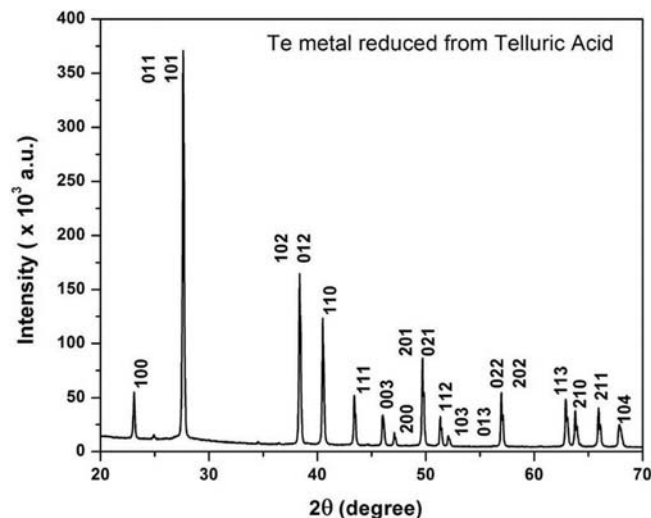


Figure 8.1: XRD analysis performed after reduction of telluric acid to Te metal followed by annealing. The peaks are marked with the (h, k, l) values corresponding to the crystalline trigonal phase of Te metal with space-group $P3_121$.

way that the geometrical correction due to cylindrical detectors is minimum and coincidence count rate is maximum with the available source strength [BUT89]. The typical activity was 10 - 20 μCi depending on the number of uranium targets used in the stack and the beam current provided for irradiation. The data were collected in LIST mode with the help of standard NIM and CAMAC electronics. The energy spectra from the $\text{LaBr}_3(\text{Ce})$ detectors are displayed with a range of 600 keV and the time spectra corresponding to two STOP detectors are displayed in a total range of 500 ns, both in 8K channels. The typical energy resolution of the detectors used in the setup is $\sim 3\%$ at 662 keV γ energy. The Full Width at Half Maxima (FWHM) of the prompt coincidence time peak obtained with the TDPAC setup at the relevant energies are discussed in Subsection 8.3.2. The statistics was gathered by repeating the irradiation, sample preparation and TDPAC counting several times in sequence.

8.3 Experimental results

The simplified decay schemes of the two nuclei, viz., ^{132}I and ^{131}I [KHA05, KHA06], as obtained from the decay of respective tellurium parents are shown in Figs. 8.2 and 8.3. In these figures, the cascade relevant to the TDPAC analysis is shown in red, the γ -rays (< 600 keV) expected in the energy spectrum are shown in blue and the higher energy γ -rays are shown in black. The determination of EQM in the neutron-rich

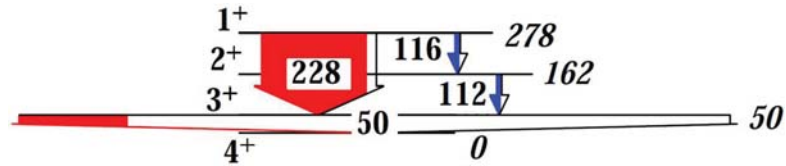


Figure 8.2: The simplified decay scheme for ^{132}I , as populated from the decay of ^{132g}Te . The γ -rays of interest in the measurement of EQM are shown in red. The two other γ -rays are shown in blue. The conversion coefficients have been used while showing the intensities of the γ lines (proportional to the width of the transitions) and the converted intensity is indicated with the white portion in the width of the transition. The data has been taken from ENSDF [KHA05].

$^{131,132}\text{I}$ involved several steps which are described in the following subsections.

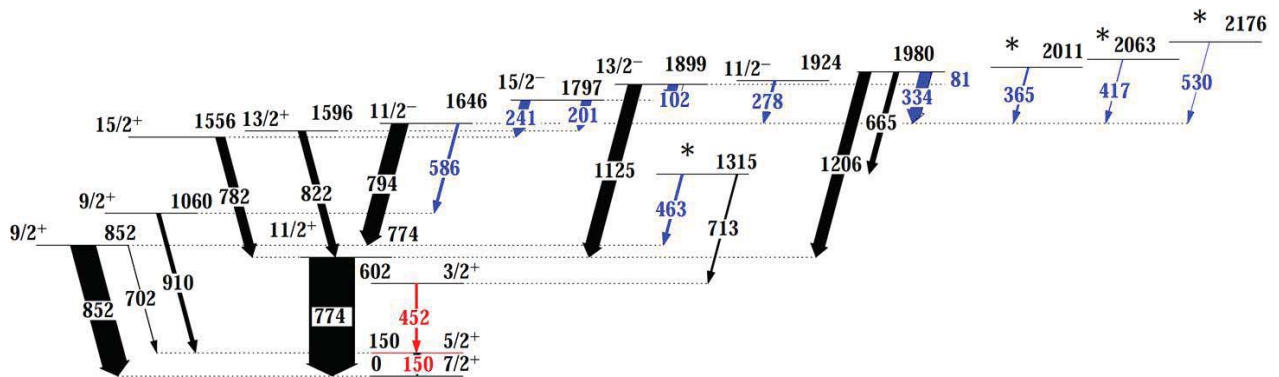


Figure 8.3: The simplified decay scheme for ^{131}I , as populated from the decay of ^{131m}Te and relevant in the present measurement. The γ -rays of interest in the measurement of EQM are shown in red. The γ -rays with energy below 600 keV are shown in blue and the higher energy γ -rays are shown in black. The conversion coefficients have been used while showing the intensities of the γ lines (proportional to the width of the transitions) and the converted intensity, if any, is indicated with the white portion in the width of the transition. The data has been taken from ENSDF [KHA06]. The J^π of the levels are adopted from Ref. [ALA19]. The levels marked with * have uncertain J^π which are not shown.

8.3.1 Determination of EFG

In the present case, the EFG at the iodine site in tellurium matrix has been obtained from the experimental data available in literature. The EFG for this system can be estimated using the known quadrupole frequencies [VIA83, LAN74] and quadrupole moments [PYY18] for the $7/2_1^+$ states of ^{129}I and ^{127}I that are shown in Row 1-3 of Table 8.1. In addition, the EFG value for iodine site in tellurium matrix has also been taken from Ref. [OOM79] that was obtained from the data of $7/2_1^+$ state of ^{129}I considering $Q = -0.553(10)$ eb (Row 4 of Table 8.1). Further, this value of EFG ($3.38(4) \times 10^{18}$ V/cm²) has been scaled with the latest

quadrupole moment for this level reported in Ref. [PYY18]. The scaled EFG comes out to be $3.87(12) \times 10^{18}$ V/cm² (Row 5 of Table 8.1).

Table 8.1: The EFG values obtained for iodine in tellurium(Te) with known values of quadrupole frequencies and quadrupole moments (Row 1-3). (a) The EFG value is quoted as given in Ref. [OOM79]. (b) Represents the V_{zz} obtained with scaling the EFG of Row 4 with the latest value of quadrupole moment [PYY18]. See text for details.

Nucleus and Host	Nuclear spin (J^π)	ν_Q (MHz)	T(K)	Q(eb) [PYY18]	V_{zz} (V/cm ²)
¹²⁷ I in Te	$7/2_1^+$	693(200) [VIA83]	293	-0.617(2)	$4.65(134) \times 10^{18}$
¹²⁹ I in Te	$7/2_1^+$	396(3) [VIA83]	4.2	-0.483(10)	$3.39(7) \times 10^{18}$
¹²⁹ I in Te	$7/2_1^+$	406(6) [LAN74]	80	-0.483(10)	$3.48(9) \times 10^{18}$
¹²⁹ I in Te	$7/2_1^+$	406(6) [LAN74]	300	-0.553(10)	$3.38(4) \times 10^{18(a)}$
¹²⁹ I in Te	$7/2_1^+$	406(6) [LAN74]	300	-0.483(10)	$3.87(12) \times 10^{18(b)}$

From the values shown in Table 8.1, it is observed that there is no considerable change in the EFG value as a function of temperature. Out of the obtained values, the value shown in Row 1 suffers from a large ($\sim 30\%$) error and was not considered for subsequent extraction of quadrupole moments in the present work. The value shown in Row 5 is also not considered as this goes against the expected trend of EFG as a function of temperature. The values shown at Row 2 and 3 are found to be similar within their errors. Subsequently, the EFG value of Row 2 ($3.39(7) \times 10^{18}$ V/cm²), consequent to its lower error value, was used for the determination of quadrupole moments for ^{131,132}I.

8.3.2 Determination of EQM using TDPAC method

The γ energy spectra obtained with the tellurium metal sample doped with active ^{131,132}Te, using Clover HPGe and LaBr₃(Ce) detectors, are shown in Fig. 8.4. The comparison of these two spectra has helped in identifying the required γ transitions and cascades for subsequent analysis. The relevant cascades connecting the levels of interest and other expected γ -rays are visible in this spectrum which corroborate with the simplified decay schemes displayed in Figs. 8.2 and 8.3. The difference in the Clover and LaBr₃(Ce) spectra may be attributed to the difference in coincidence time window used for generation of the spectra, the difference in attenuation in the entrance windows of the detectors and the applied CFD thresholds. The quadrupole moment measurements were performed for the 50 keV, 3_1^+ level of ¹³²I ($t_{1/2} = 1.120(15)$ ns [TAN09]) and

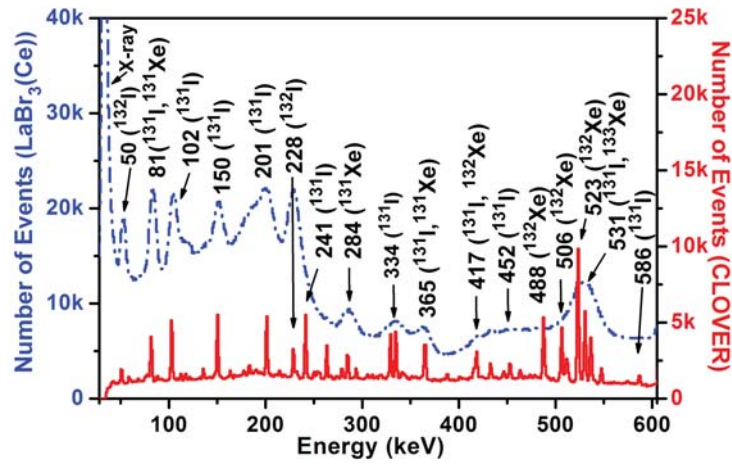


Figure 8.4: The representative total projection obtained with the BGO suppressed Clover HPGe and the $\text{LaBr}_3(\text{Ce})$ detectors are plotted. The comparison clearly identified the photopeaks required for the subsequent TDPAC analysis and other γ peaks that are generated from the decay of radiochemically separated tellurium activity.

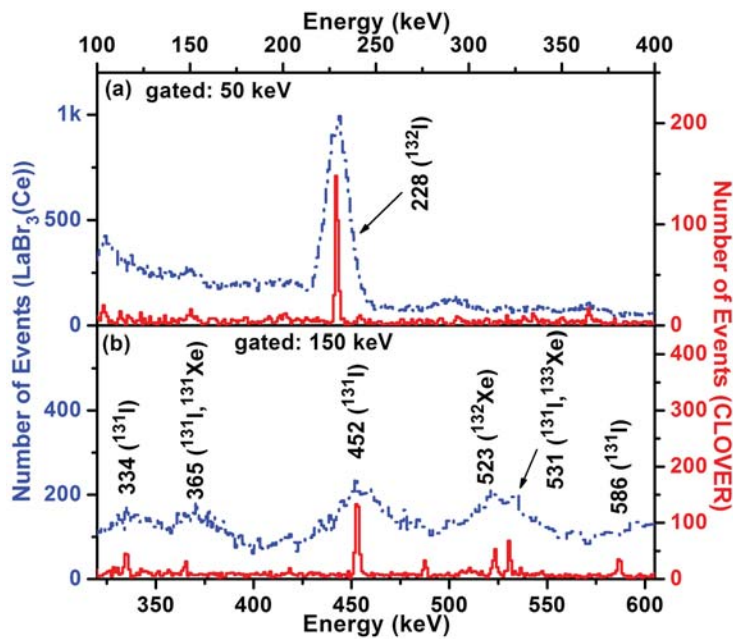


Figure 8.5: The representative gated projections are shown for (a) 50 keV and (b) 150 keV, obtained from the data taken with Clover HPGe and the $\text{LaBr}_3(\text{Ce})$ detectors, respectively, corresponding to the 228-50 keV and 452-150 keV cascades of ^{132}I and ^{131}I , respectively. These projections were used for the generation of coincidence time spectra with $\gamma - \gamma$ energy ('START-STOP') gating in two $\text{LaBr}_3(\text{Ce})$ detectors. The close lying contamination peaks from the daughter products, that might arise from the coincidence with underlying Compton background, are also marked.

150 keV, $5/2_1^+$ level of ^{131}I ($t_{1/2} = 0.95(5)$ ns [KHA06]), respectively, using TDPAC technique. The energy projections from $\text{LaBr}_3(\text{Ce})$ - $\text{LaBr}_3(\text{Ce})$ coincidences, corresponding to the two cascades of interest, are shown in Fig. 8.5 and compared with that obtained from Clover-Clover coincidences.

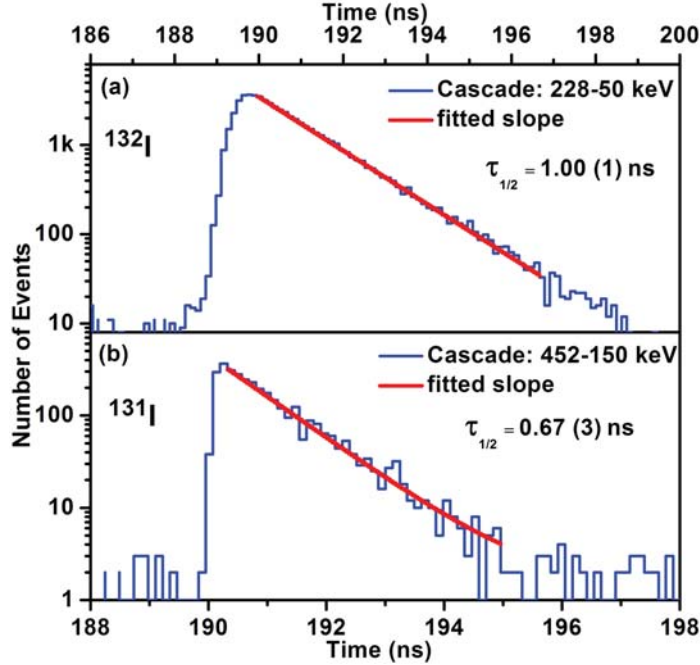


Figure 8.6: The representative background subtracted time projections are shown for (a) 228-50 keV and (b) 452-150 keV, respectively, obtained from the data taken with the TDPAC setup. The time values in the x-axis is the time difference measured with the TAC module having a total range of 500 ns. The feeding transitions were selected from the ‘START’ detector and the decaying transition from the ‘STOP’ detectors of the setup.

The time spectra were generated from double coincidence data in two LaBr_3 (‘START’ and ‘STOP’) detectors by selection of narrow energy gates corresponding to the 228-50 keV and 452-150 keV cascades, respectively. The feeding transition was selected with the ‘START’ and the decaying transition was selected with the ‘STOP’ detector while generating the time spectra. The chance coincidences present in the time spectra, if any, was found by gating on the Compton background just near the photopeak and subtracted appropriately. A set of representative time spectra for the two relevant cascades of ^{132}I and ^{131}I are shown in Fig. 8.6 along with the measured half-lives that were obtained by fitting the observed slope. The correctness of the time spectra was ensured by comparing the measured half-lives with the known values available in literature. In the present work, the half-lives for the 3_1^+ level of ^{132}I and the $5/2_1^+$ level of ^{131}I come out to be 1.005(6) ns and 0.76(10) ns, respectively. During analysis, the FWHM of the prompt coincidence

peak at relevant energies were also obtained from the prompt time curves generated using ^{106}Ru source and selecting the energies from the Compton profile of the spectra from ‘START’ and ‘STOP’ detectors. These values were found to be 567(6) ps and 386(8) ps, for the 228-50 keV cascade of ^{132}I and 452-150 keV cascade of ^{131}I , respectively. The time spectra generated with the complete data set was used for the subsequent TDPAC analysis.

The TDPAC spectra ($A_2G_2(t)$ vs Time), obtained for the 50 keV level of ^{132}I and 150 keV level of ^{131}I , have been shown in Fig. 8.7 using the 228-50 keV and 452-150 keV cascades, respectively, along with their corresponding Fourier transforms (FT). The fitting of the experimental data points was performed for a time interval of 7 ns. A Kaiser-Bessel window function [BUT15] was used to generate the Fourier transform. This window function was used to reduce the side lobes around the central peak. The fitted parameters were obtained based on the condition to obtain a minimum χ^2 value for least square fitting.

The unperturbed angular correlation coefficient (A_2) for the 228-50 keV cascade of ^{132}I comes out to be -0.05(1) in the present work and it is in reasonable agreement with the earlier measured value of -0.042(10) (see Section 5.4 of Chapter 5). For the 452-150 keV cascade of ^{131}I , the experimental value of +0.08(2) is slightly higher than the previously observed value of +0.058(8) [TAN67]. The deviation from the theoretical unperturbed angular correlation coefficients, viz., -0.0714 for 1-E2-3-M1-4 cascade of ^{132}I and 0.05 for 3/2-M1-5/2-M1-7/2 cascade of ^{131}I , could be elucidated considering a very small mixing of higher multipoles in the associated γ transitions. In the present case, it was found that an E2 mixing of $\sim 0.09\%$ in the 50 keV transition ($\delta_m = -0.03$) and a pure E2 nature of 228 keV transition explains the observed anisotropy. The result is in good agreement with the previous prediction as discussed in Subsection 5.4 of Chapter 5. In case of ^{131}I , both the 150 keV and 452 keV transitions are known as mixed as per the conversion electron measurement [BEY67]. In this measurement, the 150 keV transition was shown to have a multipole mixing of M1 (90%) + E2 (10%) and the 452 keV as mixed M1 + E2 transition. It is found that a mixing of $\sim 1.4\%$ of E2 in 452 keV ($\delta_m = +0.12$), in addition to the 10% E2 mixing ($\delta_m = +0.33$) in 150 keV, explains the observed anisotropy for this cascade.

During the data analysis, the asymmetry parameter η was kept as 0.73(2) [LAN74] for both ^{131}I and ^{132}I , following the good precision obtained in the Mössbauer spectroscopy data with iodine nucleus in tellurium matrix. In the analysis, the ω_Q is found from the combination of all the transition frequencies among the different hyperfine states. Hence, the difference in ω_Q values for ^{131}I ($J = 5/2$) and ^{132}I ($J = 3$) is due to the spin of the intermediate state as well as the non-zero η value. The uncertainty in the frequency determination

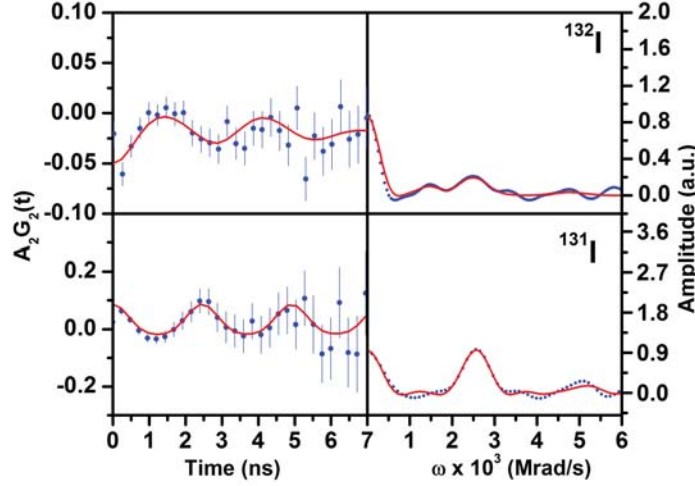


Figure 8.7: TDPAC spectra (left) and their Fourier transforms (right) for the 50 keV, 3_1^+ level of ^{132}I and 150 keV, $5/2_1^+$ level of ^{131}I , respectively. The blue circles correspond to the experimental data and the red solid lines represent the fitting.

has been obtained while least-square fitting of the experimental data with theoretical function (Eq. 5.22) through χ^2 optimization that has to take into account the correlations among different parameters including the inhomogeneity parameter δ . The inhomogeneity parameter δ was varied and finally fixed at 10% that was found to give the best χ^2 value and lowest error for the quadrupole frequency. The values of quadrupole coupling constant (ν_Q) were derived from ω_Q values obtained from the fitting and are tabulated in Table 8.2 along with the other relevant parameters like excitation energy (E_x), spin-parity (J^π), level half-life ($t_{1/2}$) and the EFG (V_{zz}).

Table 8.2: The values for V_{zz} , ω_Q and Q-mom, obtained in the present work for the first excited levels of $^{131,132}\text{I}$. The sign of the EQM could not be determined in the present experiment and only magnitudes are shown.

Nucl.	E_x (keV)	J^π	Cascade (keV)	$t_{1/2}$ (ns)	V_{zz} (V/cm ²)	ν_Q (MHz)	Q-mom. (EQM) (eb)		
							Pres. work	Ref. [OOM79]	Ref. [STO16, IAEA]
^{132}I	50	3_1^+	228-50	1.005(6)	$3.39(7) \times 10^{18}$	204(16)	(-)0.25(2)	(-)0.23(7)	(-)0.20(6)
^{131}I	150	$5/2_1^+$	452-150	0.76(10)	$3.39(7) \times 10^{18}$	247(6)	(-)0.30(1)	-	-

Taking the values of V_{zz} (EFGs) as $3.39(7) \times 10^{18}$ V/cm² (as shown in Row 2 of Table 8.1), the quadrupole moment of 50 keV state of ^{132}I ($J^\pi = 3_1^+$) and that of 150 keV state of ^{131}I ($J^\pi = 5/2_1^+$) are

extracted and shown in Table 8.2. The quadrupole moment of the 3_1^+ level of ^{132}I was found to be $(-)0.25(2)$ eb which is in close agreement with the earlier works [STO16, OOM79, IAEA]. The extracted quadrupole moment for the $5/2_1^+$ level in ^{131}I comes out to be $(-)0.30(1)$ eb that gives the first experimental data for this level. The errors quoted for the EQM are calculated from the error in quadrupole frequency and the error in the experimental EFG values. As the TDPAC method is not capable of determining the sign of the quadrupole moment, negative sign has been adopted following the systematics and the same have been quoted in Table 8.2 as well as in all the subsequent discussions.

8.4 Discussion

The EQMs of the 150 keV, $5/2_1^+$ level of ^{131}I and 50 keV, 3_1^+ level of ^{132}I , measured in the present work, have been compared with the data in the neighboring nuclei and are used to study the evolution of collectivity in the odd-Z, odd-A nuclei around ^{132}Sn . In addition, the LBSM calculations have been performed to interpret the present experimental data. The evolution of collectivity and the shell model interpretations are discussed in the following two subsections.

8.4.1 Evolution of collectivity

In order to understand the evolution of collectivity from the measured quadrupole moments of the first $5/2^+$ and the $7/2^+$ levels of iodine nuclei up to $N = 82$, the known quadrupole moments for these levels, including the one measured in the present work, are plotted as a function of neutron number (N) in Fig. 8.8. In this plot, the maximum and minimum values of quadrupole moments, known for a particular level, have been taken from the IAEA compilation [IAEA] along with the adopted values from Ref. [STO16]. This shows that, although the quadrupole moments of the $7/2_1^+$ levels in odd-A iodine nuclei show a linear dependence on neutron number from $N = 74 - 80$ (dotted black line of Fig. 8.8 (a)), the quadrupole moments of the $5/2_1^+$ levels depict a different scenario. Grossly, the quadrupole moments of the $5/2_1^+$ levels of odd-A iodine nuclei display not so linear dependence on the neutron number. However, it might be noticed that two different linear extrapolations are quite possible with different sets of data available for this level.

The adopted values for the $5/2_1^+$ levels from $N = 72$ to 76 follow a particular linear dependence on neutron number (dashed red line in Fig. 8.8 (b)) that was considered in Ref. [HAF64]. The corresponding linear extrapolation up to $N = 82$ predicted a higher value of quadrupole moment for the $5/2_1^+$ level than

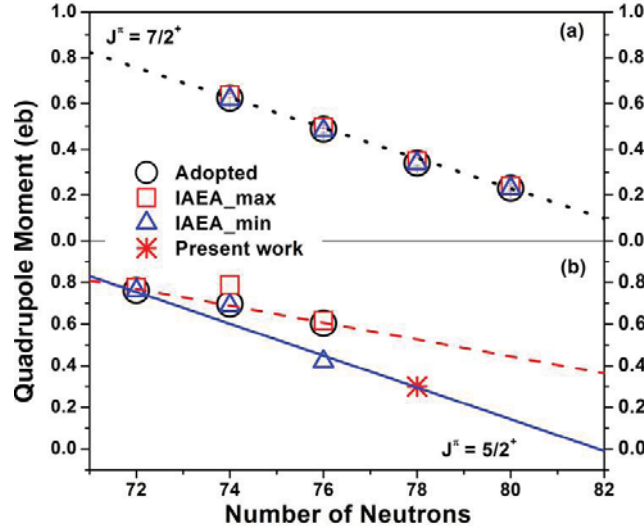


Figure 8.8: Experimental quadrupole moments (magnitude) for the (a) $7/2_1^+$ and (b) $5/2_1^+$ levels of odd-A I are shown as a function of neutron number. The adopted values of quadrupole moments have been taken from Ref. [STO16], the maximum and minimum values, known for a particular isotope, have been taken from the IAEA compilation [IAEA]. Errors have been considered but not visible in some cases as the corresponding error bars are smaller than the size of the symbol used. The value at $N = 78$ for the $5/2_1^+$ level of ^{131}I is measured in the present work and is shown. Linear extrapolations up to $N = 82$ are shown for $7/2^+$ level (black dotted line) and $5/2^+$ level (red dashed and blue solid lines) with different data sets. See text for details.

that for the $7/2_1^+$ level (~ 0.1 eb). However, a different slope for the linear extrapolation is obtained considering the adopted value at $N = 72$, the lowest value at $N = 76$ and the value at $N = 78$ that is measured in the present work (solid blue line in Fig. 8.8 (b)). This latter extrapolation also provides a lower value of quadrupole moment at $N = 82$ for the $5/2_1^+$ level compared to that for the $7/2_1^+$ level. The single particle estimates [HOR55] for $N = 82$ iodine comes out to be -0.217 eb for $7/2_1^+$ level and -0.185 eb for the $5/2_1^+$ level. For the calculation, the configurations of $\pi g_{7/2}^1$ ($J = 7/2$) and $\pi d_{5/2}^1$ ($J = 5/2$), respectively, have been considered for the $7/2_1^+$ and $5/2_1^+$ levels.

In order to understand the global scenario on the evolution of deformation for the first $5/2^+$ levels in the odd-Z, odd-A nuclei around ^{132}Sn , the deformation parameter (β_2) has been extracted from the measured quadrupole moments (Q_s) using Eqs. (8.1) and (8.2) given below.

$$Q_0 = Q_s \frac{(2J+3)(J+1)}{3K^2 - J(J+1)} \quad (8.1)$$

$$\beta_2 = \frac{\sqrt{5\pi}}{3ZR^2} Q_0 \quad (8.2)$$

where Q_0 is the intrinsic quadrupole moment, K is the component of spin (J) along the intrinsic symmetry axis, $R = R_0 A^{1/3}$ and $R_0 = 1.2$ fm. Considering strong coupling limit, $K = J$ was considered in the present calculation by following Ref. [BUJ07].

In Fig. 8.9, the deformation parameters β_2 have been plotted as a function of N , for few odd- Z and odd- A nuclei around ^{132}Sn . It is observed that the deformation decreases monotonically as one approaches $N = 82$, establishing the spherical character at shell closure. The deformation for $5/2_1^+$ level of ^{131}I , measured in the present work, also fits closely with the systematics.

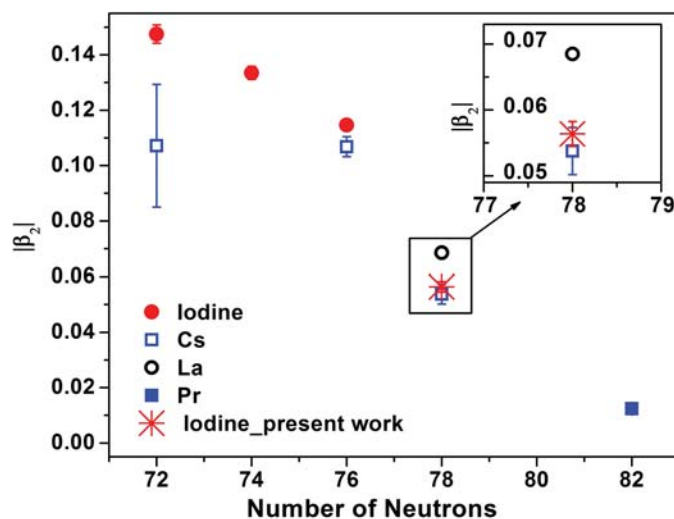


Figure 8.9: Deformation (magnitude), as deduced from the experimental quadrupole moments, are plotted with neutron numbers. The experimental quadrupole moments for the $5/2_1^+$ levels of odd- A iodine (I), Cesium (Cs), Lanthanum (La) and Praseodymium (Pr) nuclei have been taken from Ref. [STO16], except that of ^{131}I that is measured in the present work. Errors have been considered but not visible in some cases as the corresponding error bars are smaller than the size of the symbol used. The error is not shown in case of La as it is very high (100%).

8.4.2 Shell model calculation

The LBSM calculations were already performed and discussed in Section 7.4 of Chapter 7 for ^{131}I nucleus using the code NUSHELLX that considered ^{100}Sn as core. In the present work, the calculation was extended for the estimation of quadrupole moment of $5/2_1^+$ level in ^{131}I using the standard effective charges ($e^p = 1.35$, $e^n = 0.35$), as was also used for the estimation of transition probabilities in Ref. [ALA19].

The calculation estimates a value of -0.34 eb for the $5/2_1^+$ level of ^{131}I that explains quite well the EQM measured in the present work ((-)0.30(1) eb). For ^{132}I , the first excited level was calculated at 75 keV and the spin parities of both the ground state and first excited level could be reproduced from the present calculation. The calculated value for the EQM of 3_1^+ level of ^{132}I , using standard effective charges, comes out to be -0.18 eb which is also close to the experimental data.

The increase in quadrupole moment for the $5/2_1^+$ levels, to a value of -0.761 (17) eb for $N = 72$ iodine, is observed with the increase in number of neutron hole pairs compared to $N = 82$ shell closure. This can be understood as due to the admixtures of different configurations to the wavefunction of the $5/2_1^+$ levels and the corresponding increase in collectivity. Such configuration mixing has been studied through measurement of spectroscopic factors for the $5/2_1^+$ levels in odd-A I nuclei through proton transfer reactions [AUB68, TOL79]. However, these data show almost constant spectroscopic factors for the $5/2_1^+$ levels with $\ell = 2$ ($J = 5/2$) and, therefore, similar contribution from the $\pi d_{5/2}$ orbital in the $5/2_1^+$ levels of $^{125-131}\text{I}$. This concludes that the sum of admixtures of all other possible particle configurations amounts to be similar for all the $5/2_1^+$ level in these iodine nuclei. So, to understand the experimental observation, it would be interesting to study the admixtures in all these $5/2_1^+$ levels of odd-A iodine isotopes from shell model calculation, as a future perspective to the present work.

Chapter 9

Testing of VENTURE for in-beam measurement: Lifetime measurement in ^{124}I

9.1 Introduction

The main aim of this present work was to test the performance of VENTURE array in case of in-beam measurement. Therefore, as a part of the thesis work, the VENTURE array has been utilized to measure the level lifetime of few states in ^{124}I . The choice of the nucleus for the in-beam testing of the array for level lifetime measurement was based on the physics motivation around $Z = 50$ and $N = 82$, which is in line with the present thesis. The same is described briefly in the following paragraph.

The nuclear structure of iodine ($Z = 53$) in the region of $A \sim 120 - 130$ is important due to the presence of shape driving orbitals, in $N/Z = 50 - 82$ subshell space, which leads the shape transitions, diverse shape effects and their coexistence in their nuclear structure. The configuration of wave functions associated with the low spin states mainly comes from the involvement of the $\pi d_{5/2}$, $\pi g_{7/2}$ orbitals, occupied by three valence proton particles, and the $\nu h_{11/2}$, $\nu s_{1/2}$ and $\nu d_{3/2}$ orbitals, occupied by extra neutron holes. Additionally, the $\pi g_{9/2}$ hole collectivity have been observed in these nuclei due to the core excitation of a $1g_{9/2}$ proton across the closed shell ($Z = 50$) and that has been understood in terms of proton-hole quadrupole-core coupling [QUA84, ISA77]. Also, different band structures based on the single particle orbitals have been observed in these nuclei, particularly, in the odd-odd iodine nuclei along with variety of states having lifetime ranging from \sim ps to ms [ENSDF]. As the knowledge of lifetime provides direct understanding of the n-n interaction and the evolution of collectivity associated with the single particle orbitals of proton and neutron thus, the

experimental information of lifetime is very important to study the structure of these nuclei.

However, the experimental data on the heavier odd-odd iodine nuclei ($A > 120$) has been very scanty and particularly, the knowledge of ^{124}I nucleus is limited to proton induced measurements with a few Ge(Li) detectors [BUR82]. A preliminary information on lifetime measurement in the order of $\sim\text{ns}$ exist in literature [MOO11] that was based on the pulsed beam technique. However, the lifetimes of the low lying states of ^{124}I , which may be in the range of few to several picoseconds, are yet till unmeasured. In the present work, taking the advantages of the ultra-fast CeBr₃ detectors, the GCD method have been explored for the in-beam γ -spectroscopic measurement to study the ps order level lifetime in ^{124}I .

9.2 Experimental details

The low lying excited states of ^{124}I nuclei were populated by using fusion evaporation, $^{nat}\text{Sb}(\alpha, \text{xn})$, reaction by bombarding energetic α -beam on ^{nat}Sb [57% ^{121}Sb and 43% ^{123}Sb] target. Due to the use of natural Sb target, ^{122}I was also produced in the reaction. The beam energy has been decided by performing the statistical PACE4 (Projection Angular-momentum coupled Evaporation) model calculation [GAV80, TAR08, PACE4] and the calculated cross-section values have been plotted as a function of projectile energy is shown in Fig. 9.1. According to the figure, the maximum production cross-section of $^{122,124}\text{I}$ is obtained in the energy range of $\sim 38\text{--}42$ MeV of α -beam on ^{nat}Sb target. Therefore, the 40 MeV ^4He beam, delivered from $K = 130$ cyclotron at VECC, Kolkata, was used to bombard the $7\text{mg}/\text{cm}^2$ ^{nat}Sb target. The target was prepared from natural antimony trioxide (Sb_2O_3) powder on a $500\ \mu\text{g}/\text{cm}^2$ thick mylar backing using centrifuge technique.

In the present work, the in-beam spectroscopic experiment has been performed and the γ -rays decaying from excited states were detected and characterized with the VENTURE [ALA17] and VENUS array [SAH18]. The detectors used in this in-beam spectroscopy was configured in the median plane geometry, as shown in Fig. 9.2, around the beam line. The VENUS array of six Compton suppressed Clover Ge detectors and VENTURE array (developed under present thesis) of six $1'' \phi \times 1''$ thick CeBr₃ detectors were kept at a distance of 26 cm and 11 cm, respectively, from the target position. The detectors were placed in such a way so that all the detectors can view the target without any obstacle.

The Mesytec sixteen channel shaper and discriminator modules have been used to process the pre-amplifier pulses from the Clover detectors whereas, the discrete NIM based pulse processing electronics have

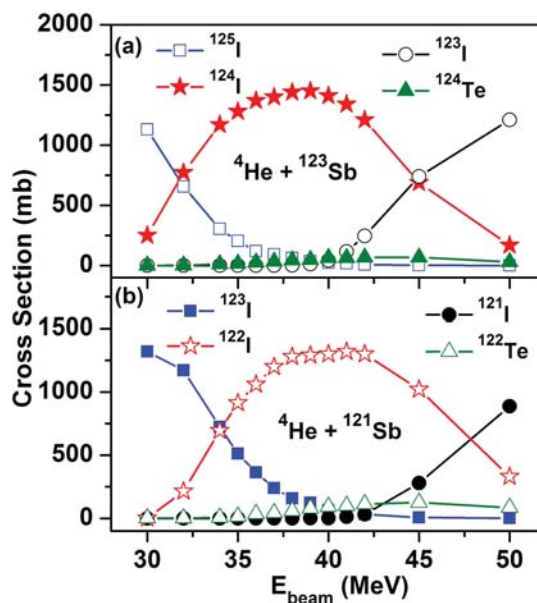


Figure 9.1: Production cross-section of the residues produced in the fusion reaction $^{123}\text{Sb}(\alpha, xn)$ using PACE IV calculation.

been used for the pulse processing of anode and dynode output of CeBr_3 detectors. The common start timing technique (see Fig. 4.10 in Chapter 4) was used for the lifetime measurement using GCD method.



Figure 9.2: In-beam setup of VENTURE array of six CeBr_3 detectors coupled to VENUS array of six Clover detectors is shown.

The zero suppressed list mode data for prompt and delayed coincidence of γ -rays, along with their timing information, have been collected from both type of detectors using the 13 bit Mesytec ADCs, CAEN VME controller and LAMPS DAQ software.

The data were gathered with MASTER trigger in different coincidence mode, viz., $[M_\gamma(\text{CeBr}_3) \geq 2]$

in double coincidence mode, $[M_\gamma(\text{clover}) \geq 2]$ in double coincidence mode and $[M_\gamma(\text{CeBr}_3) \geq 2 \text{ .AND. } M_\gamma(\text{Clover}) \geq 1]$ in triple coincidence mode. The main aim to collect the first type of data, $M_\gamma(\text{CeBr}_3) \geq 2$, was to explore the measurement of level lifetimes of a few strongly populated low lying levels in $^{122,124}\text{I}$ nuclei produced in the in-beam experiment, using the GCD technique. The second type of data, $M_\gamma(\text{clover}) \geq 2$, was gathered to generate the Clover-Clover matrix to verify the known level scheme of $^{122,124}\text{I}$ and to identify the de-excited γ -rays used for the successive ps lifetime measurement. The third type of data, $[M_\gamma(\text{CeBr}_3) \geq 2 \text{ .AND. } M_\gamma(\text{Clover}) \geq 1]$, was collected to study the feasibility and future design of the ps timing experiments with γ tagging with the Clover HPGe detectors using prompt in-beam γ spectroscopy. To generate the prompt time calibration curve required for measurement of level lifetime using GCD method, the necessary data was gathered with the standard source of ^{152}Eu .

9.3 Generation of PRD curve

The $M_\gamma(\text{CeBr}_3) \geq 2$ coincidence data taken with the source ^{152}Eu have been used to generate the PRD curve for the present in-beam setup of VENTURE array. The delayed and anti-delayed time distribution corresponding to different cascades present in ^{152}Eu source have been projected and the obtained centroid differences have been plotted as a function of feeding energies. Finally, a single smooth PRD curve has been generated (see Fig. 9.3 (a)) with the similar procedure as discussed in Section 4.6 of Chapter 4. The curve has been fitted using Eq. (4.22). The fitting parameters have been used to determine the PRD values within the fitting range. The fit residuum for the data points of PRD curve has been shown in Fig. 9.3 (b) with respect to 3σ deviation, where σ is the standard deviation.

9.4 Analysis and results

In the present thesis work, the raw list files of triple coincidence were sorted and made two types of coincidence data: $\text{CeBr}_3\text{-CeBr}_3\text{-Clover}$ and $\text{Clover-Clover-CeBr}_3$ by incorporating the logic program in software analysis with LAMPS. So, the second set of data is basically from four fold coincidence events and so have extremely low statistics. The total energy projections of both CeBr_3 and Clover detector are shown in Fig. 9.5 where, the CeBr_3 spectrum was obtained from $\text{CeBr}_3\text{-CeBr}_3\text{-Clover}$ triple coincidence data and the Clover spectrum was obtained from $\text{Clover-Clover-CeBr}_3$ triple coincidence data. The presented total energy projections are displayed without subtraction of the underlying background.

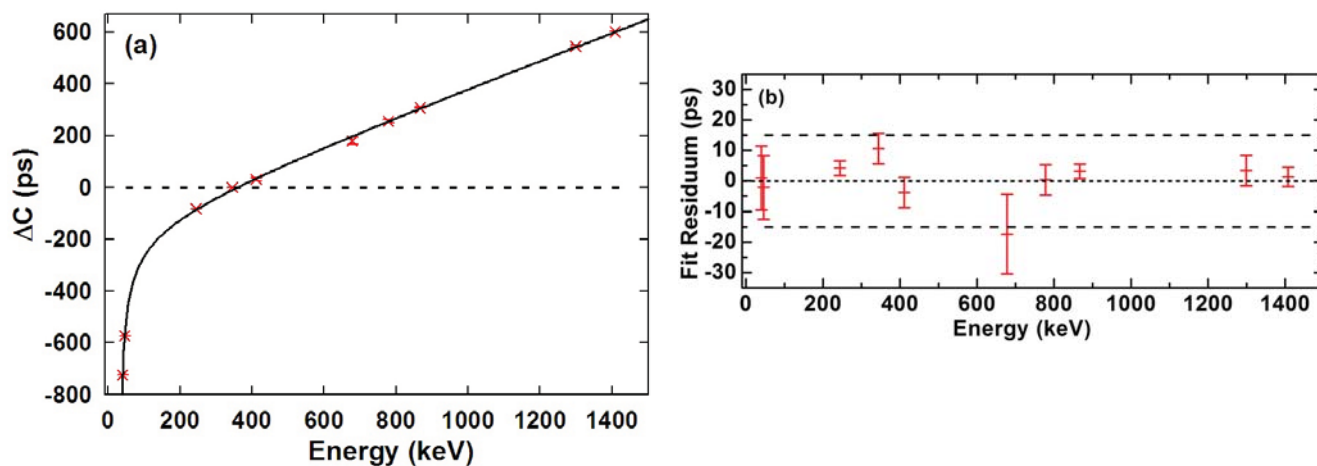


Figure 9.3: The PRD curve (a) obtained with the VENTURE array of in-beam setup and the fit residuum (b) along with 3σ have been shown.

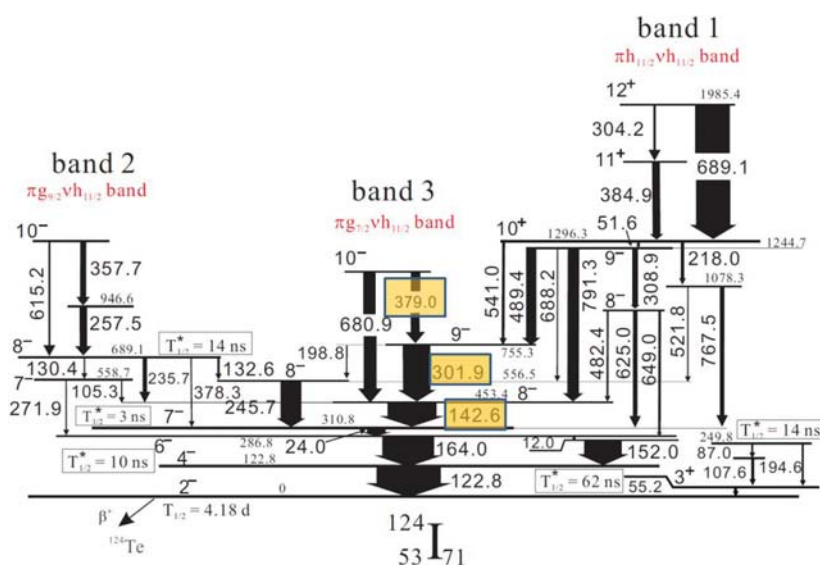


Figure 9.4: The level scheme of ^{124}I taken from Ref. [MOO11] has been shown.

Due to large Compton background in the energy spectrum of CeBr_3 and so many closely spaced γ energies decayed from two nuclei populated with significant cross-section, it was very difficult to select the particular γ peaks in CeBr_3 detector without contribution of other γ peaks due to limitation of energy resolution of this detector. Therefore, the CeBr_3 - CeBr_3 -Clover triple coincidence data were helpful to reduce the said problem while an energy gate was used in Clover detector and hence, the energy gates of feeding and decaying γ -rays were selected in CeBr_3 detector from the Clover gated energy spectrum. The energy gates used in Clover detector having high energy resolution, drastically reduced the Compton events in the

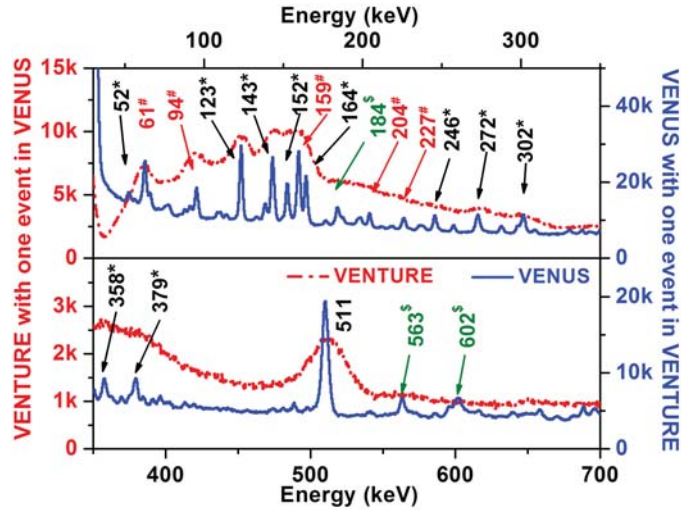


Figure 9.5: The total energy projections of both CeBr_3 (red, dot) and Clover (blue, solid) obtained from CeBr_3 - CeBr_3 -Clover and Clover-Clover- CeBr_3 triple coincidence data, respectively, have been shown. The strong photopeaks from ^{122}I and ^{124}I are marked with \star and $\#$ signs, respectively. The $\$$ sign has been used to mark photopeaks which may be new transitions or may come from other nuclei that have been also produced in the same fusion reaction.

gated spectrum and also reduced the chance of contamination due to the neighbouring γ peaks. Therefore, an easier selection of γ peaks of interest in CeBr_3 detector were possible.

In the present work, the lifetime of 8^- and 9^- states in ^{124}I (see Fig. 9.4) have been measured using GCD method. The relevant results are given in Table 9.1. Figs. 9.6 and 9.7 demonstrates the energy selection procedure. In case of lifetime measurement of 8^- in ^{124}I , the energy gate at 143 keV was selected, as shown in Fig. 9.6 (a), from the projected energy spectra of CeBr_3 , obtained with double gate at 379 keV and 302 keV in Clover and CeBr_3 , respectively, from the CeBr_3 - CeBr_3 -Clover triple coincidence data. For a comparison with the Clover data, the similar energy gate at 379 keV in Clover and 302 keV in CeBr_3 were used to project the Clover energy spectrum from the Clover-Clover- CeBr_3 triple coincidence data. The comparison of these two spectra was helpful to identify the unresolved photopeak around the energy of interest and also, in selecting the energy gate for lifetime measurement. In the similar procedure, in case of feeding γ -ray, 302 keV, as shown in Fig. 9.6 (b), the double gated energies [379 keV in Clover and 143 keV in CeBr_3] have been projected and compared using both CeBr_3 - CeBr_3 -Clover and Clover-Clover- CeBr_3 triple coincidence data. Therefore, the delayed and anti-delayed time distributions for 302-143 keV γ - γ cascade have been projected from the CeBr_3 - CeBr_3 -Clover data, as shown in Fig. 9.8 (a). During the projection of time distributions from the CeBr_3 - CeBr_3 TAC, the Clover gate in 379 keV has always been used with the

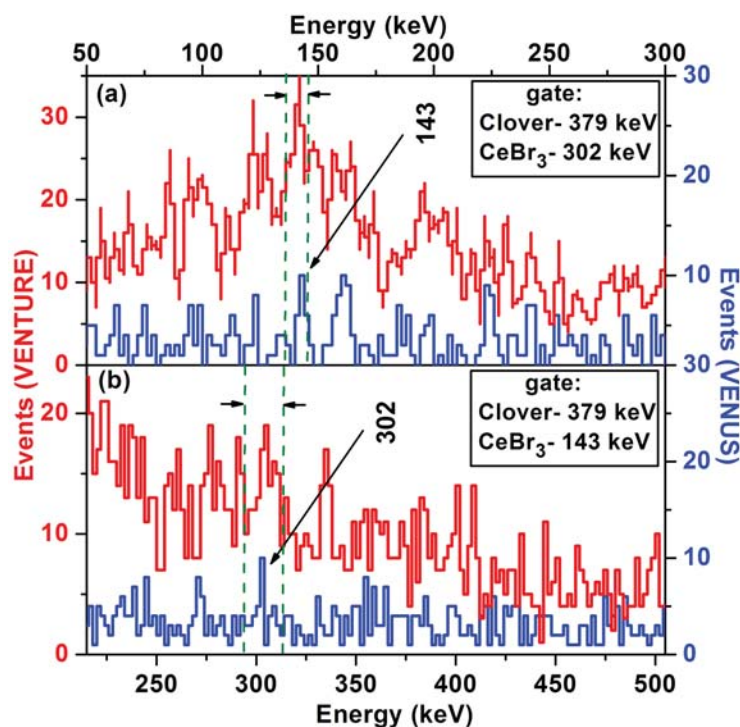


Figure 9.6: The CeBr₃ (red) and Clover (blue) gated energy spectrums from CeBr₃-CeBr₃-Clover and Clover-Clover-CeBr₃ triple coincidence data, respectively, are shown. (a) The 143 keV energy has been projected in both Clover and CeBr₃ with the double gate at 379 keV in Clover and at 302 keV in CeBr₃ and (b) The 302 keV energy has been projected in both Clover and CeBr₃ with the double gate at 379 keV in Clover and at 143 keV in CeBr₃.

presence of feeding and decaying energy gates in CeBr₃ detectors. Therefore, from the knowledge of the measured centroid difference (ΔC) and the PRD values, the lifetime of the 8^- , 453 keV level of ^{124}I has been measured and listed in Table 9.1.

Similar procedure was used to measure the lifetime of 9^- , 755 keV level of ^{124}I . In this case, Clover energy gate was used at 143 keV to project and select the feeding γ -ray 379 keV and the decaying γ -ray 302 keV from both the triple coincidence data, as shown in Fig. 9.7. and The corresponding delayed and anti-delayed time distributions for 302-143 keV $\gamma - \gamma$ cascade have been shown in Fig. 9.8 (b). Due to low statistics all the time distribution spectra have been compressed from 8k channel to 1k.

The lifetimes measured in the present work with the GCD method are summed up in Table 9.1 along with some relevant information.

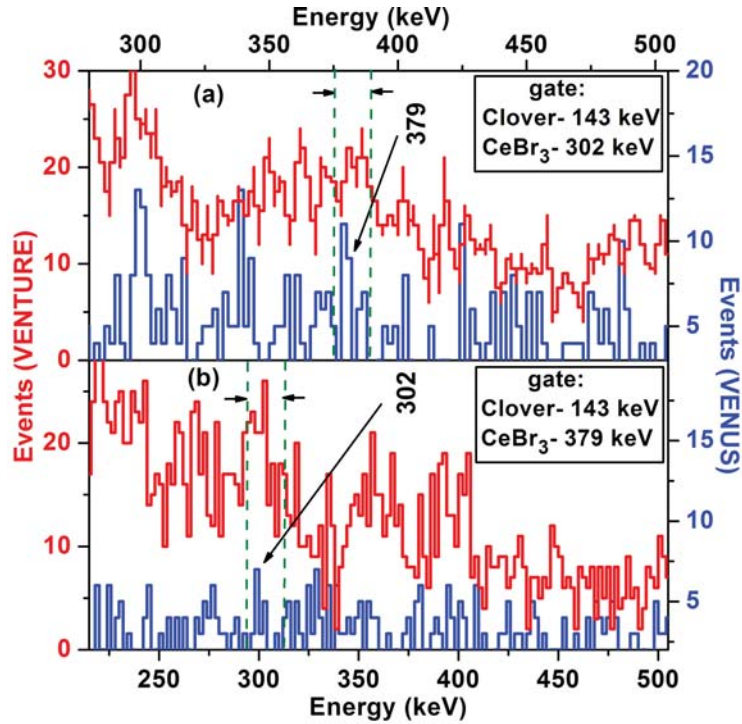


Figure 9.7: The CeBr₃ (red) and Clover (blue) gated energy spectrums from CeBr₃-CeBr₃-Clover and Clover-Clover-CeBr₃ triple coincidence data, respectively, are shown. (a) The 379 keV energy has been projected in both Clover and CeBr₃ with the double gate at 143 keV in Clover and at 302 keV in CeBr₃ and (b) The 302 keV energy has been projected in both Clover and CeBr₃ with the double gate at 143 keV in Clover and at 379 keV in CeBr₃.

Table 9.1: The measurement of lifetime of different levels in ¹²⁴I in the present work using VENTURE array have been shown.

Level	E_x (keV)	Cascade (keV)	$ \Delta C $ ps	$ \text{PRD} $ ps	τ ps
8^-	453	302-143	360 (20)	147 (14)	107 (12)
9^-	755	379-302	122 (16)	53 (14)	35 (11)

9.5 Discussion

The work represents the performance of CeBr₃ detectors, for the first time, for the measurement of level lifetime with the GCD method in case of in-beam experiment. Due to low statistics, We couldn't able

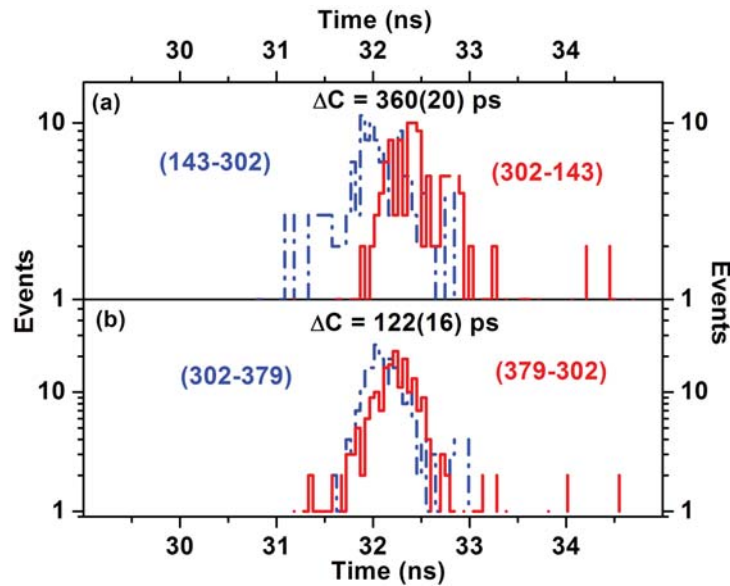


Figure 9.8: The delayed and anti-delayed TAC spectra of cascade (302-143) and (379-302) keV of ^{124}I , used for the lifetime measurement in GCD method, are shown. The red solid line corresponds to the delayed time distribution and the blue dotted line correspond to the anti-delayed time distribution.

to subtract the effect of background contribution from the measured centroid difference and also, didn't measure the ns order lifetime with the slope method. Therefore, from the present work, it has been realised that the triple coincidence data have been helpful to perform the lifetime measurement and also, the statistics of the data need to be increased for the accurate measurement. Therefore, an array with more number of detectors is needed to collect the data and hence, a modification of VENTURE array is required.

Bibliography

- [ACK15] U. Ackermann *et al.*, Nucl. Instr. and Meth. in Phys. Res. A **786** (2015) 5.
- [ADL78] J.P. Adloff, Radiochimica Acta **25** (1978) 57.
- [AKK12] S. Akkoyun *et al.*, Nucl. Instr. and Meth. in Phys. Res. A **668** (2012) 26.
- [ALAM15] S.S. Alam *et al.*, Proc. of DAE-BRNS Symposium on Nuclear Physics **60** (2015) 270.
- [ALA16a] S.S. Alam *et al.*, Proc. of DAE-BRNS Symposium on Nuclear Physics **61** (2016) 316.
- [ALA16b] S.S. Alam *et al.*, Proc. of DAE-BRNS Symposium on Nuclear Physics **61** (2016) 318.
- [ALA16c] S.S. Alam *et al.*, Proc. of DAE-BRNS Symposium on Nuclear Physics **61** (2016) 320.
- [ALA17] S.S. Alam *et al.*, Nucl. Instr. and Meth. in Phys. Res. A **874** (2017) 103.
- [ALA18] S.S. Alam *et al.*, Proc. of DAE-BRNS Symposium on Nuclear Physics **63** (2018) 356.
- [ALA19] S.S. Alam *et al.*, Phys. Rev. C **99** (2019) 014306.
- [ALA20] S.S. Alam *et al.*, Eur. Phys. J. A **56** (2020) 269.
- [ALL11] J.M. Allmond *et al.*, Phys. Rev. C **84** (2011) 061303(R).
- [ALL14] J.M. Allmond *et al.*, Phys. Rev. Lett. **112** (2014) 172701.
- [AND76] G. Andersson *et al.*, Nucl. Phys. A **268** (1976) 205.
- [ANG02] G. de Angelis *et al.*, Phys. Lett. B **535** (2002) 93.
- [AUB68] R.L. Auble, J. B. Ball and C.B. Fulmer, Phys. Rev **169** (1968) 955.

- [BAR68] M. Baranger and E. Vogt, *Advances in Nuclear Physics*, Vol. 10, Plenum press, N.Y, (1968) 197.
- [BAS07] B. Bastin *et al.*, *Phys. Rev. Lett.* **99** (2007) 022503.
- [BAY50] Z. Bay, *Calculation of Decay Times from Coincidence Experiments*, *Phys. Rev.* **77** (1950) 419.
- [BET36] H.A. Bethe and R.F. Bacher, *Rev. Mod. Phys.* **8** (1936) 82.
- [BEY67] L.M. Beyer and W.H. Kelly, *Nucl. Phys. A* **104** (1967) 274.
- [BHA01a] P. Bhattacharyya *et al.*, *Phys. Rev. Lett.* **87** (2001) 062502.
- [BHA01b] P. Bhattacharyya *et al.*, *Phys. Rev. C* **64** (2001) 054312.
- [BHA13] T. Bhattacharjee *et al.*, *Phys. Rev. C* **88** (2013) 014313.
- [BIL11] R. Billnert *et al.*, *Nucl. Instr. and Meth. in Phys. Res. A* **647** (2011) 94.
- [BIS16] S. Biswas *et al.*, *Phys. Rev. C* **93** (2016) 034324.
- [BLA05] F. Le Blanc *et al.*, *Phys. Rev. C* **72** (2005) 034305.
- [BOH37] N. Bohr and F. Kalckar. *Kgl. Danske Videnskabernes Selskab, Math.-Fys. Meddelelser* 14, No. 10 (1937).
- [BRA47] E.L. Brady and M. Deutsch, *Phys. Rev.* **72** (1947) 870.
- [BRA48] E.L. Brady and M. Deutsch, *Phys. Rev.* **74** (1948) 1541.
- [BRO85] B.A. Brown *et al.*, *MSU-NSCL Report No. 524* (1985).
- [BRO05] B.A. Brown *et al.*, *Phys. Rev. C* **71** (2005) 044317.
- [BRO14] B.A. Brown and W.D.M. Rae, *Nucl. Data Sheets* **120** (2014) 115.
- [BRO] B.A. Brown, W.D.M. Rae, E. McDonald and M. Horoi, *NuShellX@MSU*, [http://www.nucl.msu.edu/~sim\\$brown/resources/resources.html](http://www.nucl.msu.edu/~sim$brown/resources/resources.html).
- [BRU86] R. Brun *et al.*, *GEANT3*, CERN - DD/EE/84-1, 1986.

- [BUC16] B. Bucher *et al.*, Phys. Rev. Lett. **116** (2016) 112503.
- [BUJ07] M. Ionescu-Bujor *et al.*, Phys. Lett. B **650** (2007) 141.
- [BUR82] J. Burde *et al.*, Nucl. Phys. A **385** (1982) 29.
- [BUR85] S.M. Burnett *et al.*, Nucl. Phys. A **432** (1985) 514.
- [BUT89] T. Butz *et al.*, Nucl. Instr. and Meth. in Phys. Res. A **284** (1989) 417.
- [BUT15] T. Butz, *Fourier Transformation for pedestrians*, **2nd Ed. Springer** pp 71 (2015).
- [CAS90] R.F. Casten, Nuclear Structure from Simple Perspectives, Oxford University Press, 1990.
- [CAU99] E. Caurier *et al.*, Phys. Rev. C **59** (1999) 2033.
- [CAU02] E. Caurier, G. Martínez-Pinedo, Nucl. Phys. A **704** (2002) 60.
- [CHA20] S. Dey Chaudhuri *et al.*, Journal of Radioanalytical and Nuclear Chemistry 324 (2020) 829.
- [COQ10] L. Coquard *et al.*, Phys. Rev. C **82** (2010) 024317.
- [COR05] L. Coraggio *et al.*, Phys. Rev. C **72** (2005) 057302.
- [DAF85] E. Dafni *et al.*, Phys. Rev. Lett **55** (1985) 1269.
- [DAN39] S.M. Dancoff and P. Morrison, Phys. Rev. **55** (1939) 122.
- [DAS99] S.K. Das, R. Guin and S.K. Saha, Eur. Phys. J. A **4** (1999) 1.
- [DEL10] I. Deloncle *et al.*, J. Phys.: Conference Series **205** (2010) 012044.
- [DEV65] S.H. Devare, R.M. Singru and H.G. Devare, Phys. Rev. B **140** (1965) 536.
- [DEW89] A. Dewald, S. Harissopulos, P.von Brentano, Zeitschrift für Physik A **334** (1989) 163.
- [DIK74] M. Dikšić, L. Yaffe and D.G. Sarantites, Phys. Rev. C **10** (1974) 1172.
- [DOB94] J. Dobaczewski *et al.*, Phys. Rev. Lett. **72** (1994) 981.
- [DOB07] J. Dobaczewski *et al.*, Prog. in Particle and Nuclear Phys. **59** (2007) 432.
- [DOL13] N. D'Olympia *et al.*, Nucl. Instr. and Meth. in Phys. Res. A **728** (2013) 31.

- [DOR04] P. Dorenbos, J.T.M. de Haas, C.W.E. van Eijk, IEEE Trans. Nucl. Sci. **51** (2004) 1289.
- [DRO08] W. Drozdowski *et al.*, IEEE Trans. Nucl. Sci. **55** (2008) 1391.
- [DUC99] G. Duchêne *et al.*, Nucl. Instr. and Meth. in Phys. Res. A **432** (1999) 90.
- [ENSDF] ENSDF data file: www.nndc.bnl.gov/ensdf.
- [FEREN] M. Ferentz and N. Rosenzweig, Table of F-Coefficients, ANL-5324.
- [FEN73] D.H. Feng, R.H. Ibarra and M. Vallieres, Phys. Lett. B **46** (1973) 37.
- [FOG94] B. Fogelberg *et al.*, Phys. Rev. Lett. **73** (1994) 2413.
- [FOS74] D.B. Fossan and E.K. Warburton, Nuclear Spectroscopy and Reaction, Part C (1974).
- [FRA51] H. Fraunfelder, Phys. Rev. **82** (1951) 549.
- [FRA55] H. Fraunfelder *et al.*, Beta- and Gamma-Ray Spectroscopy, Edited by K. Siegbahn, Chap.XIX, North Holland (1955).
- [FRA65] H. Fraunfelder and R.M. Steffen, Alpha Beta and Gamma Ray Spectroscopy, K. Siegbahn, Ed. Vol II, Chap. XIX, North Holland, Amsterdam(1965).
- [FRA13] L.M. Fraile *et al.*, Nucl. Instr. and Meth. in Phys. Res. A **701** (2013) 235.
- [FRA17] L.M. Fraile, J. Phys. G: Nucl. Part. Phys. **44** (2017) 094004.
- [FRE61] J.B. French, M. H. McFarlane, Nucl. Phys. A **26** (1961) 168.
- [FRE08] D.De Frenne and A. Negret Nucl. Data Sheet **109** (2008) 943.
- [GAV80] A. Gavron, Phys. Rev. C **21** (1980) 230.
- [GAU08] P. Gauss *et al.*, Nucl. Instr. and Meth. in Phys. Res. A **608** (2008) 297.
- [GOE46] G. Goertzel, Phys. Rev. **70** (1946) 897.
- [GRA07] H. Grawe, K. Langanke, and G. Martínez-Pinedo, Rep. Prog. Phys. **70** (2007) 1525.
- [GRO87] M. Grodzicki *et al.*, J. Phys. B: At. Mol. Phys. **20** (1987) 5595.

- [HAA73] H. Haas and D.A. Shirley, *J. Chem. Phys.* **58** (1973) 3339.
- [HAF64] D.W. Hafemeister, G. Depasquali and D.H. Dewaard, *Phys. Rev.* **135** (1964) B1089.
- [HAM40] D.R. Hamilton, *Phys. Rev.* **58** (1940) 122.
- [HAM09] Hamamatsu Photonics, Photomultiplier Tube R9779 Specifications, 2009 [www.hamamatsu.com].
- [HAR00] B. Harss *et al.*, *Rev. Sci. Instrum.* **71** (2000) 380.
- [HEER] Ernst Heer and Theodore B. Novey, *The interdependence of Solid State Physics and Angular Distribution of Nuclear Radiations*, University of Rochester, Rochester, New York, and Argonne National Laboratory, Lemont, Illinois.
- [HIL53] D.L. Hill and J.A. Wheeler, *Phys. Rev.* **89** (1953) 1102.
- [HIN91] B. Hinfurtner *et al.*, *Phys. Rev. Lett* **67** (1991) 812.
- [HOR13] M. Horoi and B. A. Brown, *Phys. Rev. Lett.* **110** (2013) 222502.
- [HOR55] Hisashi Horie and Akito Arima, *Phys. Rev.* **99** (1955) 778.
- [HYM64] L.G. Hyman, R.M. Schwarcz and R.A. Schluter, *Rev. Sci. Instrum.* **35** (1964) 393.
- [IAEA] <https://www-nds.iaea.org/nuclearmoments/>
- [ILI16] S. Ilieva *et al.*, *Phys. Rev. C* **94** (2016) 034302.
- [ION07] M. Ionescu-Bujor *et al.*, *Phys. Lett. B* **650** (2007) 141.
- [ISA77] P. Van Isacker *et al.*, *Nucl. Phys. A* **292** (1977) 125.
- [JAK02] G. Jakob *et al.*, *Phys. Rev. C* **65** (2002) 024316.
- [JAN05] R.V.F. Janssens, *Nature* **435** (2005) 897.
- [KAY18] L. Kaya *et al.*, *Phys. Rev. C* **98** (2018) 014309.
- [KHA05] Yu. Khazov *et al.*, *Nucl. Data Sheets* **104** (2005) 497.
- [KHA06] Yu. Khazov, I. Mitropolsky, A. Rodionov, *Nucl. Data Sheets* **107** (2006) 2715.

- [KHA11] Yu. Khazov, A. Rodionov and F.G. Kondev, Nucl. Data Sheet **112** (2011) 855.
- [KHAL04] J. Al-Khalili and E. Roeckl (Eds), The Euro. Lec. on Phys. with Exotic Beams, Vol. 1, 2004, p3.
- [KHAL06] J. Al-Khalili and E. Roeckl (Eds), The Euro. Lec. on Phys. with Exotic Beams, vol. 2, 2006.
- [KIB08] T. Kibédi *et al.*, Nucl. Instr. and Meth. in Phys. Res. A **589**, 202 (2008).
- [KIS63] L.S. Kisslinger and R.A. Sorensen, Rev. Mod. Phys. **35** (1963) 853.
- [KNO10] G. Knoll, Radiation Detection and Measurement, 4th Ed., John Wiley & Sons Inc., 2010.
- [KRA87] K.S. Krane. Introductory Nuclear Physics. Wiley, 1987.
- [LAMPS] <https://www.tifr.res.in/~pell/lamps.html>.
- [LAN74] G. Langouche *et al.*, Phys. Rev. B **9** (1974) 848.
- [LAV83] M. Laval *et al.*, Nucl. Instr. and Meth. in Phys. Res. A **206** (1983) 169.
- [LEC14] Paul Lecoq, Alexander Gektin, Mikhail Korzhik, Inorganic Scintillators for Detector Systems, Springer, 2017 (Chapter 5).
- [LEO94] W.R. Leo, Techniques for nuclear and particle physics experiments, Springer (1994).
- [LHE75] G. Lhersonneau *et al.*, Phys. Rev. C **12** (1975) 609.
- [LIU09] S.H. Liu *et al.*, Phys. Rev. C **79** (2009) 067303.
- [LOZ11] R.L. Lozeva *et al.*, Phys. Lett. B **694** (2011) 316.
- [LUT13] G. Lutter *et al.*, Nucl. Instr. and Meth. in Phys. Res. A **703** (2013) 158.
- [MAC71] E.S. Macias and W.B. Walters, Nucl. Phys. A **161** (1971) 471.
- [MACH] H. Mach, The initial plans for a fast timing array at DESPEC, <http://nuclear.fis.ucm.es/fasttiming/files>.
- [MAC89] H. Mach, R.L. Gill, M. Moszyński, Nucl. Instr. and Meth. in Phys. Res. A **280** (1989) 49.
- [MAC95] H. Mach *et al.*, Phys. Rev. C **51** (1995) 500.

- [MAC96] R. Machleidt, F. Sammarruca, and Y. Song, Phys. Rev. C **53**, R1483 (1996).
- [MAH92] J.P. Maharana *et al.*, Phys. Rev. C **46** (1992) R1163.
- [MAJ09] A. Maj *et al.*, The paris project, Acta Physica Pol. B **40** (2009) 565.
- [MAR10] N. Mărginean *et al.*, Eur. Phys. J. A **46** (2010) 329.
- [MAS05] P. Mason *et al.*, Phys. Rev. C **72** (2005) 064315.
- [MAY49] M.G. Mayer, Phys. Rev. **75** (1949) 1969.
- [MAY50] M.G. Mayer, Phys. Rev. **78** (1950) 16.
- [MEY76] R.A. Meyer *et al.*, Phys. Rev. C **13** (1976) 1617.
- [MIZ00] T. Mizusaki, RIKEN Acc. Progr. Report **33** (2000) 14.
- [MOO11] C.B. Moon *et al.*, Jour. of the Korean Phys. Society **59** (2011) 1525.
- [MOR76] H. Morinaga and T. Yamazaki, In-beam Gamma Ray Spectroscopy, North-Holland Pub. Company, Oxford, 1976.
- [MOS89] M. Moszyński and H. Mach, Nucl. Instr. and Meth. in Phys. Res. A **277** (1989) 407.
- [MUE06] W.F. Mueller *et al.*, Phys. Rev. C **73** (2006) 014316.
- [MUH08] Curran D. Muhlberger, Angular Correlation of Gamma Rays, University of Maryland, College Park, May 9, 2008.
- [MUR10] S. Muralithar *et al.*, Nucl. Instr. and Meth. in Phys. Res. A **622** (2010) 281.
- [NAV90] O. Naviliat-Cuncic *et al.*, Nucl. Instr. and Meth. in Phys. Res. A **287** (1990) 487.
- [NAV98] P. Navrátil and B. R. Barrett, Phys. Rev. C **57** (1998) 3119.
- [NIL55] S.G. Nilsson, Mat. Fys. Medd. Dan. Vid. Selsk. **29** (1955).
- [NIL69] S.G. Nilsson *et al.*, Nucl. Phys. A **131** (1969) 1.
- [NNDC] www.nndc.bnl.gov/ensdf/

- [NOM17] K. Nomura, R. Rodríguez-Guzmán and L.M. Robledo, Phys. Rev. C **96** (2017) 064316.
- [OMT95] J.P. Omtvedt *et al.*, Phys. Rev. Lett. **75** (1995) 3090.
- [OOM79] H. Ooms *et al.*, Nucl. Phys. A **321** (1979) 180.
- [OTS01] T. Otsuka *et al.*, Phys. Rev. Lett. **87** (2001) 082502.
- [OTS05] T. Otsuka *et al.*, Phys. Rev. Lett. **95** (2005) 232502.
- [PACE4] <http://lise.nsl.msu.edu/pace4>.
- [PET06] P. Petkov, A. Dewald, P. von Brentano, Nucl. Instr. and Meth. in Phys. Res. A **560** (2006) 564.
- [PHOTO] Photomultiplier Tubes Catalogue [www.photonis.com].
- [PUD80] G. Puddu, O. Scholten and T. Otsuka, Nucl. Phys. A **348** (1980) 109.
- [PYY18] P. Pyykkö, Molecular Physics **116** (2018) 1328.
- [QUA84] M.A. Quader *et al.*, Phys. Rev. C **30** (1984) 1772.
- [QUA11] F.G.A. Quarati *et al.*, Nucl. Instr. and Meth. in Phys. Res. A **629** (2011) 157.
- [QUA13] F.G.A. Quarati *et al.*, Nucl. Instr. and Meth. in Phys. Res. A **729** (2013) 596.
- [QUA14] F.G.A. Quarati *et al.*, Nucl. Instr. and Meth. in Phys. Res. A **735** (2014) 655.
- [RAE] W.D.M. Rae, NuShellX, <http://www.garsington.eclipse.co.uk>.
- [RAM01] S. Raman, C.W. Nestor, Jr., and P. Tikkanen, Atomic Data and Nucl. Data Tab. **78** (2001) 1.
- [RAU04] R. Raut *et al.*, Proc. of DAE-BRNS Symposium on Nuclear Physics, **47B** (2004) 578.
- [REG10] J.-M. Régis *et al.*, Nucl. Instr. and Meth. in Phys. Res. A **622** (2010) 83.
- [REG12] J.-M. Régis *et al.*, Nucl. Instr. and Meth. in Phys. Res. A **684** (2012) 36.
- [REG13] J.-M. Régis *et al.*, Nucl. Instr. and Meth. in Phys. Res. A **726** (2013) 191.

- [REG14] J.-M. Régis *et al.*, Nucl. Instr. and Meth. in Phys. Res. A **763** (2014) 210.
- [REG16a] J.-M. Régis *et al.*, Nucl. Instr. and Meth. in Phys. Res. A **823** (2016) 72.
- [REG16b] J.-M. Régis *et al.*, Nucl. Instr. and Meth. in Phys. Res. A **811** (2016) 42.
- [REG17] J.-M. Régis *et al.*, Phys. Rev. C **95** (2017) 054319.
- [REGA12] P.H. Regan, Applied Radiation and Isotopes **70** (2012) 1125.
- [ROB72] Rosalie Robinette, J.G. Cosgrove and R.L. Collins, Nucl. Instr. and Meth. **105** (1972) 509.
- [ROB14] Oliver J. Roberts *et al.*, Nucl. Instr. and Meth. in Phys. Res. A **748** (2014) 91.
- [ROS98] C. Rossi Alvarez, IL NUOVO CIMENTO VOL. **111** A, N. 6-7 Giugno-Luglio 1998.
- [RUD15] M. Rudigier *et al.*, Phys. Rev. C **91** (2015) 044301.
- [SAH18] A. Saha *et al.*, Nucl. Phys. A **976** (2018) 1.
- [SAH18a] A. Saha, Thesis paper, 2018, p12.
- [SAR01] Sukhendusekhar Sarkar and M. Saha Sarkar, Phys. Rev. C **64** (2001) 014312.
- [SAR04] Sukhendusekhar Sarkar and M. Saha Sarkar, Eur. Phys. J. A **21** (2004) 61.
- [SCH68] A.Z. Schwarzschild and E.K. Warburton, Annu. Rev. Nucl. Sci. **18** (1968) 265.
- [SEL15] K. Selvakumar *et al.*, Phys. Rev. C **92** (2015) 064307.
- [SHA03] K.S. Shah *et al.*, IEEE Trans. Nucl. Sci. **50** (2003) 2410.
- [SHA05] K.S. Shah *et al.*, IEEE Trans. Nucl. Sci. **52** (2005) 3157.
- [SHE02] J. Shergur *et al.*, Phys. Rev. C **65** (2002) 034313.
- [SIF06] R. Sifi *et al.*, Hyperfine Interact **171** (2006) 173.
- [SPE89] R.H. Spear, Atomic Data and Nucl. Data Tables **42** (1989) 55.
- [STE55] Rolf M. Steffen (1955): Extranuclear effects on angular correlations of nuclear radiations, Advances in Physics, **4:15**, 293.

- [STEP13] D. Steppenbeck *et al.*, Nature **502** (2013) 207.
- [STO16] N.J. Stone, Atom. Data and Nucl. Data Tables **111** (2016) 1.
- [STO89] Craig A. Stone, Scott H. Faller and William B. Walters, Phys. Rev. C **39** (1989) 1963.
- [TAN67] P.N. Tandon and H.G. Devare, Nucl. Phys. A **102** (1967) 203.
- [TAN92] I. Tanihata *et al.*, Phys. Lett. B **289** (1992) 261.
- [TAN09] M. Tanigaki *et al.*, Phys. Rev. C **80** (2009) 034304.
- [TAR08] O.B. Tarasov, D. Bazin, Nucl. Instr. and Meth. in Phys. Res. B **266** (2008) 4657.
- [TER15] E. Teruya *et al.*, Phys. Rev. C **92** (2015) 034320.
- [TOL79] A. Szanto de Toledo, H. Hafner and H.V. Klapdor, Nucl. Phys. A **320** (1979) 309.
- [VIA83] R. Vianden, Hyperfine Interactions **15/16** (1983) 1081.
- [VOG17] A. Vogt *et al.*, Phys. Rev. C **96** (2017) 024321.
- [WAL84] W.B. Walters, Phys. Rev. C **29** (1984) 991.
- [WAR04] D. Warner, Nature **430** (2004) 517.
- [WAT09] H. Watanabe *et al.*, Phys. Rev. C **79** (2009) 064311.
- [WEI35] C.F. Von Weizsäcker, Z. Phys. **96** (1935) 431.
- [WEI51] V.F. Weisskopf, Phys. Rev. **83** (1951) 1073.
- [WIE16] J. Wiederhold *et al.*, Phys. Rev. C **94** (2016) 044302.
- [XIE96] H. Xie *et al.*, Nucl. Phys. A **599** (1996) 560.
- [ZWA85] D. Zwarts, Comp. Phys. Comm. **38** (1985) 365.

Thesis Highlight

Name of the Student: Shaikh Safikul Alam

Name of the CI/OCC: Variable Energy Cyclotron Centre **Enrolment No.:** PHYS04201404007

Thesis Title: Development of Fast Timing Array at VECC and its Application in Nuclear Structure Study around $Z = 50$ and $N = 82$ Shell Closure

Discipline: Physical Sciences **Sub-Area of Discipline:** Low Energy Experimental Nuclear Physics

Date of viva voice: 18th June, 2021

The study of nuclei around double shell closure ^{132}Sn , far from the β -stability line, is very important to understand the interplay between single-particle and collective behaviors of nuclear structure. The measurement of electromagnetic transition rates, i.e. inverse of nuclear level lifetime, is very important to address this phenomena. Moreover, the measurement of Electric Quadrupole Moment (EQM) provides the amount of deformation from sphericity. However, the experimental knowledge, till now, for these n-rich nuclei is very scanty due to the experimental difficulty in accessing this region. Taking the advantages of availability of state-of-the-art scintillation detectors, viz. $\text{LaBr}_3(\text{Ce})$, CeBr_3 etc., combined with the fission reaction followed by radiochemical separation of the fission fragments, it is possible to explore the low lying states of these nuclei. As most of nuclear level lifetime lie in the sub-nanosecond to picosecond region, therefore, development of a γ - γ fast timing array is of utmost necessity for the measurement of lifetime along with EQM in these nuclei.

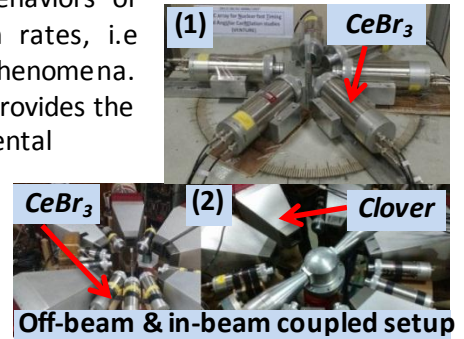


Fig.1 VENTURE array (1) Stand-alone mode (2) Coupled with VENUS array

For this purpose, individual 1" ϕ x 1" thick CeBr_3 detectors coupled to Hamamatsu R9779 photomultiplier tubes (PMT) have been characterized and the fast timing array, VECC Array for Nuclear fast Timing and Angular Correlation Studies (VENTURE), has been developed at VECC, Kolkata. The array (Fig.1) could be used in its stand-alone mode as well as with the array of Clover HPGe detectors like VENUS or INGA. The VENTURE array has been tested for both off-beam and in-beam experiments to explore the direct lifetime measurement technique, Generalised Centroid

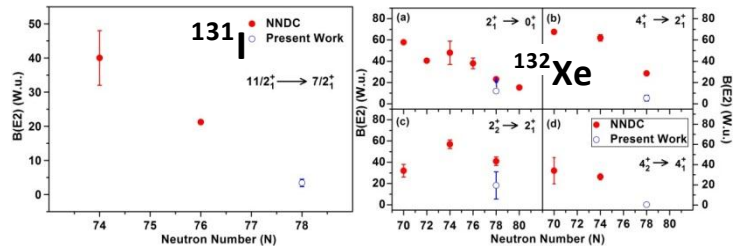


Fig.2 $B(E2)$ value corroborates with shell closure at $N=82$.

Difference (GCD) method based on Mirror Symmetric Centroid Difference (MSCD) method.

The developed facility, first of its kind of India, has been used for the measurement of nuclear level lifetime in n-rich nuclei ^{131}I , ^{132}Xe . The measured transition probabilities corroborate with double shell closure of ^{132}Sn (Fig.2) and establishes the presence of octupole correlation in ^{131}I .

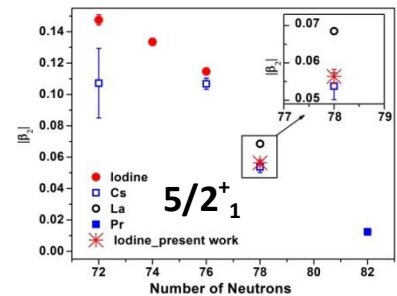


Fig.3 Deformation corroborates with shell closure at $N=82$.

An angular correlation table has also been developed at VECC to study the possibility of EQM measurement using Integral PAC (IPAC) and Time differential PAC (TDPAC) technique. The TDPAC method has been used to measure the EQM in ^{131}I and ^{132}I . The obtained deformation and quadrupole moment corroborates the shell closure at $N=82$ (Fig.3).